FINITE ELEMENT ANALYSIS OF BOX-GIRDER BRIDGES

A thesis
submitted in partial fulfilment of the requirements
for the degree of
Doctor of Philosophy in Civil Engineering
at the University of Canterbury

by

Thomas Allan Moore

University of Canterbury
Christchurch, New Zealand
1975

ABSTRACT

This thesis presents an efficient numerical method for the structural analysis of box-girder bridges.

The box-girders are assumed to behave as thin spatial plate structures, for which the finite element method is shown to provide an accurate mathematical model when quadrilateral shaped thin planar shell elements, with a linear variation of thickness and the three translational and rotational degrees of freedom at each vertex, are employed. Three dimensional beam elements with eccentric nodes are incorporated to model the kerbs, stiffeners, and piers of bridges.

This finite element approach was used to perform linear elastic analyses of an extensive range of box-girder and slab bridges, the results of which are compared with published experimental or prototype measurements.

The method was extended to enable the geometrically nonlinear response of imperfect flat plates and stiffened plate girders to be computed. Results are compared with analytical solutions, and experimental results where these are available.

To Bev and Zeala

ACKNOWLEDGEMENTS

The research for this thesis was carried out in the Department of Civil Engineering, University of Canterbury, under the overall guidance of its Head, Professor H.J. Hopkins.

The author wishes to express his deepest gradtitude to Dr. Athol J. Carr under whose supervision the investigation was conducted, and to Dr. Nigel Cooke for his assistance in this respect.

Grateful acknowledgement is made of the support and guidance also given by Dr. M.J.N. Priestley and Dr. P.J. Moss, other members of the Department's staff, Mr. R. Taylor and fellow students, and Mr. P. Hirst, who provided technical assistance during the experimental measurements.

The friendly and efficient service provided by the entire staff of the University's Computer Centre is greatly appreciated.

The presentation of this thesis was facilitated by the assistance of the staff of the Canterbury University Engineering School Library with special mention due to Mrs. P. Thomas, the draughting service provided by Mrs. V. Grey and Mr. W. McClelland, the photography service provided by Mr. H. Patterson, the cooperation of the typists, Mrs. A. Watt and Mrs. D. Ball, and the helpful advice of the printer Mr. W. Boyle.

I wish to record my appreciation of the numerous researchers who have contributed to my awareness by publishing the results and conclusions of their work.

CONTENTS

LIST OF FIGURES

Page

LIST OF TABLES

LIST OF SYMBOLS

A list of the most commonly used symbols and their meaning follows. Subscripts have been left off those symbols for which their use follows accepted notation in signifying the members of a series, the members of a vector, or the elements of a matrix.

a) Scalars

a,b	Dimensions of a two dimensional element
c	Elements of the matrix of linear elastic material properties, scalar amplification factor
d	Depth of a beam, derivative operator
f	General function, displacement field
h	Element or plate thickness
i,j	Nodal point designation
l	Length
m,n	Number of numerical integration sampling points in longitudinal and transverse directions of an element respectively
n	Number of element nodal points
r	Radius of curved beam
s,t	Parametric element coordinate system
t	Element or plate thickness
u,v,w	Displacement components in x,y,z directions respectively
vol	Undeformed volume of an element
w_o	Initial out-of-flatness of a plate
w_c	Central transverse deflection of a plate or beam
x,y,z	Local element cartesian coordinates (right-handed system of coordinates)
A	Arbitrary coefficient
D	Flexural rigidity of a plate
E	Young's modulus of elasticity
E_x,E_z	Eccentricities of a node of a beam element from the centroid measured in element x and z directions respectively
F	Applied point load,general function
G	Shear modulus
H	Depth of a beam
I	Moment of inertia

$\|J\|$	Determinant of the Jacobian matrix
L	Length of a plate or the span of a bridge
M	Bending moment
N	Displacement function
P	Applied point load
Pa	Pascal (unit of stress)
P_{cr}	Critical (buckling) load
$\overline{P}$	Load parameter
R	Radius of curvature
R_{ij}	Domain of a rectangular element $x_{i-1} \leqslant x \leqslant x_i$, $y_{j-1} \leqslant y \leqslant y_j$
T	Temperature
U	Strain energy of a continuum
U_x, U_y, U_z	Components of the displacement of a particle in the x,y, and z directions respectively
V	Total potential energy of a continuum
W	Magnitude of applied load
$W_{i,j}$	Weighting of $(i,j)^{th}$ numerical integration point
X,Y,Z	Global coordinate system (right-handed system of coordinates)
α	Included angle between the diagonals of the CQ12 element, coefficient of thermal expansion
α_i, β_i	Generalised nodal deformation parameters
β	Angle between local and global coordinate axis
β_n	Ratio of the magnitude of the applied load at the previous $(n-1)^{th}$ and present n^{th} load increment
∂	Partial derivative operator
γ_{xy}	Shear strain in the x-y plane
δ	Nodal deformation
$\Theta x, \Theta y, \Theta z$	Components of rotations measured about x,y,z axes (positive direction determined by right-hand screw rule)
μs	Microstrain (unit of strain)
ν	Poisson's ratio
π	Ratio of the circumference of a circle to the diameter
σ	Stress component
ω	Frequency of damped vibratory motion
Δ	Denotes an incremental part of the quantity it precedes, midspan deflection of a bridge

Σ	Denotes summation of the indices of the quantity it precedes
$\int$	Integration operator
Φ, Ψ, W	Weighting functions of the displacement field of the CQ12 element
$(\dot{})$	Derivative of quantity in parentheses will respect to $\bar{P}$
$(),()$	Derivative of quantity in first parenthesis with respect to quantity in second parenthesis

(b) Vectors and Matrices

$< >$	Row vector
$\{ \}$	Column vector
$[ ]$	Matrix. Note: [15] denotes reference number 15
d	Vector of displacement gradients contributing to the strains
e	Vector of membrane components of Green's strain tensor
f	Generalised consistent load vector, force imbalance vector
k	Element stiffness matrix
p	Vector of nodal parameters of CQ12 element before condensation
q	Vector of nodal parameters of a subelement of CQ12 element
A	Matrix relating the element displacements to the generalised nodal deformation parameters
B	Matrix relating the generalised strains of an element to the nodal deformation parameters
$\bar{B}$	Matrix relating the generalised strains of a continuum to the nodal deformation parameters
D	Matrix defining displacement gradients from displacement coordinates, linear elastic constitutive matrix
E	Vector of components of Green's strain tensor
H	Symmetric matrix relating geometrically nonlinear component of strains to displacement gradients
I	Identity matrix
J	Jacobian matrix relating derivatives with respect to s and t axis to the derivatives with respect to the x and y axes
K	Stiffness matrix in terms of nodal displacements
K^e	Element stiffness matrix
K_o, K_i, K_g	Elastic, initial displacement, and geometric components of the geometrically nonlinear stiffness matrix
K_s, K_t	Secant and tangent stiffness matrix
L	Vector relating linear component of strains to displacement gradients, transformation matrix relating local nodal parameters to global nodal parameters.

M	Moment vector, transformation matrix from parametric to cartesian coordinates
N	Vector of nodal forces per unit width
N_1, N_2	Assembled first and second degree components of geometrically, nonlinear stiffness matrices
$\hat{N}_1, \hat{N}_2$	Integrands for first and second degree stiffness matrices
P	Matrix of element displacement functions
Q^b	Vector of generalised thermal bending forces
Q^{Pl}	Vector of generalised thermal membrane forces
R	Vector of generalised nodal forces
R^*	Vector of pseudo forces due to geometric nonlinearity
S	Vector of membrane components of the 2nd Piola-Kirckhoff stress tensor, transformation matrix
ε	Vector of generalised element strains
σ	Vector of stresses
δ	Vector of nodal deformations
λ	Matrix of direction cosines
ϕ, ψ	Vector of the components of rotation about the local x and y axes (positive direction determined by right-hand screw rule)
ϕ^{pl}, ϕ^b	Vector of membrane forces and bending forces necessary to suppress thermal dilation and flexure of an element respectively
Δ	Vector of element deformations
χ	Curvature vector

(c) Subscripts

a,b,c	Subtriangles of HCT element
i	Refers to a node
$\underset{\sim}{i}, \underset{\sim}{j}, \underset{\sim}{k}$	Unit vectors of displacement of an arbitrary point in the x, y, and z directions respectively
i,j,....s	General indices
n	Increment number
o	Internal nodal point of HCT or CQ12 element before condensation
t	Thermal effect in an unconstrained element (left subscript)

(d) Superscripts

b	Refers to bending action
e	Element parameter
n	Nonlinear elastic component
o	Linear elastic components
pℓ	Refers to plane stress action
T	Transpose of matrix
-1	Inverse of matrix

INTRODUCTION

A large number of box-girder bridges have been constructed of either steel or prestressed concrete over the last two decades [54, 74, 89, 99], and this has motivated the National Roads Board of New Zealand to initiate a coordinated research programme directed towards developing improved methods for the structural analysis of concrete box-girders in particular [73, 74].

The typical cross-section of a concrete box-girder consists of a deck and a soffit slab which are connected via inclined or vertical webs to form a single or multi-cellular structure. Transverse diaphragms are incorporated at the abutment and interior support sections to transfer web shear forces to the bearings, and in some circumstances are included between the support sections to prevent distortion of the cross-section.

The objective of this research was to develop an efficient numerical method for the analyses of box-girder bridges of arbitrary plan and variable cross-section, and to present numerical results for an extensive range of structures and compare them with experimental or prototype measurements. In this way the accuracy and the scope of the method can be assessed.

The range of structures analysed include multi-cell, multi-span, skew, curved, and branching box-girder bridges of non-prismatic cross-section, subjected to static loading and vertical temperature gradients. The analyses were based on the assumptions that the structure behaves in a linear elastic manner, and is composed of an uncracked homogeneous material. These assumptions are generally accepted as being sufficiently accurate for design purposes.

The method was extended so that it is applicable to the analysis of the geometrically nonlinear response of thin-walled box-girders. Self-correcting initial value and Newton-Raphson incremental/iterative schemes were employed to solve the nonlinear equilibrium equations defining the compression and shear buckling of imperfectly flat plates and stiffened plate girders, idealised as an assembly of finite elements. The results are compared with analytical solutions, alternative numerical solutions, and experimental measurements where these are available.

CHAPTER ONE

THE FINITE ELEMENT DISPLACEMENT METHOD AND IT'S APPLICATION TO BOX-GIRDER BRIDGES

I-1 THE FINITE ELEMENT DISPLACEMENT METHOD

I-1.1 Idealisation

The finite element method of structural analysis is now a well established technique, and has been described in numerous tests and survey papers [20, 32, 67, 68, 117, 118]. A continuum is subdivided by a mesh of imaginary lines or surfaces into an assemblage of discrete 'finite elements' which are interconnected at a number of nodal points situated on their boundaries. The deformations at these nodal points are selected as the basic unknown parameters of the problem, approximating the infinite number of degrees of freedom of a real continuum.

I-1.2 Element displacement and strain fields

Displacement functions must be chosen to uniquely define the state of displacement within the element in terms of the deformations at each node i of the element. Thus, for a two dimensional element in the (x,y) cartesian plane with n nodal points

$$\{\Delta(x,y)\} = \sum_{i=1}^{n} [N_i(x,y)]\{\delta_i\} \qquad \ldots \quad (I\text{-}1)$$

where $\{\Delta(x,y)\}$ represents the displacement at any point within the element and N_i is the displacement function relating the element displacement to the deformation parameters $\{\delta_i\}$ of node i.

If the generalised element stress and strain vectors, $\{\sigma\}$ and $\{\varepsilon\}$ are defined such that the integral over the element volume of half their scalar product represents the strain energy of the element, the generalised strain at any point within the element may be related to the nodal deformations as follows

$$\{\varepsilon\} = \sum_{i=1}^{n} [B_i(x,y)]\{\delta_i\} = [B]\{\delta\}^e \qquad \ldots \quad (I\text{-}2)$$

where the matrix $[B_i(x,y)]$ is obtained by differentiating the

displacement function $[N_i(x,y)]$, and superscript e denotes element parameters.

I-1.3 Element stress field

Assuming a linear elastic material and zero initial strains and stresses, the element stresses are related to the strains by the following expression

$$\{\sigma\} = [D]\{\varepsilon\}$$

$$= [D][B]\{\delta\}^e \qquad \ldots \quad (I\text{-}3)$$

where the constitutive matrix $[D]$ is a function of the elastic material properties [117]. The procedure for including the effect of initial thermal strains is described in Chapter VIII.

I-1.4 Total potential energy of the element

The total potential energy V^e of an element is defined by the expression

$$V^e = U^e - \left(\{\delta\}^e\right)^T \{R\}^e$$

where U^e is the strain energy of the element, and $\{R\}^e$ is the system of generalised nodal forces which equilibrate the boundary forces and any distributed loads within the element, and may be evaluated in terms of the nodal parameters by first considering the definition of the generalised strain and stress vectors

$$V^e = \frac{1}{2}\int_{vol} \{\varepsilon\}^T \{\sigma\}\, d\,vol - \left(\{\delta\}^e\right)^T \{R\}^e$$

then substituting from equations (I-2) and (I-3)

$$V^e = \frac{1}{2}\left(\{\delta\}^e\right)^T \int_{vol} [B]^T [D][B]\, d\,vol\, \{\delta\}^e - \left(\{\delta\}^e\right)^T \{R\}^e$$

where vol denotes the volume of the element.

I-5.1 Total potential energy of the continuum

The finite number of possible displacement configurations available to the continuum are defined by summing the displacement functions of the individual elements, so the generalised strain vector at any point within the continuum

$$\{\varepsilon\} = \sum_e [B]\{\delta\}^e = [\bar{B}]\{\delta\}$$

$$\text{where} \quad [\bar{B}_i] = [B_i]^e$$

when the point at which the strain is to be evaluated occurs within a particular element e, and i is a nodal point associated with that element. If the node i is not associated with that element

$$[\bar{B}_i] = 0$$

The total potential energy V of the continuum may be written

$$V = \frac{1}{2}\{\delta\}^T \int_{vol} [\bar{B}]^T [D] [\bar{B}] \, d\,vol \, \{\delta\} - \{\delta\}^T \{R\}$$

where the integral is now taken over the whole region, and the vector $\{R\}$ represents the applied nodal forces only, because the interelement forces are self equilibrating, and therefore do not contribute to the total potential energy of the assembled structure.

I-1.6 Equilibrium, stationary total potential energy

The equilibrium configuration may be determined from the principle of stationary potential energy [43], which states that *among all the displacements of an admissible form, those which satisfy the equilibrium conditions make the potential V assume a stationary value.* i.e.,

$$\frac{\partial V}{\partial \{\delta\}} = \frac{\partial}{\partial \{\delta\}} \frac{1}{2} \left(\{\delta\}^T \int_{vol} [\bar{B}]^T [D] [\bar{B}] d\,vol \{\delta\} - \{\delta\}^T \{R\} \right)$$

$$= \{0\}$$

which yields

$$\int_{vol} [\bar{B}]^T [D] [\bar{B}] \, d\,vol \, \{\delta\} = \{R\}$$

I-1.7 Assembly of element stiffness matrix

The matrix $\int_{vol} [\bar{B}]^T [D] [\bar{B}] \, d\,vol$ represents the stiffness [K] of the continuum and, considering the relationship between $[\bar{B}_i]$ and $[B_i]$, may be conveniently assembled by summing the stiffness matrices of the individual elements

$$[K_{ij}] = \sum_e [K_{ij}]^e \qquad \ldots \quad (I\text{-}4)$$

where $$[K_{ij}]^e = \int_{vol} [B_i]^T [D] [B_j] \, d\,vol \qquad \ldots \quad (I\text{-}5)$$

I-1.8 The solution procedure

If the structure is subjected to generalised nodal forces $\{R\}$, the resulting nodal deformations $\{\delta\}$ may be calculated by solving the system of simultaneous linear equations

$$[K]\{\delta\} = \{R\}$$

The stiffness matrix [K] of a linear elastic structure is symmetric, positive definite [105], and provided the equilibrium equations are suitably arranged is strongly banded because the displacements are specified in a piecewise manner throughout the continuum, with each nodal parameter only influencing adjacent elements. Numerous efficient equation solving processes are available [32] for evaluating the nodal deformations, which may then be substituted into equation (I-3) to evaluate the element stresses.

I-1.9 Conditions on the element displacement functions

In order that the finite element idealisation may provide an accurate representation of the actual continuum each element must be capable of deforming similarly to the corresponding region of the continuum. Therefore the critical operation in the displacement method formulation of an element stiffness matrix is the definition of the element deformation characteristics.

The displacement functions should be chosen to satisfy the following criteria [117];

i) The element has zero internal strain energy when the nodal deformations are consistent with a rigid body translation or rotation.

ii) All the constant generalised strain states are reproducible within the element.

iii) The strains at the interfaces between elements are finite, which implies a certain continuity of displacement from one element to another. When the generalised strains are defined as first derivatives of the displacements, such as with plane stress problems, only the displacements have to be continuous between elements. However, if the generalised strains are defined as second derivatives of the displacements, such as with plate bending problems, the first derivatives of the displacements (the plate rotations) must also be continuous [10,20].

I-1.10 Convergence of the solution with mesh refinement

If the selected displacement function satisfies these conditions the total potential energy of the finite element idealisation will represent an upper bound to that of the actual linear elastic continuum. If the initial strains and stresses are zero both the strain energy and the computed direct influence coefficients will constitute a lower bound solution [101], and the finite element solution will converge monotonically to the true solution as the mesh is systematically refined [33, 67, 72]. Therefore the use of a fully compatible (conforming) displacement function is an important factor is establishing the reliability of a finite element analysis. However, a failure to satisfy the third (compatibility) criterion does not necessarily prevent convergence to the true solution [113]. Also, there are a number of hybrid stress and hybrid displacement elements which have been developed using alternative formulations which, although not fully compatible, satisfy the equilibrium requirements and give accurate results [25, 112].

The minimising of the total potential energy of the idealised structure ensures satisfaction of the equilibrium conditions only within the limits of the available deformation modes, but a closer approximation can be obtained by increasing the number of nodal parameters used to prescribe the deformations. This may be achieved by incorporating additional parameters at each node, such as the derivatives of the displacements, increasing the number of nodes per element, or using a finer mesh of elements to subdivide the structure.

I-2 SELECTION OF THE DISPLACEMENT FUNCTIONS

I-2.1 Form of assumed functions

The selection of appropriate displacement fields can be accomplished directly for some classes of elements by using the well-known interpolation technique of numerical analysis (e.g. Lagrangian, Hermitian interpolation) [39, 117]. Thus for a two dimensional element

$$\{\Delta\} = [N(x,y)]\ \{\delta\}^e \qquad \ldots \quad (I\text{-}6)$$

If these interpolations are difficult to apply the displacement function is usually selected as a polynomial expression in cartesian coordinates relating the fundamental displacement to a set of generalised displacement parameters $\{\alpha\}$,

$$\{\Delta\} = [f(x,y]\{\alpha\} \qquad \ldots \quad (I\text{-}7)$$

although it is possible to use trigonometric functions, as described in Section III-5. The number of linearly independent generalised parameters $\{\alpha\}$ must be equal to the number of element degrees of freedom $\{\delta\}^e$, to which they are related by considering the geometric boundary conditions

$$\{\delta\}^e = [A]\{\alpha\}$$

The terms of the matrix [A] are functions of the element dimensions and, provided the function $f(x,y)$ is selected according to the criteria discussed in the following section, the matrix will not be singular

$$\{\alpha\} = [A]^{-1}\ \{\delta\}^e$$

and the fundamental displacements may be related to the nodal parameters as follows

$$\{\Delta\} = [f(x,y)]\,[A]^{-1}\ \{\delta\}^e$$

I-2.2 Selection of the displacement function

To ensure monotonic convergence to the correct solution with mesh refinement, the displacement functions must satisfy the rigid body, constant strain, and compatibility criteria discussed in Section I-1.9.

The minimum number of degrees of freedom, measured with respect to the element coordinate system, required at each vertex node to satisfy these criteria is illustrated in Fig. I-1 for five types of elements. An improved element representation may be achieved by incorporating additional degrees of freedom, in the form of higher order derivatives of the fundamental displacements, provided undesirable continuities of strain are not enforced across element boundaries [117].

The procedure for selecting a displacement function is described using the plane stress element of sides 2a, 2b, described in Fig. I-1d, as an example. The fundamental displacements of a plane stress element are $< u,v >$, and the vector of generalised strain is defined as

$$\{\varepsilon\} = < \frac{\partial u}{\partial x} , \frac{\partial v}{\partial y} , \frac{\partial u}{\partial y} + \frac{\partial v}{\partial x} >^T$$

so the inclusion of the rigid body and constant strain modes is achieved if the polynomial terms $1,x,y$ are included in the displacement functions $u(x,y)$ and $v(x,y)$. If a rectangular element with four nodes is to be formulated the terms of these displacement functions must be selected in groups of four. The simplest possible element will be obtained by adding one more term to the three essential terms $1,x,y$, the selection of which is guided by the knowledge that;

i) The overall rate of convergence will be governed by the highest order of complete polynomial [102], although additional terms which do not complete the next higher order polynomial will usually improve the accuracy of the element.

ii) It is generally undesirable to include terms which make the displacement function unsymmetric with respect to the coordinate axes, and therefore violate the conditions of isotropy, i.e., the inclusion of the term x^2y without xy^2 will result in an element with greater rigidity in one direction than another.

iii) Interelement compatibility of the displacement function along the side of an element can only be maintained if the displacement function is uniquely defined by the selected nodal parameters on that side only.

The choice of the fourth term is now well defined because the selected nodal parameters of (u,v) at each element corner will only permit the unique specification of a linear variation of displacement along the element boundaries, so the term xy is selected. The displacement functions may now be written

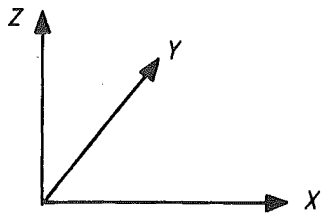

Fig. I-1a GLOBAL COORDINATE SYSTEM

Example of Application	Type of Element	Minimum Nodal Degrees of Freedom <δ>	Fundamental Displacements <Δ>
Portal Frame	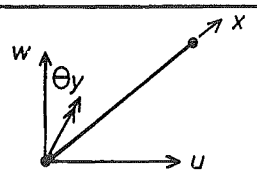 Fig. I-1b 2-D BEAM ELEMENT.	u , w , θy	u , w(x)
Space Frame	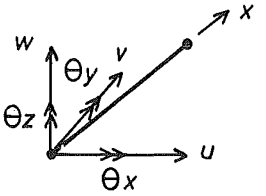 Fig. I-1c 3-D BEAM ELEMENT.	u , v , w , θx , θy , θz	u , v , w , θx(x)
Shear Wall	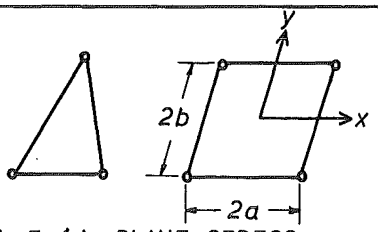 Fig. I-1d PLANE STRESS.	u , v	u , v (x , y)
Floor Slab	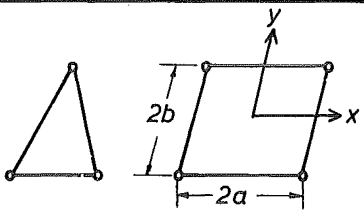 Fig. I-1e PLATE BENDING.	w , θx , θy	w(x , y)
Massive Dam	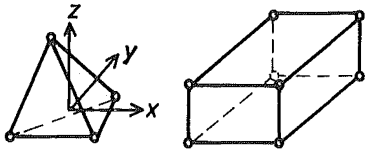 Fig. I-1f 3-DIMENSIONAL STRESS.	u , v , w	u , v , w(x , y , z)

FIGURE I-1 MINIMUM DEGREES OF FREEDOM

$$< u,v > \;=\; < 1,x,y,xy > \begin{bmatrix} \alpha_1 & \beta_1 \\ \alpha_2 & \beta_2 \\ \alpha_3 & \beta_3 \\ \alpha_4 & \beta_4 \end{bmatrix}$$

and if the coefficients α_i , β_i ; $i = 1,4$ are related to the nodal parameters u_i , v_i ; $i = 1,4$ by evaluating $< u,v >$ at the four corners, the function may be expressed in the form

$$< u,v > = \frac{1}{4} < (1 - \frac{x}{a})(1 - \frac{y}{b}) \;,\; (1 + \frac{x}{a})(1 - \frac{y}{b}) \;,\; (1 + \frac{x}{a})(1 + \frac{y}{b}) \;,$$

$$(1 - \frac{x}{a})(1 + \frac{y}{b}) > \begin{bmatrix} u_1 & v_1 \\ u_2 & v_2 \\ u_3 & v_3 \\ u_4 & v_4 \end{bmatrix} \qquad \ldots \quad (I\text{-}8)$$

This displacement function may be used to derive a fully compatible rectangular plane stress element according to the procedure outlined in Section I-1.

I-3 PARAMETRIC ELEMENTS

In this section a technique is described which may be used to generalise rectangular elements to a quadrilateral shape (and which may be extended to facilitate the generation of two or three dimensional elements with curved boundaries). The technique involves mapping the geometrically simple rectangular element, with displacement function $N^o(x,y)$, into two dimensional surfaces. Therefore an admissible transformation $M(s,t)$ is sought which maps from the (x,y) cartesian coordinate system (the physical space), into the (s,t) coordinate system (the analysis space), where the elements assume a simple geometry in the form of a two dimensional square bounded by the sides $s = \pm 1$, $t = \pm 1$.

The transformation is admissible if $M(s,t)$ is single-valued, continuous, and possesses continuous first partial derivatives over the element, and if the determinant of the Jacobian of the transformation does not vanish at any point within the element.

The transformation for a general two dimensional mapping, illustrated in Fig. I-2, is defined by the relationship

$$< x,y > \; = \; [M(s,t)]\,[x_e, y_e]$$

where $[x_e, y_e]$ are the cartesian coordinates of the selected element geometric nodes. The displacement function of the transformed element may be expressed in terms of the parametric (s,t) coordinates by substituting $\frac{x}{a} = s$, $\frac{y}{b} = t$ into the displacement function derived for rectangular elements with sides of length $2a$, $2b$, and the origin of the cartesian coordinate system located at the element centroid. Thus

$$\{\Delta\} \; = \; [N^o(x,y)]\;\{\delta\}^e \; = \; [N(s,t)]\{\delta\}^e$$

As an example, consider the plane stress element formulated in Section I-2.2. The displacement function of equation (I-8) may now be expressed in the form

$$< u,v > \; = \; \sum_{i=1}^{4} \frac{1}{4}\,(1 + s\,s_i)\,(1 + t\,t_i) < u_i, v_i > \qquad \ldots \quad (I\text{-}9)$$

where s_i, t_i are the values of s and t at the corner node i $(i = 1,4)$. A planar rectangular element may be generalised to a planar quadrilateral shaped element by the use of the admissible transformation

$$< x,y > \; = \; \sum_{i=1}^{4} \frac{1}{4}\,(1 + s\,s_i)\,(1 + t\,t_i) < x_i, y_i > \qquad \ldots \quad (I\text{-}10)$$

where the geometric nodes i coincide with the corner nodes associated with the displacement function. However, when a geometric transformation is employed during the derivation of an element stiffness matrix it is necessary to check that the rigid body and constant strain states are still reproducible after the mapping. This may be achieved for plane stress elements by substituting successively; $u_i, v_i = A$ corresponding to an arbitrary rigid body translation of the element, and $u_i, v_i = Ax_i$, and Ay_i, corresponding to the constant strain states, into the displacement function

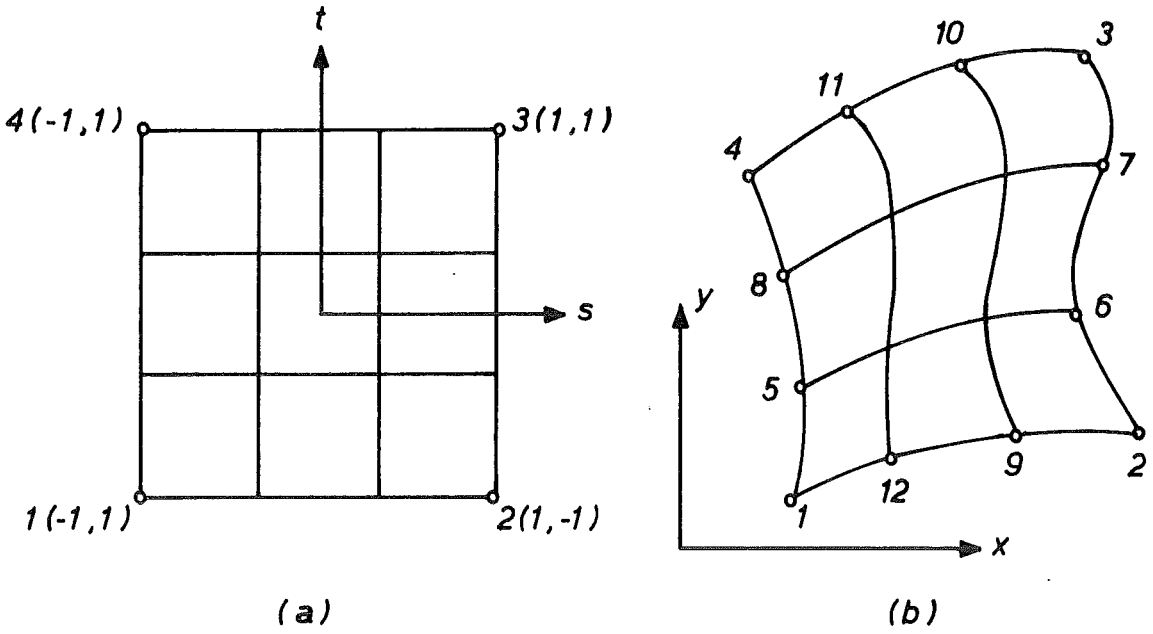

FIGURE I-2 TWO DIMENSIONAL MAPPING

$$< u,v > = \sum_{i=1}^{4} [N_i(s,t)] < u_i, v_i >$$

If the resulting expressions simplify to $< u,v >= A$, $< u,v > = Ax$, and $< u,v > = Ay$ respectively, where x and y are related to the geometric nodes by the geometric transformation $M(s,t)$, then the transformation is permissible.

Zienkiewicz et al [116] have shown that if the same function is used for the displacement and geometric transformation function ($N(s,t) = M(s,t)$), then the rigid body and constant strain modes are guaranteed to be represented in the element displacement field. However, these functions need not be identical. For example, the rectangular plane stress element, with degrees of freedom u_i, v_i at the corner nodes only, can be transformed to a planar element with cubically varying curved sides (shown in Fig. I-2b) by the transformation

$$< x,y > = \sum_{i=1}^{4} \frac{1}{32} (1 + s s_i) (1 + t t_i) [- 10 + 9(s^2 + t^2)] < x_i, y_i >$$

$$+ \sum_{i=5}^{8} \frac{9}{32} (1 + s s_i) (1 - t^2) (1 + 9 t t_i) < x_i, y_i >$$

$$+ \sum_{i=9}^{12} \frac{9}{32} (1 + t t_i) (1 - s^2) (1 + 9 s s_i) < x_i, y_i >$$

This is an admissible conforming transformation since along any element side x and y are uniquely defined by the geometric nodes along that side only. However, inspection of the displacement function indicates that the transformed element is no longer capable of representing the constant strain modes. Conversely, rectangular plate bending and plane stress elements with cubically varying displacement functions may be successfully transformed to a general quadrilateral shape by using the linear trans- transformation of equation (I-10), as described in Chapters II and III.

Palacol and Stanton [68] and Zienkiewicz et al [117], have suggested that planar rectangular elements may also be generalised to three dimensional surfaces by transformations of the form

$$< x,y,z > = [M(s,t)] < x_e, y_e, z_e >$$

but this has not been developed to the stage of practical application.

Fried [37] has demonstrated a disadvantage associated with using the parametric technique to generate elements of complex geometry: He considers a one dimensional element and lets the geometric transformation be written in the form $x = x(s^q)$, where q is the order of the transformation. If the element displacement field is interpolated by the function $u = U(s^P)$, where P is the order of the displacement function, then $u = F(x^{P/q})$, where F is a polynomial function. Therefore, if the geometric transformation is of order greater than one, (i.e. $q > 1$), then the order of the displacement function is effectively reduced, which may result in a slower rate of convergence and a loss of accuracy of the solution. The generalisation to curved sided planar elements for the deck and soffit slabs of curved box-girders was not considered here for this reason.

Following the selection of a conforming geometric transformation $[M(s,t)]$, and the expression of the displacement function in terms of the parametric (s,t) coordinates, the formation of the element stiffness matrix proceeds as before; The standard form of the element stiffness matrix was shown in Section I-1.7 to be

$$[K]^e = \int_{vol} [B]^T [D] [B] \, d\,vol \qquad \ldots \quad (I\text{-}11)$$

where $[B]$ relates the generalised strains of the element to the nodal displacement parameters. However the generalised strains will generally be defined as cartesian derivatives of the displacements and must therefore be related to the derivatives with respect to the parametric (s,t) coordinates;

$$\begin{bmatrix} \partial N/\partial s \\ \partial N/\partial t \end{bmatrix} = \begin{bmatrix} \partial x/\partial s & \partial y/\partial s \\ \partial x/\partial t & \partial y/\partial t \end{bmatrix} \begin{bmatrix} \partial N/\partial x \\ \partial N/\partial y \end{bmatrix} = [J] \begin{bmatrix} \partial N/\partial x \\ \partial N/\partial y \end{bmatrix} \qquad \ldots \quad (I\text{-}12)$$

where $[J]$ is the Jacobian matrix of the transformation $[M(s,t)]$

$$\begin{bmatrix} \partial N/\partial x \\ \partial N/\partial y \end{bmatrix} = [J]^{-1} \begin{bmatrix} \partial N/\partial s \\ \partial N/\partial t \end{bmatrix} \qquad \ldots \quad (I\text{-}13)$$

The presence of the inverse of the Jacobian, $[J]^{-1}$, in the integrand necessitates that the integral of equation (I-11) be performed numerically, the procedure for which is described in Chapter VII.

I-4 APPLICATION TO BOX - GIRDER BRIDGES

I-4.1 Thin plate theory

Box-girder bridges are assumed to behave as thin spatial plate structures, for which the following finite element idealisation was adopted; Plate bending and plane stress elements were combined to derive thin planar shell finite elements,which were then assembled to form a three dimensional idealisation of the box-girder, as shown in Fig. I-3, and incorporating the following assumptions;

i) The linear elastic structural response is consistent with the assumptions of Kirckhoff's classical thin plate theory [104] (see Section II-1).

ii) Transverse shear deformations are negligible. This assumption is realistic for thin homogeneous plates because the ratio of deflection due to shear/deflection due to flexure is of the order of Et^2/GL^2, where t is the thickness, L is the length of the plate, and E and G are the modulii of elasticity and shear respectively. If the webs or slabs are thick it is possible to adapt plate bending elements to include transverse shear deformations [45], but these effects were not investigated here.

The idealised box-girder was constructed as an assemblage of deck, cantilever, and soffit slabs, and inclined web slabs, as illustrated in Fig. I-3. Transformations were applied to the stiffness matrices of the web elements to incorporate the effect of their orientation to the deck slab elements.

The webs of curved box-girder bridges constitute segments of a conical frustrum, but were idealised for this work as a folded series of planar elements because it is difficult to include the deformation modes associated with rigid body translations and rotations within the displacement functions of non-planar elements, as discussed in Chapter IV.

I-4.2 Tapered thickness elements

The planar thin shell finite element was derived with variable plate thickness, interpolated linearly from the thickness defined at the four corner nodes, to enable the haunched deck slab members of box-girders to be represented. Haunches are often incorporated within the deck slab to reduce the shear stresses and the transverse flexural stresses above the webs of the structure.

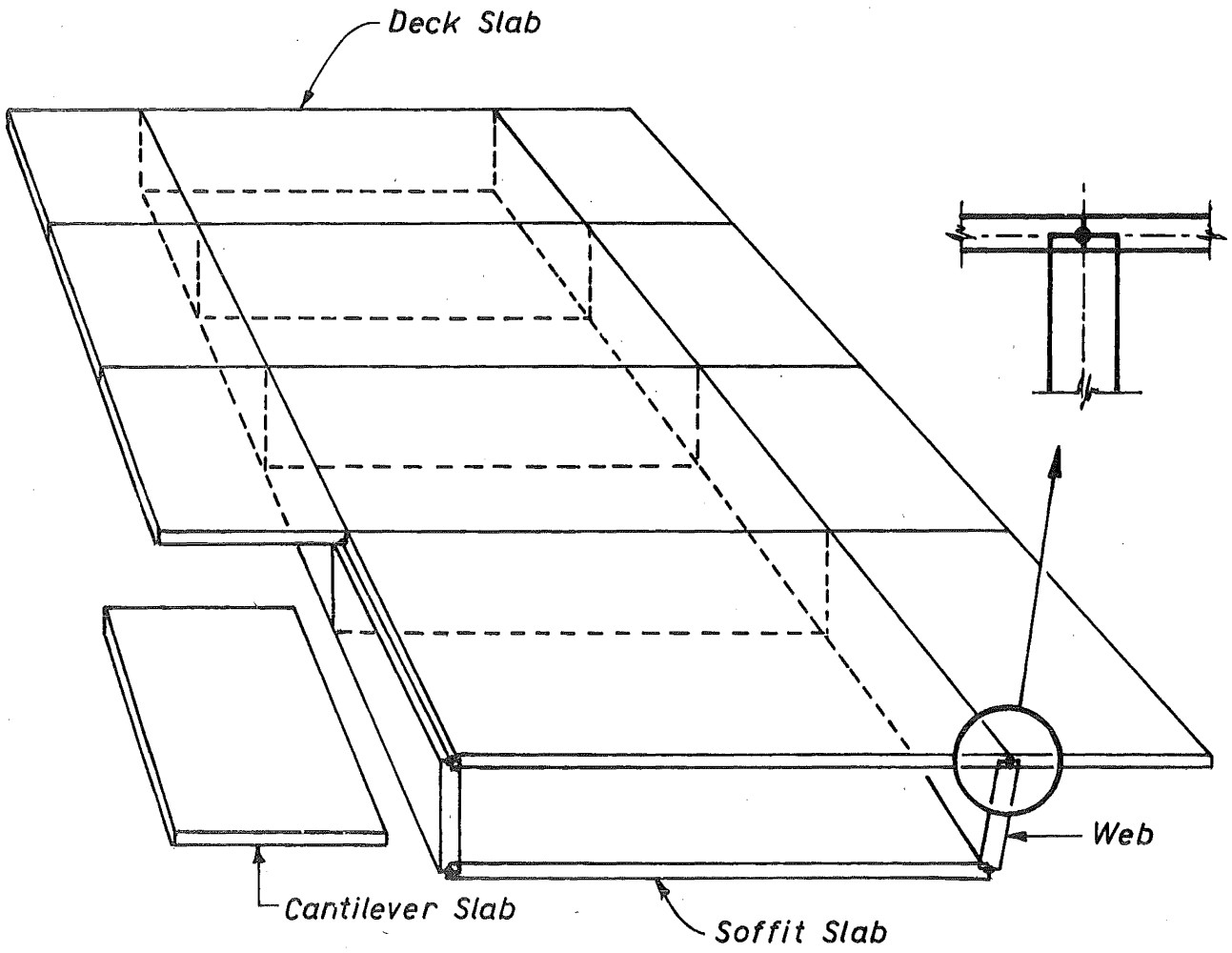

FIGURE I-3 ASSEMBLY OF ELEMENTS

The integrand of equation (I-11), defining the element stiffness matrix, is a linear function of the thickness for plane stress elements, and a cubic function for plate bending elements, as demonstrated in Chapter II. The integrand associated with tapered elements will therefore be of a higher order than for constant thickness elements and consequently , if a numerical integration scheme is used, a larger number of sampling points may be necessary to achieve the required degree of accuracy, as discussed in Chapter VII.

The use of elements with a linear variation of thickness and low order displacement functions will involve approximations, even when they are employed to simulate regions with simple realistic stress distributions. Consider,for example, a tapered thickness element loaded so as to impose a linear distribution of membrane stress or bending moment across the element. The membrane strain-displacement and curvature-displacement relationships are required to be of an order greater than one because of the thickness variation. The elements used for this work are based upon linear variations of strain and curvature, so the computed distributions of membrane strain and curvature will tend towards a best linear approximation of the exact solution. However, neither the compatibility, rigid body, or constant strain criteria are violated so convergence to the correct solution with mesh refinement is guaranteed, except that some discrepancy may occur due to the assumption that the structural behaviour of the haunched deck slab member may be represented by thin plate theory.

I-4.3 Combination of thin and thick shell elements

The application of thin plate theory may lead to errors in the computed stress distributions across regions where thick haunches are incorporated within the deck slab,and the assumptions associated with Kirckhoff's thin plate theory [104] are violated, or the overlapping of the web and haunched deck slab elements is of consequence. This overlapping (see Fig. I-3) will not increase the moment of inertia of the box-section significantly,but the increase of the effective web span, idealised as the distance from the centreline of the soffit slab to the centreline of the haunched deck slab, will influence the transverse behaviour of the web and the distribution of longitudinal stresses.

Thin plate theory was employed throughout this work because the three dimensional stress state which occurs in the region where a web intersects a severely haunched slab has only a local influence, and the

associated errors were considered acceptable. When a knowledge of this local influence is required, and a complete three dimensional analysis is not economically justifiable, it may be possible to incorporate a special tapered thickness element with thin plate action along one edge and thick shell [117] or three dimensional behaviour along the opposite edge, facilitated by the inclusion of nodes at the top and bottom extreme fibres.

The special element could be used as a transition to regions where the assumptions of thin plate theory are not applicable and complex three dimensional elements are used. This approach has not been formulated here.

CHAPTER TWO

PLATE BENDING ELEMENT

II-1 INTRODUCTION

A survey of plate bending elements is presented, from which the most suitable candidate for modelling the flexural behaviour of box-girder bridges is selected.

Kirchhoff's assumptions [104] are employed during the formulation to simplify the plate bending theory from one associated with three-dimensional elasticity, to a two dimensional theory for which transverse shear deformations are neglected. i.e., it is assumed:

i) Elements of the plate originally perpendicular to the middle plane remain perpendicular to the middle surface after deformation of the plate.

ii) Normal stresses acting on planes parallel to the middle plane are negligible.

iii) Deflections of the middle surface are small compared with the thickness of the plate.

The generalised strains of a plate bending element are the curvatures $\{\chi\}$

$$\{\chi\} = \begin{Bmatrix} \dfrac{\partial^2 w}{\partial x^2} \\ \dfrac{\partial^2 w}{\partial y^2} \\ -2\dfrac{\partial^2 w}{\partial x \partial y} \end{Bmatrix}$$

where x and y refer to the coordinate system illustrated in Fig. II-1, and the conjugate generalised stresses $\{M\}$ are the bending and twisting moments per unit length in the x and y direction [104]

$$\{M\} = \begin{Bmatrix} M_{xx} \\ M_{yy} \\ M_{xy} \end{Bmatrix}$$

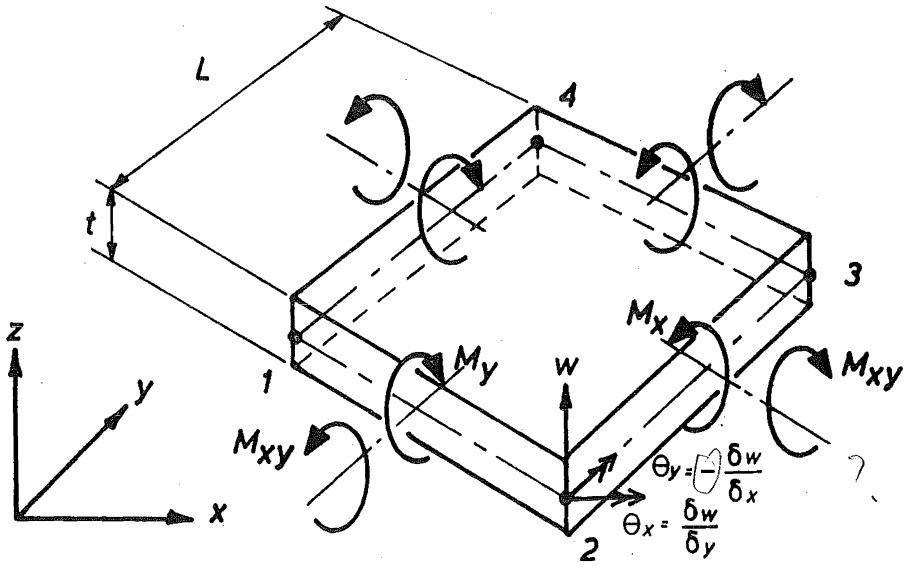

FIGURE II-1 STRESS RESULTANTS IN PLATE BENDING

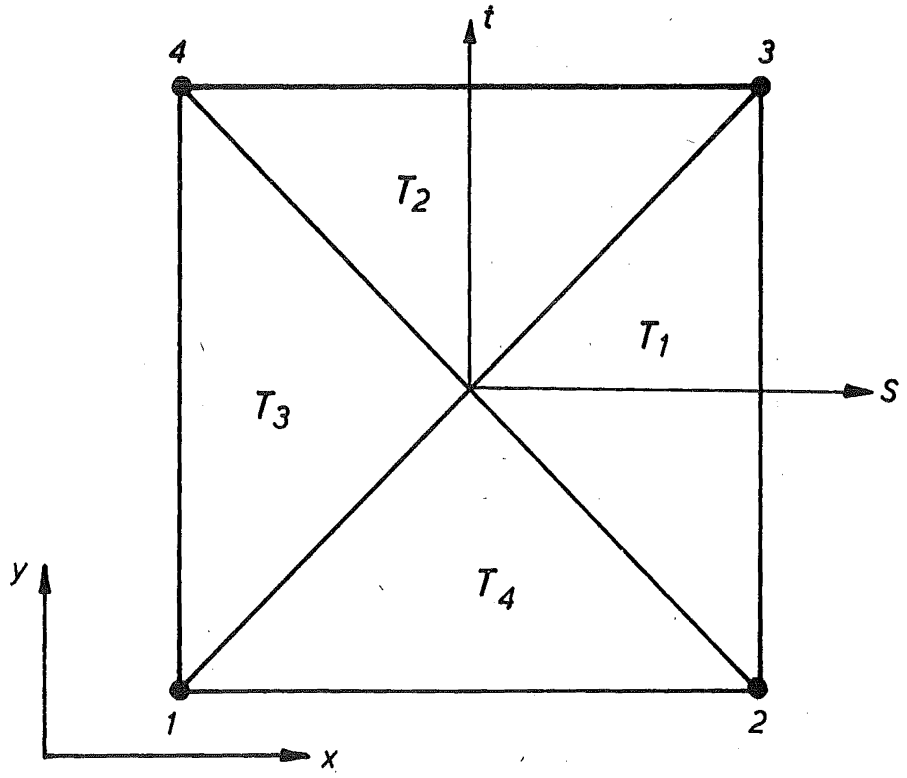

FIGURE II-2 SUBDIVISION OF THE BIRKHOFF-GARABEDIAN ELEMENT

II-2 SELECTION OF DISPLACEMENT FUNCTION

The deformation of a plate can be completely defined by the lateral displacement w, so a displacement function $w(x,y)$ is sought. The selection of this function is guided by the criteria discussed in Chapter I;

i) Any constant state of curvature should be reproducible within the element, i.e., the displacement function should contain all the terms of a complete second order polynomial in x and y .

ii) The requirement of deformation continuity between the elements should be imposed not only on the lateral displacement $w(x,y)$ but also on the first derivatives (slopes) to ensure that the curvatures do not become infinite across the element interfaces.

To obtain at least a near satisfaction of slope continuity between elements the three displacement components w, Θx $(= \frac{\partial w}{\partial y})$ and Θy $(= -\frac{\partial w}{\partial x})$, shown in Fig. II-1, must be included as nodal parameters. However, if a displacement function satisfying the compatibility conditions is found with only these three degrees of freedom at the corner nodes, it must be such that at the corner nodes this function is not continuously differentiable and the cross derivative $\frac{\partial^2 w}{\partial x \partial y}$ is not unique [117].

(i.e., $\frac{\partial^2 w}{\partial x \partial y} \neq \frac{\partial^2 w}{\partial y \partial x}$)

This difficulty could be overcome by specifying the cross derivative as one of the nodal parameters, but this is not permissible at nodes where a number of element interfaces meet at different angles (as with non-rectangular element meshes), unless all the second derivatives are included as nodal parameters to maintain continuity of cross derivatives in several sets of orthogonal directions. However, this violates physical requirements if the plate stiffness varies abruptly from element to element, because the enforcement of curvature continuity across the element interfaces is then excessive.

It was therefore decided to accept the non-unique definition of the cross derivatives at the corner nodes. This non-uniqueness does not violate the compatibility criteria.

Additional constraints are imposed on the selection of the displacement function by the requirement that the plate bending element must be coupled with a plane stress element to form a planar thin shell element capable of representing the structural behaviour of box-girder bridges economically, i.e.,

i) The introduction of midside nodes is to be avoided because they are at most common to only two elements and consequently are inefficient, resulting in a disproportionate increase in the bandwidth of the structural stiffness matrix.

ii) The displacement function should be complete to at least the third order in x and y because the overall rate of convergence with mesh refinement will be governed by the highest order of complete polynomial [37].

iii) The geometry of the plate bending element should be either triangular, or of a general quadrilateral shape, to enable curved and skewed box-girder bridges to be idealised.

iv) The performance of the element should not deteriorate significantly as the aspect ratio of the element, defined as the ratio of the length/width of the element, deviates from a value of one, to enable slender bridge structures to be analysed without resort to an uneconomically fine element subdivision in the longitudinal direction of the bridge.

v) A large number of integration points are required to numerically integrate the strain energy gradient exactly, so elements for which this expression can be integrated analytically are expected to be computationally more efficient.

Four plate bending finite elements which satisfy most of these conditions are discussed in the next sections, and their performances are compared in Section II-7 where they are employed to analyse several test problems.

II-3 ACM ELEMENT (Adini, Clough and Melosh [19])

A rectangular element of a plate lying in the x-y plane, with degrees of freedom w, θx, and θy at each corner, is shown in Fig. II-1. The following 12 term polynomial is selected to define the displacement function

$$W = \alpha_1 + \alpha_2 x + \alpha_3 y + \alpha_4 x^2 + \alpha_5 xy + \alpha_6 y^2 + \alpha_7 x^3 + \alpha_8 x^2 y + \alpha_9 xy^2 + \alpha_{10} y^3 + \alpha_{11} x^3 y + \alpha_{12} xy^3 \quad \ldots \text{(II-1)}$$

where α_1 , α_2 , ... α_{12} are coefficients to be related to the nodal parameters.

All the rigid body and constant generalised strain modes are reproducible because the polynomial is complete to the second order.

The performance of the element does not deteriorate in accuracy when the aspect ratio of the sides becomes large [19], as demonstrated in Section II-7, but the displacement function is not compatible in normal slope: along the element interfaces the gradient of w normal to the boundary has a cubic variation (e.g. $\frac{\partial w}{\partial x}$ is a cubic function of y along the line x = constant). Only two normal slope parameters are specified on any boundary, so the cubic variation is not defined uniquely, and in general a discontinuity of normal slope will occur between the corner nodes. This incompatibility often results in a more flexible element of good accuracy when rectangular meshes are used,and has therefore been very popular for bridge analyses in the past [54] when suitable conforming elements were not available.

To generalise the ACM element to a quadrilateral shape it is necessary to express the displacement function in terms of the parametric coordinates (s,t) illustrated in Fig. I-2.

$$w = \alpha_1 + \alpha_2 s + \alpha_3 t + \alpha_4 s^2 + \alpha_5 st + \alpha_6 t^2 + \alpha_7 s^3 + \alpha_8 s^2 t + \alpha_9 s t^2 + \alpha_{10} t^3 + \alpha_{11} s^3 t + \alpha_{12} s t^3 \quad \ldots \quad (II\text{-}2)$$

The two coordinate systems are related by the transformation

$$< x,y > = \sum_{i=1}^{4} \frac{1}{4} (1 + s s_i)(1 + t t_i) < x_i, y_i > \quad \ldots \quad (II\text{-}3)$$

where subscript i denotes the nodal designation.

The arbitrary coefficients α_1 , α_2 , ... α_{12} may be determined by evaluating the parameters w_i , $\frac{\partial w}{\partial s_i}$, and $\frac{\partial w}{\partial t_i}$ at the four corners ($s = \pm 1$, $t = \pm 1$), and solving the resulting system of linear simultaneous equations. Thus

$$w = \sum_{i=1}^{4} \frac{1}{8}(1 + s s_i)(1 + t t_i)(2 + s s_i + t t_i - s^2 - t^2)w_i$$

$$- \sum_{i=1}^{4} \frac{1}{8} s_i (1 + s s_i)(1 + t t_i)(1 - s^2) \frac{\partial w}{\partial s_i}$$

$$- \sum_{i=1}^{4} \frac{1}{8} t_i (1 + s s_i)(1 + t t_i)(1 - t^2) \frac{\partial w}{\partial t_i} \qquad \ldots \quad (II\text{-}4)$$

The parameters $\frac{\partial w}{\partial s_i}$ and $\frac{\partial w}{\partial t_i}$ may be related to the nodal parameters $\Theta x_i = \frac{\partial w}{\partial y_i}$ and $\Theta y_i = -\frac{\partial w}{\partial x_i}$ by the chain rule of partial differentiation The element curvatures $< \frac{\partial^2 w}{\partial x^2}, \frac{\partial^2 w}{\partial y^2}, -2\frac{\partial^2 w}{\partial x \partial y} >^T$ may then be defined in terms of the second derivatives $\frac{\partial^2 w}{\partial s^2}$, $\frac{\partial^2 w}{\partial t^2}$ and $\frac{\partial^2 w}{\partial s \partial t}$, by repeated application of the chain rule, and thus expressed as a function of the nodal parameters w_i, Θx_i, Θy_i. This practice is described by Lim and Moffat [54].

The derivation of the element stiffness matrix proceeds in the standard manner described in Chapter I. However, the analytical integration of the strain energy gradient now appears impossible, except for elements of simple rectangular or parallelogram geometry, because the determinant of the Jacobian of the transformation is present in the denominator. Numerical integration involving a product application of the Gaussian quadrature formulae [49] in the s and t directions, was therefore used here.

Lim and Moffat [54] have demonstrated that in the case of rectangular or parallelogram elements it is only necessary to use three integration points in each direction in order to obtain a stiffness matrix identical to that obtained by analytical integration. However, as the geometry of the element deviates from that of a parallelogram more sampling points are required for the results of the integration to converge.

Computational tests have shown that the accuracy of the results obtained with this element deteriorate as the angle between any two opposite sides increases above 30° [54]. This is because the displacement function of equation (II-4) does not satisfy the constant curvature criterion for a general quadrilateral element. Consider the constant curvature deformation $w = Ax^2$ where A is an arbitrary constant. This deformation may be

expressed in terms of the parametric coordinates by substituting from equation (II-3), i.e.,

$$x = \text{function } (1, s, t, st)$$

(The term st disappears for a parallelogram element because $\sum_{i=1}^{4} s_i t_i x_i = 0$).

Thus

$$w = A.\ \text{Function } (1, s, t, s^2, st, t^2, s^2t, st^2, s^2t^2)$$

However, the term s^2t^2 is not included in the displacement function of equation (II-4) so this function cannot represent all the constant curvature states of deformation when quadrilateral elements are employed, although the error doesn't appear to be significant when opposite sides are nearly parallel [54].

II-4 BG ELEMENT (Birkhoff, Garabedian [8])

Rather than attempt to define a displacement function which is valid over the entire element, it is possible to subdivide the element into regions and employ a different expansion over each region, provided the individual expansions are compatible up to the first derivatives across the interior region boundaries as well as the exterior element boundaries.

The BG element was generated from a scheme for smooth surface interpolation suggested by Birkhoff and Garabedian [8]. Suppose that w and the normal slope $\frac{\partial w}{\partial n}$ are given on the boundary of a plane rectangular region R in the (x,y) plane, and that values of $w(x_i,y_i)$ are also specified on a rectangular grid of points. The problem is to interpolate $w(x,y)$ as smoothly as possible through these points, so as to match the given values of w and $\frac{\partial w}{\partial n}$ at the boundary mesh-points.

The procedure is to first pass a set of cubic 'spline' curves $w(x_i,y)$ and $w(x,y_i)$ through the given points. This will fix the tangential slopes $\frac{\partial w}{\partial x}$ and $\frac{\partial w}{\partial y}$ at the corners of the rectangular elements R_{ij} : $x_{i-1} \leqslant x \leqslant x_i$, $y_{j-1} \leqslant y \leqslant y_j$ of R . Next, interpolate the normal slope $\frac{\partial w}{\partial n}$ linearly along the edges of the element so as to maintain continuity of slope. Finally, each rectangular element R_{ij} is divided into subtriangles as shown in Fig. II-2, and a smooth surface which is continuous in slope throughout the element, and continuous in curvature within each subtriangle, is fitted to the boundary values of w and $\frac{\partial w}{\partial n}$.

It is convenient to introduce the parametric coordinates (s,t) at this stage to generalise the rectangular element R_{ij} to a quadrilateral shape. Consider a square element in the analysis space. It is

necessary to find a family of 12 functions $F_i(s,t)$; i = 1,12 such that

$$w = \sum_{i=1}^{12} \alpha_i F_i(s,t) \qquad \ldots \quad (II\text{-}5)$$

which assume linearly independent values of w, $\frac{\partial w}{\partial s}$ and $\frac{\partial w}{\partial t}$ at each corner $(\pm 1, \pm 1)$, and which are associated with cubic variations of the displacement w , and linear variations of the normal slope $\frac{\partial w}{\partial n}$ along the element boundaries. A methodical approach to the derivation of these 12 functions is available when the possible symmetries and antisymmetries of the functions under the four-group generated by reflections about the transverse and longitudinal axes are considered. This approach has been described by Birkhoff and Garabedian [8], and also by Deak and Pian [30, 73], who have demonstrated that three of the functions must be defined separately over the subtriangles illustrated in Fig. II-2, with a discontinuity of the second derivatives across the element diagonals.

If the parameters $w, \frac{\partial w}{\partial s}$ and $\frac{\partial w}{\partial t}$ are evaluated at the corners $(\pm 1, \pm 1)$ of the element, by differentiating equation II-5, the coefficients α_1 , α_2 , ... α_{12} may be related to these parameters to yield an explicit form of the displacement function.

$$w = \sum_{i=1}^{4} \frac{1}{8} (1 + s s_i) (1 + t t_i) (2 + s s_i + t t_i - s^2 - t^2) w_i$$

$$- \sum_{i=1}^{4} \frac{1}{8} t_i (1 + s s_i) (1 + t t_i) (1 - t^2) \frac{\partial w}{\partial t_i}$$

$$- \sum_{i=1}^{4} \frac{1}{8} s_i (1 + s s_i) (1 + t t_i) (1 - s^2) \frac{\partial w}{\partial s_i}$$

$$- \sum_{i=1}^{4} \frac{1}{16} s_i t_i st (1 - s^2)(1 - t^2) w_i$$

$$
\begin{aligned}
&- \sum_{i=1}^{4} \frac{1}{8} s_i \Big(- t\, t_i (1 - s^2 - \frac{1}{4} s\, s_i) - s_i t_i/4\ (- s^3 t + 3t^3 s - s^3 t^3) \\
&- s_i t_i \{(T_1+T_3)\ \frac{1}{4}\ (s^3 t^3 - s^5 t - 3st^3 + 3s^3 t) + (T_2+T_4)\frac{1}{4}(st^5 - s^3 t^3 - 3st^3 + 3s^3 t)\} \\
&- t_i\ \{T_1(2st-2t) + T_2(s^2-2t+t^2) + T_3(-2st-2t) + T_4(-s^2-2t-t^2)\}\Big) \frac{\partial w}{\partial s_i} \\
&- \sum_{i=1}^{4} \frac{1}{8} t_i \Big(- s\, s_i (1 - t^2 - \frac{1}{4} t\, t_i) - s_i t_i/4\ (3s^3 t - t^3 s - s^3 t^3) \\
&+ s_i t_i\ \{(T_1+T_3)\ \frac{1}{4}\ (s^3 t^3 - s^5 t - 3st^3 + 3s^3 t) + (T_2+T_4)\frac{1}{4}\ (st^5 - s^3 t^3 - 3t^3 + 3s^3 t)\} \\
&- s_i \{T_1(s^2-2s+t^2) + T_2(2st-2s) + T_3(-s^2-2s-t^2) + T_4(-2st-2s)\}\Big)\ \frac{\partial w}{\partial t_i}
\end{aligned}
\qquad \ldots \quad \text{(II-6)}
$$

where $T_1 = 1$ if $-s \leqslant t \leqslant s$ (see Fig. II-2)
$T_2 = 1$ if $-t \leqslant s \leqslant t$
$T_3 = 1$ if $s \leqslant t \leqslant -s$
$T_4 = 1$ if $t \leqslant s \leqslant -t$

The coefficients T_i ; $i = 1,4$ are zero outside these regions.

The displacement function of the BG element defined by equation (II-6) is the same as that for the ACM element (see equation (II-4)), except that corrective functions have been added to enforce compatibility of normal slope at the element boundaries.

This element will automatically satisfy the constant curvature criterion when employed in a rectangular form because the displacement function of equation (II-6) includes all the terms of a complete 2nd order polynomial. However, the constant curvature criterion is not satisfied for a general quadrilateral element because, as with the ACM element, the term s^2t^2 is not included in the displacement function. The performance of the element is therefore likely to be unsatisfactory for highly distorted quadrilaterals.

Numerical integration was used to evaluate the stiffness matrix of the element, using a triangular scheme [42] with three equally weighted integration points for each subtriangular element located at the subelement midsides, as described in Chapter VII. This scheme will integrate exactly a quadratically varying strain energy density, and was found to produce results virtually identical to those obtained from analytical integration [30, 73] when applied with rectangular elements to analyse the plate structures described in Section II-7.

II-5 HCT ELEMENT (Hsieh, Clough, Tocher [6, 15, 19, 117)

The HCT element is a fully compatible triangular plate bending element, with nodal parameters $w, \theta x, \theta y$ at each vertex, and is formed by assembling three subtriangular elements a, b and c connected at an internal point 0, as shown in Fig. II-3.

The derivation of the element displacement function is based on the assumption of an independent complete cubic polynomial displacement expression for the subelements, involving 10 terms each. These terms correspond to the nine corner degrees of freedom, including w, θx , and θy at the internal point 0, for each subelement, and the midside normal slope on the external boundary. The displacement expression for subelement a is given by

$$w_a = \alpha_1 + \alpha_2 x + \alpha_3 y + \alpha_4 x^2 + \alpha_5 xy + \alpha_6 y^2 + \alpha_7 x^3 + \alpha_8 x^2 y + \alpha_9 xy^2 + \alpha_{10} y^3 \quad \ldots \quad (II-7)$$

and a similar expression is assumed for the other two subelements.

The displacement function of the complete element involves a total of 30 generalised nodal parameters α_i , and is to be expressed in terms of the nine degrees of freedom $w, \theta x, \theta y$ at each vertex and the three normal slopes at the external midsides. Therefore 12 of the 30 coefficients α_i can be defined, the remaining 18 constraint conditions are provided by the requirements of compatibility between subelements.

a) Enforcing compatibility of deformations at the subelement corners yields 3 constraints at each vertex. I.e., a total of 3 x 3 = 9 constraints.

b) To achieve subelement compatibility at the internal junction point 0 requires 3 compatibility equations to connect subelement a to subelement b, and 3 equations to connect subelement b to subelement c, resulting in a total of 2 x 3 = 6 constraints.

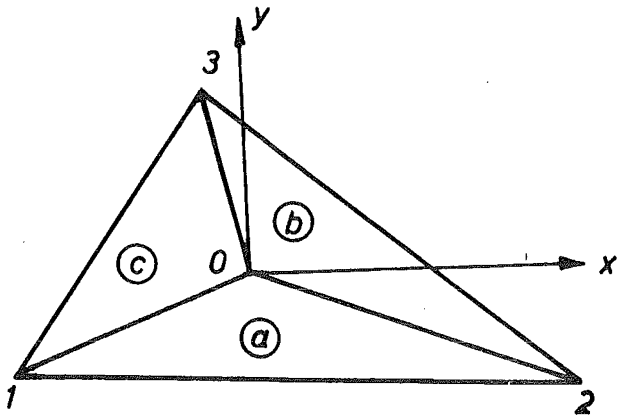

FIGURE II-3 SUBDIVISION OF THE HCT ELEMENT

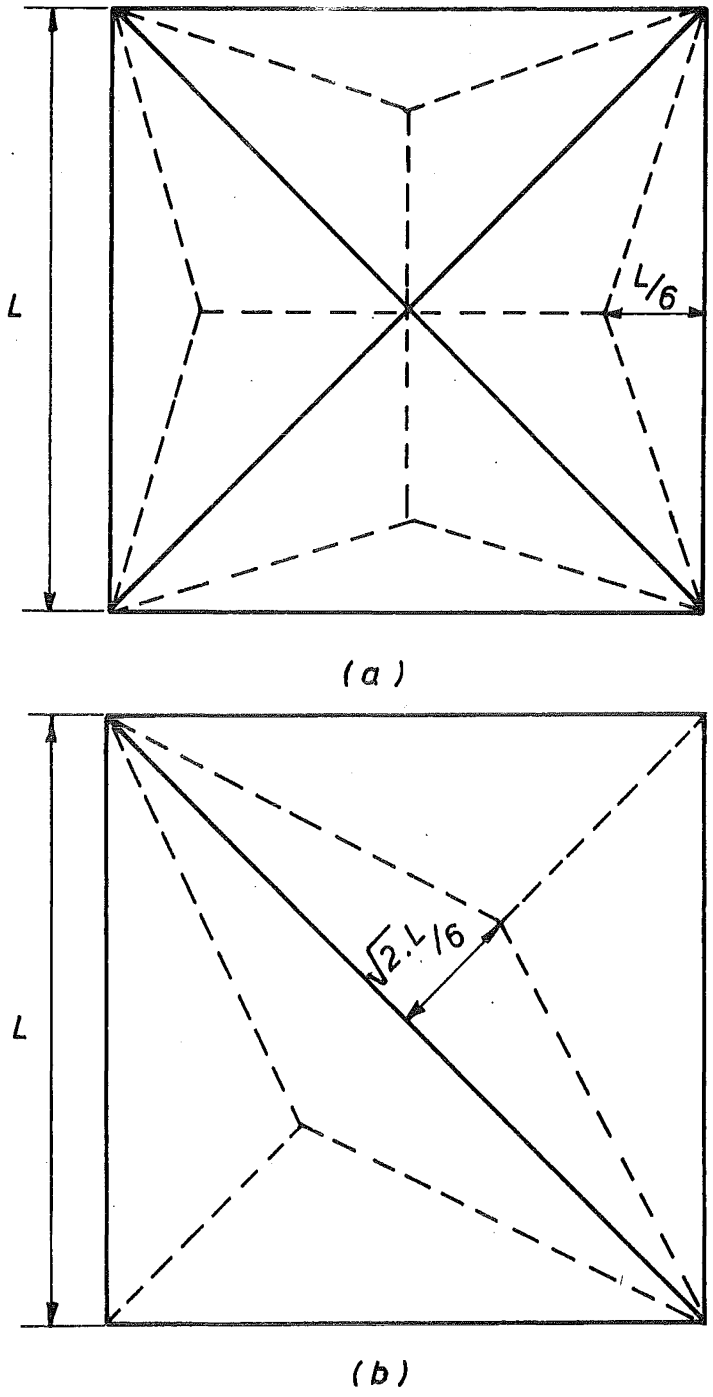

FIGURE II-4 ASSEMBLY OF HCT ELEMENTS TO FORM A QUADRILATERAL

c) It is evident from inspection of the subelement displacement expression, equation (II-7), that the normal slope along the sides of the subelements varies parabolically, requiring 3 nodal parameters to uniquely define this slope. Two of these are specified by the normal resultant of the vertex slopes at the ends of a side.

Complete compatibility across the internal boundaries is ensured by constraining the normal slopes at the midside to have the same values from adjacent elements. This will yield 1 x 3 = 3 constraints.

A total of 18 constraints are therefore required to satisfy internal compatibilities, so the 30 coefficients α_i can be related to the 12 nodal degrees of freedom.

The computationally inefficient midside nodes may be eliminated by constraining the midside normal slope to take the average value of the normal slopes at the ends of the respective sides. This results in the fully compatible HCT element, which has nine degrees of freedom and a linear variation of normal slope along the external boundaries.

Bazely et al [6] have demonstrated that the displacement function of the HCT element may alternatively be derived by adding corrective functions to the displacement function of an incompatible 9 parameter triangular element. However, the enforcement of compatibility of deformations on the element boundaries results in excessive stiffness, as demonstrated in Section II-7.

A quadrilateral shaped element may be formed by either combining four HCT triangular elements and eliminating the nodal parameters at the intersection of the two diagonals by a static condensation procedure [71], or by combining two HCT elements. However, when these two schemes are used to form a square element, with the internal junction points 0 located near the subelement centroids, the aspect ratio of the subtriangular will be of the order of 1/6 and $\sqrt{2}/6$ respectively, as illustrated in Figures II-4a and II-4b. The application of these quadrilateral elements is generally restricted to meshes for which the aspect ratios are less than two because the accuracy deteriorates significantly for elongated elements, as shown in Section II-7.

II-6 CQ12 ELEMENT

II-6.1 Introduction

This fully compatible quadrilateral element is derived by eliminating the midside normal slope parameters of Fraeijs de Veubeke's CQ16 element [34, 35], following the procedure used with the HCT element. The CQ12

element thus has degrees of freedom $w, \theta x, \theta y$ at the four corners only.

It was anticipated [36] that constraining the normal slope along the boundaries to a linear variation may result in an element that is grossly over-stiff at coarse meshes, but this was not found to be the case, as evidenced from the numerical results presented in Section II-7. Although this element does deteriorate in accuracy as the aspect ratio deviates from a value of one, the deterioration is demonstrated in Section II-7 to be less severe than for the HCT element. Also, the displacement function is complete to the 3rd order and the strain energy gradient may be integrated analytically. The CQ12 element is therefore likely to be most suitable for box-girder analyses, and has recently been used for shell analyses [46]. However, few comparisons of the element performance have been presented in the literature.

II-6.2 Alternative approaches

Before describing the formulation used to derive the element stiffness, which follows closely that employed by De Veubeke [34, 35], two possible approaches are outlined briefly to demonstrate similarities with previous elements. The approach in all cases will be to derive the displacement function associated with the 16 parameter CQ16 element first.

i) Zienkiewicz [117] has suggested that this element may be derived by subdividing the quadrilateral into three overlapping regions, and defining the displacement function in three parts

$$w = w_a + w_b + w_c$$

as shown in Fig. II-5. The first component, which is defined over the whole region, is a complete cubic with ten coefficients

$$w_a = \alpha_1 + \alpha_2 x + \alpha_3 y + \alpha_4 x^2 + \alpha_5 xy + \alpha_6 y^2$$

$$+ \alpha_7 x^3 + \alpha_8 x^2 y + \alpha_9 xy^2 + \alpha_{10} y^3$$

The other two components are defined in a piecewise manner. Let $A_b = 1$ in triangle b and zero elsewhere, and let $A_c = 1$ in triangle c and zero elsewhere, then

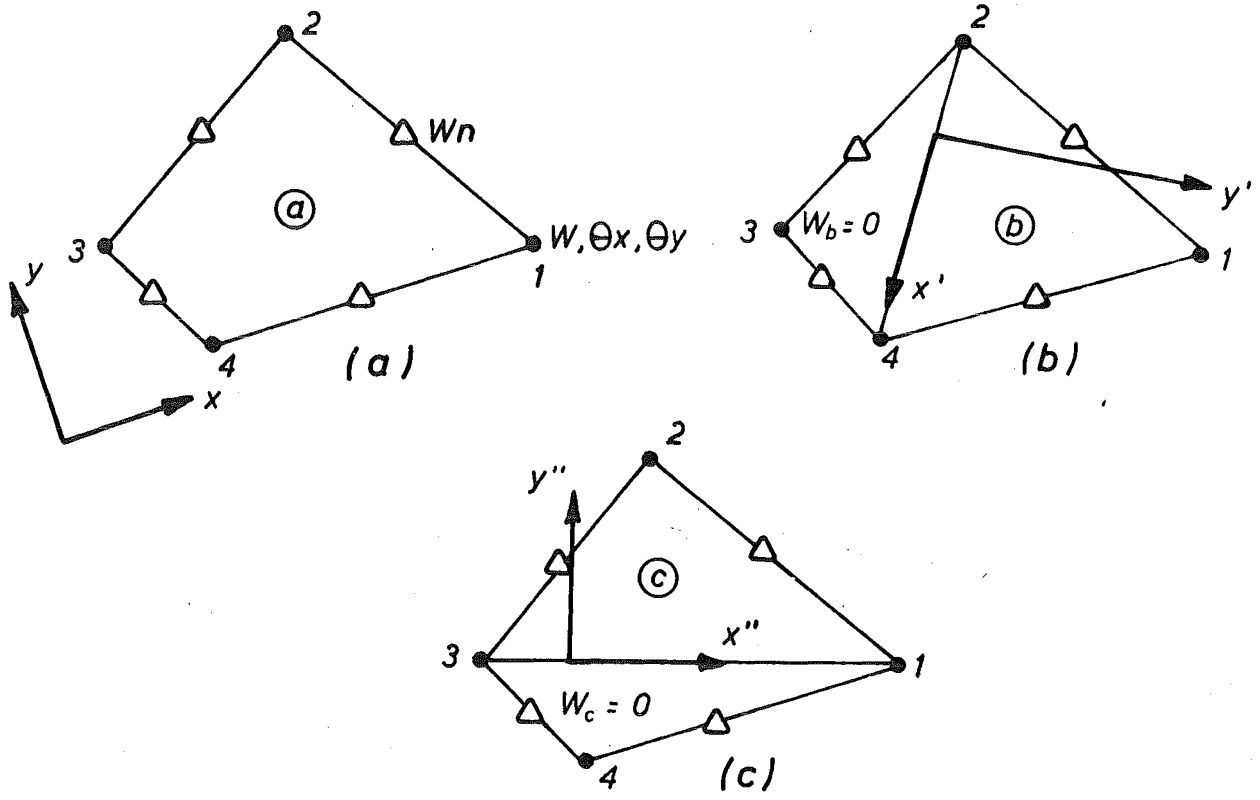

FIGURE II-5 LOCAL COORDINATES

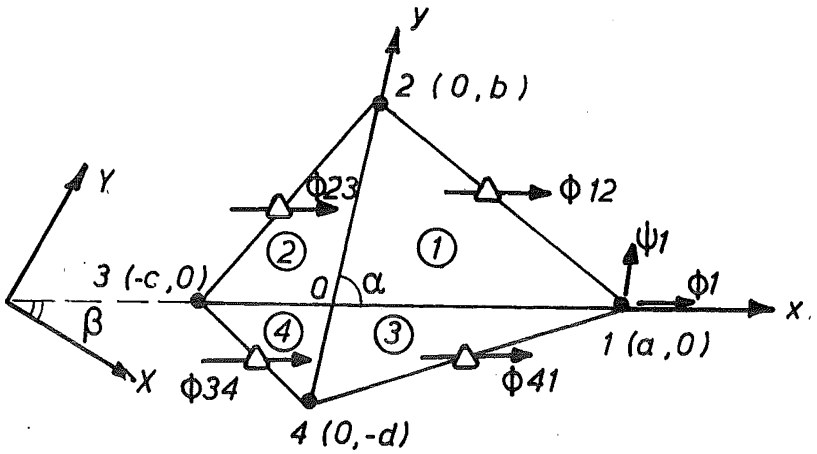

FIGURE II-6 SUBDIVISION OF CQ12 ELEMENT

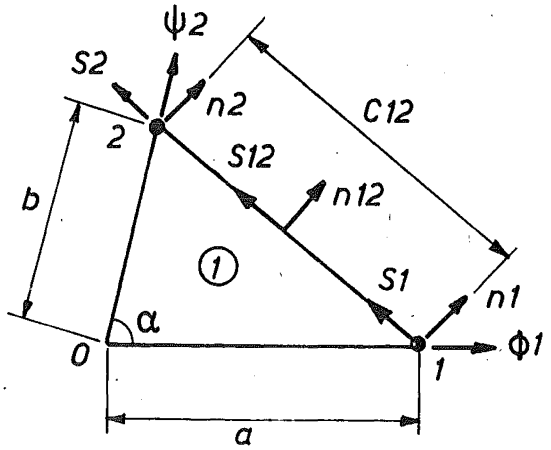

FIGURE II-7 ELIMINATION OF MIDSIDE NODES

$$w_b = \left(\alpha_{11} y'^2 + \alpha_{12} y'^3 + \alpha_{13} x' y'^2 \right) \cdot A_b$$

$$w_c = \left(\alpha_{14} y''^2 + \alpha_{15} y''^3 + \alpha_{16} x'' y''^2 \right) \cdot A_c$$

where (x',y') and (x'',y'') are the local coordinates defined in Fig. II-5. These two functions are continuous up to the first derivative with respect to the local coordinates, having zero value and slopes on the corresponding region interfaces. The sixteen coefficients $\alpha_1 - \alpha_{16}$ may be related to the sixteen degrees of freedom constituted by the three corner parameters $w, \Theta x, \Theta y$ and the normal midside slopes.

ii) An alternative approach, employed by De Veubeke [34,35] and also by Chan and Kabaila [16], is to divide the quadrilateral element into four triangular subelements 1, 2, 3, 4, bounded by the diagonals and connected at the internal intersection point 0. The derivation of the element displacement function is based on the assumption of an independent complete cubic polynomial displacement expression for the four subelements, involving ten terms each. These correspond to the nine vertex degrees of freedom $w, \Theta x, \Theta y$, and the midside normal slope on the external boundary of the subelement.

The displacement function of the complete element has a total of 40 generalised nodal parameters α_i, and is to be expressed in terms of the sixteen degrees of freedom, defining 16 of the 40 coefficients α_i. The remaining 24 constraint conditions are provided by the requirements of compatibility between subelements.

a) Enforcing compatibility of deformations at the subelement corners yields 3 compatibility equations at each corner, i.e., a total of 3 x 4 = 12 constraints.

b) To achieve subelement compatibility at the internal intersection point 0 requires 3 compatibility equations to connect the first subelement to the second, 3 equations to connect the second subelement to the third, and 3 equations to connect the third to the fourth, i.e., a total of 3 x 3 = 9 constraints.

c) Continuity of the parabolically varying normal slope across the element diagonals is ensured if the twisting curvatures w,xy, from all four subtriangles, are constrained to be equal at the internal intersection point 0. This results in 3 x 1 = 3 constraints.

A total of 24 constraints are therefore required to satisfy internal compatibilities, so the 40 coefficients α_1 can be related to the

16 degrees of freedom to define the displacement function of a fully compatible element which may be expressed as a piecewise continuous polynomial

$$w = w^1 + w^2 + w^3 + w^4$$

These two approaches are identical in concept, and the second approach, which is analogous to the formulation described for the HCT element, was employed for this work.

II-6.3 Element displacement function

It is convenient to use the diagonals, with included angle α, to define a natural oblique coordinate system, (x,y), as illustrated in Fig. II-6. This is because two of the sides of each subtriangle are defined by the lines $x = 0$ and $y = 0$ respectively, and consequently the constraint equations only involve equalities between individual coefficients. Also, the relationships between the polynomial coefficients α_i and the nodal parameters become much simpler.

The displacement expression for subelement j may be written

$$w^j = \alpha_1^j + \alpha_2^j x + \alpha_3^j y + \alpha_4^j x^2 + 2\alpha_5^j xy + \alpha_6^j y^2$$

$$+ 4\left(\alpha_7^j x^3 + \alpha_8^j x^2 y + \alpha_9^j xy^2 + \alpha_{10}^j y^3\right) ; \quad j = 1,4 \qquad \ldots \quad (II-8)$$

Considering subelement 1 (see Fig. II-6), the ten coefficients α_i^1 ; $i = 1, 10$ can be evaluated in terms of the local nodal parameters w_0 , w_1 , w_2 , ϕ_0 , ϕ_1 , ϕ_2 , ψ_0 , ψ_1 , ψ_2 and ϕ_{12} , as described by Fraeijs de Veubeke [35], where $\phi_i = \frac{\partial w}{\partial x_i}$, $\psi_i = \frac{\partial w}{\partial y_i}$; $i = 0, 1, 2, 3, 4$ and $\phi_{ij} = \frac{\partial w}{\partial x_{ij}}$ is the slope at the middle of side $i - j$. Along the interface $x = 0$

$$w = \alpha_1^1 + \alpha_3^1 y + \alpha_6^1 y^2 + 4\alpha_{10}^1 y^3$$

$$w,x = \alpha_2^1 + 2\alpha_5^1 y + 4\alpha_9^1 y^2$$

Considering subelement 2, along the interface $x = 0$

$$w = \alpha_1^2 + \alpha_3^2 y + \alpha_6^2 y^2 + 4\alpha_{10}^2 y^3$$

$$w,x = \alpha_2^2 + 2\alpha_5^2 y + 4\alpha_9^2 y^2$$

The necessary constraints on the coefficients necessary to ensure compatibility of the deflections and slopes between subelements 1 and 2 are

$$\alpha_i^1 = \alpha_i^2 \quad ; \quad i = 1, 2, 3, 5, 6, 9, 10$$

which eliminates 7 coefficients.

A total of 24 coefficients may be eliminated by enforcing compatibility along the internal boundaries of each subelement in turn [35]. This leaves 16 independent coefficients.

$$\alpha_i^1 \; ; \; i = 1,2,\ldots,10 \quad \text{and} \quad \alpha_4^2 \, , \, \alpha_7^2 \, , \, \alpha_8^2 \, , \, \alpha_6^3 \, , \, \alpha_9^3 \, , \, \alpha_{10}^3$$

which, by substituting into the four sets of expressions defined by equation (II-8), are related to the nineteen nodal parameters at nodes 0, 1, 2, 3, 4 and the midsides of the external boundaries. Only sixteen of these parameters are linearly independent; Equating the four coefficients

$$\alpha_5^1 = \alpha_5^2 = \alpha_5^3 = \alpha_5^4$$

which has the effect of enforcing compatibility of the twisting curvature w,xy at the intersection point 0, the parameters w_o , ϕ_o , and ψ_o may be related to the sixteen independent degrees of freedom [35].

Thus the displacement function of the CQ16 element is derived.

To enable the assembly of a mesh of quadrilateral elements to proceed without difficulty it is necessary to relate the midside slopes ϕ_{ij} to the element degrees of freedom. Consider subelement 1, shown in Fig. II-7. The transverse slopes S_1 , S_2 in the direction of side 1-2 may be expressed in terms of the parameters ϕ_1 ,ψ_1 and ϕ_2 , ψ_2 respectively.

$$C_{12}\, S_1 = -a\phi_1 + b\psi_1$$

$$C_{12}\, S_2 = -a\phi_2 + b\psi_2$$

where C_{12} is the length of side 1 - 2. Then, considering the cubic variation of w along side 1 - 2, the transverse slope S_{12} at mid distance along side 1 - 2 may be written

$$4C_{12}S_{12} = 6(W_2 - W_1) - (S_1 + S_2)$$

or, substituting the expressions for S_1 and S_2

$$4C_{12}S_{12} = 6(W_2 - W_1) + a\phi_1 - b\psi_1 + a\phi_2 - b\psi_2$$

Now, ϕ_{12} may be written in terms of S_{12} and n_{12}

$$C_{12}\phi_{12} = b \sin\alpha\, n_{12} - (a - b\cos\alpha)\, S_{12}$$

where n_{12} is the normal at mid distance along side 1 - 2. Substituting the expression for S_{12}

$$\phi_{12} = \frac{b\sin\alpha}{C_{12}} n_{12} - \left[\frac{a - b\cos\alpha}{4C_{12}^2}\right]\left[6(W_2 - W_1) + a(\phi_1 + \phi_2) - b(\psi_1 + \psi_2)\right] \quad \ldots \text{(II-9)}$$

The normal slopes n_1 and n_2 at the corner nodes may also be related to the slopes ϕ_1, ψ_1 and ϕ_2, ψ_2 respectively. (See Fig. II-7).

$$n_1 = \frac{(a - b\cos\alpha)}{C_{12}}\left[\frac{1}{\sin\alpha}\psi_1 - \frac{a}{b\sin\alpha}\phi_1\right] + \frac{C_{12}}{b\sin\alpha}\phi_1 \quad \ldots \text{(II-10)}$$

$$n_2 = \frac{(a - b\cos\alpha)}{C_{12}}\left[\frac{1}{\sin\alpha}\psi_2 - \frac{a}{b\sin\alpha}\phi_2\right] + \frac{C_{12}}{b\sin\alpha}\phi_2 \quad \ldots \text{(II-11)}$$

The variation of the midside normal slope may be constrained to remain linear on the boundaries of the quadrilateral element by defining

$$n_{12} = \frac{1}{2}(n_1 + n_2)$$

Substituting equations (II-10) and (II-11) into equation (II-12), an expression relating the midside slope to the element degrees of freedom is obtained

$$\phi_{12} = \frac{1}{2}(\phi_1 + \phi_2) - \frac{(a - b\cos\alpha)}{C_{12}^2}\left[1.5\,(W_2 - W_1) + 0.75\,a(\phi_1 + \phi_2) - 0.75\,b(\psi_1 + \psi_2)\right] \quad \ldots \text{(II-13)}$$

where $C_{12}^2 = a^2 + b^2 - 2ab\cos\alpha$

Similarly for the other three subelements,

$$\phi_{23} = \frac{1}{2}(\phi_2 + \phi_3) - \frac{(c + b\cos\alpha)}{C_{23}^2}\left[1.5\,(W_3 - W_2) + 0.75\,C(\phi_2 + \phi_3) + 0.75\,b(\psi_2 + \psi_3)\right] \quad \ldots \text{(II-14)}$$

$$\phi_{34} = \frac{1}{2}(\phi_3 + \phi_4) - \frac{(c - d\cos\alpha)}{C_{34}^2}\left[1.5\,(W_3 - W_4) + 0.75\,C(\phi_3 + \phi_4) - 0.75\,d(\psi_3 + \psi_4)\right] \quad \ldots \text{(II-15)}$$

$$\phi_{41} = \frac{1}{2}(\phi_4 + \phi_1) - \frac{(a + b\cos\alpha)}{C_{41}^2}\left[1.5\,(W_4 - W_1) + 0.75\,a(\phi_4 + \phi_1) + 0.75\,d(\psi_4 + \psi_1)\right] \quad \ldots \text{(II-16)}$$

Thus, the sixteen coefficients α_i^j of the displacement functions are related to the twelve degrees of freedom $w, \theta x, \theta y$

The natural local coordinate system (x,y), defined by the diagonals of the elements, is not invariant when passing from one element to another, so it is necessary to measure the deformations with respect

to the global cartesian coordinate system (X,Y), shown in Fig. II-6. This is achieved by applying the transformations

$$\phi = \frac{\partial w}{\partial x} = \frac{\partial w}{\partial X}\frac{X_{10}}{a} + \frac{\partial w}{\partial Y}\frac{Y_{10}}{a} \qquad \text{where} \quad X_{ij} = X_i - X_j$$

$$\psi = \frac{\partial w}{\partial y} = \frac{\partial w}{\partial X}\frac{X_{20}}{b} + \frac{\partial w}{\partial Y}\frac{Y_{20}}{b} \qquad Y_{ij} = Y_i - Y_j$$

... (II-29)

The displacement functions may now be related to the twelve cartesian degrees of freedom w_i , $\Theta x_i = \frac{\partial w}{\partial Y_i}$ and $\Theta Y_i = \frac{\partial w}{\partial X_i}$ in terms of the local parameters (x,y). The local curvatures $\frac{\partial^2 w}{\partial x^2}$, $\frac{\partial^2 w}{\partial y^2}$, $\frac{\partial^2 w}{\partial x \partial y}$ are obtained by differentiating the displacement function, and the cartesian curvatures defined by a transformation matrix which incorporates the angle β between the two coordinate systems, defined in Fig. II-6.

$$\begin{Bmatrix} \frac{\partial^2 w}{\partial X^2} \\ \frac{\partial^2 w}{\partial Y^2} \\ \frac{\partial^2 w}{\partial X \partial Y} \end{Bmatrix} = \begin{bmatrix} \text{Cos}^2\beta + \text{Sin}^2\beta\,\text{Cot}^2\alpha & \text{Sin}^2\beta/\text{Sin}^2\alpha & 2\text{Sin}\beta\,\text{Cos}\beta/\text{Sin}\alpha \\ -2\text{Sin}\beta\,\text{Cos}\beta\,\text{Cot}\alpha & & -2\text{Cos}\alpha\text{Sin}^2\beta/\text{Sin}^2\alpha \\ \text{Sin}^2\beta + \text{Cos}^2\beta\,\text{Cot}^2\alpha & \text{Cos}^2\beta/\text{Sin}^2\alpha & -2\text{Sin}\beta\,\text{Cos}\beta/\text{Sin}\alpha \\ +2\text{Sin}\beta\,\text{Cos}\beta\,\text{Cot}\alpha & & +2\text{Cos}\alpha\,\text{Cos}^2\beta/\text{Sin}^2\alpha \\ (\text{Sin}^2\beta - \text{Cos}^2\beta)\text{Cot}\alpha & \text{Sin}\beta\,\text{Cos}\beta/\text{Sin}^2\alpha & \text{Cos}^2\beta - \text{Sin}^2\beta/\text{Sin}\alpha \\ +\text{Sin}\beta\,\text{Cos}\beta\,(\text{Cot}^2\alpha - 1) & & -2\text{Sin}\beta\,\text{Cos}\beta\,\text{Cos}\alpha/\text{Sin}^2\alpha \end{bmatrix} \begin{Bmatrix} \frac{\partial^2 w}{\partial x^2} \\ \frac{\partial^2 w}{\partial y^2} \\ \frac{\partial^2 w}{\partial x \partial y} \end{Bmatrix}$$

The curvature of the quadrilateral element may thus be defined in a piecewise manner, and the element stiffness matrix evaluated in the standard manner described in Chapter I.

II-6.4 Integration of the strain energy gradient

Fraeijs de Veubeke [35] has described a simple method by which the the strain energy gradient associated with the CQ16 element may be integrated analytically, and the adaption of this method to the CQ12 element presents no difficulties. However, the use of analytical integration required more than twice the amount of computer time needed to evaluate exactly the stiffness matrix of a constant thickness element using the 3 point numerical integration scheme of Hammer [42], described in Chapter VII, over each subtriangle. However, it is possible that the computational effort required to perform the integration analytically may be considerably reduced by the use of improved programing techniques.

Numerical integration was preferred for this work, for which the following procedure was employed: First, the relationship between the local (x,y) and the global (X,Y) coordinates shown in Fig. II-6 was defined

$$x = X\cos\beta - Y\sin\beta - (X\sin\beta + Y\cos\beta)\cos\alpha/\sin\alpha$$

$$y = (X\sin\beta + Y\cos\beta)/\sin\alpha$$

The global stiffness matrix of the element may be written in the form

$$[K] = \int\int_{Area} F(X,Y)\,dX\,dY$$

where $F(X,Y)$ represents the strain energy per unit area, the definition of which differs from one subelement to another, and was evaluated numerically

$$[K] = \sum_{i=1}^{m}\sum_{j=1}^{n} W_{ij}\, F(X_i,Y_j)$$

where W_{ij} is the weighting of the $(i,j)^{th}$ sampling point.

II-6.5 Consistent loading

In order to translate externally applied loads into generalised loads concentrated at the nodes, in a manner consistent with the formulation of the element stiffness matrix [K], the nodal forces and moment must be defined so as to perform the same virtual work when acting through the

nodal displacements and rotations respectively, as that performed by the applied loads during the deformation. The formulation employed to determine the consistent nodal loading representing an applied point loading is described in Appendix A.

II-7 COMPARISONS OF ELEMENT PERFORMANCE

II-7.1 Deflections

i) Simply supported square plate.

A series of uniform meshes of both the CQ12 and BG plate bending elements were used to idealise a simply supported square plate, subjected to a central point load. Only one quarter of the plate was analysed, making use of symmetry about the transverse and longitudinal centrelines. The variations of central deflection with the number of mesh divisions along one half-side of the plate are plotted in Fig. II-8. The results from the two elements are virtually identical and plot on the same line. The variations of central deflection computed with finite element idealisations constructed from the HCT element [19], the ACM element [19], and from Clough's 16 parameter quadrilateral Q16 element, which is a fully compatible element derived by combining two LCT12 triangles [21] and condensing out the internal node, are also plotted in Fig. II-8. The computed deflections from all the elements converge monotonically to the exact solution [104] from below, except for the incompatible ACM element. The CQ12 element produces results which are more accurate than those obtained from the HCT element, but less accurate than those of the Q16 element, which has additional nodal parameters. The results from the ACM element are of similar accuracy to those of the CQ12 element, and exhibit a similar rate of convergence.

ii) Clamped square plate

These same five elements were used to analyse one quarter of a clamped square plate subjected to a central point load. The variations of central deflection with the number of mesh divisions along one half-side of the plate are plotted in Fig. II-9. The ACM element, in contrast to the other elements, does not exhibit monotonic convergence of the deflection to the exact solution with mesh refinement. The central deflection computed from the coarse mesh analysis is of superior accuracy however, because the relaxation of the normal slope compatibility constraint has permitted the element to deform in a more flexible manner than the fully compatible elements. The CQ12 and BG elements again

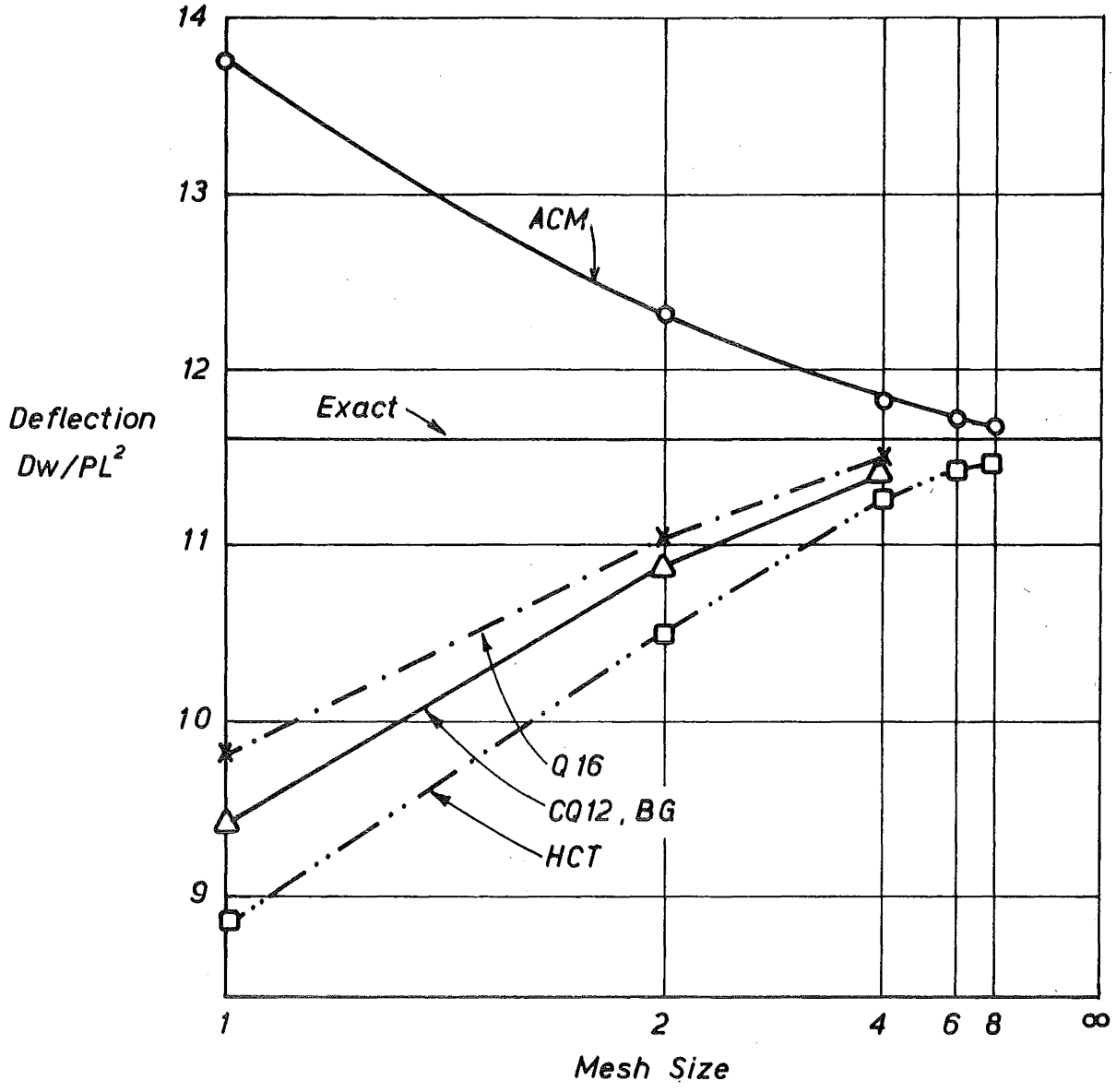

FIGURE II-8 CENTRAL DEFLECTION OF SIMPLY SUPPORTED SQUARE PLATE CENTRAL POINT LOAD

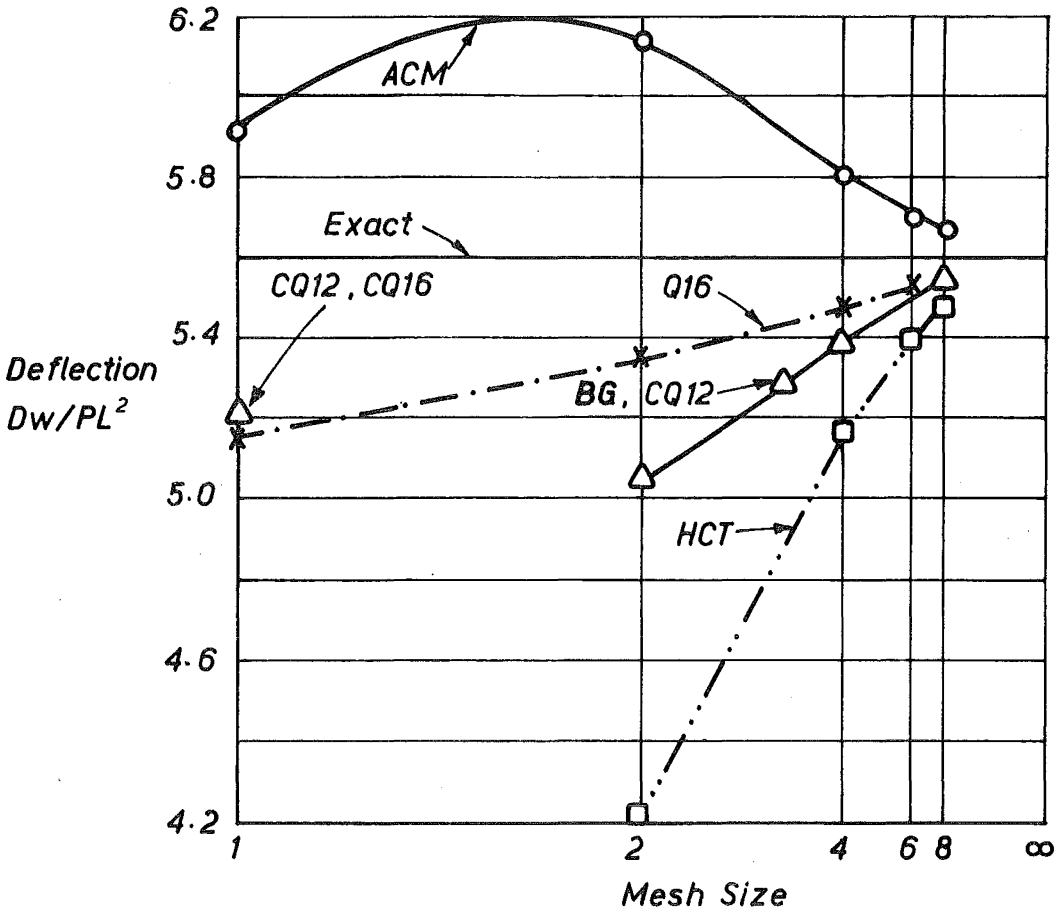

FIGURE II-9 CENTRAL DEFLECTION OF CLAMPED SQUARE PLATE CENTRAL POINT LOAD

produce results which plot on the same curve, and with an accuracy considerably better than that obtained from the HCT element, but not as good as that from the Q16 element, except when only one element is used to simulate the plate quarter. The CQ12 results computed with this idealisation are identical to those obtained with the CQ16 element,[35, 117], because the constraint applied to the normal slope across the boundaries of the CQ16 element, to derive the 12 parameter element, comply with the physical boundary conditions of the plate.

II-7.2 Bending moments

A square plate subjected to a central point load was analysed with first clamped, then simply supported edges, using a uniform (4 x 4) mesh of both CQ12 and ACM elements to idealise one quarter of the plate. The computed distributions of transverse bending moment at the nodes along the transverse centreline are shown in Fig. II-10, the results from each of the two elements common to a node are plotted separately. The ACM element has been shown to give a 'best linear fit of the bending moment distribution' at all stages of the subdivision [117] when the nodal moments are calculated by averaging the bending moments computed at the corner of each element connected to the node. In contrast, the incompatible 9 parameter LCT9 plate bending element [117] has been shown to produce more accurate results when the bending moments are evaluated at the centroid of the element, because the linear variation of moments across the element does not represent the best linear fit to the actual distribution. It is evident from Fig. II-10 that the variation of bending moment obtained by assuming a linear distribution through the nodal moments of the CQ12 element, calculated by averaging the appropriate nodal values of each constituent element meeting at that node, follows closely the variation of the ACM element. This procedure of presenting the bending moment distributions computed from a mesh of CQ12 elements was therefore adopted throughout this work.

II-7.3 Aspect ratio

A number of simply supported rectangular plates, with aspect ratio varying from a value of 1 to 6, were subjected to a central transverse point load and the response analysed using both 4 x 4 meshes and 8 x 8 meshes of HCT, CQ12 and ACM elements to model the plates. The variations of the percentage error of the computed central deflection with the

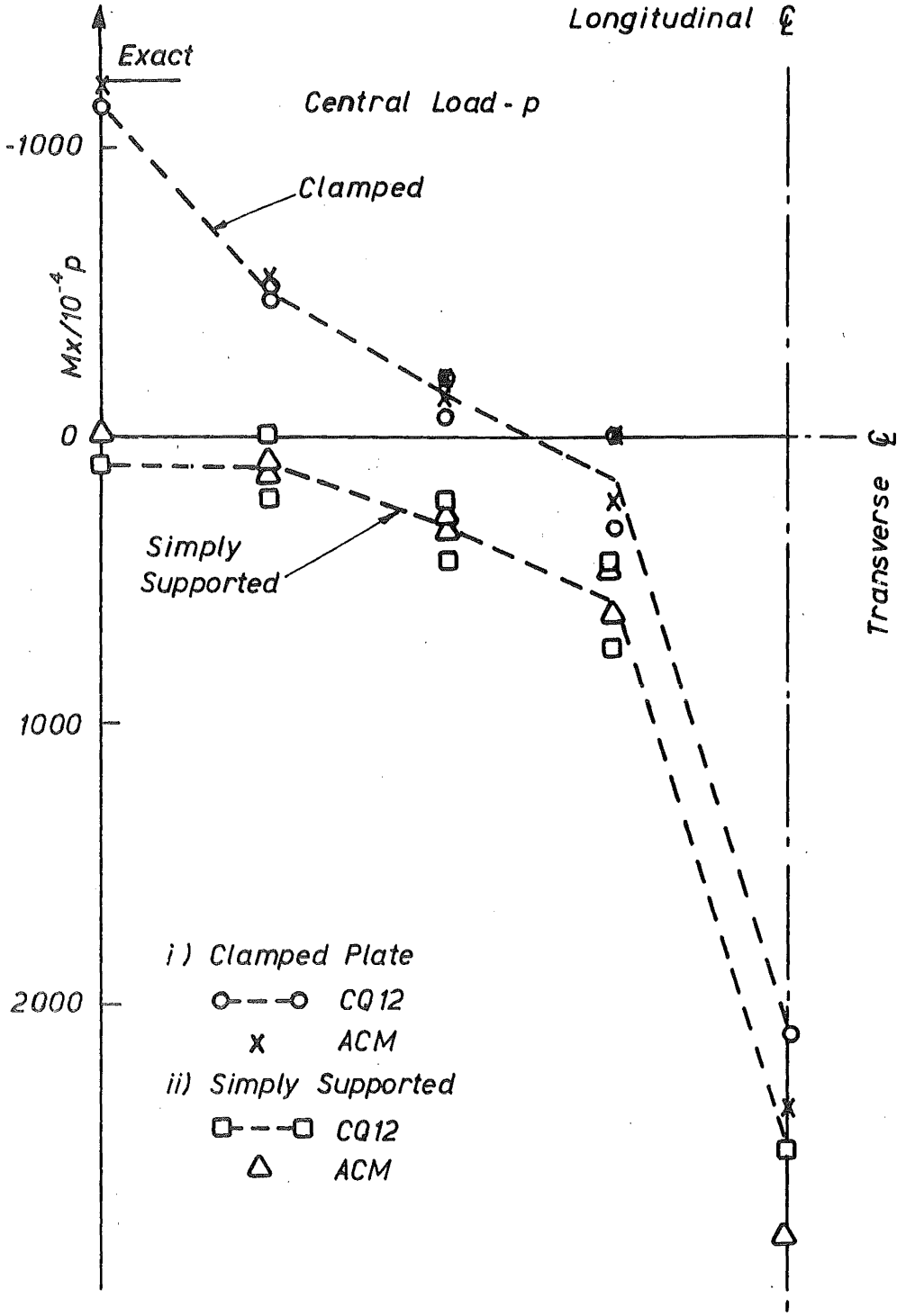

FIGURE II-10 BENDING MOMENT ALONG CENTRELINE OF SQUARE PLATE

aspect ratio of the elements are plotted in Fig.II.11a for the 4 x 4 mesh, and in Fig.II.11b for the 8 x 8 mesh idealisation. The performance of the CQ12 element deteriorates as the aspect ratio deviates from a value of one. However, this deterioration is not as severe as that associated with the HCT element. The central deflection computed from the ACM element oscillates from being too large for square element, to being too small when the aspect ratio is increased to a value of 6. However, the accuracy does not deteriorate significantly as the aspect ratio is increased.

II-7.4 Conclusions

The CQ12 plate bending element is considered to be more suitable for application to box-girder bridge analysis than the ACM, BG, or HCT elements because;

i) The accuracy of the results obtained from the analysis of square plates subjected to a central point load with various uniform mesh idealisations of CQ12 plate bending elements is similar to that obtained from the BG and ACM elements, but these latter elements cannot represent constant curvature states when generalised to a quadrilateral shape, and thus may produce erroneous results when applied to the analysis of curved box-girder bridges. Also, the displacement function of the ACM element is not fully compatible so there is no guarantee of a bounded solution. Although local violations of slope continuity of rectangular shaped elements do not necessarily prevent convergence to the correct solution when the mesh is refined [108, 117], the convergence of the stress field is much more seriously affected [35].

ii) The HCT element deforms in an over-stiff manner at coarse meshes and the performance deteriorates rapidly as the aspect ratio deviates from a value of one. The performance of the CQ12 element deteriorates less rapidly when the aspect ratio is increased, and the element has been employed with an aspect ratio of between 4 and 5 to analyse box-girder bridges, for which the computed results are shown in Chapter IX to be of good accuracy.

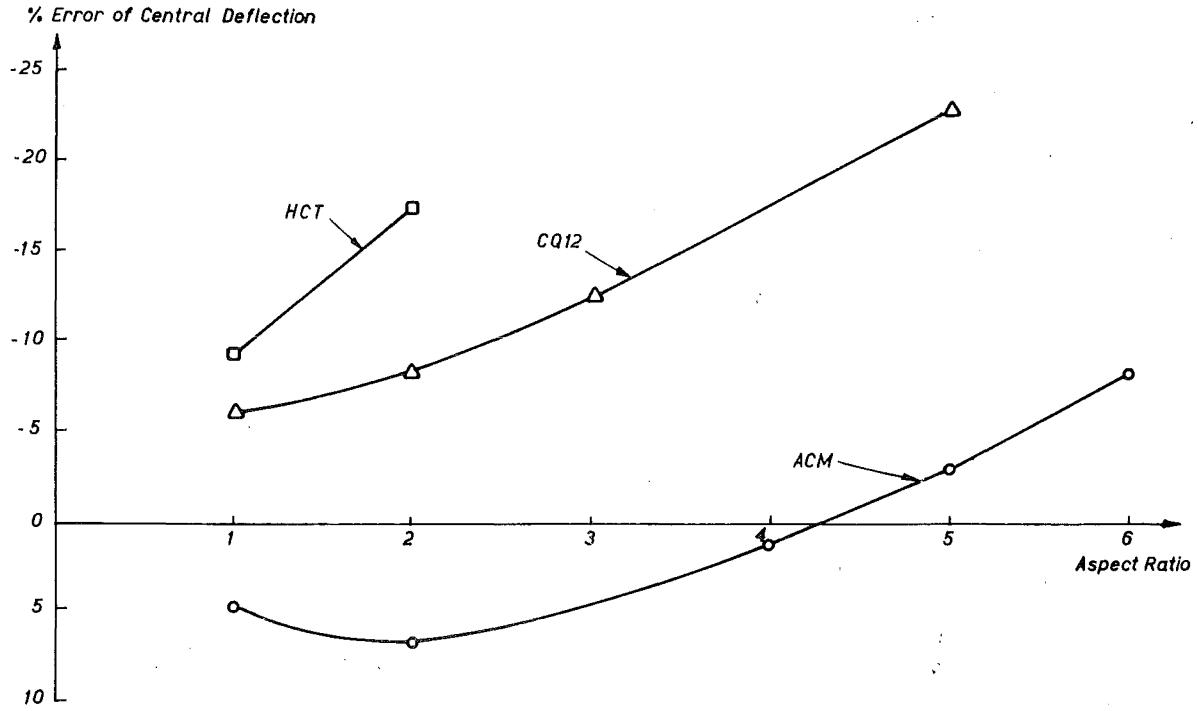

(a) 4 x 4 MESH OF ELEMENTS

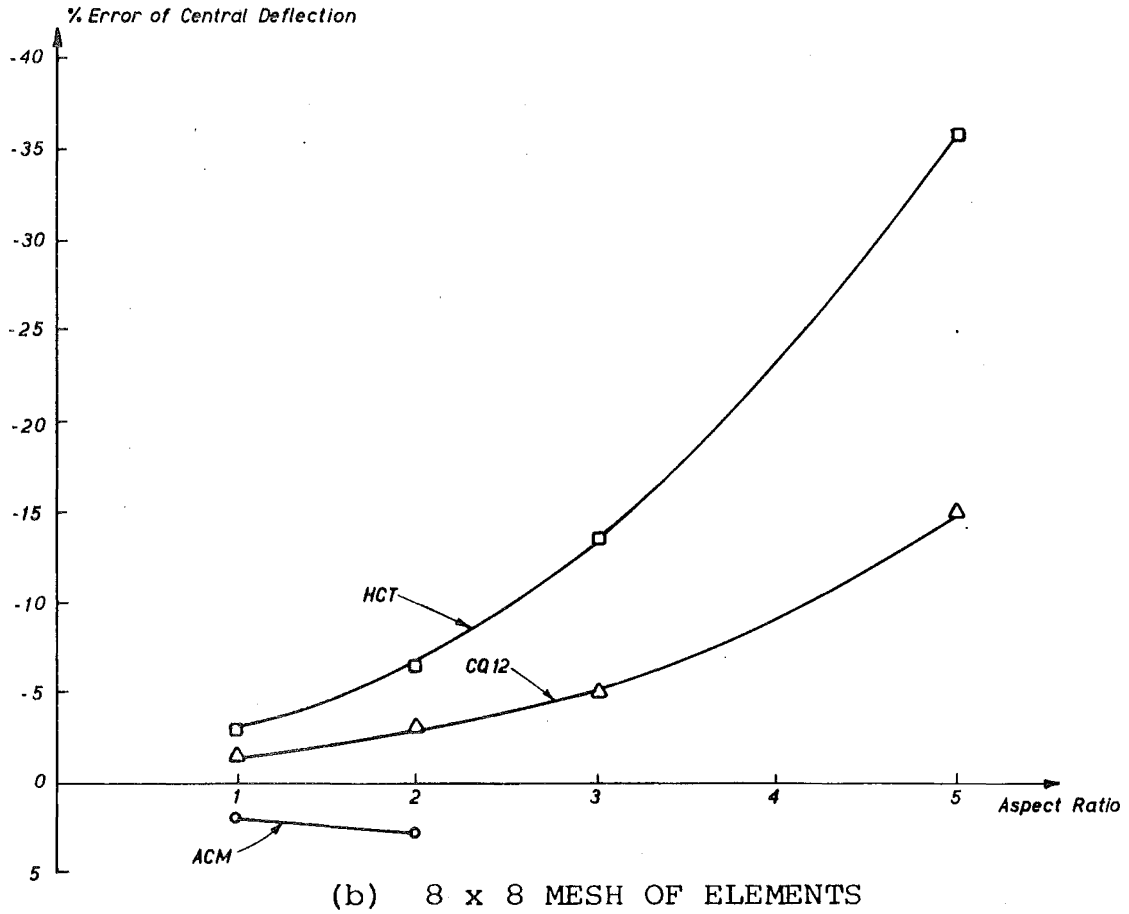

(b) 8 x 8 MESH OF ELEMENTS

FIGURE II-11 CENTRAL DEFLECTION VERSUS ASPECT RATIO

CHAPTER III

PLANE STRESS ELEMENT

III-1 REQUIREMENTS OF THE DISPLACEMENT FUNCTION

A survey of plane stress elements is presented from which the most suitable candidate for modelling the membrane behaviour of bix-girder bridges is selected.

The generalised membrane strains are defined as

$$\{\varepsilon\}^T = \langle \varepsilon_x , \varepsilon_y , \varepsilon_{xy} \rangle = \langle u,x,\ v,y,\ u,y + v,x \rangle$$

where x and y refer to the cartesian coordinate system illustrated in Fig. III-1, so the selection of suitable displacement functions, u(x,y) and v(x,y), is fundamental to the derivation of a plane stress element stiffness matrix. These functions should comply with the following criteria:

i) The displacement function is fully compatible and capable of reproducing any constant strain state of deformation.

ii) When non-coplanar elements meet at a junction, such as at the intersection of the webs and the deck slab, the in-plane displacement of the element is compatible with the cubically varying out-of-plane CQ12 displacement function w(x,y) of the adjoining element. Although a violation of compatibility here is not very significant with respect to the overall behaviour of the box-girder, it may cause considerable local fluctuations of the nodal slopes along the web-flange junction [55].

iii) The plane stress element has degrees of freedom $u_i, v_i, \Theta z_i$ at each corner node i to enable efficient coupling with the CQ12 plate bending element which has nodal parameters w_i, Θx_i, Θy_i. The definition of the rotational degree of freedom Θz is necessarily arbitrary since there is no unique value of in-plane rotation, apart from a rigid body movement, at a point in a two dimensional continuum. However, if the in-plane rotation Θz is not included as a nodal parameter cross-coupling between the in-plane rotational stiffness and the out-of-plane bending stiffness of adjoining non-coplanar elements will be neglected. The former stiffness may be much larger than the latter, especially in the case of thin plates, and therefore may have a significant effect on the flexural stresses which are developed.

iv) An assembly of the plane stress elements is capable of representing beam behaviour accurately with only one element employed down the depth of the beam idealisation. In this way the element can be conveniently used to represent the webs of box-girder bridges, resulting in a reduction of the computational effect required for the analysis.

v) The performance of the element does not deteriorate significantly when the aspect ratio of the element is increased from a value of one to about four, avoiding the necessity for refined element subdivisions when bridges of longer span are analysed.

III-2 SURVEY OF ELEMENTS

II-2.1 Element nomenclature

Four sided elements are designated by four character names according to the notation of Sisodiya et al [94]. The first two characters define the element geometry, i.e. QL for a quadrilateral and PQ for a parallelogram. The third character is C or N depending on whether the displacement function conforms with the interelement compatibility requirements or not. The fourth character is numeric and indicates the number of degrees of freedom per node.

When an alternative element is derived by replacing or modifying the displacement function of these elements the second character is altered (e.g. QK or QM instead of QL), and when additional displacement modes are incorporated a prefix character is added (e.g. AQL instead of QL).

The fully compatible triangular elements are designated CST, LST, or QST according to whether the displacement functions permit a constant, linear, or quadratic variation of strain across the element.

II-2.2 QLC2 element

Early attempts at thin plate finite element analyses of box-girder bridges employed the simple quadrilateral QLC2 element [92] which has nodal parameters u_i , v_i at the four corners, from which the in-plane displacements of the element are interpolated linearly.

$$< u,v > = \sum_{i=1}^{4} \frac{1}{4} (1 + s\, s_i)(1 + t\, t_i) < u_i, v_i >$$

where (s,t) are the parametric coordinates defined in Section I-7. However, this element has four major deficiencies:

i) The linear variation of inplane transverse displacement u along the longitudinal edge s = constant is not compatible with the cubic variation of the out-of-plane displacement w associated with the CQ12 plate bending component of an adjacent non-coplanar element.

ii) The nodal parameters Θz_i are not included in the formulation of the element stiffness matrix, so cross-coupling between the in-plane rotational stiffness and the out-of-plane bending stiffness of adjoining non-coplanar elements is neglected. A one-to-one correspondence must be assumed between the rotations about the local transverse axis of the web and the local transverse axis of the flange.

iii) The use of only one QLC2 element down the depth of the web of a box-girder bridge results in significant errors in the modelling of beam behaviour [55, 92, 93].

iv) The midspan deflections computed from the analyses of a series of simply supported beams, modelled with an 8 x 2 mesh of elements, were associated with an increase in percentage error from 9.6% to 67% as the aspect ratio was increased from a value one to four [93]. This element is therefore not very suitable for box-girder bridge analyses according to the criteria adopted for this work.

III-2.3 QST element

The displacement functions $u(x,y)$, $v(x,y)$ of the QST element have a cubic variation in both the x and y directions and are associated with the nodal parameters u_i, v_i $\frac{\partial u}{\partial x_i}$, $\frac{\partial v}{\partial y_i}$ and $\frac{\partial u}{\partial y_i}$, $\frac{\partial v}{\partial x_i}$ [15]. The parameters $\frac{\partial u}{\partial y_i}$, $\frac{\partial v}{\partial x_i}$ may be conveniently replaced by the parameters $\frac{1}{2}\left(\frac{\partial v}{\partial x} + \frac{\partial u}{\partial y}\right)_i$ and $\frac{1}{2}\left(\frac{\partial v}{\partial x} - \frac{\partial u}{\partial y}\right)_i$, the latter term represents the average in-plane fibre rotation of an element which may be defined as Θz_i. However the inclusion of the strain degrees of freedom $\varepsilon_{x_i} = \frac{\partial u}{\partial x_i}$, $\varepsilon_{y_i} = \frac{\partial v}{\partial y_i}$, and $\frac{1}{2}\gamma_{xy_i} = \frac{1}{2}\left(\frac{\partial v}{\partial x} + \frac{\partial u}{\partial y}\right)_i$, in addition to enforcing undesirable strain continuity between elements of different thickness requires the assumption of a one to one transformation of these parameters from the local to global coordinates [15] because the degrees of freedom ε_{x_i} , γ_{xy_i} , and γ_{yz_i} , with which these parameters would couple for an invariant transformation, are

not included. This assumption results in serious errors at the 'tee intersection' of the deck slab, web, and cantilever slab and consequently the QST element is unsuitable for box-girder analyses.

III-2.4 QLC4 element [13, 73]

The transverse displacement function of the QLC4 element is defined with a cubic variation in the longitudinal (y) direction and a linear variation in the transverse (x) direction, and the longitudinal displacement function with a linear variation in the longitudinal direction and a cubic variation in the transverse direction. The element has nodal parameters u_i, v_i, $\frac{1}{2}\gamma_{xy_i} = \frac{1}{2}\left(\frac{\partial v}{\partial x} + \frac{\partial u}{\partial y}\right)_i$, and $\Theta z_i = \frac{1}{2}\left(\frac{\partial u}{\partial x} - \frac{\partial u}{\partial y}\right)_i$, at the corners, and although derived as a rectangular element [13] may be extended in application to a general quadrilateral by expressing the displacement function in terms of the parametric coordinates (s,t) [4].

A series of cantilevers, subjected to a point load at the free ends, were idealised [74] with a 9 x 3 mesh of QLC4 elements for which the computed deflections varied by less than 4% of the aspect ratio was increased from one to four. However, the inclusion of the shear strain as a nodal parameter necessitates the use of approximations in the transformation from local to global coordinates when the elements are not coplanar, as discussed in the previous section.

II-2.5 QLN3 element

Scordelis [90] has derived a rectangular element with displacement functions $u(x,y)$ and $v(x,y)$ which have a cubic variation in both directions, but are only associated with the nodal parameters u_i, v_i, and $\Theta z_i = \frac{1}{2}\left(\frac{\partial v}{\partial x} - \frac{\partial u}{\partial y}\right)_i$. The application of this element may be extended to a general quadrilateral shape by the use of parametric coordinates [90, 91] with the displacement functions expressed as an assemblage of basic functions

$$u = \sum_{i=1}^{4} \alpha_i F_i^1(s) F_i^1(t) + \sum_{i=1}^{4} \alpha_{i+4} F_i^3(s) F_i^2(t)$$

$$v = \sum_{i=1}^{4} \alpha_{i+8} F_i^1(s) F_i^2(t) + \sum_{i=1}^{4} \alpha_{i+4} F_i^2(s) F_i^3(t)$$

where $F_i^1(s) = \frac{1}{2}(1 + s\,s_i)$, $F_i^2(s) = \frac{1}{4}s_i(1 + s\,s_i)(1 - s^2)$

and $F_i^3(s) = \frac{1}{4}(1 + s\,s_i)(2 + s\,s_i - s^2)$

The displacement functions are not fully compatible, even for rectangular elements, because although the average fibre rotations $\frac{1}{2}\left(\frac{\partial v}{\partial x} - \frac{\partial u}{\partial y}\right)_i$ for each of the four elements joining at a general nodal point i are constrained to have the same value, there will be an angular discontinuity between the common edges of the adjacent elements, proportional to the difference in shear strain $\gamma_{xy_i} = \left(\frac{\partial v}{\partial x} + \frac{\partial u}{\partial y}\right)_i$ existing in the elements joined at nodal point i. However, Scordelis [90] has concluded from the results of numerical studies that the effect of this discontinuity is small.

III-2.6 QKC3 element

McLeod [60] has derived a fully compatible rectangular element with displacement functions

$$u = \alpha_1 + \alpha_2 x + \alpha_3 y + \alpha_4 xy + \alpha_5 y^2 + \alpha_6 xy^2$$

$$v = \alpha_7 + \alpha_8 x + \alpha_9 y + \alpha_{10} xy + \alpha_{11} x^2 + \alpha_{12} yx^2$$

for which the coefficients α_i are related to the nodal parameters u_i , v_i , Θz_i where $\Theta z = \frac{\partial v}{\partial x}$ or $-\frac{\partial u}{\partial y}$ at alternative corner nodes around the element perimeter. Elements of type A and type B must be defined according to whether the rotational degrees of freedom at node 1 is $\frac{\partial v}{\partial x}$ or $-\frac{\partial u}{\partial y}$, and the element types A or B allocated so that no pair of coplanar elements with a common edge have the same type designation. In this way a unique rotation will be defined at each node [60].

The definition of the rotational degree of freedom is necessarily arbitrary, and the concept of using rotations $\Theta z = -\frac{\partial u}{\partial y}$, $\frac{1}{2}\left(\frac{\partial v}{\partial x} - \frac{\partial u}{\partial y}\right)$, $\frac{\partial v}{\partial x}$ etc, is not fully tractible to physical explanation. This is unfortunate from an engineering standpoint but does not affect the accuracy of the results obtained. However, this element is not generally suitable for box-girder bridge analysis because an even number of elements must be used around the cross-section of each cell to match element types at the intersection of the webs and flanges. Also, the parabolic variation of transverse in-plane displacement along the longitudinal edges of the element is not compatible with the cubic variation of the out-of-plane displacement of adjoining non-coplanar elements.

III-2.7 QLC3 element

The QLC3 element was derived by Sisodiya, Cheung, and Ghali [94], and is of a general quadrilateral shape with corner degrees of freedom u_i , v_i and $\Theta z_i = -\left(\frac{\partial u}{\partial y_t}\right)_i$, where y_t is the distance along longitudinal lines s = constant (see Fig. III-1), measured with respect to the cartesian coordinate system.

The longitudinal displacement function $v(s,t)$, and the transverse displacement function $u(s,t)$, may be derived by considering polynomial expansions in terms of the parametric coordinates (s,t)

$$v = \alpha_1 + \alpha_2 s + \alpha_3 t + \alpha_4 st \qquad \ldots \quad (III\text{-}1)$$

$$u = \alpha_5 + \alpha_6 s + \alpha_7 t + \alpha_8 st + \alpha_9 t^2 + \alpha_{10} st^2 + \alpha_{11} t^3 + \alpha_{12} st^3 \qquad \ldots \quad (III\text{-}2)$$

where $\alpha_1, \alpha_2, \ldots . \alpha_{12}$ are determined by evaluating u, v, and $\frac{\partial u}{\partial t}$ at the four corners $(s = \pm 1, t = \pm 1)$ and solving the resulting system of linear simultaneous equations. Thus,

$$v = \sum_{i=1}^{4} \frac{1}{4} (1 + s s_i) (1 + t t_i) v_i \qquad \ldots \quad (III\text{-}3)$$

$$u = \sum_{i=1}^{4} \frac{1}{8} (1 + s s_i) (1 + t t_i) (2 + t t_i - t^2) u_i - \sum_{i=1}^{4} t_i /8 (1 + s s_i) (1 + t t_i) (1 - t^2) \frac{\partial u}{\partial t_i} \qquad \ldots \quad (III\text{-}4)$$

It is necessary to relate $\frac{\partial u}{\partial t_i}$ to $\Theta z_i = -\left(\frac{\partial u}{\partial y_t}\right)_i$ where

$$y_t = [a_4 (1 - s) + a_2 (1 + s)] t/4$$

$$x_s = [a_1 (1 - t) + a_3 (1 + t)] s/4$$

and a_i ; i = 1,4 are the lengths of the sides of the quadrilateral element, as shown in Fig. III-1. This may be achieved by application of the chain rule of partial differentiation

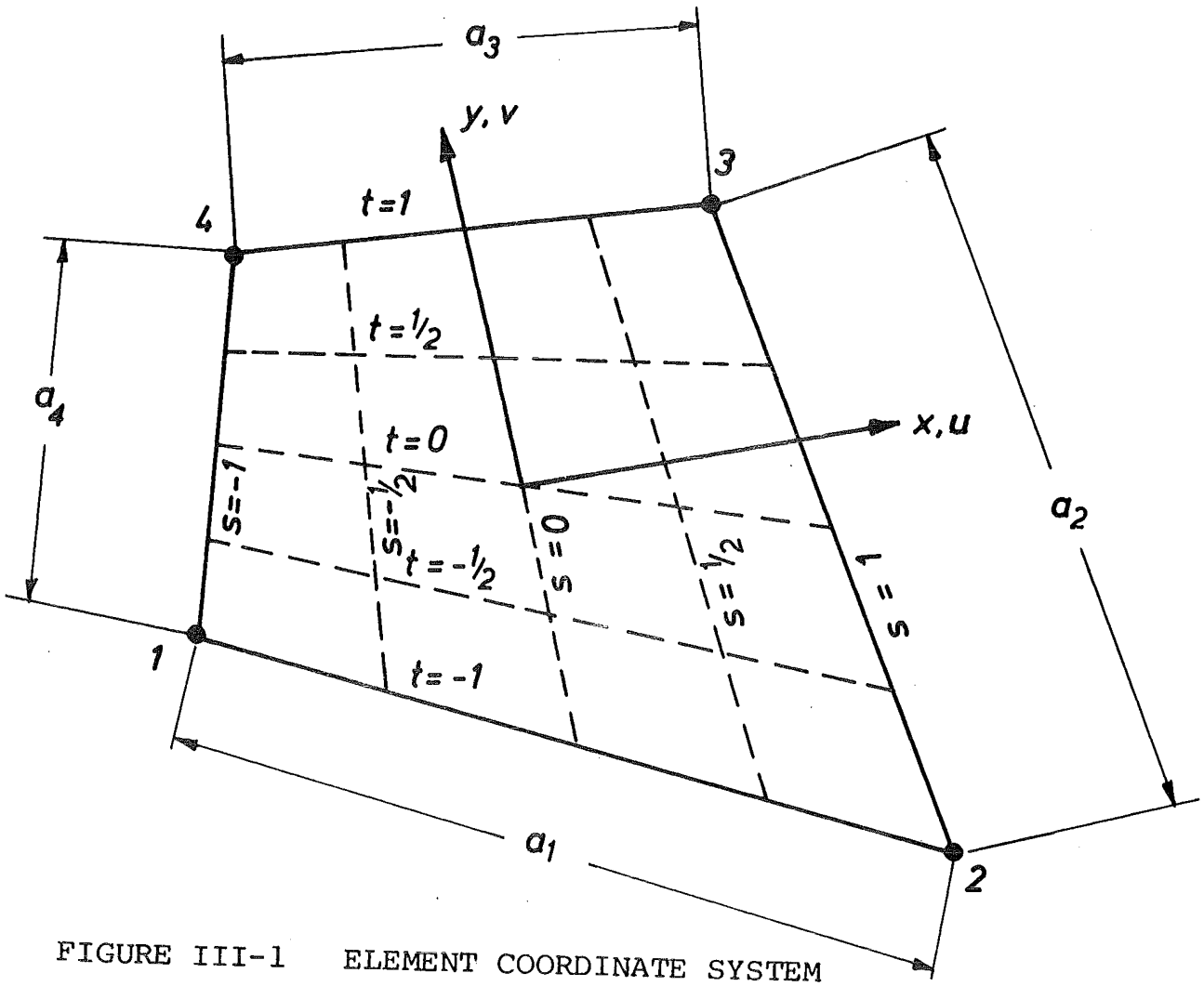

FIGURE III-1 ELEMENT COORDINATE SYSTEM

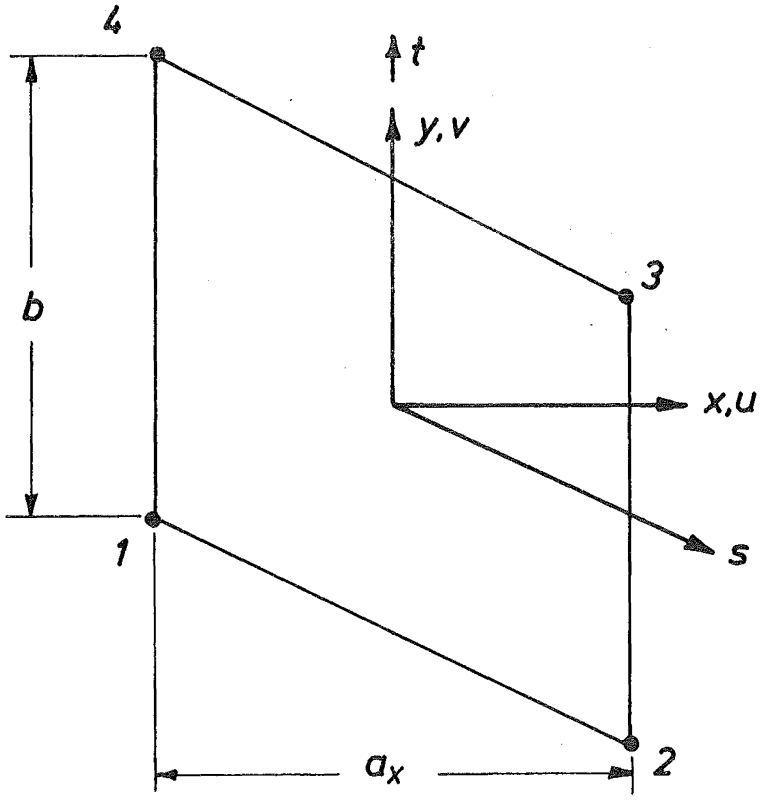

FIGURE III-2 PMC3 PARALLELOGRAM ELEMENT

$$\frac{\partial u}{\partial t} = \frac{\partial u}{\partial x_s}\frac{\partial x_s}{\partial t} + \frac{\partial u}{\partial y_t}\frac{\partial y_t}{\partial t}$$

$$= 1/|J| \left[\frac{\partial u}{\partial s}\frac{\partial y_t}{\partial t} - \frac{\partial u}{\partial t}\frac{\partial y_t}{\partial s}\right]\frac{\partial x_s}{\partial s} + \frac{\partial u}{\partial y_t}\frac{\partial y_t}{\partial t}$$

where $|J| = \frac{\partial x_s}{\partial s}\frac{\partial y_t}{\partial t} - \frac{\partial y_t}{\partial s}\frac{\partial x_s}{\partial t}$,

and evaluating $\frac{\partial u}{\partial t}$ at the nodes. The resulting expression is substituated into equation (III-4) to obtain the transverse displacement function

$$u = \sum_{i=1}^{4} \frac{1}{8}(1 + s\,s_i)(1 + t\,t_i)(2 + t\,t_t - t^2)u_i$$

$$- \sum_{i=1}^{4} s_i t_i/16(1 + t\,t_i)(1 - t^2)\alpha_i\, s\, u_i$$

$$+ \sum_{i=1}^{4} t_i/16(1 + s\,s_i)(1 + t\,t_i)(1 - t^2)\beta_i \left(-\frac{\partial u}{\partial y_t}\right)_i$$

... (III-5)

where $\alpha_1 = \alpha_2 = (a_3 - a_1)/a_1$

$\alpha_3 = \alpha_4 = (a_3 - a_1)/a_3$

and

$\beta_1 = (3a_4a_1 + a_1a_2 + a_3a_4 - a_2a_3)/4a_1$

$\beta_2 = (3a_1a_2 + a_2a_3 + a_1a_4 - a_3a_4)/4a_1$

$\beta_3 = (3a_3a_2 + a_3a_4 + a_2a_1 - a_1a_4)4a_3$

$\beta_4 = (3a_3a_4 + a_4a_1 + a_3a_2 - a_1a_2)/4a_3$

The displacement functions were assumed to take the form of polynomials which include all the linear terms, so the rigid body and constant strain criteria are automatically satisfied. However, the longitudinal sides of two adjacent elements connected end to end could have different directions in a mesh of quadrilaterals. It follows that θz_i is not uniquely defined at the common node i in this case so interelement compatibility may be violated, but results from numerical tests indicate that this incompatibility is not serious [94]. Possibly of greater consequence will be the

incompatibility of the transverse displacement (see equation III-5), along the longitudinal element interfaces when α_i ; i = 1,4 is not equal to zero. i.e., when the length of the two transverse sides 1-2 and 3-4 are not equal. A method of overcoming this difficulty is discussed in Section III-3.

III-2.8 PQC3 element

Sisodiya, Cheung, and Ghali [94] derived the stiffness matrix of the parallelogram shaped PQC3 element by employing the transverse displacement function of equation (III-4) and the longitudinal displacement function

$$v = \sum_{i=1}^{4} \frac{1}{4} (1 + s\,s_i)(1 + t\,t_i)\, v_i$$

$$+ \sum_{i=1}^{4} \frac{3}{8} \frac{a_x}{b} s_i t_i (1 - s^2)(1 - t^2)\, u_i$$

$$- \sum_{i=1}^{4} \frac{3}{8} \frac{a_x}{b} (1 - s^2)(1 - 2t\,t_i - 3t^2) \left(\frac{\partial u}{\partial y_t}\right)_i \quad \ldots \quad \text{(III-6)}$$

where a_x and b are the transverse and longitudinal element dimensions defined in Fig. III-2.

The rotational degree of freedom is defined as $\Theta z_i = -\frac{\partial u}{\partial y_i}$, which may be incorporated into the displacement functions of equations (III-4) and (III-6) by substituting

$$\frac{\partial u}{\partial t_i} = \frac{\partial u}{\partial y_i} \frac{\partial y}{\partial t_i} + \frac{\partial u}{\partial x_i} \frac{\partial x}{\partial t_i}$$

$$= \frac{1}{2} \Theta z_i . YYY(i) \quad \ldots \quad \text{(III-7)}$$

where $YYY(i) = 2 \frac{\partial y}{\partial t_i}$

Note that $\frac{\partial x}{\partial t_i} = 0$ for a parallelogram element with the local y axis of the element conveniently defined parallel to the longitudinal sides.

A method of generalising this element to a trapezium shape which has only the longitudinal sides parallel is described in Section III-4.

III-2.9 QLC2 - QLC3

Scordelis [91] has presented a system of elements which may be employed to perform economical analyses of cellular structures with vertical webs. The deck and soffit slabs of the structure are idealised with thin shell elements, composed of the QLC2 plane stress element and a twelve parameter plate bending element, with nodal degrees of freedom u_i , v_i , w_i , Θx_i , and Θy_i . The vertical webs are idealised with spar elements, composed of the QLC3 plane stress element with nodal parameters u_i , v_i , Θz_i , and the ONEW plate bending element which has a simple "one-way" out-of-plane displacement function

$$w = \alpha_1 + \alpha_2 x + \alpha_3 y + \alpha_4 xy + \alpha_5 x^2 + \alpha_6 x^2 y + \alpha_7 x^3 + \alpha_8 x^3 y$$

with nodal degrees of freedom w_i and $\Theta y_i = -\frac{\partial w}{\partial x_i}$. The in-plane rotation Θz of the webs will have a one to one correspondence with the out-of-plane rotation Θx of the deck and soffit slabs provided that webs are vertical. This approach was rejected for this work because it is only rigourously applicable to a restricted class of structures.

III-3 QMC3 ELEMENT

The stiffness matrix of the quadrilateral QMC3 element is derived by using the displacement functions of equations (III-3) and (III-4) associated with the QLC3 element, but using an alternative definition for the rotational parameter Θ_z in order to avoid introducing incompatibilities of the transverse displacement $u(s,t)$ across the longitudinal element boundaries $s = \pm 1$.

The in-plane rotational degree of freedom at node i is defined as

$$\Theta z_i = \left(- 2 \frac{\partial u}{\partial t_i} \right) / YYY(i) \qquad \ldots \quad (III-8)$$

with the local y axis parallel to a line with the average slope of the two longitudinal sides 1-4 and 2-3. This is identical to the definition employed by Lim, Kilford, and Moffat [55] when the two longitudinal sides are parallel. Substituting equation (III-8) into equation (III-4) leads to the displacement function

$$u = \sum_{i=1}^{4} \frac{1}{8} (1 + s\,s_i)(1 + t\,t_i)(2 + t\,t_i - t^2)u_i$$

$$+ \sum_{i=1}^{4} t_i/16\ YYY(i)\ (1 + s\,s_i)(1 + t\,t_i)(1 - t^2)\Theta z_i \qquad \ldots \quad (III\text{-}9)$$

$$v = \sum_{i=1}^{4} \frac{1}{4} (1 + s\,s_i)(1 + t\,t_i)\,v_i$$

All the rigid body and constant strain states are included, and the element if fully compatible except when the longitudinal sides of two adjacent elements, connected end to end, are not colinear. In this case Θz_i is not uniquely defined at the common nodes. However, the associated violation of compatibility does not appear to be serious, as can be seen from the test examples of Figures III-5 and III-8.

The displacement functions of the QMC3 element permit a close representation of beam action when the local y axis of the element is orientated in the longitudinal direction of the beam, as demonstrated in Section III-7. This special feature can be used to advantage when idealising the webs of box-girder bridges, especially since the performance of the element does not deteriorate significantly as the aspect ratio of the element deviates from a value of one [94].

The use of the QMC3 element to represent the membrane behaviour of the members of a box-girder will ensure compatibility with a non-coplanar CQ12/QMC3 element when they are connected along the longitudinal sides 2-3 or 1-4 (see Fig. III-1). Furthermore, they will couple efficiently because $\Theta z_i = -2\left(\frac{\partial u}{\partial t}\right)_i$ / YYY(i) is included as a nodal parameter, and is treated as a true in-plane rotation of the element when transforming the stiffness matrix from local to global coordinates

III-4 PMC3 ELEMENT

This element has a higher order longitudinal displacement function than the QMC3 element and may therefore provide a better representation of longitudinal extensional strain. Also, the local stress fluctuations which may occur across the element interfaces of a curved web idealisation are expected to be reduced.

The PMC3 element is trapezium shaped with parallel longitudinal sides, and may be derived by employing the transverse displacement function

of the QMC3 element (see equation (III-9)), and modifying the longitudinal displacement function of equation (III-6) to form the fully compatible expression

$$v = \sum_{i=1}^{4} \frac{1}{4}(1 + s\,s_i)(1 + t\,t_i)\,v_i$$

$$+ \sum_{i=1}^{4} \frac{3}{8}\gamma/YYY(i)\,(1 - s^2)(1 - t^2)\,u_i$$

$$+ \sum_{i=1}^{4} s_i/16\,(1 - s^2)(1 - 2t\,t_i - 3t^2)\Theta z_i$$

... (III-10)

where $\Theta z_i = -2\left(\frac{\partial u}{\partial t}\right)_i / YYY(i)$ $\left[= -\left(\frac{\partial u}{\partial y}\right)_i\right.$ for a trapezium shaped element, and $\gamma = \frac{1}{2}[x(2) - x(1) + x(3) - x(4)]$.

The transverse displacement function and the first part of the longitudinal displacement function have been shown to satisfy the rigid body motion, constant strain, and compatibility criterion in the previous section. It remains to show that the constant strain states $u = A$, $u = Ax$, and $u = Ay$ are not associated with longitudinal deformations defined from equation (III-10)

i) $u = A$; The nodal deformations associated with the zero strain state are $v_i = 0$, $u_i = A$, $\Theta z_i = 0$. Substituting into equation (III-10)

$$v = (1-s^2)(1-t^2)\,\frac{3A}{8}\left[(1-1)/(y(4)-y(1)) + (1-1)/(y(3)-y(2))\right] = 0$$

ii) $u = Ay$; The nodal deformations associated with this constant strain state are $v_i = 0$, $u_i = Ay_i$, and $\Theta z_i = -A$. Substituting into equation (III-10)

$$v = (1-s^2)(1-t^2)\,A\frac{3}{8}\gamma\left[\frac{y(1)-y(4)}{y(4)-y(1)} + \frac{y(3)-y(2)}{y(3)-y(2)}\right] + \frac{A}{16}\gamma\sum_{i=1}^{4}\left[s_i(1-s^2)(1-3t^2)\right.$$

$$\left. - 2s_i t_i\,t\,(1-s^2)\right] = 0$$

iii) $u = Ax$; The nodal deformations associated with this constant strain state are $v_i = 0$, $u_i = Ax_i$, $\Theta z_i = -2\left(\frac{\partial u}{\partial t}\right)_i / YYY(i)$. Now

$$\frac{\partial u}{\partial t} = \frac{\partial u}{\partial x}\,\frac{\partial x}{\partial t} + \frac{\partial u}{\partial y}\,\frac{\partial y}{\partial t}$$

Define $RRR(i) = 2\,\frac{\partial x}{\partial t_i}$ then $\Theta z_i = -A.RRR(i)/YYY(i)$

Substituting into equation (III-10)

$$v = (1-s^2)(1-t^2)\,A\frac{3}{8}\gamma\left[-RRR(1)/YYY(1) + RRR(2)/YYY(2)\right]$$

$$+ \frac{A}{16}\gamma\sum_{i=1}^{4}\left[-RRR(i)/YYY(i)s_i(1-s^2)(1-2\,tt_i - 3t^2)\right]$$

The longitudinal displacement V is equal to zero for a trapezium shaped element because in this case RRR(i) = 0 ; i = 1,4 .

The PMC3 element is fully compatible except that Θz_i is not defined uniquely at common nodes when the longitudinal sides of adjacent elements, connected end to end, are not colinear.

The QMC3 element is preferred for the linear elastic analyses of box-girder bridges because the PMC3 element is limited to a trapezium shape with the longitudinal sides parallel and is therefore not applicable to bridges with variable depth or complex plan geometry. However, the PMC3 element is preferred for the geometrically nonlinear analyses of those structures for which it can be used, such as prismatic spatial plate structures, because it is important to employ relatively high order in-plane displacement functions when using the Total Lagrangian Formulation to model the large deflection response, as discussed in Chapter X.

III-5 SUPERPOSITION OF ADDITIONAL DISPLACEMENT MODES

It may be possible to improve the performance of the QMC3 element by incorporating additional displacement modes, the amplitudes of which are associated with internal degrees of freedom and eliminated by static condensation [71].

Wilson [111] has added modes to the displacement function of the QLC2 element to enable better representation of beam behaviour

$$u = \alpha_1 + \alpha_2 x + \alpha_3 y + \alpha_4 xy + \alpha_5(1-y^2) + \alpha_6(1-x^2)$$

$$v = \alpha_7 + \alpha_8 x + \alpha_9 y + \alpha_{10} xy + \alpha_{11}(1-y^2) + \alpha_{12}(1-x^2)$$

The AQLC2 element derived from these displacements functions is not fully compatible but when only one element is used down the depth of a rectangular beam idealisation the results are of considerably greater accuracy than obtained with the QLC2 element, as demonstrated in Fig. III-7. However, this improved accuracy is not repeated for non-rectangular

elements because the constant strain states of deformation cannot now be represented correctly [25].

Krahula and Polehemus [50] chose to add fully compatible trigometric terms to the displacement function of the QLC2 element. They considered a rectangular element of sides a, b and used a cartesian coordinate system with the origin at node 1, defining the displacement functions as follows;

$$u = \alpha_1 + \alpha_2 x + \alpha_3 y + \alpha_4 xy + \sum_{m=1}^{\infty} \sum_{n=1}^{\infty} a_{mn} \operatorname{Sin} \frac{m\pi x}{a} \operatorname{Sin} \frac{n\pi y}{b}$$

$$v = \beta_1 + \beta_2 x + \beta_3 y + \beta_4 xy + \sum_{m=1}^{\infty} \sum_{n=1}^{\infty} b_{mn} \operatorname{Sin} \frac{m\pi x}{a} \operatorname{Sin} \frac{n\pi y}{b}$$

If the total potential energy is minimised with respect to the coefficients a_{mn} and b_{mn} the following relationships are obtained [50]

$$a_{mn} = 8(1+\nu)\beta_4/\pi^4(1-\nu)mn\ [m^2/a^2(1-\nu) + n^2/2b^2]\quad m,n\ \text{odd}$$

$$b_{mn} = 8(1+\nu)\alpha_4/\pi^4(1-\nu)mn\ [n^2/b^2(1-\nu) + m^2/2a^2]\quad m,n\ \text{odd}$$

$$a_{mn},\ b_{mn} = 0\quad m,n\ \text{even}$$

The transverse and longitudinal displacement functions are now coupled. It has been shown [50] that the accuracy of some of the terms of the element stiffness matrix is significantly improved, even when only three trigonometric terms (m = 5, n = 5) are added to the displacement functions of the QLC2 element. However, if these trigonometric terms were added to the displacement functions of the QMC3 element the evaluation of the coefficients a_{mn} , b_{mn} would present a formidable task.

A longitudinal displacement function, similar to that employed for the PMC3 element, may be methodically derived by applying the static condensation procedure [71] to the expression

$$v = \alpha_1 + \alpha_2 s + \alpha_3 t + \alpha_4 st + (1 - s^2)(1 - t^2)(\alpha_5 + \alpha_6 t)$$

However, this approach requires a large amount of computational effort so a trial and error procedure is often preferred.

The employment of additional compatible modes has not lead to great improvements in element accuracy, apart from in specialised

applications, and is now being overshadowed by the development of hybrid displacement and hybrid stress elements which exhibit excellent performance [25, 112].

III-6 DERIVATION OF ELEMENT STIFFNESS MATRIX

The element strain-displacement relationship may be derived from the displacement functions by the application of the chain rule of partial differentiation

$$\begin{Bmatrix} \frac{\partial u}{\partial x} \\ \frac{\partial v}{\partial y} \\ \frac{\partial u}{\partial y} + \frac{\partial v}{\partial x} \end{Bmatrix} = \begin{bmatrix} 1 & 0 & 0 & 0 \\ 0 & 0 & 0 & 1 \\ 0 & 1 & 1 & 0 \end{bmatrix} \frac{1}{|J|} \begin{bmatrix} \frac{\partial y}{\partial t} - \frac{\partial y}{\partial s} & 0 & 0 \\ -\frac{\partial x}{\partial t} & \frac{\partial x}{\partial s} & 0 & 0 \\ 0 & 0 & \frac{\partial y}{\partial t} - \frac{\partial y}{\partial s} \\ 0 & 0 & -\frac{\partial x}{\partial t} & \frac{\partial x}{\partial s} \end{bmatrix} \begin{Bmatrix} \frac{\partial u}{\partial s} \\ \frac{\partial u}{\partial t} \\ \frac{\partial v}{\partial s} \\ \frac{\partial v}{\partial t} \end{Bmatrix} \quad \ldots \text{(III-11}$$

$$= \frac{1}{|J|} [F] \begin{Bmatrix} \frac{\partial u}{\partial s} \\ \frac{\partial u}{\partial t} \\ \frac{\partial v}{\partial s} \\ \frac{\partial v}{\partial t} \end{Bmatrix} \quad \text{where the determinant of the Jacobian } |J| = \begin{pmatrix} \frac{\partial x}{\partial s} & \frac{\partial y}{\partial t} - \frac{\partial x}{\partial t} & \frac{\partial y}{\partial s} \end{pmatrix}$$

$$= \frac{1}{|J|} [F] [G] \{\delta^e\} \qquad \text{where} \begin{Bmatrix} \frac{\partial u}{\partial s} \\ \frac{\partial u}{\partial t} \\ \frac{\partial v}{\partial s} \\ \frac{\partial v}{\partial t} \end{Bmatrix} = [G] \{\delta^e\}$$

The strain-displacement relationship may therefore be expressed in a concise form

$$\begin{Bmatrix} \frac{\partial u}{\partial x} \\ \frac{\partial u}{\partial y} \\ \frac{\partial v}{\partial x} \\ \frac{\partial v}{\partial y} \end{Bmatrix} = [B(s,t)] \{\delta^e\}$$

where $[B(s,t)] = \frac{1}{|J|} [F] [G]$

The element stiffness matrix [K] may now be evaluated using the procedure outlined in Chapter I

$$[K] = \int_{-1}^{1} \int_{-1}^{1} [B(s,t)]^T [D] [B(s,t)] h(s,t) |J| ds dt$$

where $h(s,t)$ is the element thickness. However, the integrand contains the determinant of the Jacobian in the denominator so the integration was performed numerically, with two sampling points of the Gauss Legendre scheme in the transverse (s) direction and four sampling points in the longitudinal (t) direction. This scheme will integrate the strain energy gradient of rectangular and parallelogram elements exactly, as discussed in Chapter VII.

III-7 NUMERICAL TESTS

Beam action predominates in the cell walls of box-girder bridges so in order to anticipate the accuracy and convergence characteristics of the QMC3 and PMC3 elements, when applied in this context, a number of prismatic and non-prismatic beams and cantilevers were analysed.

III-7.1 Prismatic cantilever

A prismatic cantilever subjected to a point load at the free end, and with degrees of freedom u_i, v_i, θz_i constrained at the built-in end, was idealised using both a 2 x 1 and 4 x 1 mesh of QMC3 and PMC3 elements, as shown in Fig. III-3. The span to depth ratio of the beam was varied from 4.0 to 8.0 to study the performance of the elements as the aspect ratio was increased.

The computed deflections at the free end and the extreme fibre stresses at point A are shown in Fig. III-3, along with the solution calculated from beam theory [94], and the results obtained from the QLC3 and PQC3 elements [94]. The QMC3 and PMC3 elements are identical to the QLC3 and PQC3 elements respectively for rectangular elements and this shows in the results where the accuracy of the solution varies by only 1% as the aspect ratio increases from a value of one. The finite element solutions agree closely with the theoretical solution even with only one element through the depth of the beam.

III-7.2 Beam with inclined faces

The QMC3 and PMC3 elements were tested as parallelograms by analysing the beam with inclined faces shown in Fig. III-4, idealised as 5 x 1 and 5 x 2 element meshes and subjected to a point load at midspan.

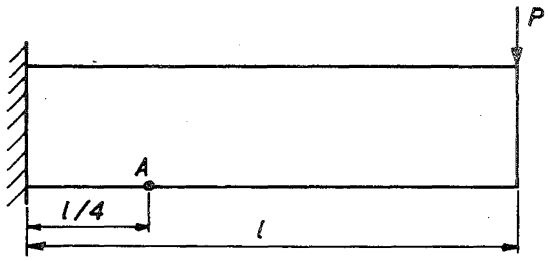

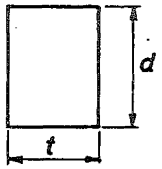

Poisson's Ratio $\nu = 0$

Finite element idealisation	Span l	Beam theory including shear deformation [94]	Finite Element Analysis					
			Deflection at free end (Multiplier: P/Et)				% of beam theory	
			PMC3	PQC3 [94]	QMC3	QLC3 [94]	QMC3	QLC3 [94]
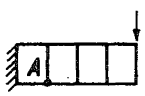	2d	36.38		35.382		35.382		97.3
	4d	265.18	259.761	259.764	259.756	259.764	98.0	98.0
	8d	2066.80		2031.530		2031.530		98.3
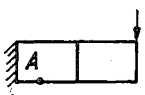	2d	36.38		33.765		33.765		92.8
	4d	265.18		247.529		247.529		93.3
	8d	2066.80	1938.88	1935.050	1937.78	1935.050	93.75	93.6
Longitudinal stresses at point A (Multiplier: P/td)								
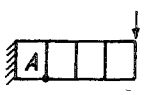	2d	9.00		8.999		9.000		100.0
	4d	18.00	17.9995	18.000	17.9995	18.000	100.0	100.0
	8d	36.00		36.000		36.000		100.0
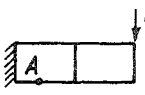	2d	9.00		9.025		9.000		100.0
	4d	18.00		18.021		18.000		100.0
	8d	36.000	36.06	35.990	36.00	36.000	100.0	100.0

FIGURE III-3 PRISMATIC CANTILEVER

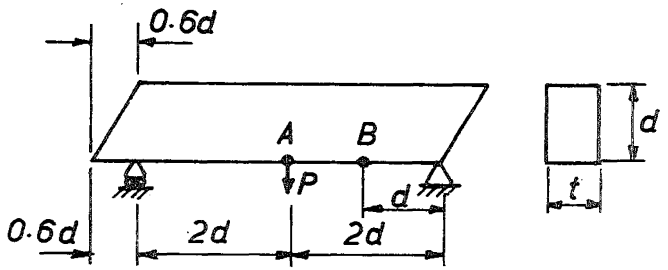

(a) BEAM DIMENSIONS

Poisson's Ratio $\nu = 0$

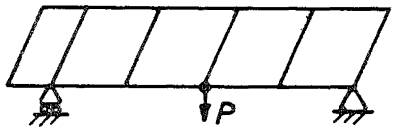

(b) FINITE ELEMENT IDEALISATION

(Variable number of equal divisions down the depth.)

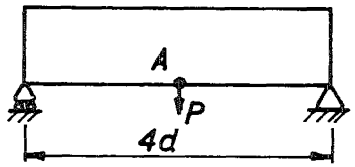

(c) BEAM THEORY APPROXIMATION

Finite element idealisation	Beam theory including shear deformation	Deflection at point A (Multiplier: P/Et)							
		PMC3		PQC3[94]		QMC3		QLC3[94]	
		Value	% of beam theory	Value	% of beam theory	Value	% of beam theory	Value	% of beam theory
5 x 1	18.19	15.75	86.6	15.76	86.6	10.74	59.2	10.74	59.2
5 x 2	18.19	17.426	95.8	17.42	95.8	15.218	83.6	15.21	83.6
Longitudinal stress at point B (Multiplier: P/td)									
5 x 1	3.0	2.861	95.5	2.901	96.7	1.556	51.9	1.556	51.9
5 x 2	3.0	3.180	106.0	3.177	105.9	2.541	84.7	2.541	84.7

FIGURE III-4 BEAM WITH INCLINED FACES

The computed midspan deflections and extreme fibre stresses at point B are presented in Fig. III-4, along with an approximate solution from simple beam theory [94], and the results obtained from the QLC3 and PQC3 elements [94]. The QMC3 and PMC3 elements are identical to the QLC3 and PQC3 elements respectively for parallelogram elements, and this shows in the results. The computed deflections converge towards the approximate beam theory solution as the mesh is refined, but the PMC3 element exhibits superior accuracy compared with the QMC3 element, due to the incorporation of a higher order longitudinal displacement function.

III-7.3 Haunched cantilever

The QMC3 element was tested as a quadrilateral by analysing the haunched cantilever shown in Fig. III-5, idealised as 5 x 1 and 5 x 2 element meshes and subjected to a point load at the free end.

The computed deflections at the free end and the extreme fibre longitudinal stresses at point A are shown in Fig. III-5, along with an approximate solution from beam theory, a solution from a three dimensional finite element analysis [94] using 20 node isoparametric hexahedra [96], and the results from the QLC3 element [94].

The results from the QMC3 differ only slightly from those of the QLC3 element and are of good accuracy, converging towards the three dimensional finite element solution as the mesh is refined. Although the haunch changes the direction of the local axes (defined in Fig. III-1) for two adjacent elements, the resulting incompatibility has no apparent effect upon the accuracy of the results.

III-7.4 Cantilever beam

The performance of the QMC3 element is compared with that of the triangular CST, LST, and QST elements, and the rectangular QLC2 and AQLC2 elements, by analysing the built-in cantilever shown in Fig. III-6, idealised with 4 x 1, 8 x 2, 16 x 4, and 32 x 8 element meshes and subjected to a parabolically varying end shear. The elasticity solution coincides with the beam theory for this problem, except in the proximity of the built-in end where the full clamping condition constitutes a mixed problem of elasticity, for which no closed form solution exists. The value given as the theoretical end deflection [15]

$$\Delta_{theory} = \frac{PL^3}{3EI} + \frac{4 + 5\nu}{2}\frac{PL}{EH} = 9.03808 \text{ mm}$$

is exact if the root is free to warp with the centreline and the edge points

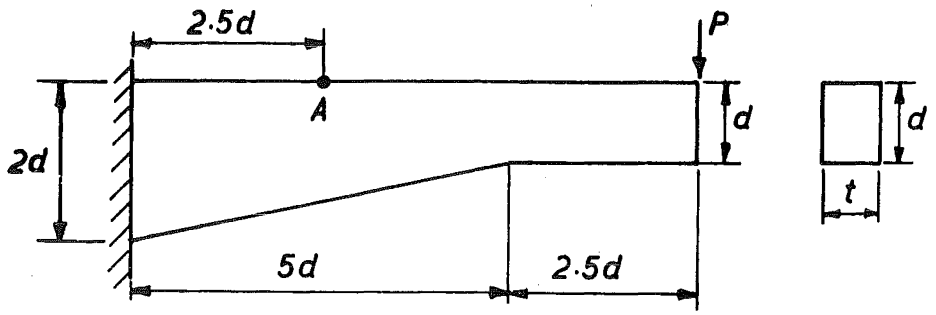

(a) CANTILEVER DIMENSIONS

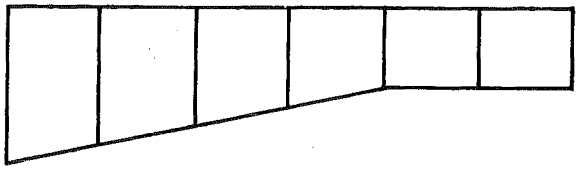

(b) FINITE ELEMENT IDEALISATION
(Variable number of divisions down the depth.)

Finite element mesh	Beam theory ignoring shear deformation [94]	Deflection at free end (Multiplier: P/Et)					
		Value			% of beam theory		
		3 - D analysis [96]	QLC3 [94]	QMC3	3 - D analysis [96]	QLC3 [94]	QMC3
6 x 1	492.80	507.12	500.08	497.03	102.9	101.4	100.85
6 x 2	492.80			503.22			102.1
		Longitudinal stress at point A (Multiplier:P/td)					
6 x 1	13.33	14.07	13.05	13.20	105.6	97.9	99.0
6 x 2	13.33			13.29			99.7

FIGURE III-5 HAUNCHED CANTILEVER

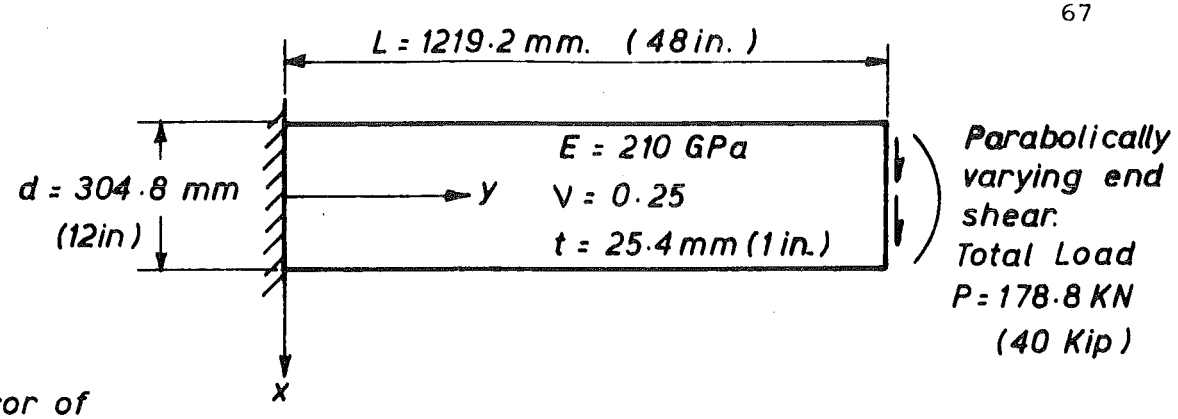

FIGURE III-6 CANTILEVER BEAM

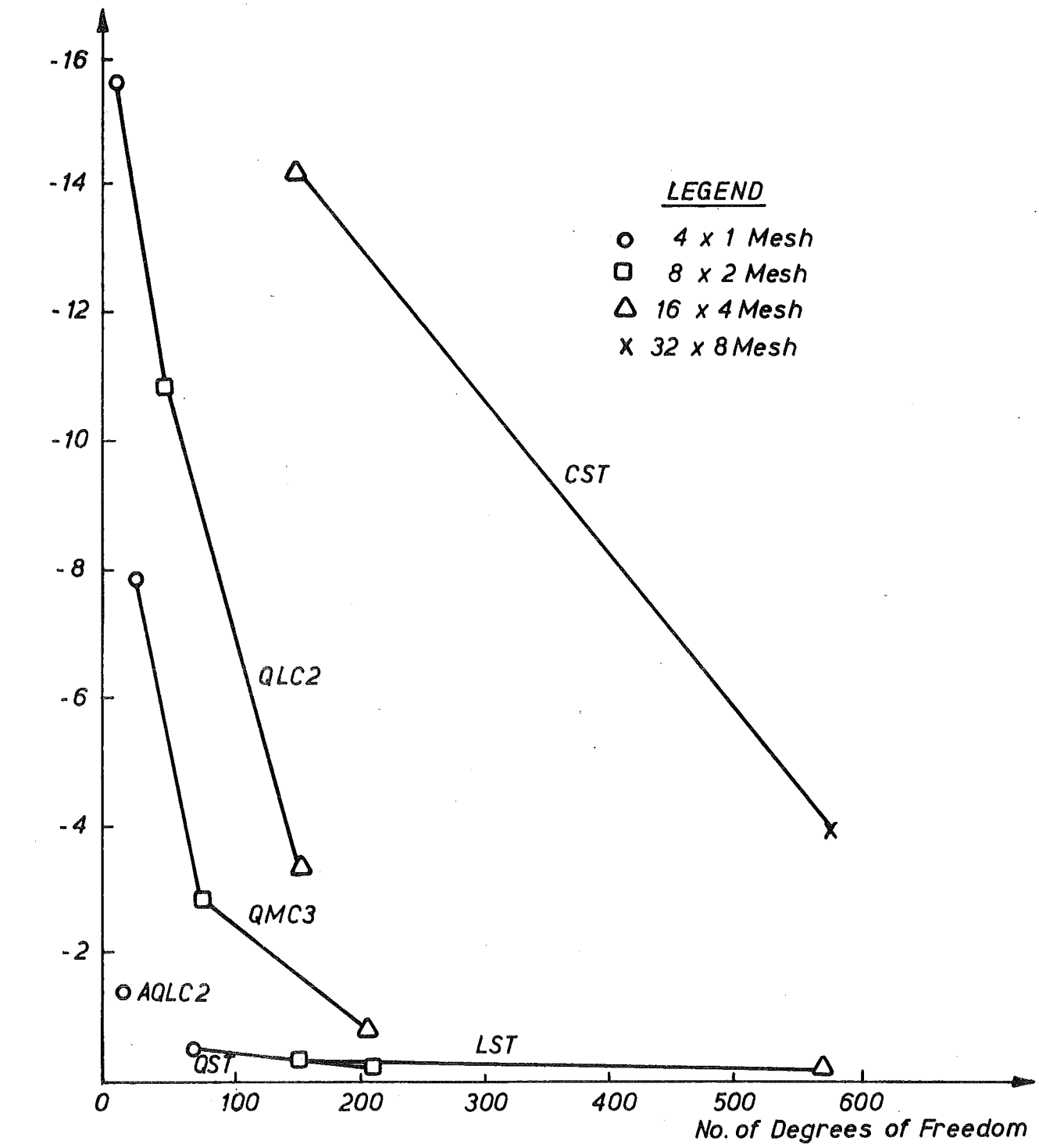

FIGURE III-7 CONVERGENCE CHARACTERISTICS OF ELEMENTS

are fixed, and therefore Δ theory is an upper bound for the exact deflection of the free end. The variations of the percentage error of the computed end deflection with the number of degrees employed in the finite element are plotted in Fig. III-7. The rate of convergence of the solution from the QMC3 element compares favourably with the other elements, and the convergence is monotonic towards the exact solution from a lower bound value. The excellent accuracy achieved with a 4 x 1 mesh idealisation of AQUAC2 elements is also evident.

III-7.5 Curved cantilever

The QMC3 and PMC3 elements were further tested as trapeziums with the longitudinal sides parallel by analysing the curved cantilever shown in Fig. III-8, idealised as both 16 x 2 and 32 x 4 element meshes and subjected to a parabolically varying end shear. An approximation must be introduced to idealise the curved cantilever with a mesh of rectilinear elements but the geometric discrepancy diminishes as the mesh is refined.

The computed deflections at the free end and the extreme fibre longitudinal stresses at the built-in end are presented in Fig. III-8, along with the solution calculated by Timoshenko and Goodier [103] from the theory of elasticity, assuming the built-in end is free to warp.

The deflections computed from the QMC3 element are of good accuracy and converge towards the theoretical solution as the mesh is refined. The curvature of the cantilever changes the direction of the local axes for two adjacent elements, but the resulting incompatibility has no apparent effect upon the accuracy of the results. However, the deflection computed with the 16 x 2 idealisation of PMC3 elements overestimates the theoretical solution, indicating that the violation of compatibility associated with this element is of a more serious nature.

The stresses computed at the built-in end do not converge to the classical solution with mesh refinement because of the differences in the boundary conditions.

III-8 CONCLUSIONS

The quadrilateral QMC3 element has been shown to provide an accurate representation of both prismatic and non-prismatic beams, and satisfies the essential requirements of a plane stress element suitable for coupling with CQ12 plate bending element to provide an economical model of the linear elastic structural behaviour of box-girder bridges.

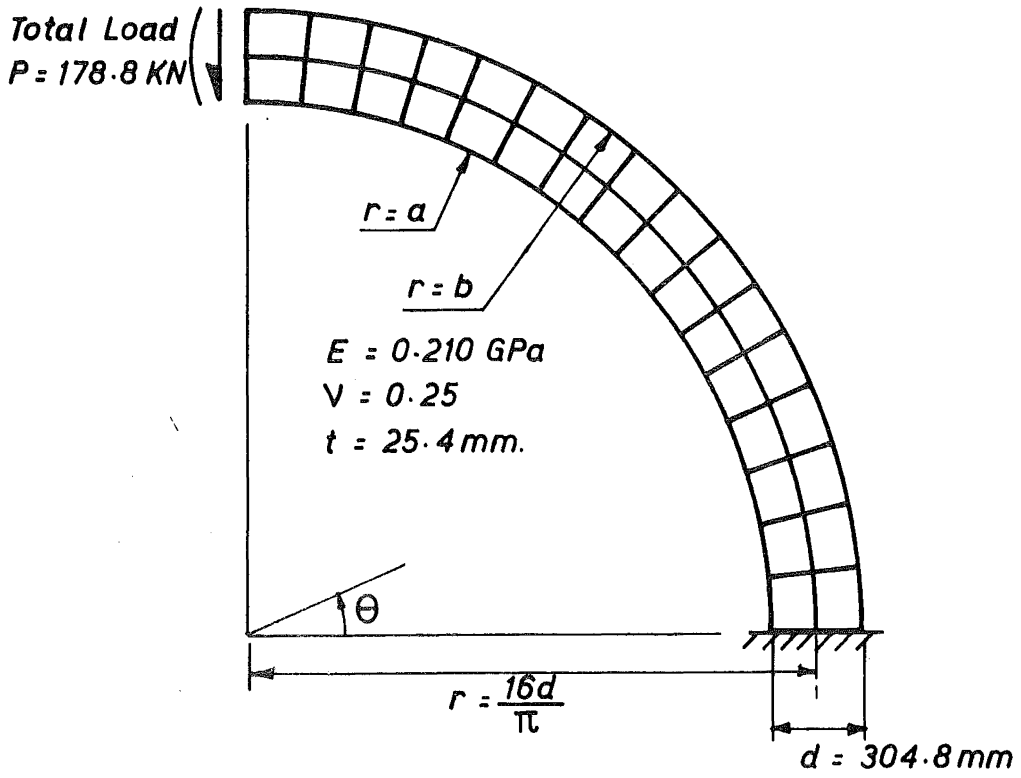

Mesh	Element	Deflection at free end	Longitudinal stress $\sigma/r=a,\theta=o$	Longitudinal stress $\sigma/r=b,\theta=o$
16 x 2	QMC3	41.3 mm	- 0.804 MPa	0.670 MPa
16 x 2	PMC3	42.5 mm	- 0.805 MPa	0.695 MPa
16 x 2	QMC3	42.0 mm	- 0.815 MPa	0.686 MPa
	Theory of elasticity [103]	42.4 mm	- 0.791 MPa	0.644 MPa

FIGURE III-8 CURVED CANTILEVER

The trapezium shaped PMC3 element is not capable of representing constant strain states when employed as a quadrilateral, and is therefore not suitable for general purpose application. However the PMC3 element is preferred for the geometrically nonlinear analysis of prismatic structures because it is important to employ higher order in-plane displacement functions when using the Total Lagrangian Formulation to model the large deflection response. The performance of the PMC3 element was shown to be superior to that of the QMC3 element when employed to analyse a beam with inclined faces, demonstrating the advantages of incorporating a higher order longitudinal displacement function.

CHAPTER IV

FORMULATION AND ASSEMBLY OF PLANAR THIN SHELL ELEMENTS

IV-1 COMPARISON OF PLANAR ELEMENT AND CURVED SURFACE ELEMENT

An element of a box-girder bridge undergoes both in-plane and flexural deformations which, for rectilinear bridges, may be simulated by superimposing a plane stress and a plate bending finite element to form a planar thin shell element. However, the webs of curved box-girders constitute singly-curved surfaces for which the structural behaviour may be more complex.

Attempts to develop a finite element method applicable to thin shell structures of arbitrary geometry in three dimensional space have followed two courses. In the first approach the shell is idealised as an assemblage of planar elements which may deform in both stretching and bending modes. This approach has been employed successfully by Zienkiewicz [117], Clough and Johnson [22], and Carr [15], but has the disadvantage that there is no coupling between bending and stretching within each planar element, and consequently a large number of elements must be used to achieve satisfactory accuracy when simulating surfaces of small radii of curvature. However, this constraint does not apply to the webs of most curved box-girders because their radii are generally large.

The second approach is to use curved surface shell elements [14, 27], which enable a closer geometrical representation of the structure to be achieved, and incorporate coupling between the bending and stretching modes within each element. However, higher order element displacement functions must now be used if the rigid body and constant strain deformation modes are to be represented correctly [27]. Cantin and Clough [14] have shown that polynomial displacement functions, similar in form to those employed to derive the QMC3 and CQ12 elements, cannot account for all the rigid body displacement modes of a conical or cylindrical shell element which would otherwise be suitable for idealising the webs of curved box-girders. It was therefore decided to adopt the first approach where both rectilinear and curved bridges are represented as an assembly of planar thin shell elements.

IV-2 SUPERPOSITION OF PLANE STRESS AND PLATE BENDING ACTIONS

A shell is defined as a structure which can be derived from a thin plate by initially forming the middle plane to a folded, singly-curved, or doubly-curved surface so an element of the structure will generally be subjected to both in-plane and bending forces during loading. If the structure consists of a folded assembly of thin plates, such as in the case of rectilinear box-girder bridges, these forces cause independent deformations within the individual planar elements, provided the local deformations are small. Therefore, the stiffness matrix of a planar thin shell element may be constructed by merely combining the plate bending stiffness $[K^b]$ of say the CQ12 element, derived in Chapter II, and the plane stress stiffness $[K^{pl}]$ of the QMC3 element, derived in Chapter III: The equilibrium equations of the plane stress and plate bending elements may be written

$$[K^{pl}]\ \{\delta^{pl}\} = \{R^{pl}\} \qquad \ldots \quad (IV\text{-}1)$$

$$[K^{b}]\ \{\delta^{b}\} = \{R^{b}\} \qquad \ldots \quad (IV\text{-}2)$$

respectively, where

$$\{\delta^{pl}\} = \begin{Bmatrix} u_i \\ v_i \\ \theta z_i \end{Bmatrix} \quad i = 1,4 \qquad \{\delta^{b}\} = \begin{Bmatrix} w_i \\ \theta x_i \\ \theta y_i \end{Bmatrix} \quad i = 1,4$$

and $\{R^{pl}\}$ and $\{R^{b}\}$ are the generalised forces associated with plane stress and plate bending actions respectively, concentrated at each node i . If the vector of the combined nodal displacements of the shell element is defined as

$$\{\delta'\}^e = \begin{Bmatrix} u_i \\ v_i \\ w_i \\ \theta x_i \\ \theta y_i \\ \theta z_i \end{Bmatrix} i = 1,4 \qquad \ldots \quad (IV\text{-}3)$$

and the vector of conjugate generalised nodal forces is defined as

$$\{R'\}^e = \left\{ \begin{array}{c} Rx_i \\ Ry_i \\ Rz_i \\ Mx_i \\ My_i \\ Mz_i \end{array} \right\}_{i = 1,4} \qquad \ldots \quad (IV\text{-}4)$$

where Mx_i, My_i and Mz_i are the nodal bending moments about the element x,y, and z axis respectively, the equilibrium equations of the assembled shell element may be written

$$\{R'\}^e = [K']^e \{\delta'\}^e \qquad \ldots \quad (IV\text{-}5)$$

by combining the equilibrium equations (IV-1) and (IV-2).

IV-3 TRANSFORMATION TO GLOBAL COORDINATES AND ASSEMBLY OF ELEMENTS

The stiffness matrix of the thin planar shell element defined from equation (IV-5) relates the generalised element forces to the element displacements and rotations measured with respect to the local (x',y',z') coordinate system, where the y' axis was defined parallel to a line with the average slope of sides 2-3 and 1-4 (see Fig. III-1) for this work, and the z' axis is perpendicular to the plane of the element. It is necessary to transform the element coordinates to a common global system (x,y,z) in order to assemble the elements and form the equilibrium equations of the total structure. The global coordinate system was arbitrarily defined with the z axis vertical and the y axis in the longitudinal direction of the structure for this work. The local element displacement and forces at a node i may be related to the global parameters by a transformation matrix [L]

$$\{\delta'\}^e = [L] \{\delta_i\}^e \;,\; \{R'_i\}^e = [L] \{R_i\}^e$$

where $$[L] = \begin{bmatrix} [\lambda] & 0 \\ 0 & [\lambda] \end{bmatrix}$$

and $[\lambda]$ is a 3 x 3 matrix of the direction cosines of the angles between the global and local axes.

$$[\lambda] = \begin{bmatrix} \lambda_{x'x} & \lambda_{x'y} & \lambda_{x'z} \\ \lambda_{y'x} & \lambda_{y'y} & \lambda_{y'z} \\ \lambda_{z'x} & \lambda_{z'y} & \lambda_{z'z} \end{bmatrix}$$

where $\lambda_{x'x}$ is the cosine of the angle between the x' and x axes, and the other terms are defined similarly,

The complete global set of nodal displacements and forces of an element are related to the local displacements and forces as follows

$$\{\delta'\}^e = [T]\{\delta\}^e \qquad \{R'\}^e = [T]\{R\}^e \qquad \ldots \quad \text{(IV-6)}$$

where

$$[T] = \begin{bmatrix} [L] & 0 & 0 & 0 \\ 0 & [L] & 0 & 0 \\ 0 & 0 & [L] & 0 \\ 0 & 0 & 0 & [L] \end{bmatrix}$$

The stiffness matrix of an an element may be expressed in terms of the global coordinate system by substituting equation (IV-6) into equation (IV-5) and, because the transformation [T] is orthogonal

$$[K]^e = [T]^T [K']^e [T]$$

where $[K]^e\{\delta\}^e = \{R\}^e$

The global element stiffness matrix may be conveniently evaluated by considering each submatrix $[K_{rs}]$, relating the displacements at node s to the forces at node r, in turn

$$[K_{rs}]^e = [L]^T [K'_{rs}]^e [L]$$

After the stiffness matrices of all the elements have been determined in the common global coordinate system the assembly of the element stiffness matrices is a matter of simple booking,

$$K_{ij} = \sum_{e}^{n} K_{ij}^{e}$$

where K_{ij} is the i,jth term of the structural stiffness matrix, and n is the number of elements used to model the structure.

IV-4 CYLINDRICAL SHELL EXAMPLE

In order to test the performance of the QMC3/CQ12 element this finite element approach was used to compute the linear elastic response of the uniformly loaded cylindrical shell illustrated in Fig. IV-1, which is simply supported on diaphragm supports at the ends and free along the longitudinal edges.

Results are presented for two idealisations of the structure, using both the 4 x 5 and 8 x 10 mesh of QMC3/CQ12 elements shown in Fig. IV-2, and are compared with those obtained from an exact cylindrical shell analysis performed by Scordelis and Lo [89], and the results presented by Carr [15] who used both a 4 x 5 and an 8 x 12 mesh of QST/HCT elements to model one quarter of the symmetric structure.

The transverse distributions of vertical, longitudinal, and transverse deflections across the midspan and support sections are plotted in Figures IV-3 and IV-4. In all cases the computed deflections converge to the fine mesh solution obtained by Carr [15] as the element idealisation is refined and agree to within 1% of the exact solution where this is available for comparison. The same trend is evident from Figures IV-5 and IV-6 where the transverse distributions of;

i) longitudinal shell force across the midspan section

ii) shear force across the midspan section

iii) transverse shell force across the midspan section

iv) transverse bending moment across the midspan section

are plotted. The forces and bending moments computed with the 8 x 10 mesh of QMC3/CQ12 elements generally agree to within 4% of the values obtained by Carr [15] using an 8 x 12 mesh of QST/HCT elements, and the results computed with the 4 x 5 mesh of QMC3/CQ12 elements are also of excellent accuracy. This is in contrast to the results obtained by Johnson [22] who combined the CST constant strain element [117] with the HCT plate bending element to contruct a 4 x 5 mesh idealisation of the structure and computed a maximum deflection at the free edge which is 38.6% smaller than the exact value [15, 22, 40].

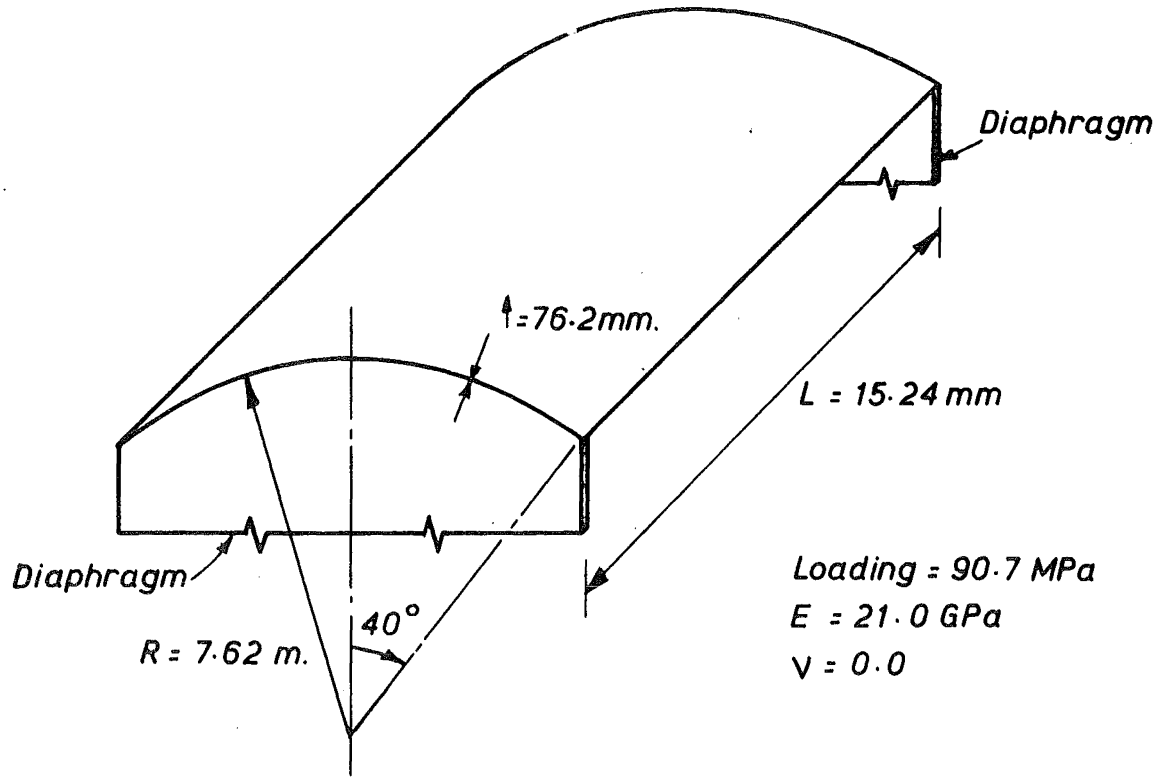

FIGURE IV-1 CYLINDER SHELL

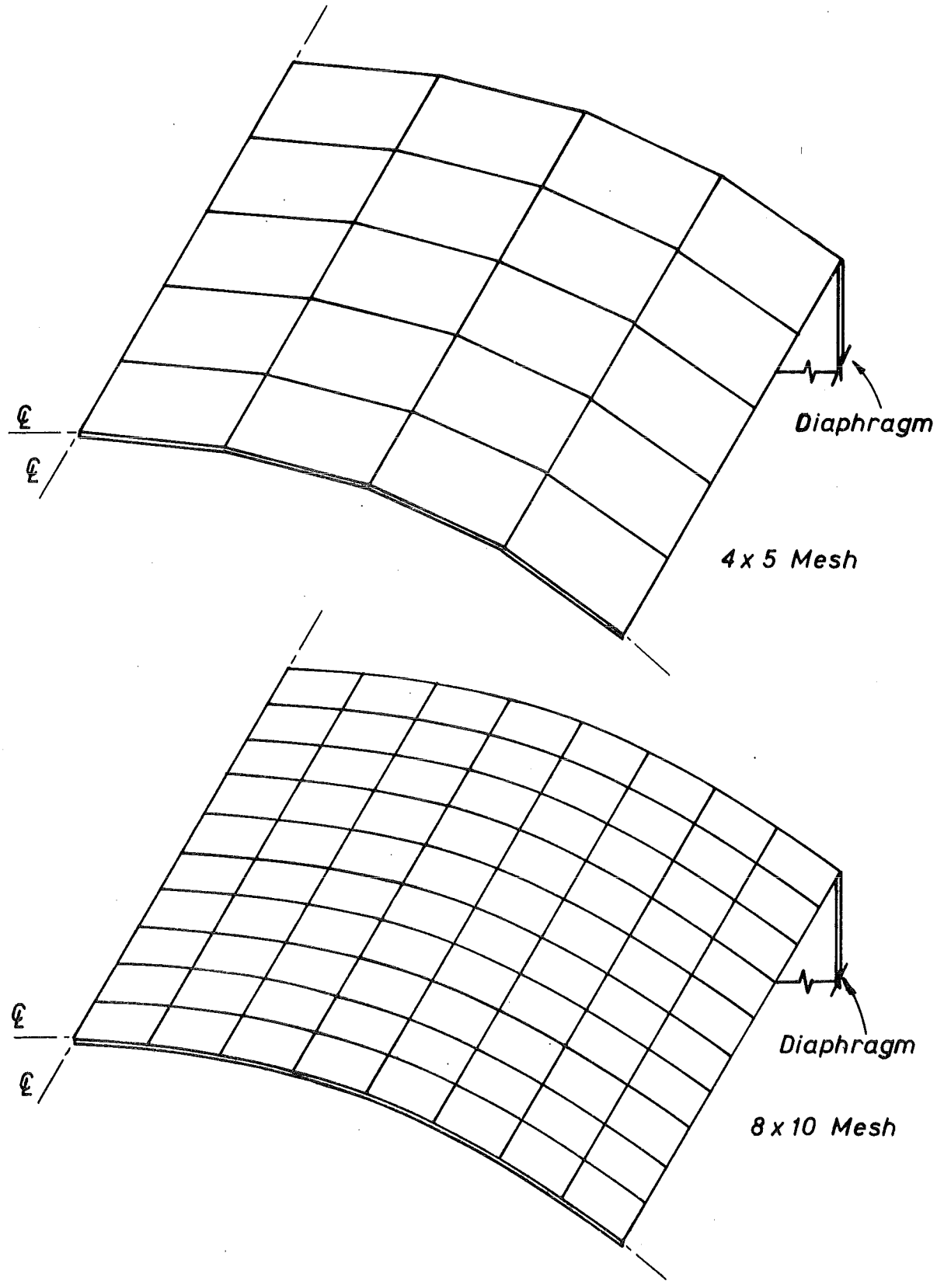

FIGURE IV-2 FINITE ELEMENT IDEALISATION
CYLINDRICAL SHELL

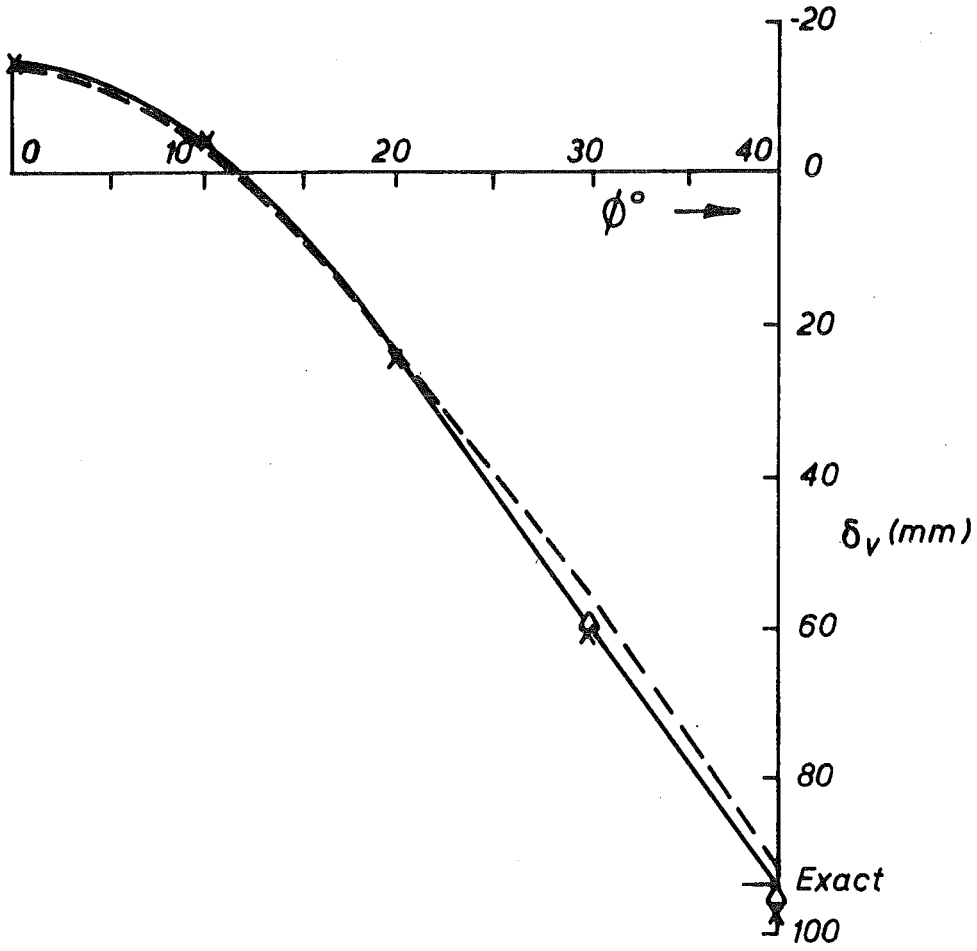

DISTRIBUTION OF VERTICAL DISPLACEMENT AT MIDSPAN

LEGEND

× 4 x 5 Mesh of QMC3/CQ 12 elts

△ 8 x 10 Mesh of " " "

---- 4 x 5 Mesh of QST/HCT elts

—— 8 x 12 Mesh of " " "

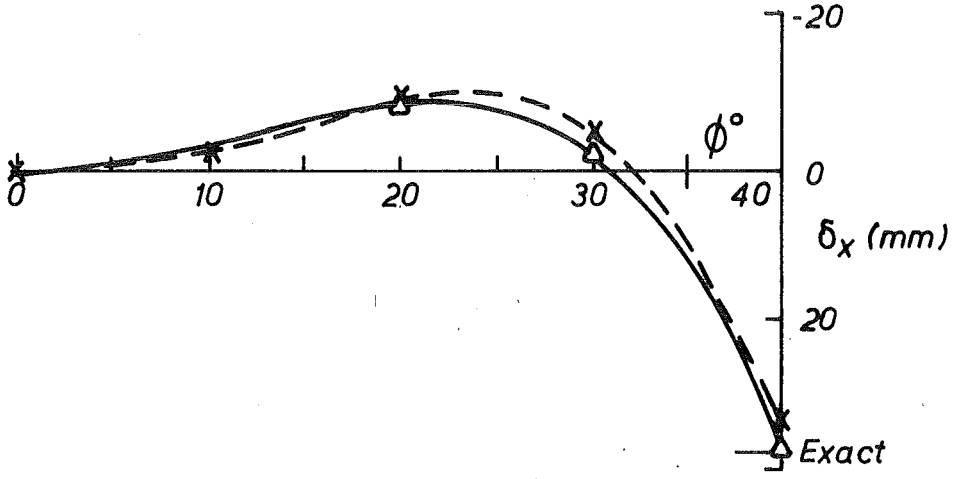

DISTRIBUTION OF LONGITUDINAL DISPLACEMENT OF END DIAPHRAGM

FIGURE IV-3 COMPARISON OF DEFLECTIONS
CYLINDRICAL SHELL

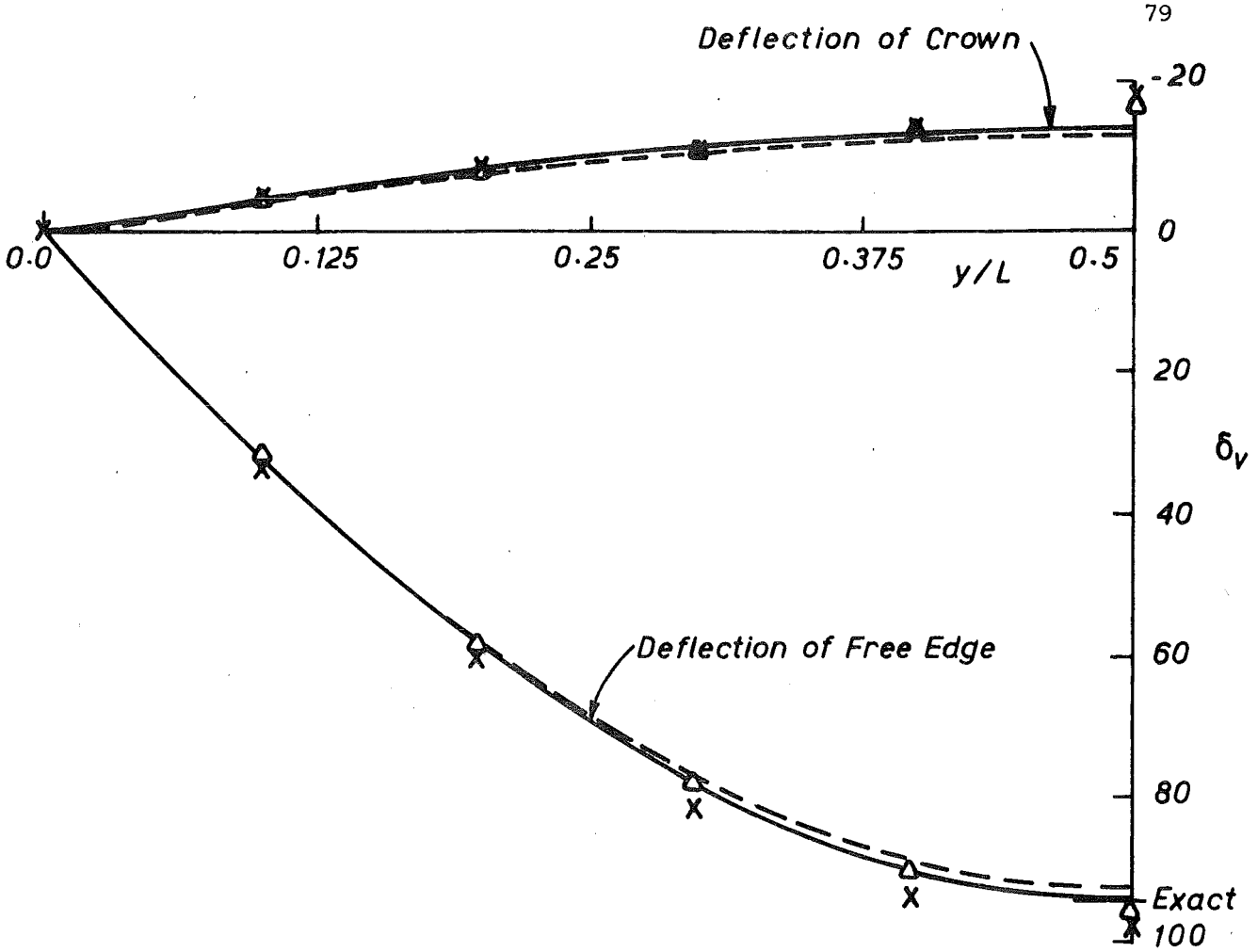

DISTRIBUTION OF VERTICAL DEFLECTION

LEGEND

× 4 x 5 Mesh of QMC3/CQ 12 elts

△ 8 x 10 Mesh of " " "

---- 4 x 5 Mesh of QST/HCT elts

—— 8 x 12 Mesh of " " "

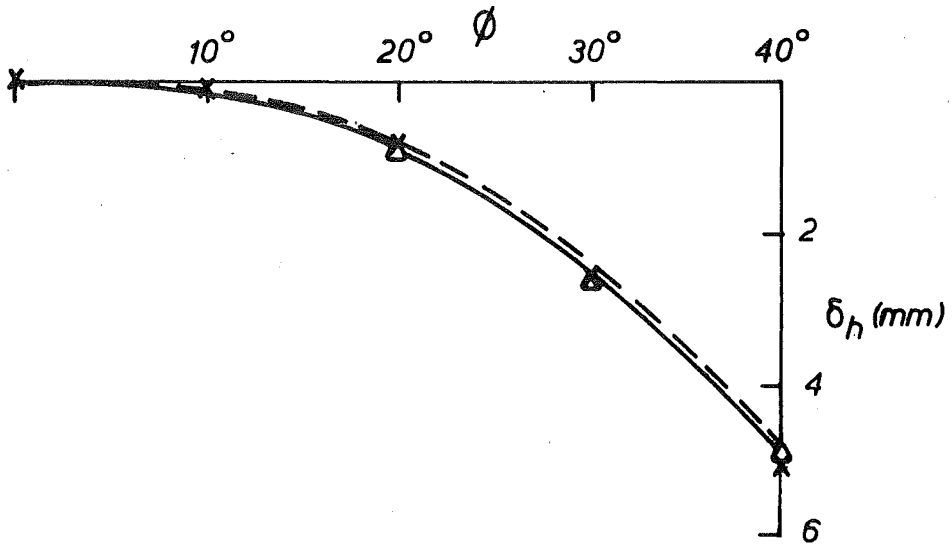

HORIZONTAL DEFLECTION AT MIDSPAN

FIGURE IV-4 COMPARISON OF DEFLECTIONS
CYLINDRICAL SHELL

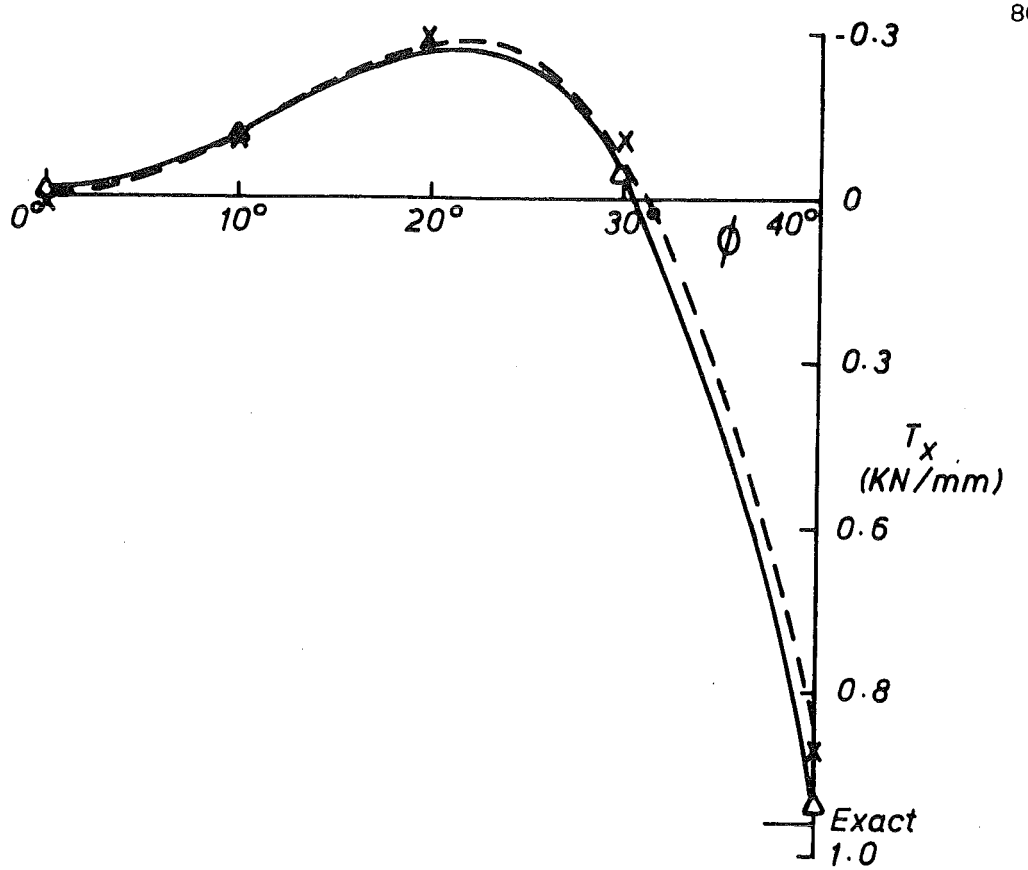

VARIATION OF LONGITUDINAL SHELL FORCE AT MIDSPAN

LEGEND

× 4 x 5 Mesh of QMC3/CQ 12 elts

△ 8 x 10 Mesh of " " "

---- 4 x 5 Mesh of QST/HCT elts

—— 8 x 12 Mesh of " " "

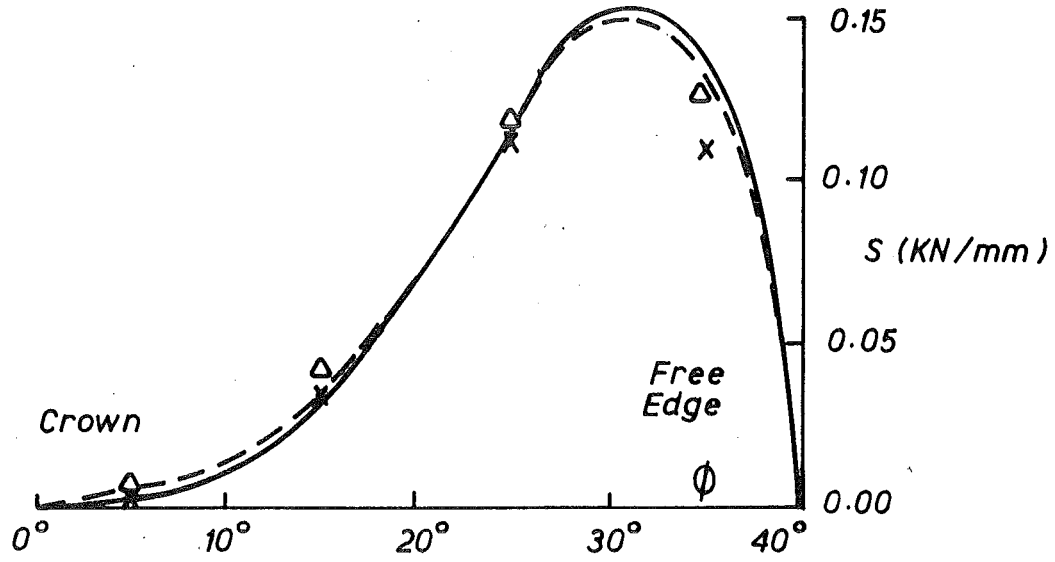

VARIATION OF SHELL SHEAR FORCE AT DIAPHRAGM END SUPPORT

FIGURE IV-5 COMPARISON OF SHELL FORCES
CYLINDRICAL SHELL

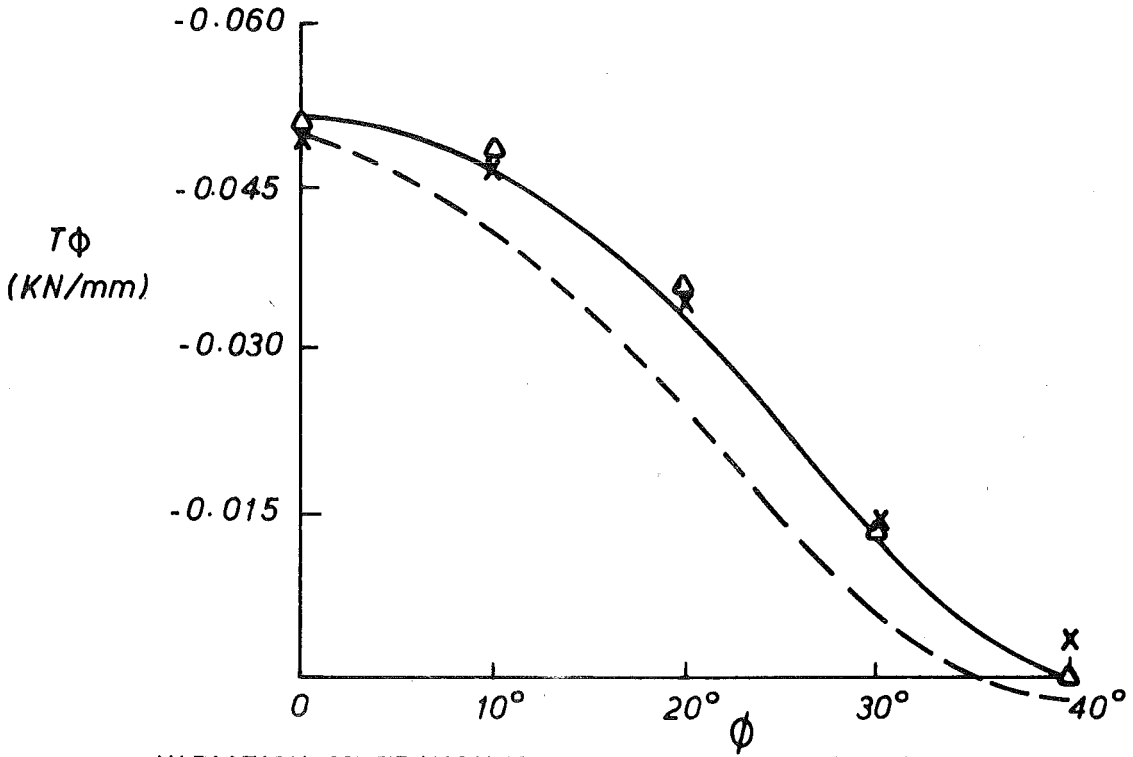

VARIATION OF TRANSVERSE SHELL FORCE AT MIDSPAN

LEGEND

× 4 x 5 Mesh of QMC3/CQ 12 elts

△ 8 x 10 Mesh of " " "

---- 4 x 5 Mesh of QST/HCT elts

—— 8 x 12 Mesh of " " "

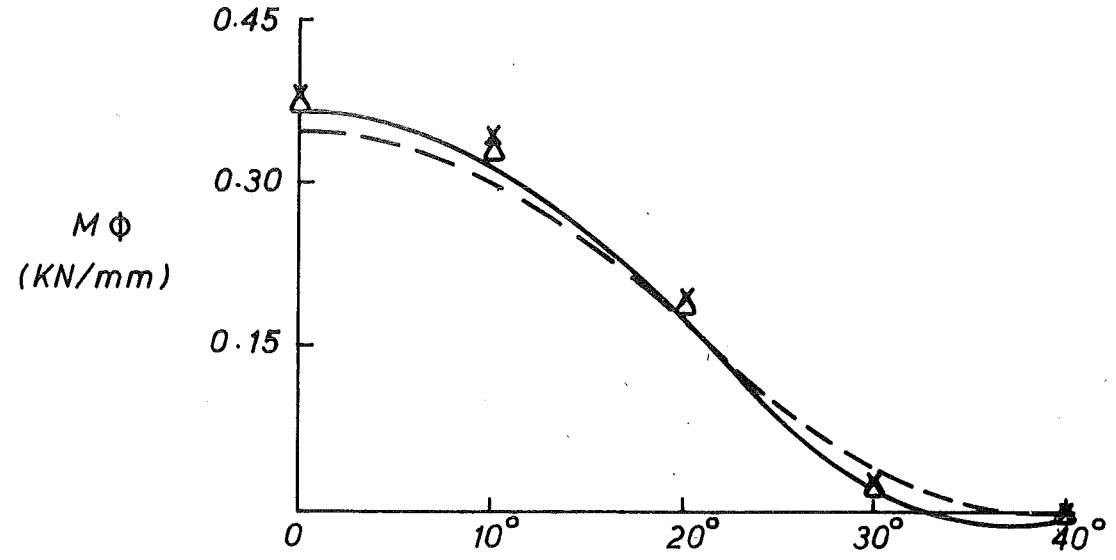

VARIATION OF TRANSVERSE SHELL MOMENT AT MIDSPAN

FIGURE IV-6 COMPARISON OF SHELL FORCES
CYLINDRICAL SHELL

IV-5 CONCLUSIONS

When the longitudinal sides of the QMC3/CQ12 element are aligned with the longitudinal sides of the idealised cylindrical shell the computed results are of similar accuracy to those obtained with the QST/HCT element which has an additional three strain degrees of freedom at each node. It may therefore be concluded that the QMC3/CQ12 element is most suitable for the analysis of cylindrical shells of this form which are characterised by large deflections of the free edges, and consequently for which the performance of the membrane component of the element is critical.

CHAPTER V

MESH GRADING OF FINITE ELEMENTS

V-1 APPLICATION

Mesh grading is a technique which enables substantial changes of element size to be incorporated within a field of finite elements, and its implementation only requires the pre and post multiplication of the element stiffness matrix by a simple transformation matrix. Therefore, the finite element idealisation of a continuum may be conveniently refined in the vicinity of stress concentrations, as demonstrated in Section V-5, and the geometric restrictions previously associated with a mesh of four sided elements may be alleviated when this technique is used.

The means of achieving these advantages without violating established compatibility conditions has been outlined by Somervaille [97], and is described in the next section with reference to the QMC3/CQ12 element.

V-2 COMPATIBILITY BETWEEN CONTIGUOUS ELEMENTS

Two contiguous elements are illustrated in Fig. V-1. The verticies of the smaller mesh graded element are numbered counterclockwise i, j, k, l, and upper case letters are used to distinguish the variables of the larger element. The nodal points of the edge containing i and j are numbered I and J.

The required compatibility of deformations between the two elements is satisfied if the set of displacements and derivatives corresponding to the minimum number of degrees of freedom of the element type, defined in Fig. I-1, are identical at all points of the common edge. Let the vectors $\{D(s)\}$ and $\{d(s)\}$ represent the set of deformations along the common edge in the large and small element respectively where the parameter s is the distance from the nodal point I. The components of these vectors are polynomial functions of the parameter s and the degree of the polynomial depends on the type of element. If the elements are fully compatible

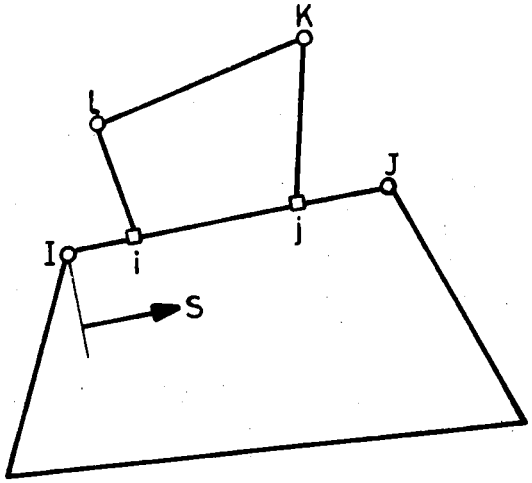

FIGURE V-1 CONTIGUOUS LARGE AND SMALL ELEMENTS

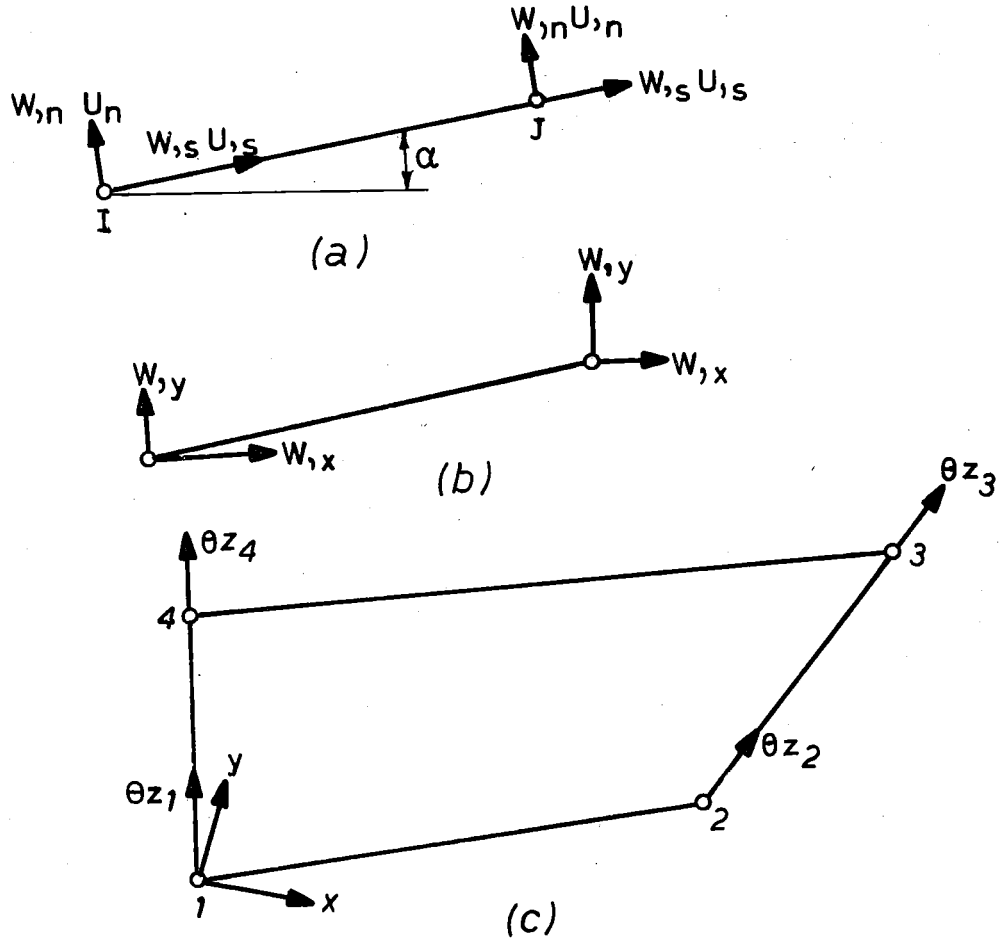

FIGURE V-2 SLOPE DIRECTIONS

$$\{D(s)\} = \{d(s)\} = [P(s)] \begin{bmatrix} c_1 \\ c_2 \\ c_3 \\ . \\ . \\ . \\ . \end{bmatrix} = [P]\{C\} \quad \ldots \quad (IV\text{-}1)$$

where the elements of the vector $\{C\}$ are polynomial coefficients, and the displacement vectors are uniquely defined by the generalised displacements at the nodal points on the common edge. Let the generalised displacements of the larger element at the master nodal points I and J be q_I and q_J respectively, then by considering the geometric boundary conditions, these generalised displacements may be expressed in terms of the coefficient vector $\{C\}$

$$\begin{Bmatrix} q_I \\ q_J \end{Bmatrix} = [B]\{C\} \quad \ldots \quad (V\text{-}2)$$

and the matrix $[B]$ is then inverted to obtain an explicit expression for the coefficient vector

$$\{C\} = [B]^{-1} \begin{Bmatrix} q_I \\ q_J \end{Bmatrix} \quad \ldots \quad (V\text{-}3)$$

Similarly the generalised displacements defined at the slave vertices i,j can be expressed in terms of the coefficient vector $\{C\}$

$$\begin{Bmatrix} q_i \\ q_j \end{Bmatrix} = [b]\{C\} \quad \ldots \quad (V\text{-}4)$$

and after substituting from equation (V-3)

$$\begin{Bmatrix} q_i \\ q_j \end{Bmatrix} = [b][B]^{-1} \begin{Bmatrix} q_I \\ q_J \end{Bmatrix} = [H] \begin{Bmatrix} q_I \\ q_J \end{Bmatrix} \quad \ldots \quad (V\text{-}5)$$

The complete set of generalised displacements $\{q\}$ defined at the vertices of the small mesh graded element may now be related to

the set $\{q^*\}$, in which some generalised displacements are defined at the master nodal points of the neighbouring element,by a transformation matrix $[T]$,

$$\begin{Bmatrix} q_i \\ q_j \\ q_k \\ q_l \end{Bmatrix} = \begin{bmatrix} [H] & [O] \\ [O] & [I] \end{bmatrix} \begin{Bmatrix} q_I \\ q_J \\ q_k \\ q_l \end{Bmatrix} \quad \ldots \quad (V\text{-}6)$$

i.e., $$\{q\} = [T]\{q^*\} \quad \ldots \quad (V\text{-}7)$$

If $\{Q\}$ is the vector of generalised forces conjugate to $\{q\}$, and $\{Q^*\}$ is conjugate to the vector of nodal displacements $\{q^*\}$, then by contragradience

$$\{Q^*\} = [T]^T \{Q\} \quad \ldots \quad (V\text{-}8)$$

The stiffness matrix $[K]$ of the small element relates $\{q\}$ and $\{Q\}$

$$\{Q\} = [K]\{q\} \quad \ldots \quad (V\text{-}9)$$

Substituting equations (V-7) and (V-8) into equation (V-9) leads to the expression

$$\{Q^*\} = [K^*]\{q^*\} \quad \ldots \quad (V\text{-}10)$$

where the required transformed stiffness matrix $[K^*]$ of the mesh graded element

$$[K^*] = [T]^T [K] [T] \quad \ldots \quad (V\text{-}11)$$

V-3 TRANSFORMATION OF THE COMPATIBLE QMC3/CQ12 SHELL ELEMENT

The degrees of freedom associated with nodal point i of the QMC3/CQ12 element consist of the displacements u, v, and w, and the rotations $\Theta x = w,y, \Theta y = -w,x$ and $\Theta z = u,T$ $(= -\frac{\partial u}{\partial t} / \frac{1}{2} YYY(i))$, where T is a vector along the longitudinal side associated with nodal point i, in the direction node 3 → node 2 (or 4 → 1), and of magnitude $\frac{1}{2} YYY(i)$, equal to half the length of this side.

The deformation vector $\{D(s)\}$ must be considered in two parts; that relating to the longitudinal edges defined by nodes 2-3 and nodes 4-1, and that pertaining to the transverse edges defined by nodes 1-2 and nodes 3-4.

V-3.1 Longitudinal edges (2-3, 4-1)

The element deformation vector $\{D(s)\}$ along these edges has components W, W,n, U, and V . Equating these components on the interface of adjacent elements ensures continuity of both displacements and slopes W,n, W,s, U,s across the interface. The polynomial expression for the vector is

$$\{D(s)\} = \begin{Bmatrix} W \\ W,n \\ U \\ V \end{Bmatrix} = \begin{bmatrix} 1 & s & s^2 & s^3 & & & & & & & & \\ & & & & 1 & s & & & & & & \\ & & & & & & 1 & s & s^2 & s^3 & & \\ & & & & & & & & & & 1 & s \end{bmatrix} \{C\} \qquad \ldots \quad (V\text{-}12)$$

where s is the distance from nodal point I.

The matrices [b] and [B] were formed in two steps. In the first operation the slopes at the vertices were defined with respect to the edge coordinate axes (s,n) shown in Fig. (V-2a), i.e.

$$\begin{Bmatrix} U_i \\ V_i \\ W_i \\ W,s_i \\ W,n_i \\ U,s_i \\ U_j \\ V_j \\ W_j \\ W,s_j \\ W,n_i \\ U,s_j \end{Bmatrix} = \begin{bmatrix} 1 & & & S_i & S_i^2 & & & & & & S_i^3 & \\ & 1 & & & & S_i & & & & & & \\ & & 1 & S_i & & & S_i^2 & S_i^3 & & & & \\ & & & 1 & & & 2S_i & 3S_i^2 & & & & \\ & & & & 1 & & & & S_i & & & \\ & & & & & 1 & 2S_i & & & & 3S_i^2 & \\ 1 & & & S_j & S_j^2 & & & & & & S_j^3 & \\ & 1 & & & & S_j & & & & & & \\ & & 1 & S_j & & & S_j^2 & S_j^3 & & & & \\ & & & 1 & & & 2S_j & 3S_j^2 & & & & \\ & & & & 1 & & & & S_j & & & \\ & & & & & 1 & 2S_j & & & & 3S_j^2 & \end{bmatrix} \{C\} \qquad \ldots \quad (V\text{-}13)$$

Thus $\begin{Bmatrix} q_i \\ q_j \end{Bmatrix} = [b_1]\ \{C\}$ ... (V-14)

To express the slopes with respect to the local element coordinate axes (x,y), shown in Figures (V-2b) and (V-2c), there is the relationship

$$\begin{Bmatrix} \Theta x \\ \Theta y \\ \Theta z \end{Bmatrix}_{i,j} = \begin{bmatrix} W,y \\ -W,x \\ U,T \end{bmatrix}_{i,j} = \begin{bmatrix} \sin\alpha & \cos\alpha & 0 \\ -\cos\alpha & \sin\alpha & 0 \\ 0 & 0 & N_{ij}M_{ij} \end{bmatrix} \begin{Bmatrix} W,s \\ W,n \\ U,s \end{Bmatrix}_{i,j}$$

$$= [R_1] \begin{Bmatrix} W,s \\ W,n \\ U,s \end{Bmatrix}_{i,j} \quad \text{... (V-15)}$$

where $N_{ij} = -1$ for Node i = 2, j = 3

$N_{ij} = +1$ for node i = 4, j = 1

and $M_{ij} = S_j/YYY(i)$

The local element y axis was chosen to align with the average direction of the two longitudinal sides defined by nodes (2 → 3) and (1 → 4) with the origin at node 1 as shown in Fig. (V-2c). M_{ij} is the ratio of the length of the longitudinal side i-j to the component of this length in the local y direction.

Consequently,

$$\begin{Bmatrix} q_i \\ q_j \end{Bmatrix} = \begin{bmatrix} [R] & [O] \\ [O] & [R] \end{bmatrix} [b_1]\ \{C\} \quad \text{... (V-16)}$$

$$= [b]\ \{C\} \quad \text{... (V-17)}$$

where $[R] = \begin{bmatrix} 1 & & & \\ & 1 & & \\ & & 1 & \\ & & & [R_1] \end{bmatrix}$ ... (V-18)

V-3.2 Transverse edges (1-2, 3-4)

The deformation vector $\{D(s)\}$ along these edges has components W, W,n, U, U,n, and V. The polynomial expression for the deformation vector is:-

$$\{D(s)\} = \begin{Bmatrix} W \\ W,n \\ U \\ U,n \\ V \end{Bmatrix} = \begin{bmatrix} 1 & s & s^2 & s^3 & & & & & & \\ & & & & 1 & s & & & & \\ & & & & & & 1 & s & & \\ & & & & & & & & 1 & s \end{bmatrix} \{C\} \quad \ldots \quad (V\text{-}19)$$

where s is the distance from nodal point I

The matrices [b] and [B] were formed in two steps. In the first operation the slopes at the verticies were defined with respect to the edge coordinate axes (s,n) shown in Fig. (V-2a). i.e.,

$$\begin{Bmatrix} U_i \\ V_i \\ W_i \\ W,s_i \\ W,n_i \\ U,n_i \\ U_j \\ V_j \\ W_j \\ W,s_j \\ W,n_j \\ U,n_j \end{Bmatrix} = \begin{bmatrix} 1 & & & & S_i & & & & & \\ & 1 & & & & S_i & & & & \\ & & 1 & S_i & & & S_i^2 & S_i^3 & & \\ & & & 1 & & & 2S_i & 3S_i^2 & & \\ & & & & 1 & & & & S_i & \\ & & & & & 1 & & & & S_i \\ 1 & & & & S_j & & & & & \\ & 1 & & & & S_j & & & & \\ & & 1 & S_j & & & S_j^2 & S_j^3 & & \\ & & & 1 & & & 2S_j & 3S_j^2 & & \\ & & & & 1 & & & & S_j & \\ & & & & & 1 & & & & S_j \end{bmatrix} \{C\} \quad \ldots \quad (V\text{-}20)$$

Thus $$\begin{Bmatrix} q_i \\ q_j \end{Bmatrix} = [b_1] \{C\} \quad \ldots \quad (V\text{-}21)$$

The slopes may be expressed with respect to the local element axes, shown in Figures (V-2b) and (V-2c), by using the relationship defined in equation (V-15)

$$\begin{Bmatrix} \Theta x \\ \Theta y \\ \Theta z \end{Bmatrix}_{i,j} = [R_1] \begin{Bmatrix} W,s \\ W,n \\ U,n \end{Bmatrix}_{i,j} \quad \ldots \quad (V\text{-}22)$$

but now $N_{ij} = -1$ for node i = 1, j = 2

$N_{ij} = +1$ for node i = 3, j = 4 ,

and M_{ij} retains the identity defined for the longitudinal sides.

The relationship $\Theta z_i = (N_{ij} M_{ij}) U, n_i$ is only strictly true for rectangular elements. This is because Θz_i is referred to the direction of the longitudinal side associated with node i, which does not correspond to the direction normal to the transverse side in other cases. However, the linear interpolation of Θz between the nodal values is still correct, so compatibility is not violated in this respect.

The procedure used to compute the elements of the matrix [b] may also be used to calculate the elements of the matrix [B], employing S_I and S_J as arguments in place of S_i and S_j.

V-4 DATA PREPARATION

The redundant verticies (see Fig. V-3a), denoted slave nodes, are not included in the set of nodal points with which structural degrees of freedom are associated, and therefore should be allocated nodal sequence numbers after all the other nodal points so they may be readily eliminated from further computational consideration.

V-5 NUMERICAL EXAMPLES

V-5.1 Centrally loaded plates

The fully compatible CQ12 plate bending element was used to analyse both a simply supported and a clamped square plate, subjected to a central transverse point load. Because of symmetry only one quarter of the plate need be considered, and was idealised with the two sets of meshes illustrated in Figures V-3 and V-4, the results of which are presented in Tables V-1 and V-2 respectively.

The incorporation of a refined element idealisation in the regions of stress concentration results in an improved accuracy of the solution, but the displacements and rotations computed with the graded meshes are generally in closer agreement with the coarse mesh solution than the fine mesh solution. This is in contrast to the results obtained by Sommervaille [97] using the CQ16 element with the mesh set 1 idealisation. It may therefore be desirable to incorporate midside normal slope parameters along the sides of CQ12 elements to which the mesh grading technique is to be applied. However, the central bending moments computed with the graded mesh of CQ12 elements are in much closer agreement with the fine mesh solution than the coarse mesh solution.

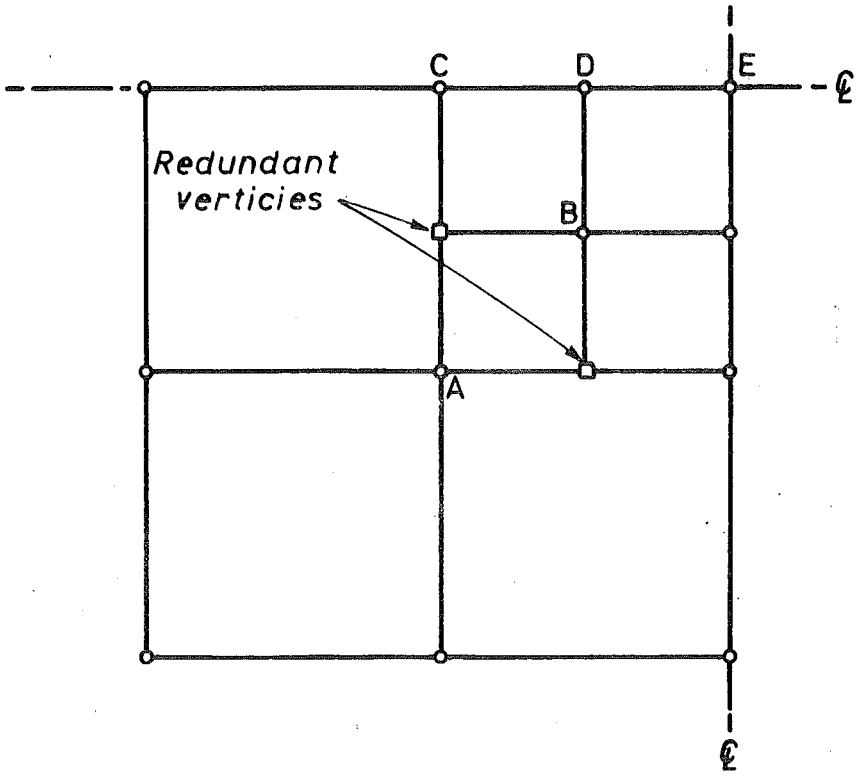

(a) Graded Mesh 1

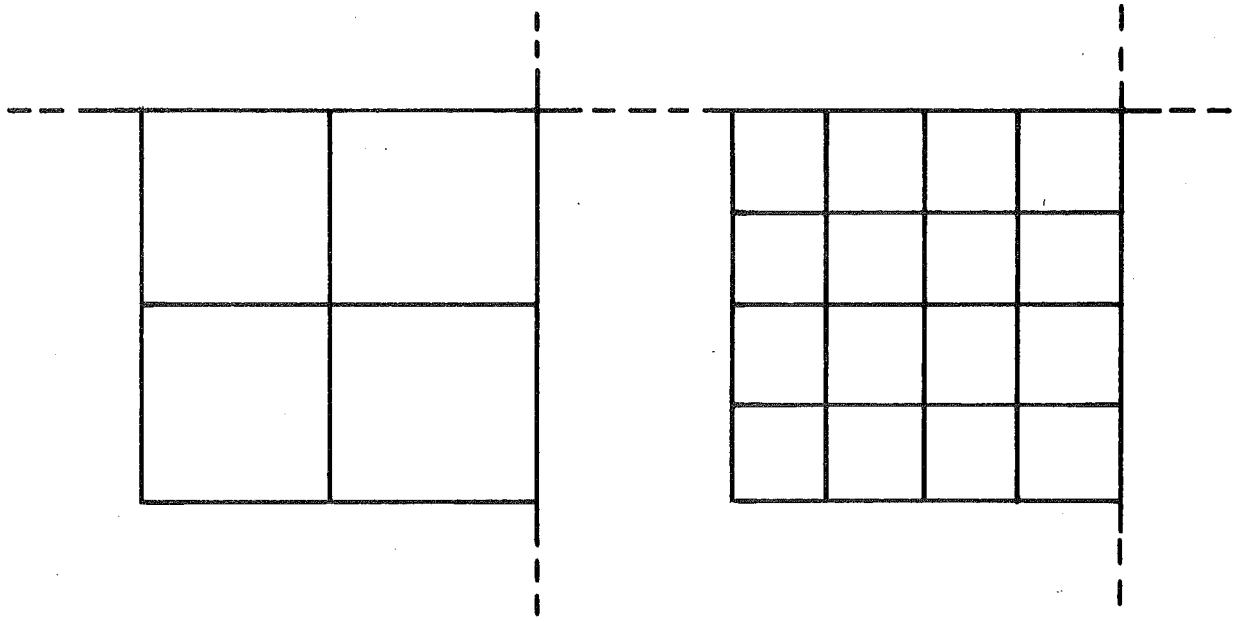

(b) Coarse Mesh 1

(c) Fine Mesh 1

FIGURE V-3 MESH SET 1, CENTRALLY LOADED PLATE

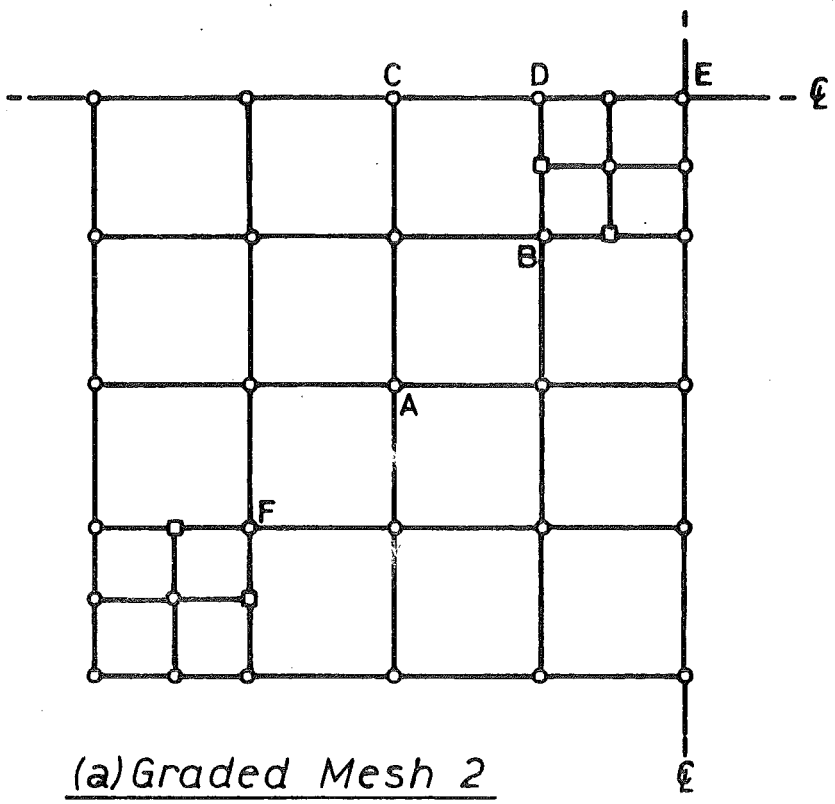

(a) Graded Mesh 2

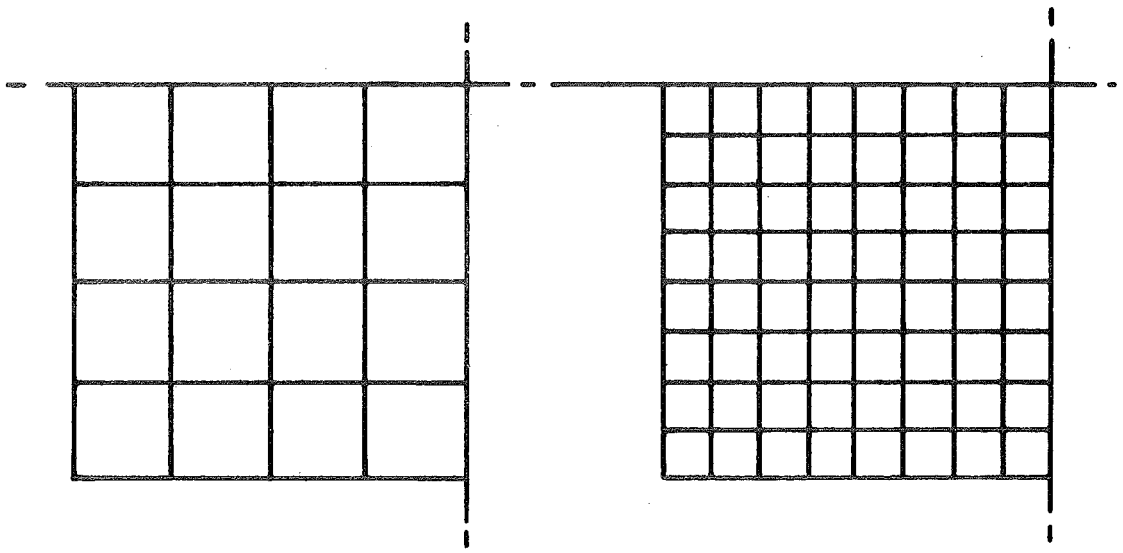

(b) Coarse Mesh 2

(c) Fine Mesh 2

FIGURE V-4 MESH SET 2, CENTRALLY LOADED PLATE

TABLE V-1 MESH SET 1 ; COMPARISON OF DEFLECTIONS, SLOPES, MOMENTS

LOCATION	FUNCTION	CLAMPED PLATE			SIMPLY SUPPORTED PLATE		
		Coarse Mesh 2 x 2	Graded Mesh	Fine Mesh 4 x 4	Coarse Mesh 2 x 2	Graded Mesh	Fine Mesh 4 x 4
A	$(wD/PL^2) \times 10^6$	10.45	10.44	10.95	41.62	41.73	43.31
B	(Deflection)		30.87	32.62		78.88	81.71
C		20.90	21.41	22.26	62.18	62.91	65.09
D			37.57	39.42		88.51	91.44
E		46.45	47.76	49.85	100.03	101.75	104.89
A	$(w,x\ D/PL^3) \times 10^6$	8.13	7.86	8.33	18.86	18.62	18.87
B	(Slope)		11.90	12.30		17.80	18.22
C		16.26	17.19	17.80	29.34	30.46	30.36
D			15.60	16.15		21.82	22.22
E	Mx/PL (Bending Moment)	0.153	0.208	0.211	0.191	0.248	0.250

TABLE V-2 MESH SET 2 ; COMPARISON OF DEFLECTIONS AND SLOPES

LOCATION	FUNCTION	Clamped Square Plate		
		Coarse Mesh 4 x 4	Graded	Fine 8 x 8
A	$(wD/PL^2) \times 10^6$	10.953	10.962	11.211
B	(Deflection)	32.6196	32.6194	33,285
C		22.259	22.260	22.631
D		39.420	39.461	40.326
E		49.854	49.833	51.174
F		0.944	0.945	0.986
A	$(w,x\ D/PL^3) \times 10^6$	8.326	8.330	8.552
B	(Slope)	12.299	12.257	12.305
C		17.797	17.807	17.798
D		16.151	16.272	16.686
F		1.714	1.726	1.886

TABLE V-3 CANTILEVER BEAM ; COMPARISON OF DEFLECTIONS AND STRESSES

	Coarse Mesh 8 x 2	Graded Mesh	Fine Mesh 16 x 4	Theory [15]
Deflection of point A (mm)	8.786	8.884	8.974	9.037
Stress at point B (kPa)	0.426	0.423	0.426	0.420

V-5.2 Cantilever beam

The QMC3 plane stress element was used to analyse the cantilever described in Fig. III-6, subjected to a parabolically varying shear force at the free end. The cantilever was idealised with the coarse,graded, and fine meshes of elements shown in Fig. V-5.

The deflection of point A at the free end and the extreme fibre stress at point B, one quarter of the span length from the fixed end, computed from the three mesh idealisations, are presented in Table V-3 for comparison. The computed deflections from the coarse, graded, and fine mesh solutions are 2.8%, 1.7% and 0.7% smaller than the theoretical solution [15] respectively, so grading the mesh results in a significant improvement in accuracy while only requiring a small amount of additional computantional effort. The computed stresses do not converge to the theoretical solution because of the approximations used to model the theoretical boundary conditions, but the results are within 1.4% of the theoretical stress.

V-6 CONCLUSIONS

The application of the mesh grading technique was associated with a significant improvement in the accuracy of finite element results when it was employed to facilitate the incorporation of a refined element idealisation in the region of stress concentrations within a cantilever beam subjected to a parabolically varying end shear, and to a lesser extent within centrally loaded plates. The number of elements required to achieve these improvements was less than half that required to achieve a uniform refinement of the element idealisation over the entire structure.

It will be advantageous to use this technique during the finite element analysis of complex box-girder bridges, not only to enable a better representation of stress concentrations to be achieved, without significant additional computational effort, but also to alleviate the geometric restrictions previously associated with an assembly of four sided elements. This is demonstrated in Sections IX-10 and IX-11 where bridges with non-uniform sections and trifurcating plan geometry are idealised.

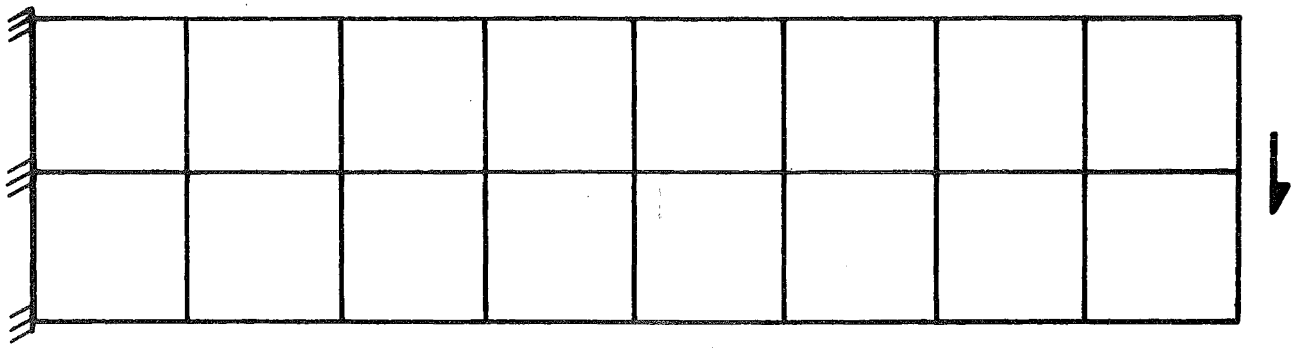

(a) Coarse Mesh

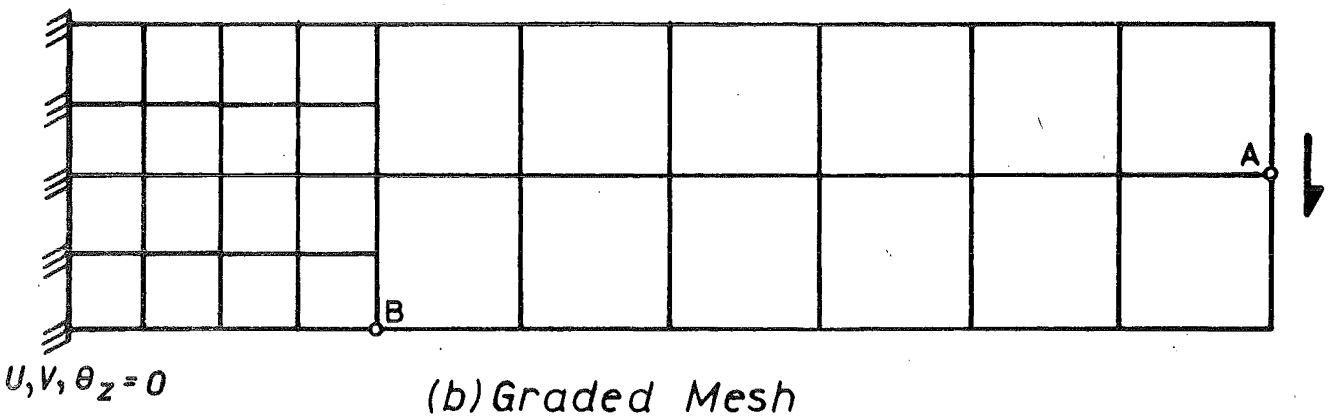

(b) Graded Mesh

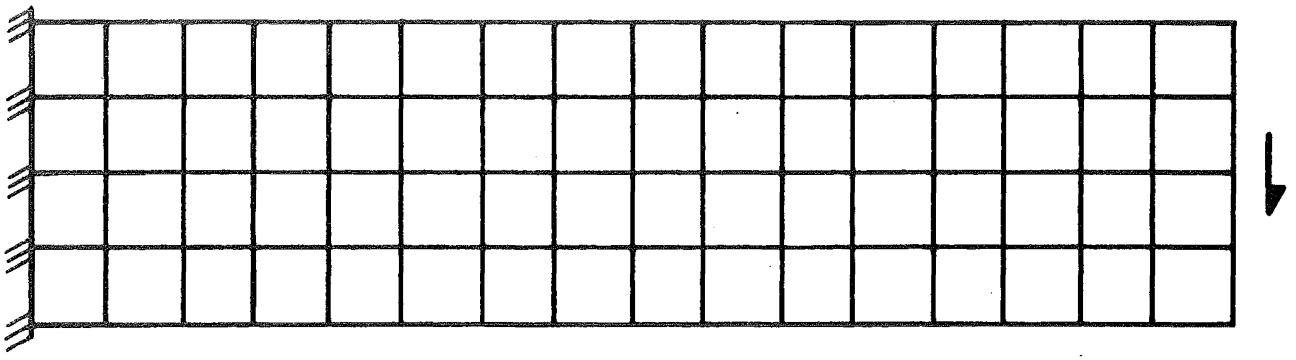

(c) Fine Mesh

FIGURE V-5 MESHES FOR CANTILEVER BEAM

CHAPTER VI

THREE DIMENSIONAL LINEAR ELASTIC BEAM ELEMENT

VI-1 INTRODUCTION

The field of application of the finite element approach described in this work can easily be extended from thin shell structures to include integral frames, piers, stiffeners, and kerbs, represented as three dimensional prismatic beam elements, because the QMC3/CQ12 element has the invariant set of three translational and three rotational degrees of freedom at each node.

VI-2 ELEMENT STIFFNESS MATRIX

The 12 x 12 linear elastic stiffness matrix $[K_c]$ of a three dimensional prismatic beam element, related to these six nodal parameters located at the centroid of the end sections, has been derived directly from consideration of slope deflection relationships and is tabulated on page 79 of reference [81]. This stiffness matrix may be alternatively derived by using the finite element displacement method with the displacement functions defined by Cheng [18].

VI-3 ECCENTRIC NODES

A beam element connected to a thin shell structure at a node n with eccentricities Ex and Ez, measured from the node n to the centroid c of the corresponding end section of the beam element, is illustrated in Fig. VI-1a. A transformation matrix [N] which relates the generalised centroidal displacements $\{\delta\}_c$ to the displacements $\{\delta\}_n$ of the eccentric node must be employed to derive the stiffness matrix relating the generalised forces to the generalised displacements at the node n. The transformation $[N_1]$ for node 1 may be defined

$$\begin{Bmatrix} u \\ v \\ w \\ \theta x \\ \theta y \\ \theta z \end{Bmatrix}_{c_1} = \begin{bmatrix} 1 & . & . & . & Ez_1 & . \\ . & 1 & . & -Ez_1 & . & Ex_1 \\ . & . & 1 & . & -Ex_1 & . \\ . & . & . & 1 & . & . \\ . & . & . & . & 1 & . \\ . & . & . & . & . & 1 \end{bmatrix} \begin{Bmatrix} u \\ v \\ w \\ \theta x \\ \theta y \\ \theta z \end{Bmatrix}_{n_1} = [N_1] \{\delta\}_{n_1}$$

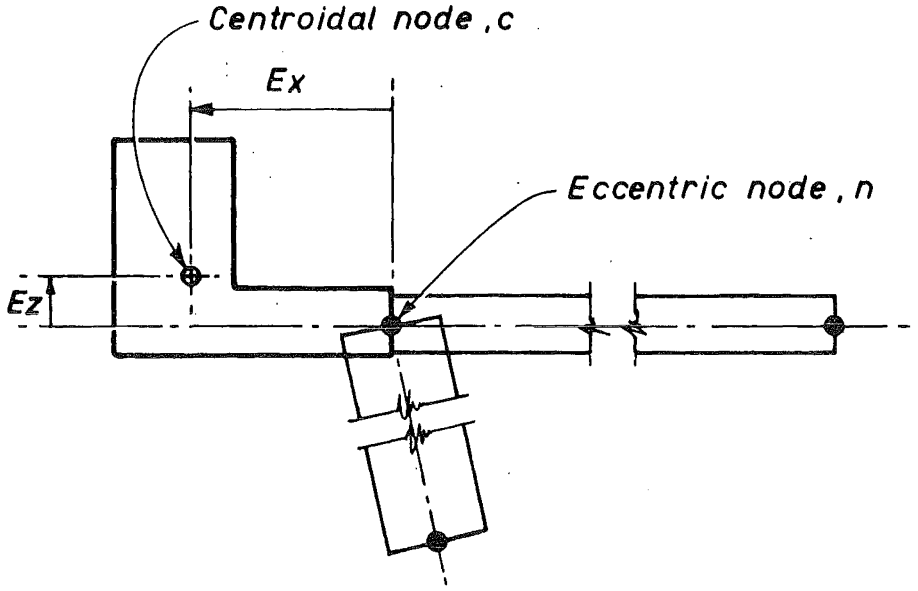

(a) ECCENTRIC CONNECTION

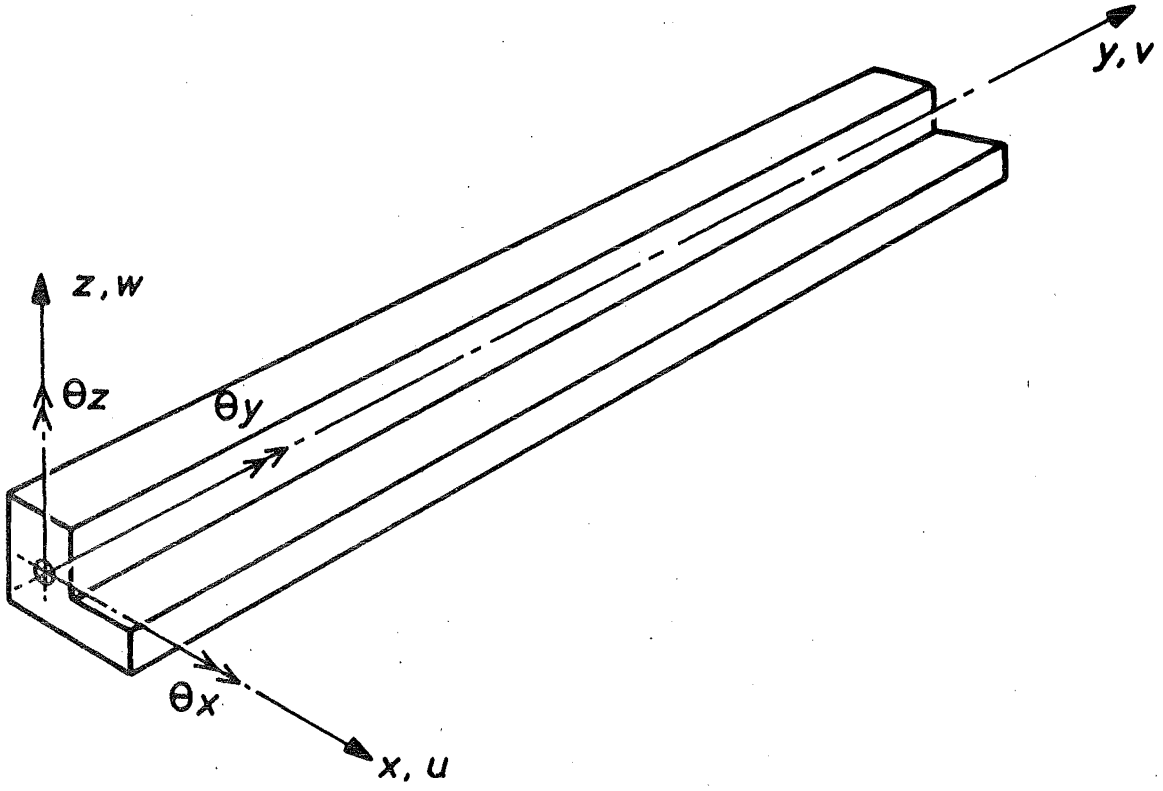

(b) LOCAL COORDINATE SYSTEM

FIGURE VI-1 BEAM ELEMENT

and provided the eccentricities are the same for node 2 at the other end of the beam, as is the case for the structures analysed in this work, the same transformation applies here

$$\{\delta\} = [N_1] \{\delta\}_{n_2} .$$

The transformation [N] for the assembled vector of generalised displacements of the element then takes the form

$$[N] = \begin{bmatrix} [N_1] & . \\ . & [N_1] \end{bmatrix}$$

and,since this transformation also applies to the generalised nodal forces, the stiffness matrix $[K_n]$ relating the generalised forces and displacements at the eccentric nodes may be evaluated as follows

$$[K_n] = [N]^{-1} [K_c] [N]$$

VI-4 TRANSFORMATION TO GLOBAL COORDINATE SYSTEM

If the local axes of the beam element defined in Fig. VI-1.b are not parallel to the corresponding global axes of the structure then, to enable the element stiffness matrices to be assembled, an additional transformation matrix [T] must be applied to evaluate the element stiffness matrix [K] relating the generalised nodal forces and displacements measured in the global coordinate system. This transformation matrix is a function of the direction cosines between the local and global axes, as discussed in Chapter IV, and since it is orthogonal, the required element stiffness matrix may be determined from the expression

$$[K] = [T]^T [K_n] [T]$$

VI-5 APPLICATION

Sisodiya et al [95] have used this procedure to incorporate frame type diaphragms into box-girder bridge analyses. Beam elements were employed during this work to represent the piers, stiffeners, and kerbs of box-girder bridges, as described in Chapter IX. The latter application resulted in a significant reduction of the bandwidth of the assembled structural stiffness matrix compared with that for a plate element representation.

CHAPTER VII

NUMERICAL INTEGRATION

VII-1 INTRODUCTION

A parametric transformation may be used to derive the element displacement functions (see Chapter I) in the form

$$\{\Delta\} = [N(s,t)]\ \{\delta\}$$

The matrix [B], relating the generalised strains to the nodal displacements, will be a function of the inverse of the determinant of the Jacobian of the transformation [J] as discussed in Chapter III

$$[J] = \frac{\partial (x,y)}{\partial (s,t)}$$

Therefore, the explicit algebraic integration of the strain energy gradient required to evaluate the element stiffness matrix

$$[K] = \int_{vol} [B]^T\ [D]\ [B]\ d\,vol$$

is extremely difficult, except for elements of simple parallelogram or triangular geometry for which the determinant has a constant value. Consequently it is more convenient to use numerical integration.

VII-2 NUMERICAL INTEGRATION

The procedure for numerical integration is well established [12, 51, 98, 117] and may be defined as follows: It is required to evaluate an integral I

$$I = \int_{-1}^{1} \int_{-1}^{1} f(s,t)dsdt$$

This integration may be performed in two parts

$$\int_{-1}^{1} f(s,t)ds = \sum_{i=1}^{n} W_i^1\ f(a_i,t) = \psi(t)$$

$$\text{and} \quad I = \int_{-1}^{1} \psi(t)\,dt = \sum_{j=1}^{m} W_j^2 \psi(b_j)$$

$$= \sum_{i=1}^{n} \sum_{j=1}^{m} W_i^1 W_j^2 f(a_i, b_j)$$

where (a_i, b_j) are the (s,t) coordinates of the $(i,j)^{th}$ integration point (sampling point) at which the integrand $f(s,t)$ is to be evaluated, and $W_i^1 W_j^2$ is the corresponding weighting.

The employment of a numerical integration scheme to evaluate the stiffness matrix of a finite element requires a large amount of computational effort because the strain energy gradient must be computed at a number of sampling points. However, the probability of algebraic error occuring during program construction is considerably reduced and the incorporation of new elements within a program is relatively simple when a numerical rather than an explicit method is used

VII-3 GAUSS-LEGENDRE SCHEME, FOUR SIDED DOMAINS

A large number of methods have been suggested for selecting the location of the sampling points and the magnitude of the weightings [51,98], but for the purposes of finite element analysis the Gauss-Legendre scheme is considered the most suitable. This method requires the least number of evaluations of the integrand because the location and the corresponding weightings of these n points in any direction is selected to give the best representation of the function. A polynomial of degree $2n-1$ in this direction may be constructed and integrated exactly [51,98] provided the function $f(s,t)$ is analytic over the closed domain of integration, a condition which is satisfied for the entire domain of the QMC3 element, and across the subtriangles of the CQ12 element.

A (2 x 4) mesh of Gauss-Legendre sampling points was selected to integrate exactly the strain energy gradient of the linear elastic QMC3 element, which has a 2nd degree variation in the transverse direction and a 6th degree variation in the longitudinal direction.

The location and weighting of the sampling points associated with a range of Gauss-Legendre schemes which integrate polynomials of any prescribed degree exactly are listed in numerous texts [51, 98, 99, 117].

VII-4 HAMMER SCHEME, TRIANGULAR DOMAINS

The Gauss-Legendre scheme could also be applied to triangular domains but the limits of integration are now a function of the coordinate variables so it is preferred in this work to use the Hammer scheme [42] which is simple to apply and numerically efficient.

To evaluate exactly the stiffness of the quadrilateral CQ12 plate bending element, for which the curvatures may be discontinuous across subtriangle boundaries, it is necessary to compute the contribution of each subtriangular element separately. The 2nd degree scheme of Hammer [42], which has sampling points at the midsides of each subtriangle with equal weighting, a total of 12 points, was employed to evaluate the linear elastic stiffness of any constant thickness CQ12 element exactly.

The location and weighting of the sampling points associated with a range of Hammer schemes which integrate polynomials of 1st, 2nd, 3rd, 5th and 7th degree exactly have been presented in Tabular form by Hammer et al [42] and also by Zienkiewicz [117].

VII-5 TAPERED THICKNESS ELEMENTS

The strain energy gradient of a tapered thickness element, which is a linear function of the thickness for plane stress elements and a cubic function for plate bending elements,will have a variation of a larger degree than for a constant thickness element so a higher order numerical scheme may be required to perform the integration accurately. A 2 x 4 mesh of Gauss-Legendre sampling points will integrate exactly the strain energy gradient of the QMC3 element with a linear variation of the thickness, but 7 points of the Hammer scheme are required over each subtriangle of the CQ12 element (a total of 28 points) to integrate exactly the fifth degree variation of the strain energy gradient associated with a linear distribution of thickness across this element.

VII-6 DISTORTED RECTILINEAR ELEMENTS

If the QMC3 element is employed with a distorted quadrilateral geometry rather than a parallelogram form it may be necessary to use more sampling points to achieve exact integration of the strain energy gradient because the Jacobian [J] of the transformation to paramatric coordinates will now be a function of the position (s,t) at which the integrand is evaluated. The 2 x 4 Gauss-Legendre scheme was used for the mildly distorted elements employed in this work, but it is necessary to use a higher order scheme to avoid a loss of accuracy when integrating severely distorted elements.

VII-7 REDUCED ORDER OF INTEGRATION

The computantional effort required to evaluate the integrand at sufficient points to integrate the stiffness of a finite element exactly may become unacceptably large in some applications, such as when second order effects are included in the strain-displacement relationships. If certain conditions are satisfied [70, 118] it is permissible to use a reduced order of integration and still achieve convergence to the correct solution as the finite element mesh idealisation of the structure is refined. This is discussed in Chapter X-8.

CHAPTER VIII

TEMPERATURE EFFECTS

VIII-1 INTRODUCTION

Diurnal temperature fluctuations may induce significant stressing in bridge structures,which have often been designed with expansion joints to isolate axial deformations due to temperature expansion effects, but until recently the effects of vertical and transverse temperature gradients have largely been ignored.

Some recent examples of thermal distress, particularly in prestressed concrete box-girder bridges, have stimulated engineers to investigate the problem in more detail. Damage caused to the New Market Viaduct has created considerable interest within New Zealand in these thermal effects and has resulted in the modification of design codes [61, 62].

VIII-2 FINITE ELEMENT ANALYSIS OF THERMAL EFFECTS

VIII-2.1 Assumptions

The following assumptions are made in developing the finite element theory to enable thin planar shell elements to be used to study these thermal effects:

i) Kirchhoff's small deflection elastic thin plate theory is applicable

ii) All material properties are isotropic

iii) Young's modulus of elasticity E, Poisson's ratio ν, and the coefficient of thermal expansion α are selected to correspond to the average temperature of the element. These material properties were in fact assumed to be independent of temperature for the thermal analyses reported in this work.

VIII-2.2 Thermal strains

Consider a small element of an elastic isotropic continuum subjected to a temperature change T. If the length of this element is dL then under the action of a uniform temperature change T the element will expand to a new length $(1 + \alpha T)dL$. Thus the thermal strains in an unrestrained element, denoted by left superscript t, may be expressed as

$$
\begin{aligned}
{}^{t}e_{xx} &= \alpha T \\
{}^{t}e_{yy} &= \alpha T \qquad \ldots \quad \text{(VIII-1)} \\
{}^{t}e_{xy} &= 0
\end{aligned}
$$

Consider now an elastic isotropic continuum assembled from a number of equal sized elements subjected to a uniform temperature increase with no external restraints applied to the continuum boundaries. Each element will expand by an equal amount in each direction and since all elements are of equal size they will still form a continuous but expanded continuum, with no thermal stresses induced. However, if the temperature increase is not uniform each element would expand by a different amount, and consequently elastic strains must be induced so each element will restrain the distortion of its neighbouring elements to maintain compatibility.

The strains $\bar{e}_{xx}$, $\bar{e}_{yy}$, and $\bar{e}_{xy}$ at any point of a heated two dimensional continuum may therefore be thought of as consisting of two parts; i) the thermal strains ${}^{t}e_{xx}$ and ${}^{t}e_{yy}$ due to thermal expansion,

ii) the elastic strains $\bar{\varepsilon}_{xx}$, $\bar{\varepsilon}_{yy}$, and $\bar{\varepsilon}_{xy}$ which maintain the displacement continuity of the continuum when it is subjected to a nonuniform temperature distribution or boundary constraints

$$
\begin{aligned}
\bar{e}_{xx} &= \bar{\varepsilon}_{xx} + {}^{t}e_{xx} \\
\bar{e}_{yy} &= \bar{\varepsilon}_{yy} + {}^{t}e_{yy} \qquad \ldots \quad \text{(VIII-2)} \\
\bar{e}_{xy} &= \bar{\varepsilon}_{xy} + 0
\end{aligned}
$$

The structural action of a thin planar shell element may be conveniently divided into plane stress and plate bending components;

$$
\begin{aligned}
\bar{e}_{xx} &= e_{xx} + \chi_{xx} \cdot z \\
\bar{e}_{yy} &= e_{yy} + \chi_{yy} \cdot z \\
\bar{e}_{xy} &= e_{xy} + \chi_{xy} \cdot z
\end{aligned}
$$

where z is the distance of the point at which the strains are measured from the neutral axis, and e_{xx}, e_{yy}, e_{xy} and χ_{xx}, χ_{yy}, χ_{xy} are the membrane strains and bending curvatures respectively.

VIII-3 PLANE STRESS

The elastic component of the membrane strains, ε_{xx}, ε_{yy} and ε_{xy}, are related to the membrane stresses by Hooke's law for linear isothermal elasticity, and may be related to the total membrane strains and the thermal membrane strains from equations (VIII-1) and (VIII-2)

$$\varepsilon_{xx} = \frac{1}{E}(\sigma_{xx} - \nu\sigma_{yy}) = e_{xx} - \alpha T(x,y)$$

$$\varepsilon_{yy} = \frac{1}{E}(\sigma_{yy} - \nu\sigma_{xx}) = e_{yy} - \alpha T(x,y)$$

$$\varepsilon_{xy} = \frac{2(1+\nu)}{E}(\sigma_{xy}) = e_{xy} - 0$$

which upon rearranging yields

$$\begin{Bmatrix} \sigma_{xx} \\ \sigma_{yy} \\ \sigma_{xy} \end{Bmatrix} = \frac{E}{(1-\nu^2)} \begin{bmatrix} 1 & \nu & 0 \\ \nu & 1 & 0 \\ 0 & 0 & (1-\nu)/2 \end{bmatrix} \begin{Bmatrix} e_{xx} \\ e_{yy} \\ e_{xy} \end{Bmatrix} - \begin{Bmatrix} E\alpha T\ (1+\nu)/(1-\nu^2) \\ E\alpha T\ (1+\nu)/(1-\nu^2) \\ 0 \end{Bmatrix}$$

and may be expressed more concisely

$$\{\sigma\} = [D^{pl}]\{e\} + \{\phi^{pl}\}$$

where the superscript pl denotes plane stress action, distinct from superscript b which will be used to denote plate bending action. The vector $\{\phi^{pl}\}$ may be interpreted physically as the membrane stresses necessary to suppress thermal expansion so the total membrane strain is zero for a confined body

The generalised force - displacement relationship of an element may be defined from the principle of stationary potential energy; If thermal effects are isolated the applied nodal forces are identically zero.

$$\{R\}^e = \{0\} = \frac{\partial}{\partial\{\delta^e\}}\left[\int_{vol}\{e\}^T[D]\{e\}\,d\,vol - \int_{vol}\{e\}^T\{\phi^{pl}\}\,d\,vol\right]$$

$$= [K^{pl}]\{\delta^e\} - \{Q^{pl}\}$$

where $[K^{pl}] = \int_{vol}[B^{pl}]^T[D^{pl}][B^{pl}]\,d\,vol$ is the plane stress

component of the element stiffness matrix and the matrix $[B^{pl}]$ relates the element membrane strains to the nodal displacements

$$\{e\} = [B^{pl}]\{\delta^e\}$$

$\{Q^{pl}\} = \int_{vol} [B^{pl}]\{\phi^{pl}\}\, d\,vol$ represents the generalised thermal membrane forces applied to the element to produce thermal expansion, and was evaluated in this work by allocating an average temperature T_i to each node i and assuming a linear interpolation of the temperature within the element.

VIII-4 PLATE BENDING

The elastic component of the curvatures at a point in the plate are related to the bending moments as follows;

$$\chi_{xx} = \frac{12}{Et^3}(M_{xx} - \nu M_{yy})$$

$$\chi_{yy} = \frac{12}{Et^3}(M_{yy} - \nu M_{xx})$$

$$\chi_{xy} = \frac{24(1+\nu)}{Et^3}(M_{xy})$$

where t is the plate thickness.
The total curvatures may be expressed in terms of the thermal and elastic components as

$$\chi_{xx} = \frac{12}{Et^3}(M_{xx} - \nu M_{yy}) + \alpha[T^2(x,y) - T^1(x,y)]/t$$

$$\chi_{yy} = \frac{12}{Et^3}(M_{yy} - \nu M_{xx}) + \alpha[T^2(x,y) - T^1(x,y)]/t$$

$$\chi_{xy} = \frac{24(1+\nu)}{Et^3}(M_{xy}) + 0$$

where $T^2(x,y)$ and $T^1(x,y)$ are the temperatures at the top and bottom extreme fibres respectively. These equations may be rearranged to yield

$$\begin{Bmatrix} M_{xx} \\ M_{yy} \\ M_{xy} \end{Bmatrix} = \frac{Et^3}{12(1-\nu^2)} \begin{bmatrix} 1 & \nu & 0 \\ \nu & 1 & 0 \\ 0 & 0 & (1-\nu)/2 \end{bmatrix} \begin{Bmatrix} \chi_{xx} \\ \chi_{yy} \\ \chi_{xy} \end{Bmatrix} - \frac{\alpha Et^3(1+\nu)}{12(1-\nu^2)} \begin{Bmatrix} (T^2 - T^1)/t \\ (T^2 - T^1)/t \\ 0 \end{Bmatrix}$$

and may be expressed more concisely

$$\{M\} = [D^b]\{\chi\} + \{\phi^b\}$$

The vector $\{\phi^b\}$ can be interpreted physically as the generalised moments and forces necessary to suppress thermal bending so the total curvatures are zero for a plate element with built-in edges.

The generalised force - displacement equations of a plate bending element may be defined from the principle of stationary potential energy, considering the flexural contributions to the strain energy;

$$\{R\}^e = \{0\} = \frac{\partial}{\partial\{\delta^e\}} \left[\int_{Area} \{\chi\}^T [D^b]\{\chi\} \, d\,Area - \int_{Area} \{\chi\}^T \{\phi^b\} \, d\,Area \right]$$

$$\text{i.e.,} \quad [K^b]\{\delta^e\} = \{Q^b\}$$

The effect of the integration normal to the plane of the plate has been incorporated within the constitutive matrix relating moment and curvature.

$[K^b] = \int_{Area} \{B^b\}^T [D^b] [B^b] \, d\,Area$ is the plate bending component of the element stiffness matrix and the matrix $[B^b]$ relates the element curvatures to the nodal displacements

$$\{\chi^b\} = [B^b]\{\delta^e\}$$

$\{Q^b\} = \int_{Area} [B^b]^T \{\phi^b\} \, d\,Area$ represents the generalised thermal plate bending forces applied to the element to produce thermal curvature, and was evaluated in this work by allocating a temperature difference $T^2(x,y) - T^1(x,y)$ to each node and assuming a linear interpolation of the temperature difference within the element. A more complex distribution of temperature could be incorporated within each element but this is not justifiable here because the cubic displacement

function of the CQ12 plate bending element will be associated with only a linear distribution of curvature within each element.

VIII-5 SOLUTION PROCEDURE

The first step in the solution procedure is to assemble the thermal forces $\{Q\}$ and the structural stiffness matrix $[K]$ according to the procedure described in Chapter IV. The generalised displacements $\{\delta\}$ are computed by solving the system of linear simultaneous equations

$$[K]\ \{\delta\} = \{Q\}$$

and may then be used to calculate the elastic components of stress and moment, which in turn must be added to the thermal components of stress and moment to obtain the total element stresses and moments

$$\begin{Bmatrix} \sigma \\ M \end{Bmatrix}^e = \begin{bmatrix} [D^{pl}] & \cdot \\ \cdot & [D^b] \end{bmatrix} \begin{Bmatrix} \delta^{pl} \\ \delta^b \end{Bmatrix} + \begin{Bmatrix} \phi^{pl} \\ \phi^b \end{Bmatrix}$$

The procedure for including thermal effects within beam elements is similar to that described here for a planar thin shell element and has been formulated by Przemieniecki [81].

VIII-6 NUMERICAL EXAMPLE

The simply supported single cell box-girder bridge illustrated in Fig. VIII-1 was subjected to a range of vertical temperature gradients and analysed using a finite element idealisation with six QMC3/CQ12 elements along the span, one element down the depth of the webs, and the transverse distribution of nodes defined in Fig. VIII-1. The following material properties were assumed, independent of temperature;
$E = 35.0$ GPa , $\alpha = 10.8 \times 10^{-6}/°C$, $\nu = 0.15$.

To test the performance of this finite element approach for analysing thermal effects a number of vertical temperature gradients, shown in Fig. VIII-2, were considered;

Case A) A constant temperature block.

Case B) A linear temperature distribution from a maximum at the top of the deck slab to zero at the bottom of the deck slab.

Case C1) A bilinear idealisation of a continuous sixth power distribution.

Case C2) This distribution was reanalysed using two elements down the depth of the web to enable a trilinear idealisation of the sixth power curve.

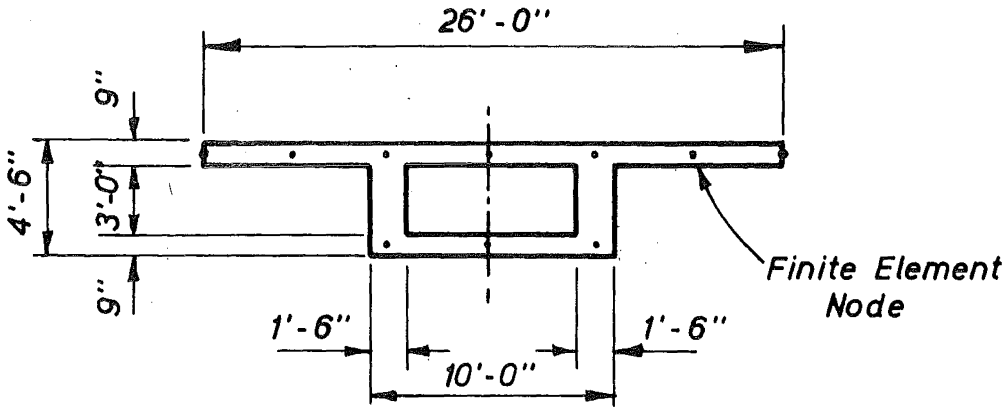

FIGURE VIII-1 TRANSVERSE NODAL POSITIONS FOR BOX-GIRDER

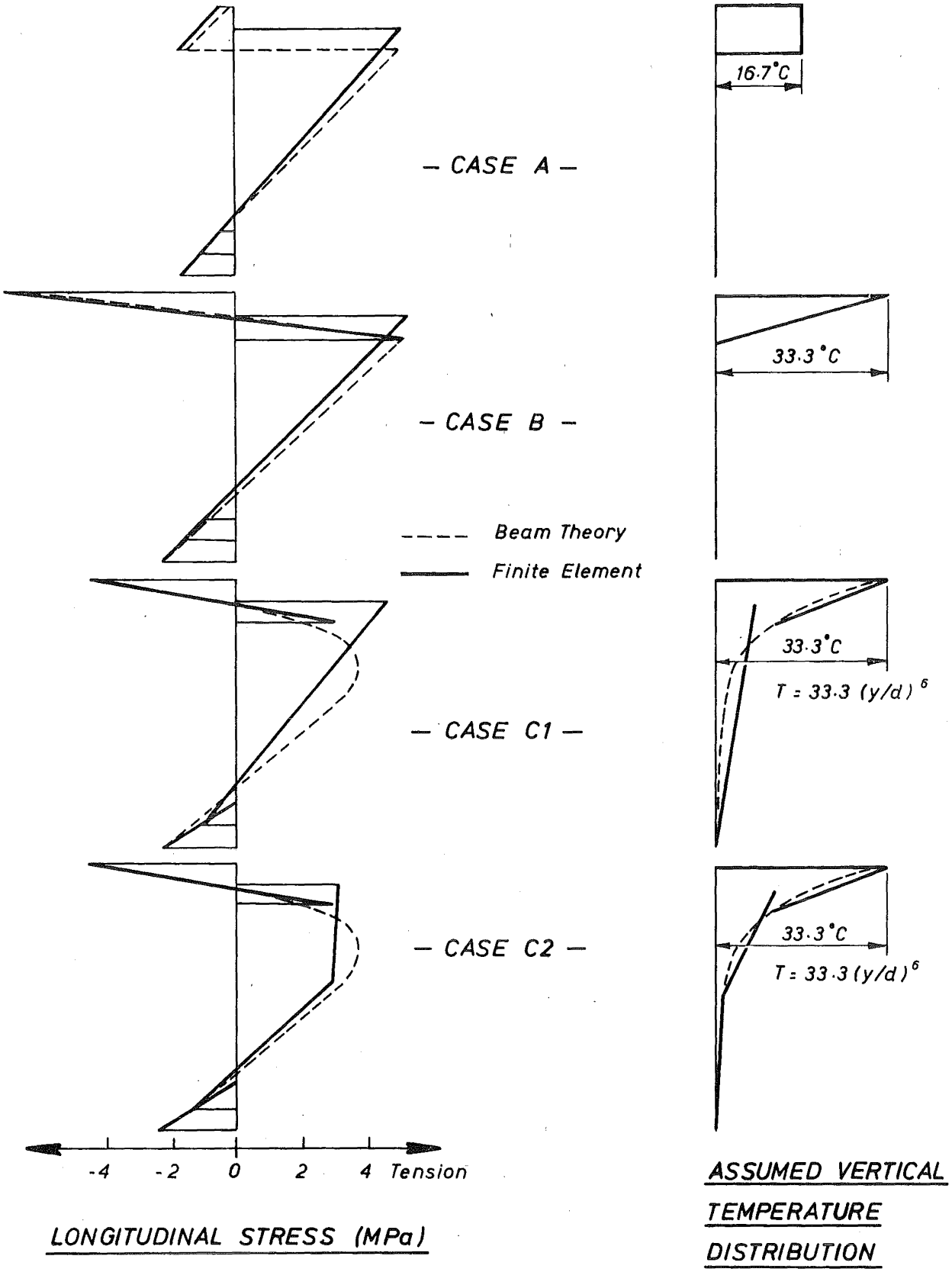

FIGURE VIII-2 COMPARISON OF LONGITUDINAL STRESS DISTRIBUTIONS

A surface temperature rise of 33.3°C (60°F) above the soffit temperature was assumed in all cases except for Case A where a temperature of 16.7°C (30°F) was adopted. The New Zealand Ministry of Works and Development design brief [62] specifies a temperature rise of 30°C with a sixth power distribution, which measurements indicate to be a realistic temperature distribution for New Zealand conditions [11, 77].

i) Longitudinal Stresses

The longitudinal stresses computed from these idealised temperature distributions are plotted in Fig. VIII-2 along with the results calculated by Priestley [77] using simple beam theory based upon an equivalent 'I' beam and considering the design temperature distributions. Agreement between the two theories is generally within 12% except that the use of the bilinear approximation of the sixth power temperature distribution (Case C1) results in some larger discrepancies between the web tension stresses. However, the accuracy of the computed tension stress distribution is increased when two elements are employed down the depth of the web to enable a trilinear idealisation of the temperature distribution.

ii) Transverse Stresses

The transverse stresses computed at the midspan sections A - A, B - B, and C - C (see Fig. VIII-3) from the QMC3/CQ12 finite element idealisation are plotted in Fig. VIII-4 for the Case B temperature distribution, and are compared with the results obtained from a plane strain finite element analysis [77] using the mesh of QLC2 elements shown in Fig. VIII-3, and the results calculated from simple beam theory considering one-way transverse behaviour [77]. The stresses computed from the three theories generally agree to within 17% at the extreme fibres of the deck slab (section A - A) and the webs (section B - B), but the nonlinear distribution of transverse stress across the web section is not modelled accurately by the simple beam theory or by the thin plate finite element idealisation. Also, the finite element analyses predict a small average tension in the deck slab where a small average compression is expected, and vice versa in the soffit slab. These discrepancies are due to the coarse mesh idealisation of the deck and soffit slabs.

VIII-7 CONCLUSIONS

Although a very coarse finite element idealisation was used to analyse the box-girder example, results for both longitudinal and transverse stresses are in close agreement with the solutions obtained from an

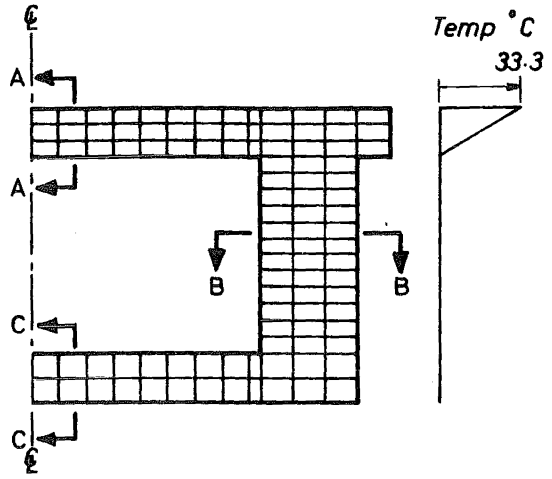

FIGURE VIII-3 PLANE STRAIN FINITE ELEMENT IDEALISATION

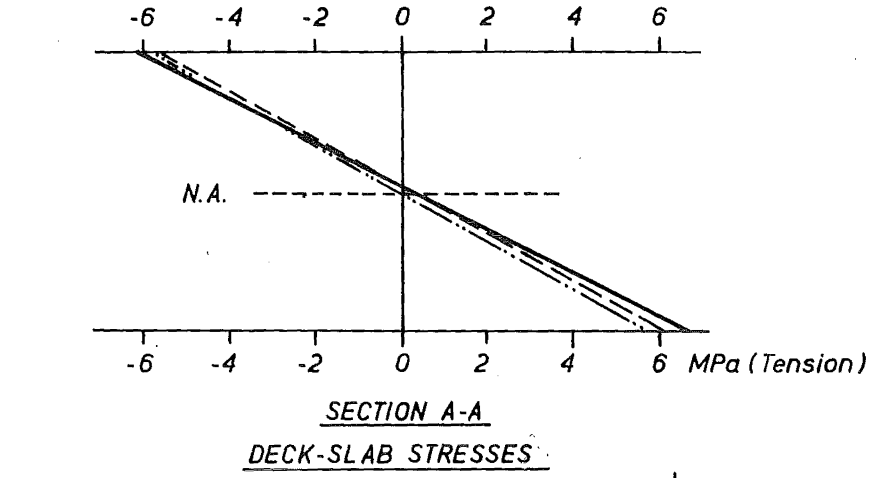

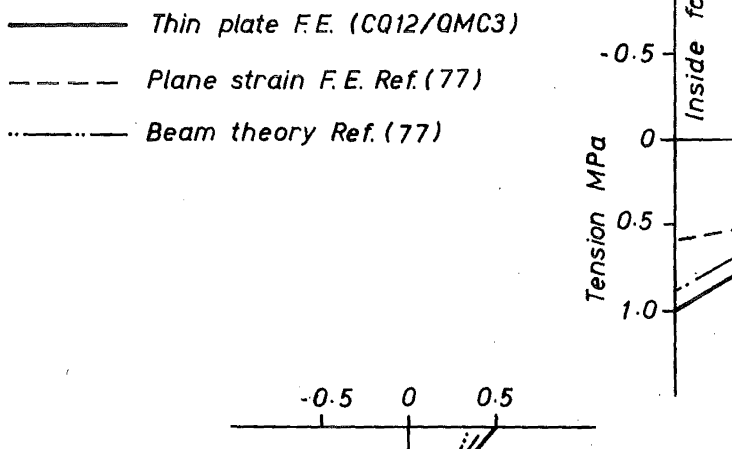

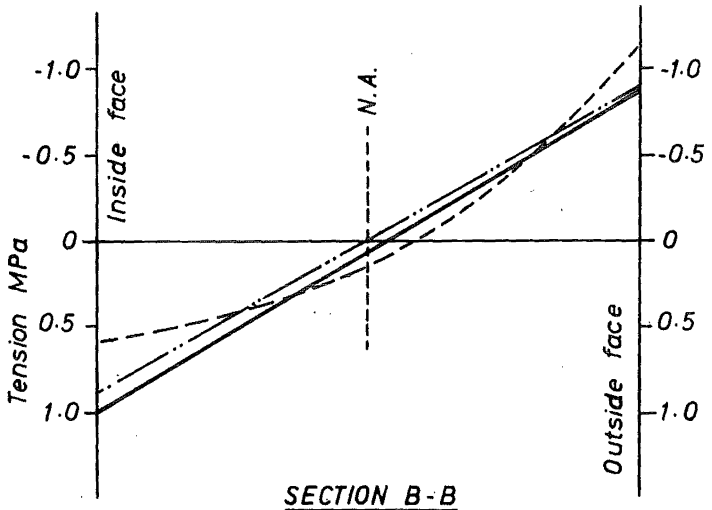

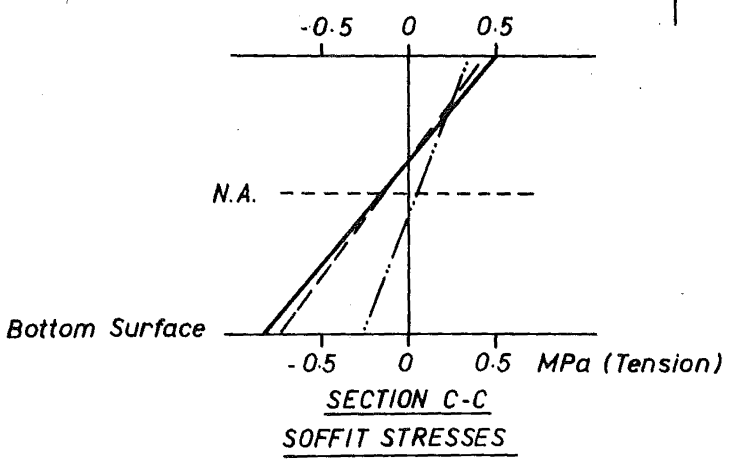

FIGURE VIII-4 COMPARISON OF TRANSVERSE STRESSES

analytical method and an alternative numerical method. It should be noted that for simply supported single span structures subjected to a sixth power vertical temperature gradient, a one or a two element idealisation of the web behaviour is associated with a computed distribution of web stresses for which the magnitude and location of the peak tension stresses is not accurate to more than 20%. However, this discrepancy is considerably reduced for continuous multispan bridges because the influence of the internal supports will impose an additional linear distribution of longitudinal stress down the depth of each cross-section.

CHAPTER IX

LINEAR ELASTIC ANALYSES OF BRIDGE SUPERSTRUCTURES

IX-1 INTRODUCTION

A number of straight, skew, and curved box-girder bridges of complex cross-section were analysed using the finite element method. Results are compared with those obtained from experimental model studies, measurement of full scale performance, and alternative numerical solutions. Finite element results are also presented for a trifurcating multi-span box-girder, subjected separately to prestress, dead and live loads, and a vertical temperature gradient.

The main objective was to analyse an extensive range of bridge structures in order to test the performance of the finite element method and the associated theory, and thus to assist with the coordinated aim [76] of devising improved design methods for box-girder bridges. Priestley [77, 79] has noted that several concrete box-girders designed in New Zealand have exhibited complex behaviour and suggests observation of the following actions;

i) the transverse variation of longitudinal and transverse stress under eccentric loading.

ii) the response to realistic vertical temperature gradients.

The following bridges were selected as the subject for an extensive programme of research into the structural behaviour of box-girder bridges, and the performance of the finite element method in simulating this behaviour:-

a) Straight bridges.

Structures A and B are small scale "araldite" models of straight, single span, prismatic box-girders with one and two single cell spines respectively. Both structures have heavy kerbs and significant transverse haunching of the deck slab, thus providing a test of the suitability of beam elements to represent kerbs, and tapered thickness thin plate elements to represent the haunched region of the deck slabs. The construction of the models and the measurement of the experimental results from these structures was performed by Priestley [79, 80] at the Central Laboratories of the Ministry of Works and Development, for the Road Research Unit of the New Zealand National Roads Board.

b) Skew bridges.

(i) A skew solid slab bridge, (ii) a skew cellular bridge and (iii) a two span skew box-girder were analysed to test the performance of the finite elements when distorted to skew parallelograms. Results are compared with those obtained from small scale experimental model studies and alternative numerical solutions.

c) Curved bridges.

(i) A curved four span solid slab structure, (ii) a curved four cell box-girder and (iii) a curved single cell continuous box-girder were analysed and results compared with those obtained from small scale experimental model studies and alternative numerical solutions.

d) Bowen Street Overpass.

This multi-cellular two span nonprismatic box-girder was analysed and results compared with those obtained from measuring the performance of the full scale structure.

e) Cumberland Street Overpass.

This curved multi-span box-girder, which trifurcates at one end and bifurcates at the other, was analysed with the additional purpose of providing information to the designers (Dunedin City Council).

IX-2 STRUCTURE A, SINGLE CELL BOX-GIRDER

IX-2.1 Description of model

Structure A is a 1:24 scale model of a straight, single span box-girder bridge and was cast from a filled epoxy resin [79] using a machined steel mould, constructed to produce a box section with dimensions corresponding to within $\pm$ 0.2 mm of those specified in Fig. IX-2.1. The elastic material properties were measured as Young's modulus E = 6.03 GPa, and Poisson's ratio ν = 0.344. The structure was simply supported over a span of 1270 mm, with 50 mm thick diaphragms incorporated at the support sections.

IX-2.2 Loading conditions

Finite element analyses of the model were performed for two loading conditions:-

i) A central wheel load of 333.6 N distributed over a 21.2 x 8.3 mm contact area. This wheel load was simulated as a system of statically equivalent nodal forces, distributed to the central and two adjacent

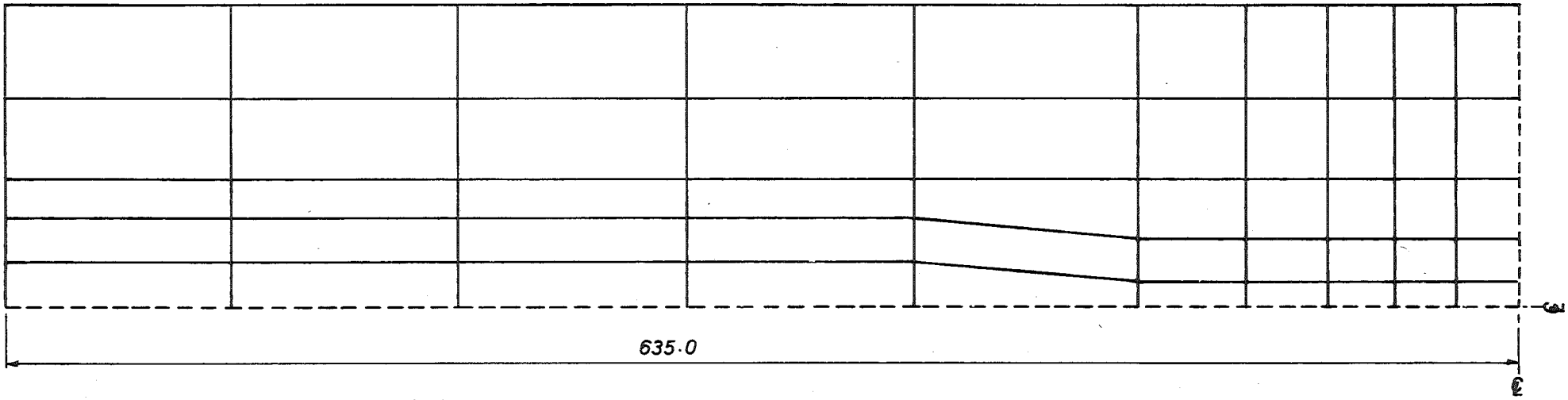

(a) FINITE ELEMENT MESH FOR DECK SLAB

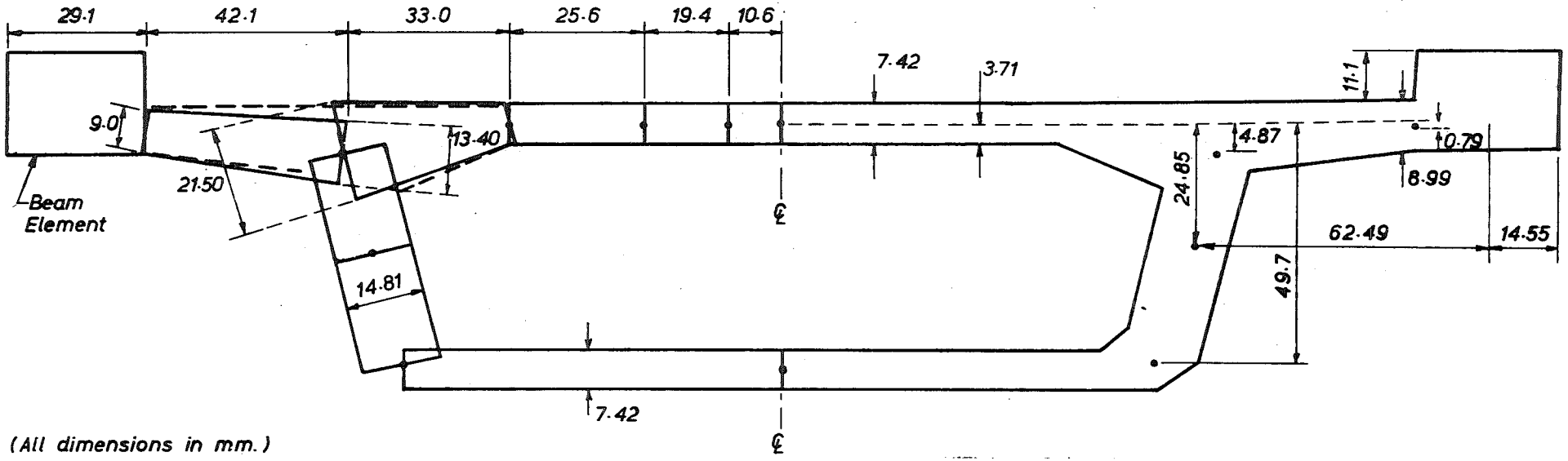

(b) FINITE ELEMENT IDEALISATION OF CROSS-SECTION

FIGURE IX-2.1 IDEALISATION OF STRUCTURE A

nodes (10.6 mm apart) along the midspan section.

ii) A wheel load of 667.2 N on the midspan section at the intersection of one web centreline and the middle surface of the deck slab.

IX-2.3 Finite element idealisation

Only one quarter of the bridge was analysed, making use of symmetry about the transverse and longitudinal centrelines, and dividing the eccentric wheel load (ii) into symmetric and antisymmetric components.

Kerbs were represented as beam elements, connected to the section via eccentric nodes, and the haunched region of the deck slab as tapered elements of linearly varying thickness.

The inclusion of four-sided diaphragm elements was not possible because a different number of nodes were used across the deck and soffit slabs. The diaphragms were therefore assumed to be rigid in their own plane, and completely flexible out of their plane.

Fig. IX-2.1a shows the 10 x 5 mesh of finite elements used to represent the deck slab, and the refinement of the mesh in the region of the central wheel load. (An alternative method of mesh grading is demonstrated in Section IX-9.)

The finite element idealisation of the cross-section is illustrated in Fig. IX-2.1b. The cross-sectional area of the idealised section is 4.8% greater than, and the moment of inertia about the transverse axis is 0.8% smaller than that of the experimental model. The cross-sectional area of the section is only significant for prestress loading so the error of the idealised section area is of no consequence for the load cases considered here.

IX-2.4 Comparison of results

Theoretical and experimental deflections, longitudinal stresses, and transverse stresses are compared across the central transverse section. The agreement is excellent with only a few small local discrepencies:-

i) Central wheel load of 333.6 N.

Finite element and experimental results are plotted in Fig. IX-2.2. Deflections and stresses across the deck, web, and soffit slabs generally agree to within 5%, except for the longitudinal stresses along the bottom of the soffit slab where the finite element stresses are 9.5% larger. Priestley [79] has deduced that the central three strain gauges along the bottom of the soffit were recording strain magnitudes that are 7% too

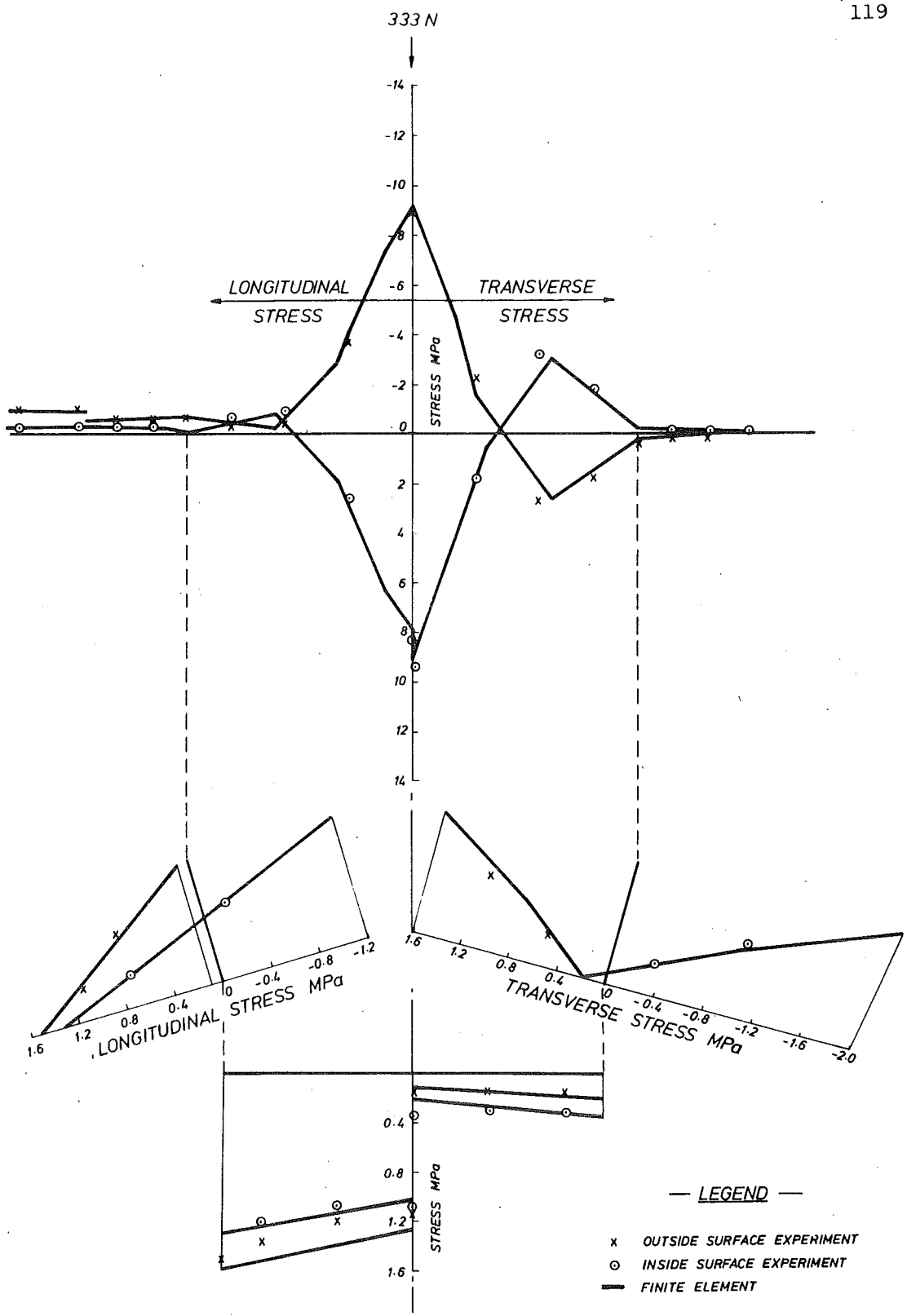

(a) STRESS DISTRIBUTIONS

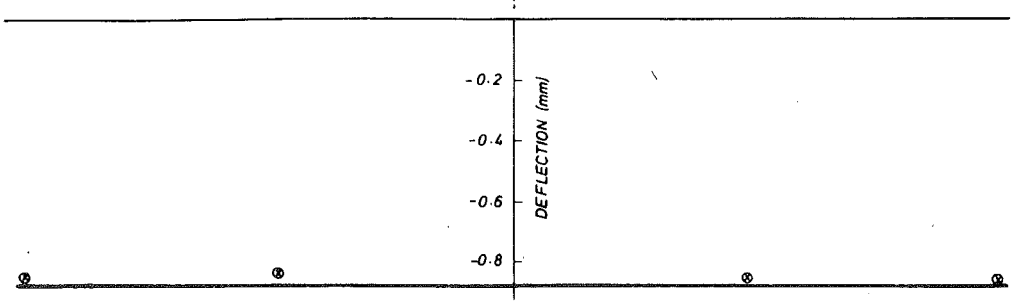

(b) DEFLECTION PROFILE

FIGURE IX-2.2 CENTRAL WHEEL LOAD

small, explaining the discrepancy here. A study of the experimentally measured stresses from prestress loading [79] indicated that, apart from these gauges, the error in measurement was within the expected experimental accuracy of $\pm$ 0.02 MPa.

ii) Wheel load of 667.2 N above one web.

Finite element and experimentally measured deflection and longitudinal stress distributions across the midspan section are plotted in Fig. IX-2.3, and the distribution of transverse stress in Fig. IX-2.4. Longitudinal stresses, transverse stresses, and deflections generally agree to within 5% across the deck and soffit slabs, and to within 15% down the webs. The larger discrepancy of web stress occurs because the thick haunches induce a complex distribution of longitudinal stress in the webs which requires a larger number of QMC3/CQ12 elements down the depth of the webs for an accurate representation. Also, there is a larger discrepancy of:-

a) the longitudinal stress along the top of the deck slab directly under the load, where the computed value is 24% larger than that measured experimentally, and down the inside surface of the top half of the loaded web. This local error is partially caused by the approximate simulation of the web/deck slab intersection, as discussed in Section I-4.3, and was found to be reduced when three elements were employed down the depth of the webs.

b) the maximum theoretical longitudinal stress along the bottom of the soffit slab, under the loaded web, is 12% larger than the experimentally measured stress. A discrepancy of this magnitude is also evident from results obtained using the finite strip and folded plate methods [79] with twice the number of elements (four) employed across the soffit slab.

There is also some additional discrepancy of transverse stress in these two regions, but it is less pronounced than for the longitudinal stresses.

IX-2.5 Discussion of structural behaviour

The following features are evident from the midspan stress distributions:-

i) Central wheel load;

a) The maximum deck slab bending stresses are of similar magnitude in both the longitudinal and transverse directions.

b) The loading has a tendency to rotate the top of the webs inward about their longitudinal axis, resulting in a net transverse compression

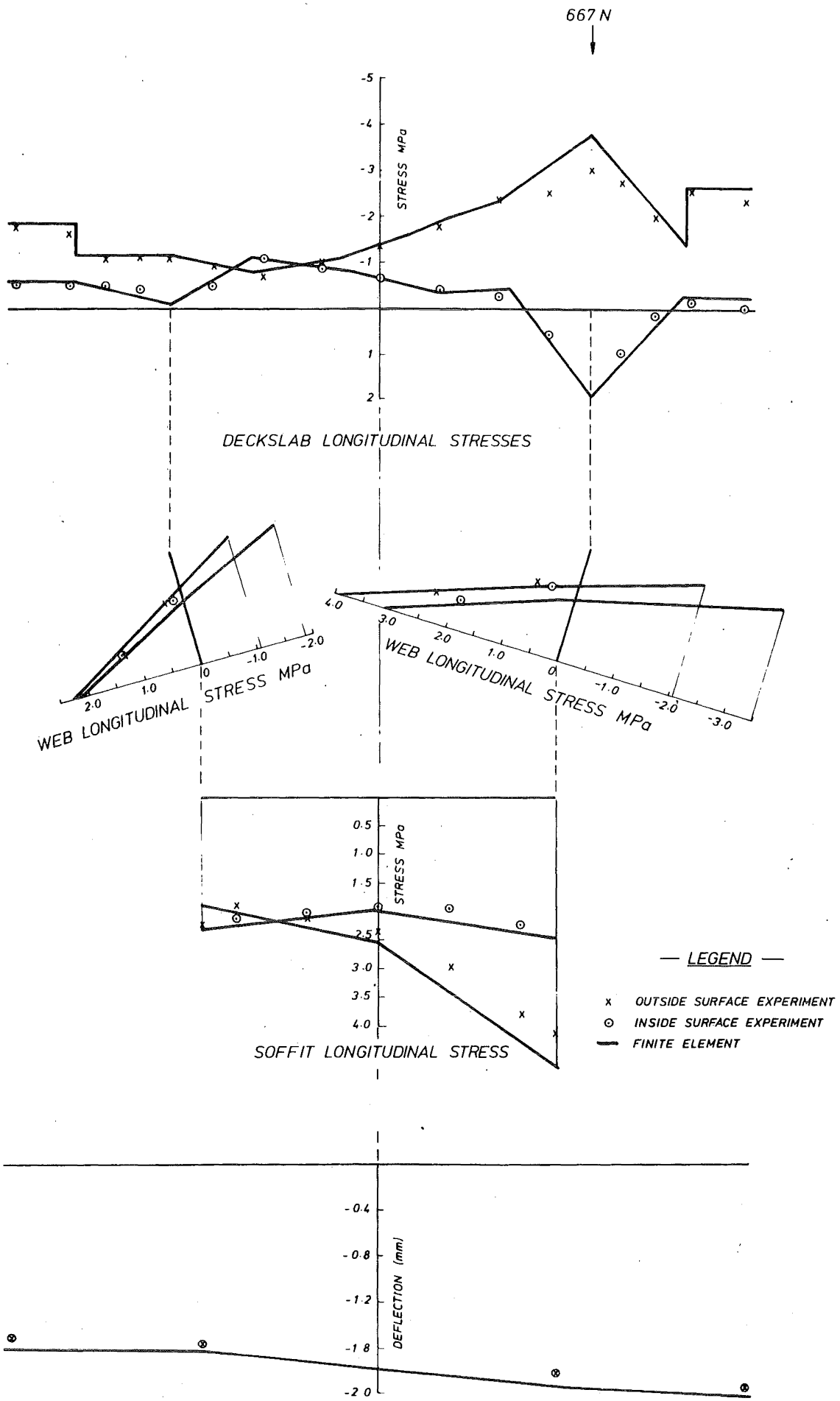

FIGURE IX-2.3 LONGITUDINAL STRESSES AND DEFLECTIONS LOAD ABOVE WEB

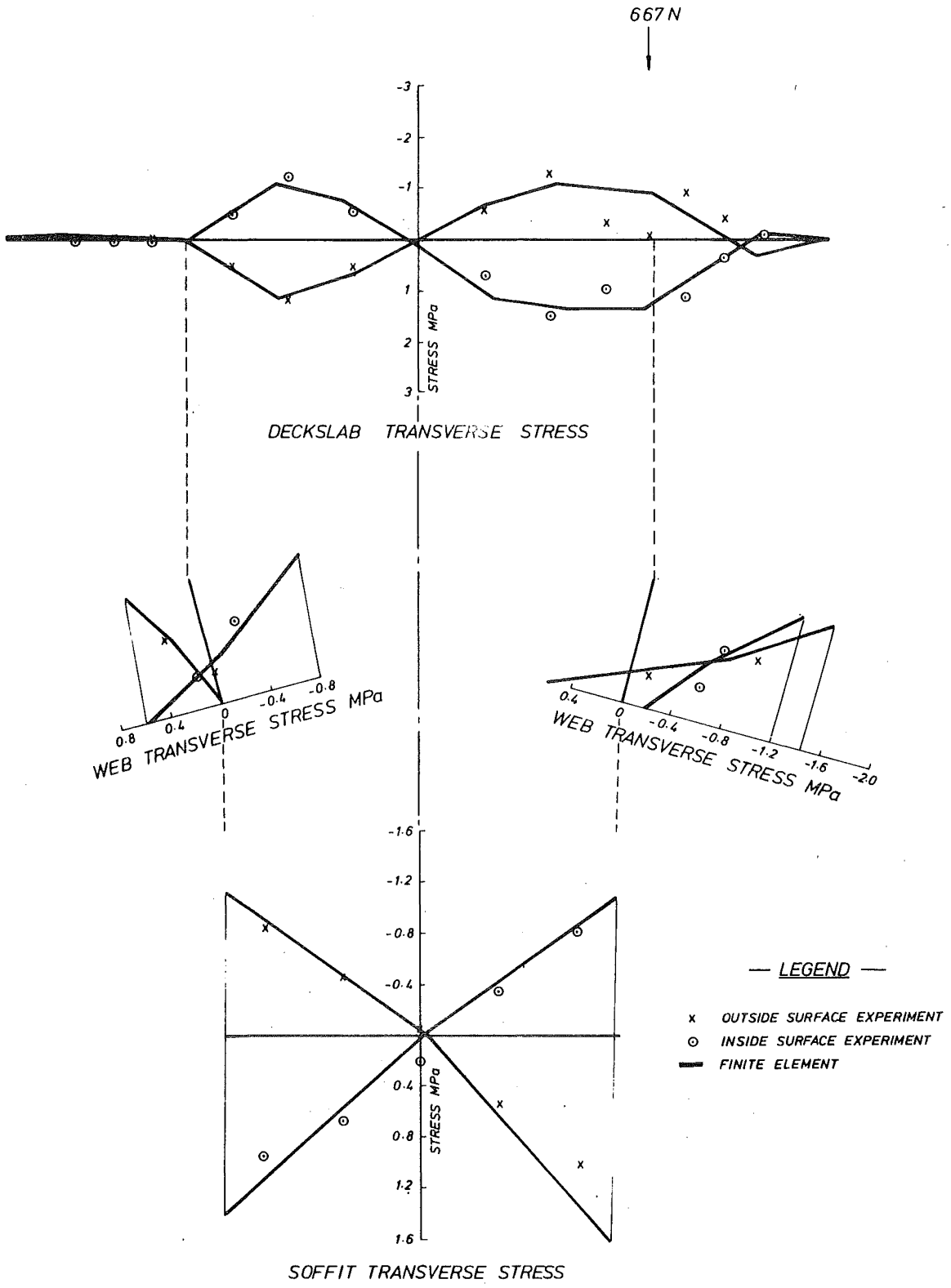

FIGURE IX-2.4 TRANSVERSE STRESSES
LOAD ABOVE WEB

in the deck slab and a net tension in the soffit slab.

c) The longitudinal stress at the top of the webs varies from 0.3 MPa on the outside to -1.3MPa on the inside of the web. This difference is due to Poisson's ratio influence from the transverse stresses and was reduced by 50% when a Poisson ratio of 0.15, corresponding to a concrete structure, was assumed.

d) A substantial shear lag effect is evident across the soffit slab, with longitudinal stresses at the centre being 25% lower than at the base of the webs.

ii) Wheel load above web;

a) The maximum transverse distortional stresses occur over the region where the deck slab begins to haunch (1.3 MPa), and at the ends of the soffit slab (1.25 MPa).

b) The maximum longitudinal warping stresses occur at the web/soffit slab intersection (0.7 MPa).

c) A shear lag effect from the symmetric component of the loading is evident across the deck and soffit slabs.

IX-3 STRUCTURE B, TWIN CELL BOX-GIRDER

IX-3.1 Description of model

Structure B is a 1:24 scale model of a straight, single span, twin spine box-girder bridge [80], which was cast from a filled epoxy resin using the same mould as for Structure A. The two single cell spines were connected via a cantilever deck slab to form the section described in Fig. IX-3.1.

The span, support conditions, and material properties are the same as for Structure A.

IX-3.2 Loading conditions

Finite element analyses of the model were performed for three loading conditions:-

i) A central wheel load of 333.6 N distributed over a 21.2 x 8.3 mm contact area: This wheel load was simulated as a system of statically equivalent nodal forces, distributed to the central and two adjacent nodes (10.6 mm apart) across the midspan section.

ii) A wheel load of 667.2 N on the midspan section at the intersection of one inside web and the middle surface of the deck slab.

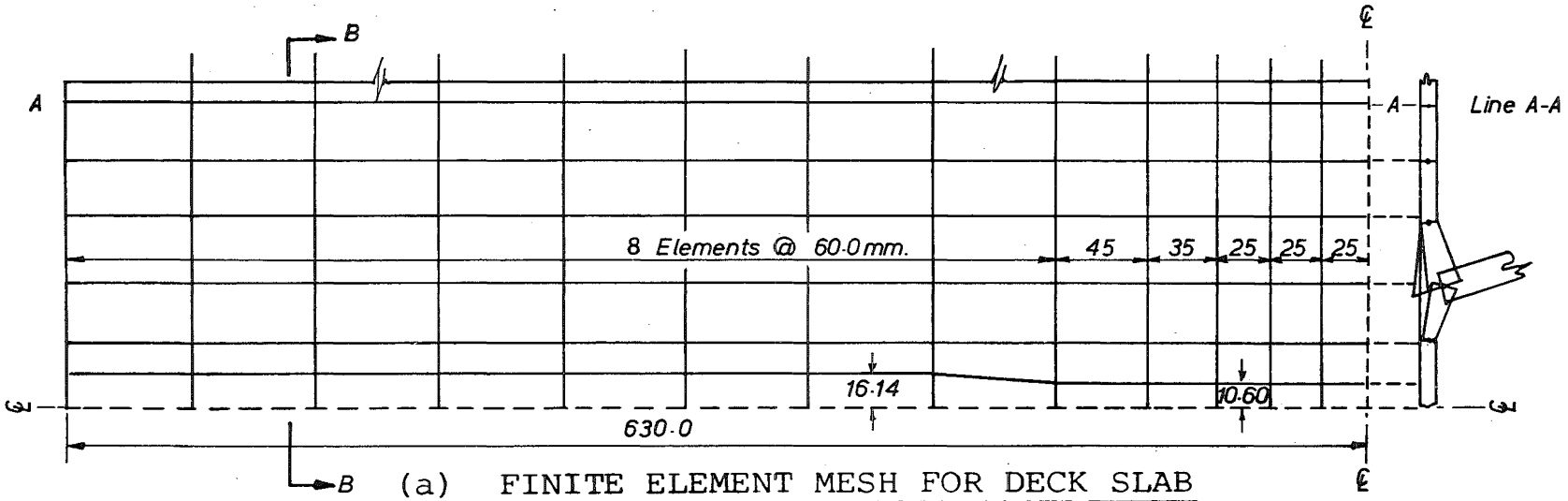

(a) FINITE ELEMENT MESH FOR DECK SLAB

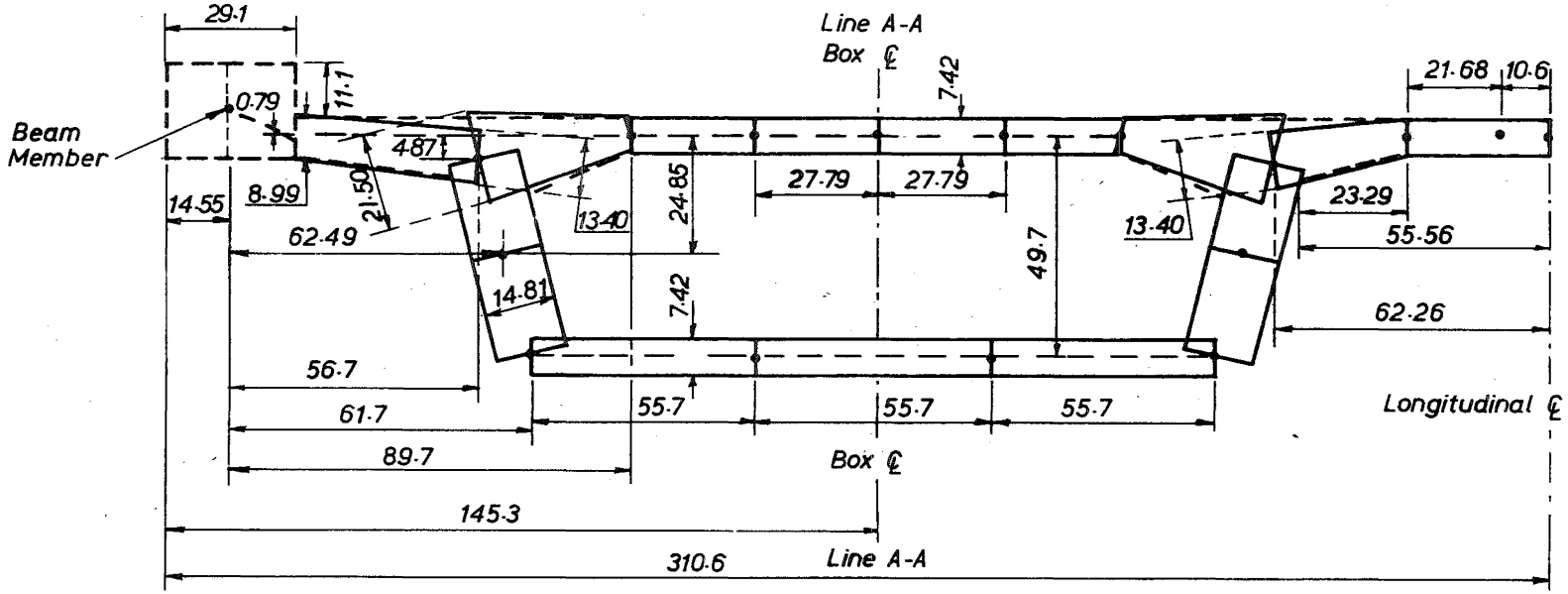

SECTION B-B (All dimensions in mm.)

(b) FINITE ELEMENT IDEALISATION OF CROSS SECTION

iii) A wheel load of 667.2 N on the midspan section at the intersection of one outside web and the middle surface of the deck slab.

IX-3.3 Finite element idealisation

Figure IX-3.1 shows; a) the finite element idealisation of the cross-section, which is based on the procedure used to model Structure A and b) the element mesh used to represent the deck slab. Thirteen elements were used along the half-span, compared with ten for Structure A. The cross-sectional area of the idealised section is 4.8% greater than, and the moment of inertia about the transverse axis is 0.8% smaller than that of the experimental model. The 4.8% error in the cross-sectional area of the idealised section does not affect the structural behaviour for the load cases considered here.

IX-3.4 Comparison of results

The agreement between theoretical and experimental results is excellent with only a few small local discrepancies. The experimental accuracy was estimated to be better than $\pm$ 0.04 MPa [80]. This estimation is based on symmetry checks of the stresses resulting from prestress load.

Theoretical and experimental deflections, longitudinal stresses, and transverse stresses across the midspan section are plotted in Figures IX-3.2 to IX-3.6 for the three loading conditions. Deflections and stresses across the deck and soffit slabs generally agree to within 5% and web stresses agree to within 15% apart from the following exceptions:-

i) Central wheel load of 333.6 N.

The longitudinal stresses (see Fig. IX-3.2) at the bottom of the soffit under the inside webs, where the finite element solution has overestimated the peak stress by 14%. Similar discrepancies are evident under the loaded webs for load cases ii) and iii), where errors of 10% and 6% occur respectively, and also from both load cases applied to Structure A.

ii) Wheel load of 667.2 N above inside web.

The longitudinal stress (see Fig. IX-3.3) and the transverse stresses (see Fig. IX-3.4) down the loaded web: The finite element solution predicts an additional compression of approximately -1.0 MPa down the inside surface of this web.

iii) Wheel load of 667.2 N above outside web.

The longitudinal stress (see Fig. IX-3.5) is overestimated by -1.0 MPa down the inside of the loaded web, also a 50% discrepancy is evident between the computed and measured transverse stresses down the

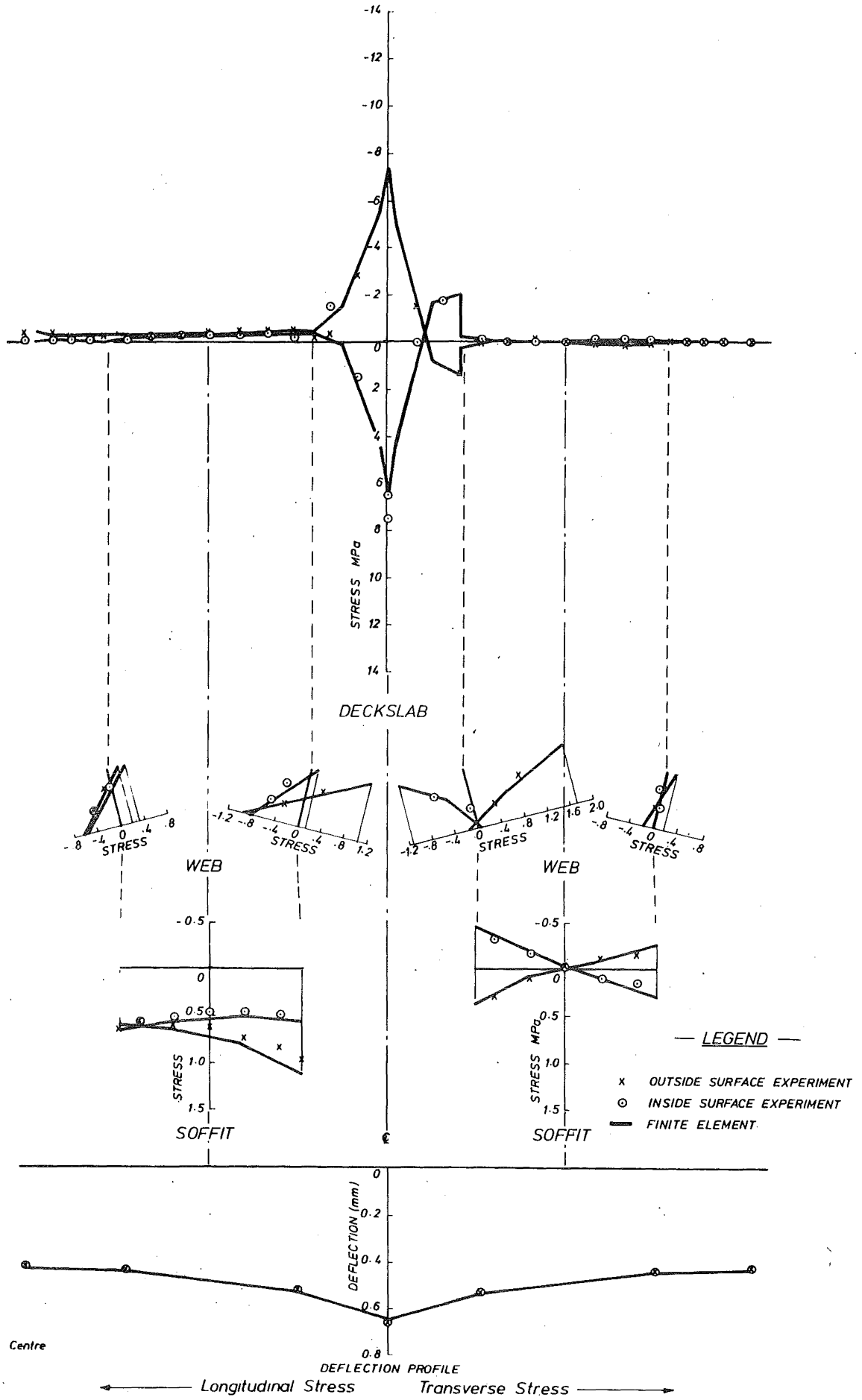

FIGURE IX-3.2 CENTRAL WHEEL LOAD

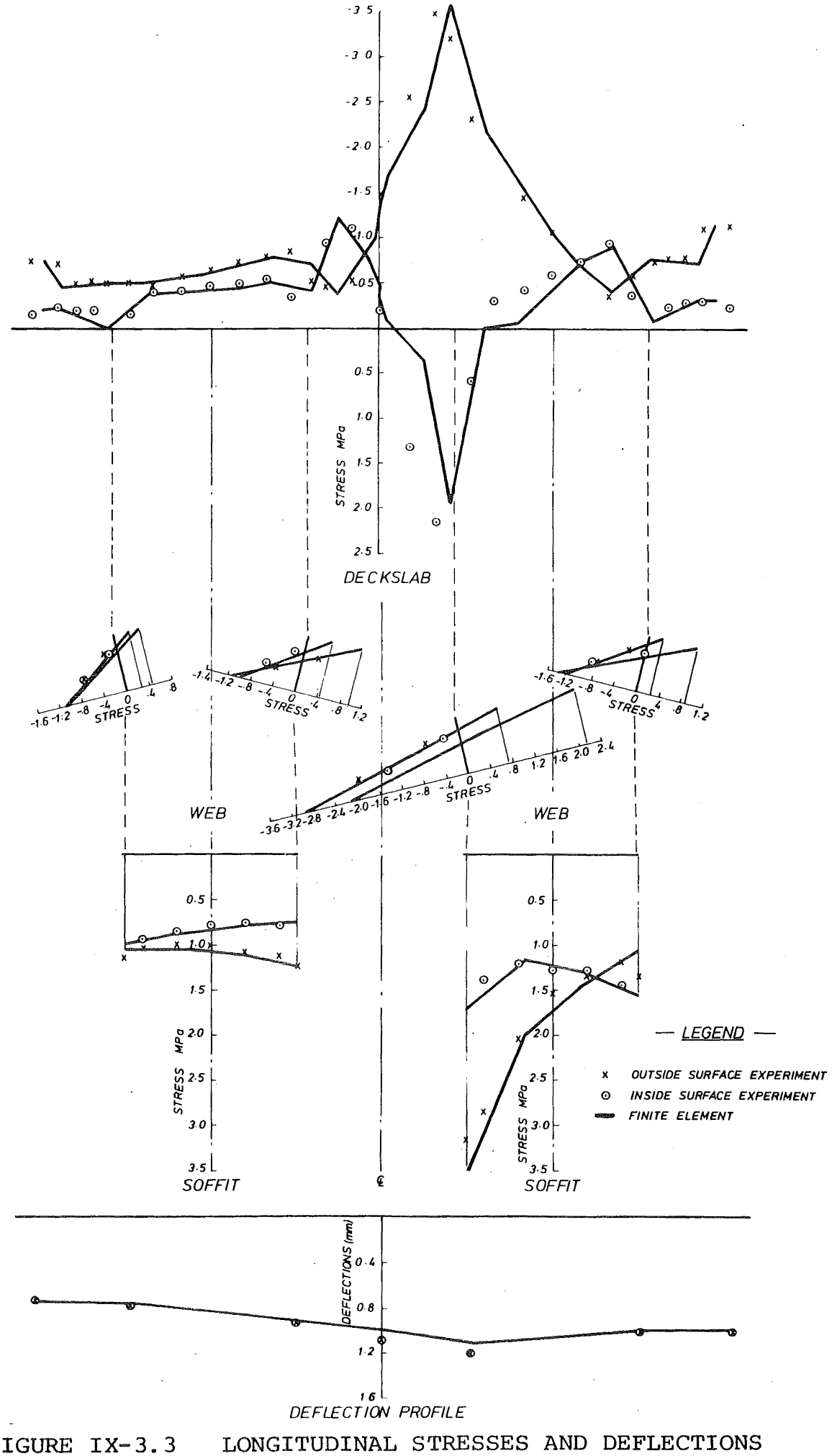

FIGURE IX-3.3 LONGITUDINAL STRESSES AND DEFLECTIONS WHEEL LOAD OVER INNER WEB

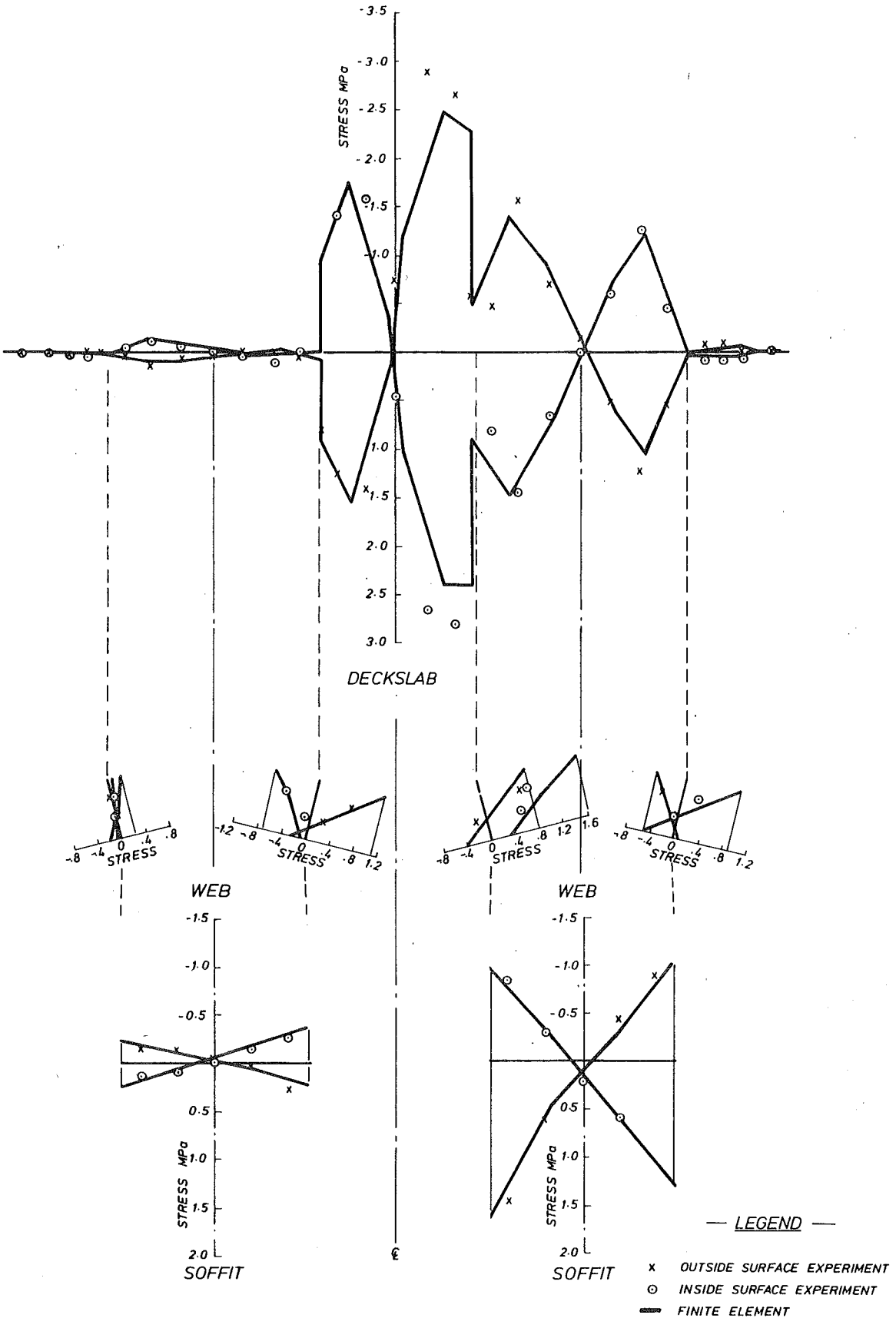

FIGURE IX-3.4 TRANSVERSE STRESSES
WHEEL LOAD OVER INNER WEB

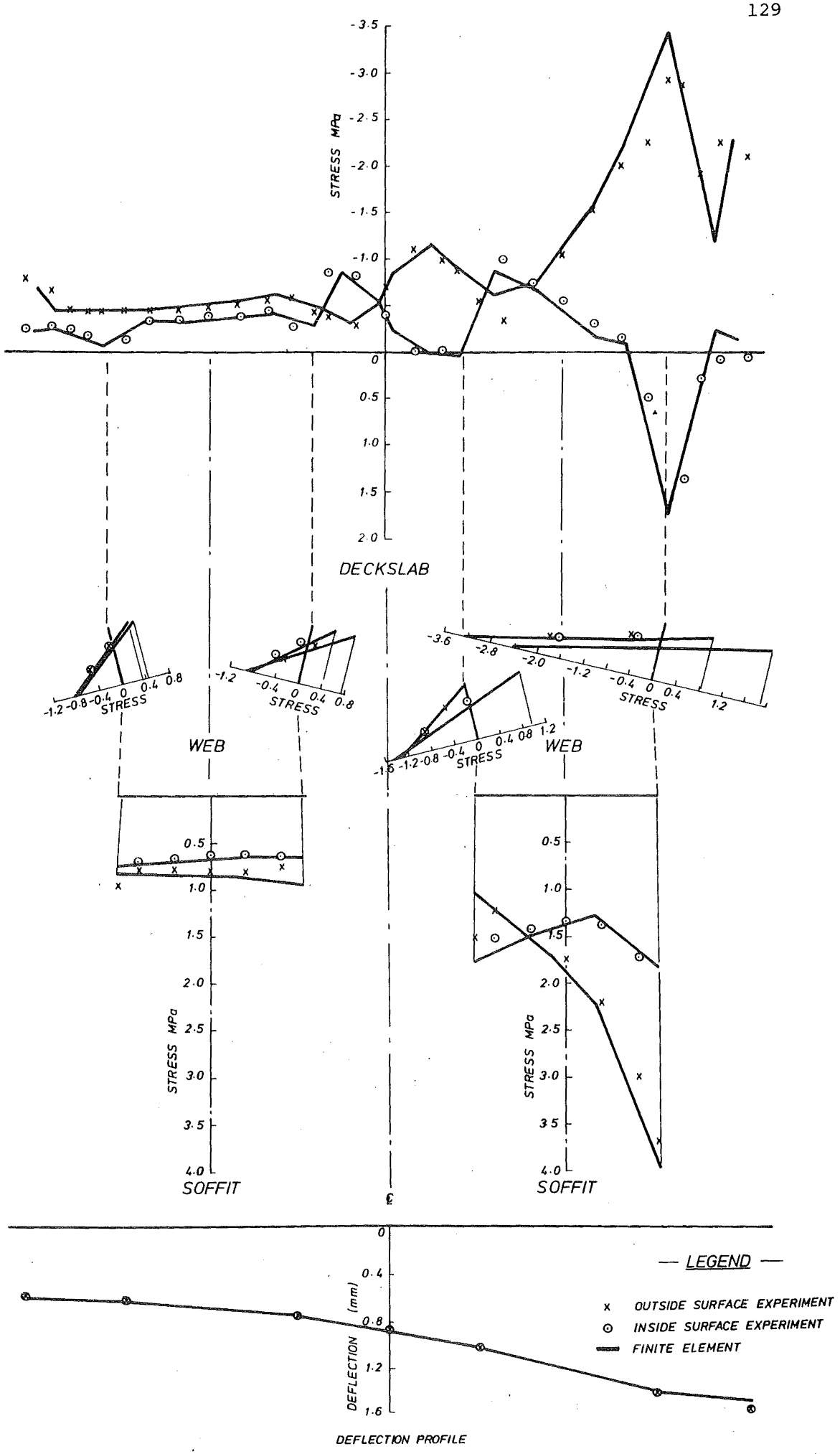

FIGURE IX-3.5 LONGITUDINAL STRESSES AND DEFLECTIONS WHEEL LOAD OVER OUTER WEB

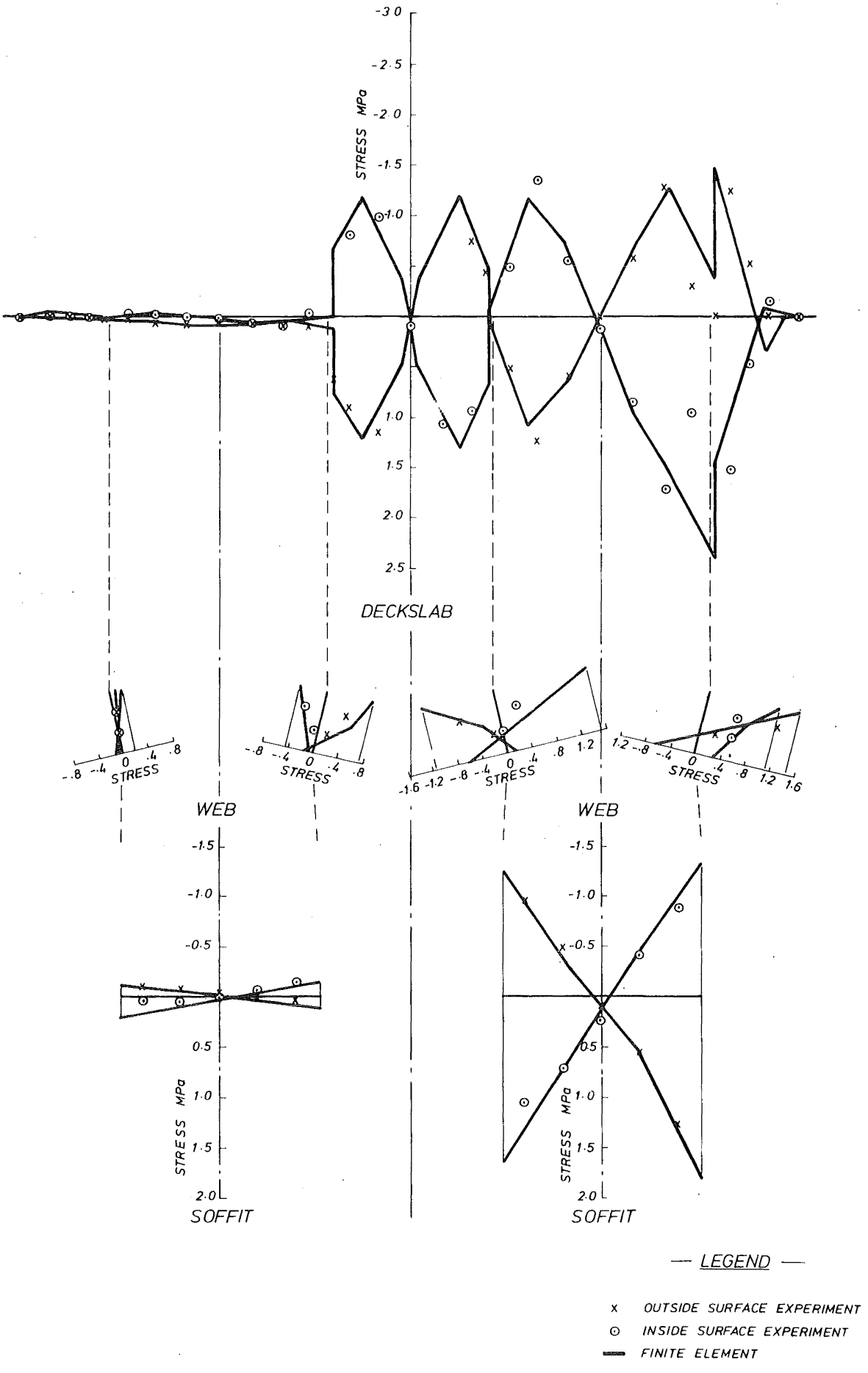

FIGURE IX-3.6 TRANSVERSE STRESSES
WHEEL LOAD OVER OUTER WEB

inside of this web. A similar error was obtained from the finite element analysis of Structure A subjected to a wheel load above one web.

IX-3.5 Discussion of structural behaviour

The following features are evident from the midspan stress distributions.

i) Central wheel load.

a) The maximum deckslab bending stresses are of similar magnitude in the longitudinal and transverse directions.

b) The longitudinal stresses at the top of the inside webs show considerable variation across the web thickness. This difference is due to Poisson's ratio influence from the transverse stresses.

ii) Wheel load above inside web.

a) The maximum transverse distortional stresses occur over the central deckslab between the cellular spines (2.13 MPa), and at the ends of the soffit slabs under the inside webs (0.9 MPa).

b) The maximum longitudinal warping stresses occur at the intersections of the soffit slabs and the inside webs (1.0 MPa).

iii) Wheel load above outside web.

a) The maximum transverse distortional stresses occur over the central deckslab between the spines (1.5 MPa), and at the ends of the soffit slabs under the outside webs (0.85 MPa).

b) The maximum longitudinal warping stresses occur at the ends of the soffit slabs under the outside webs (1.0 MPa).

The maximum transverse distortional stress is located across the central deckslab for both eccentric loading cases, and is 41.5% larger with the load over the inner web than with the load over the outer web. This larger distortional stress could be reduced by incorporating a soffit slab between the two cellular spines, converting the structure into a three cell, single spine bridge.

IX-4 ROBINSON SKEW SLAB, [86]

IX-4.1 Model description

A 45° skew solid slab; simply supported along two opposite edges and free along the other two edges, was loaded transversely at point A, shown in Fig. IX-4.1. The following dimensions and material properties were measured [86]; Slab thickness = 0.25 in (6.35 mm), $E = 30 \times 10^6$ lb/in^2 (20.9 GPa), and $\nu = 0.3$.

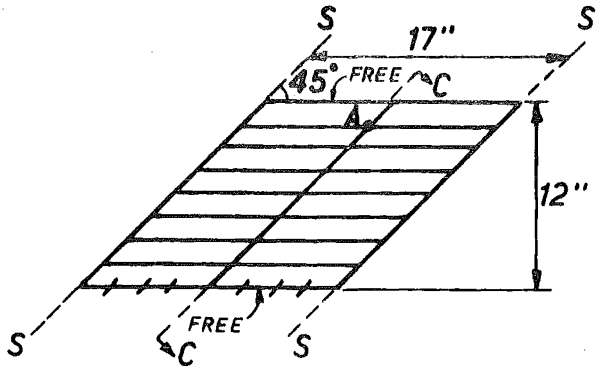

FIGURE IX-4.1 SKEW SLAB

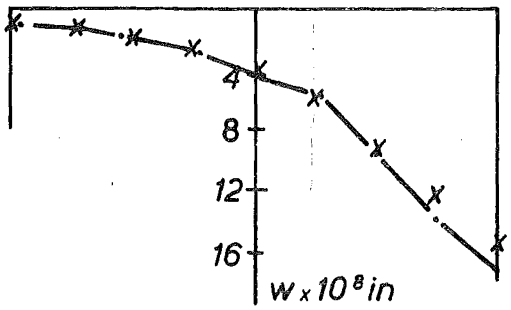

FIGURE IX-4.2 DEFLECTION ACROSS LINE C-C

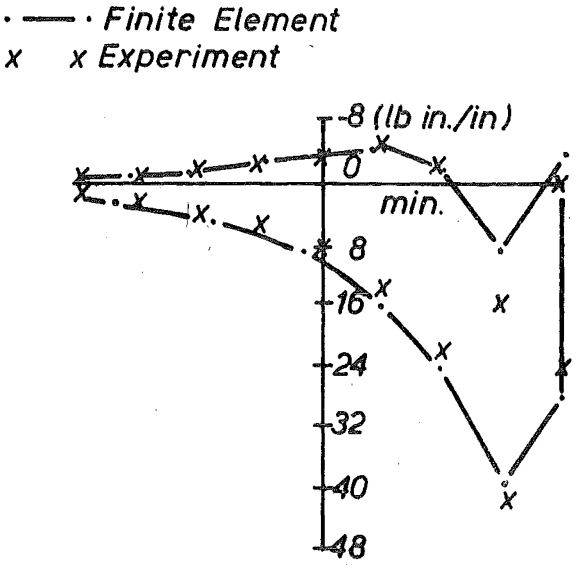

FIGURE IX-4.3 PRINCIPAL BENDING MOMENTS ACROSS LINE C-C

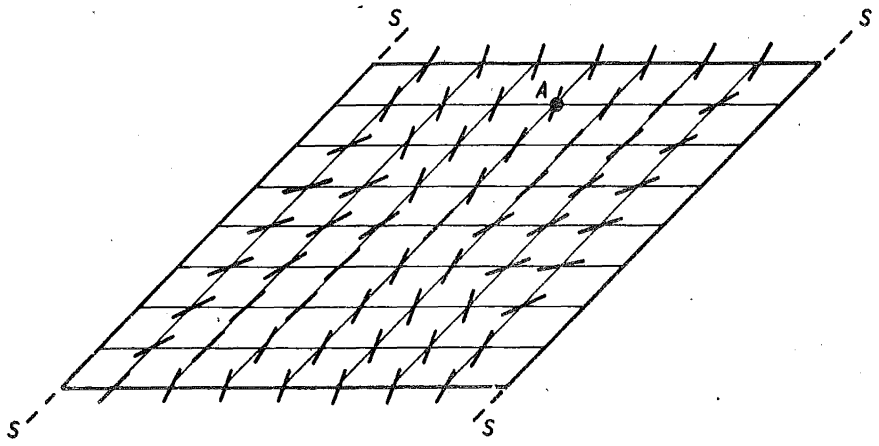

FIGURE IX-4.4 AXES OF MAXIMUM PRINCIPAL BENDING MOMENTS

IX-4.2 Comparison of results

The distributions of deflection and principal bending moment across the midspan line C - C (see Fig. IX-4.1), computed with an 8 x 8 mesh of CQ12 plate bending elements, are plotted in Figures IX-4.2 and IX-4.3 respectively, along with those measured experimentally by Robinson [86].

The theoretical deflections agree to within 5% of those measured experimentally, except in the region under the load where the maximum theoretical deflection is 10.4% larger. A similar discrepancy is evident from the results obtained by Zienkiewicz [115] using a 4 x 8 mesh of triangular elements to simulate the slab.

The agreement between theoretical and experimental principal bending moments is within 7% except for the peak values; The maximum principal bending moment is underestimated by only 7%, but the theoretical minimum principal bending moment is 38% smaller than the measured value. This discrepancy arises because the 8 x 8 mesh idealisation is not sufficiently accurate to represent the stress concentrations under the load.

The computed axes of maximum principal bending moment are plotted in Fig. IX-4.4. The moment axes generally run parallel to the lines of support but near the centre of the two lines of support the axes tend to run parallel to the diagonal between the two acute angled corners.

IX-5 SAWKO AND COPE SKEW CELLULAR BRIDGE [88]

IX-5.1 Model description

Fig. IX-5.1 shows the geometry of a 30° skew cellular concrete bridge model which was reinforced transversely and prestressed longitudinally [88]. The structure has five equal sized cells and is simply supported over a single span.

The concrete material properties were measured as; $E = 27.7$ GPa, $\nu = 0.15$.

IX-5.2 Loading conditions

Two load cases were considered, with point loads of 10 kN applied at points 1 and 2 respectively (see Fig. IX-5.1).

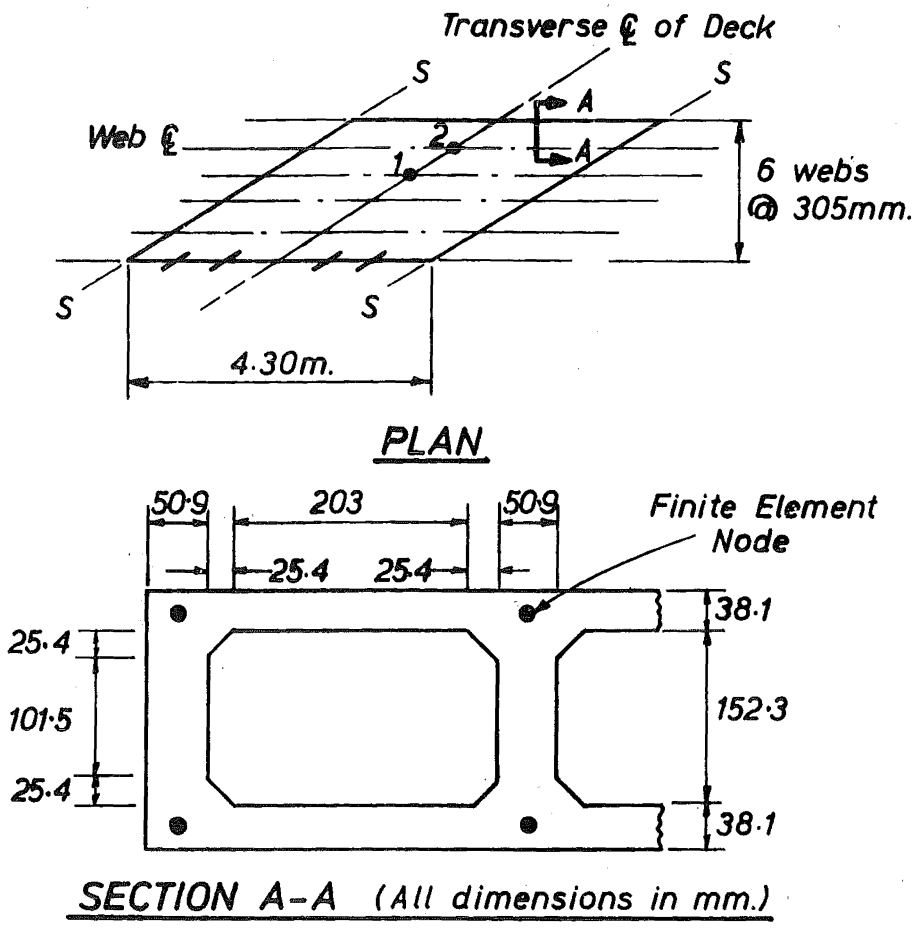

FIGURE IX-5.1 DETAILS OF SKEW CELLULAR BRIDGE MODEL

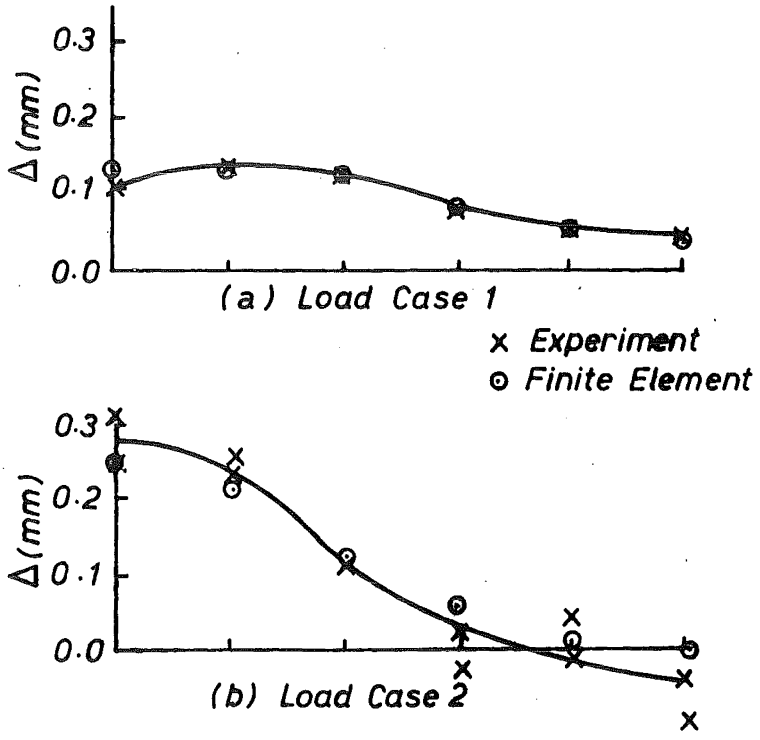

FIGURE IX-5.2 DEFLECTION ACROSS TRANSVERSE CENTRELINE

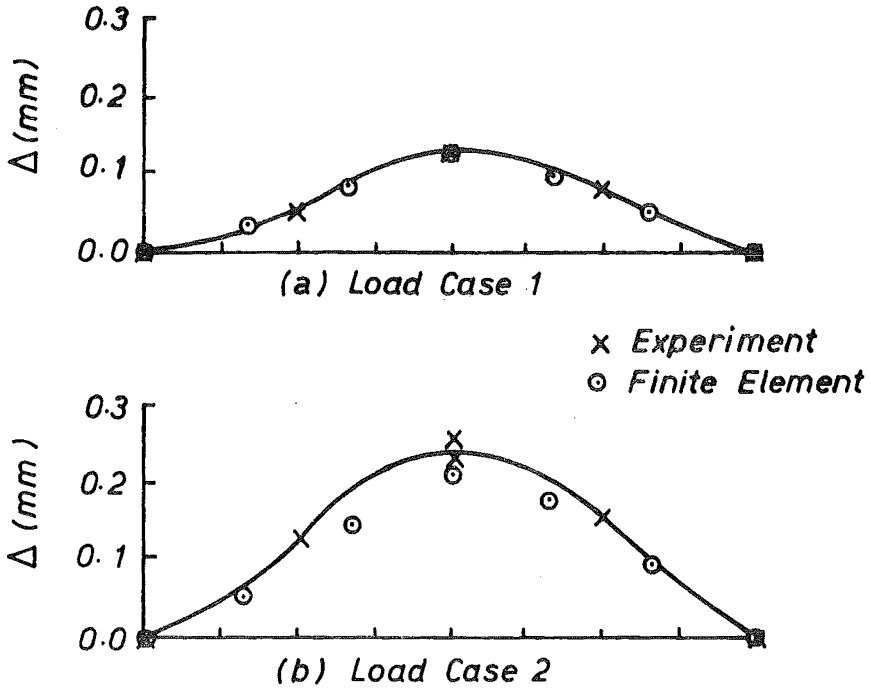

FIGURE IX-5.3 DEFLECTIONS ALONG LOADED RIB

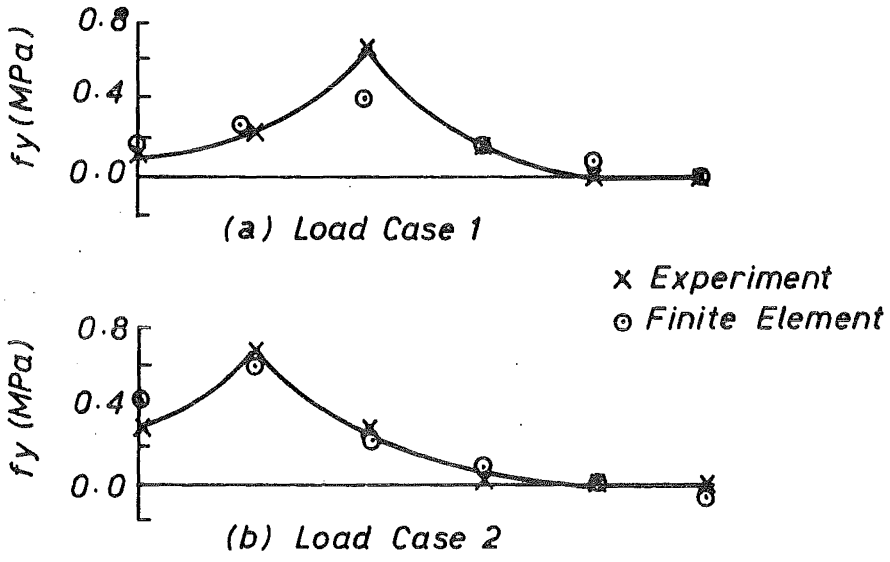

FIGURE IX-5.4 LONGITUDINAL STRESSES ACROSS TRANSVERSE CENTRELINE

IX-5.3 Finite element idealisation

The coarse (6 x 5) mesh of finite elements, illustrated in Fig. IX-5.1, with six elements of equal length along the span, five elements of the same width as the cells across the deck and soffit slabs, and one element down the depth of the webs, was employed to model the structural behaviour of the bridge. A finer mesh idealisation was not possible because of bandwidth limitations incorporated within the program. The fillets at the top and bottom of the webs were neglected.

IX-5.4 Comparison of results

The computed deflections and longitudinal stresses are compared with those measured experimentally by Sawko and Cope [88]. The experimental and theoretical deflection profiles across the transverse centreline, and along the loaded web, are shown in Figures IX-5.2 and IX-5.3 respectively. Agreement is generally within 7% for load case 1, except for local discrepancies at the free edges; the maximum computed deflection of the free edge nearest the load is 18% too large, and the maximum deflection of the other free edge is underestimated by 20%. A large variation between experimental deflections at the top and the bottom of the web was measured for load case 2, with a maximum variation of 22% of the peak deflection. The experimental deflections were therefore considered as a 'best fit' smooth curve through the measured points for the purpose of comparison. The theoretical deflection at the centre of the free edge nearest the load is 10% smaller than the average measured value. Also, the finite element solution does not predict uplift along the other free edge. These discrepancies are also evident from finite element solutions computed by Sawko and Cope [88] using a finer (14 x 10) mesh of elements.

The experimental and theoretical extreme - fibre longitudinal stresses across the transverse centreline are plotted in Fig. IX-5.4. Agreement is generally within 11% of the maximum stress, except that the peak stress is underestimated by 34% for load case 1, and the stress along the free edge nearest the load is overestimated by 37% for load case 2. The coarse mesh used for the finite element analysis does not permit an accurate representation of the large stress concentrations present in the region of the loads, but similar discrepancies are also evident from the solution computed by Sawko and Cope [88], using a 14 x 10 mesh of nonconforming finite elements, from which the peak stresses are overestimated.

IX-6 SISODIYA, CHEUNG AND GHALI SKEW BOX-GIRDER [94]

IX-6.1 Model description

A perspex model of a two span 40° skew single cell box-girder bridge [94], simply supported on piers under the two webs, without diaphragms, was analysed with a load P applied at point 1, as shown in Fig. IX-6.1.

IX-6.2 Finite element idealisation

The skew box-girder was analysed using two meshes of QMC3/CQ12 finite elements;

i) Mesh A

Ten elements were employed along the length of the bridge (see Fig. IX-6.1d), and the cross-section idealised as shown in Fig. IX-6.1b. The haunched deck and soffit slabs were modelled with uniform average thickness elements.

ii) Mesh B

Twenty elements were employed along the bridge, halving the elements of Mesh A, and the idealisation of the cross-section was improved by using two elements down the depth of the webs, incorporating nodes along the longitudinal centreline of the deck and soffit slabs, and using tapered thickness elements to represent the haunched deck and soffit slabs.

The 'hinged' piers were modelled with beam elements of negligible flexural stiffness.

Finite element results are also presented from a finite element analysis performed by Sisodiya, Cheung and Ghali [94], who used the nonconforming QLC3/ACM element with the Mesh A idealisation.

IX-6.3 Comparison of results

The deflections, longitudinal strains and pier reactions, measured experimentally and computed from the finite element models, are listed in Table IX-6.)

The theoretical deflections, predicted from the two Mesh A idealisations agree to within 4.5% at points 1 and 2 (see Fig. IX-6.1d) and to within 12.4% at points 3 and 4. However, when the finite element mesh is refined convergence to the experimental deflections is not evident. The maximum theoretical deflection at point 1 is 12.2% smaller, and the theoretical deflection at point 3 is 76.5% larger than that measured experimentally. This discrepancy may be due to imperfections in the

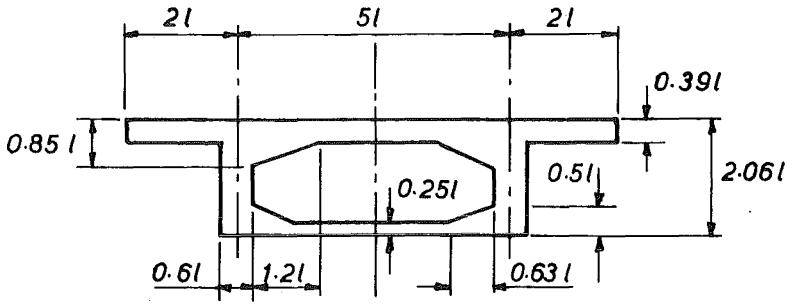

(a) CROSS SECTION

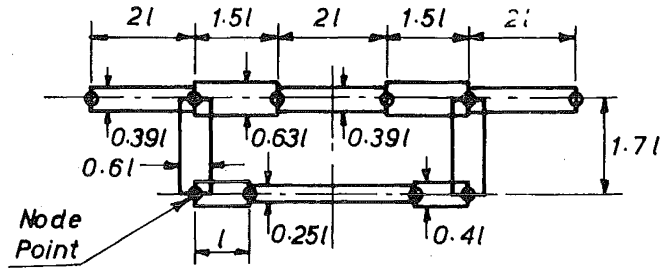

(b) MESH A IDEALISATION OF SECTION A-A

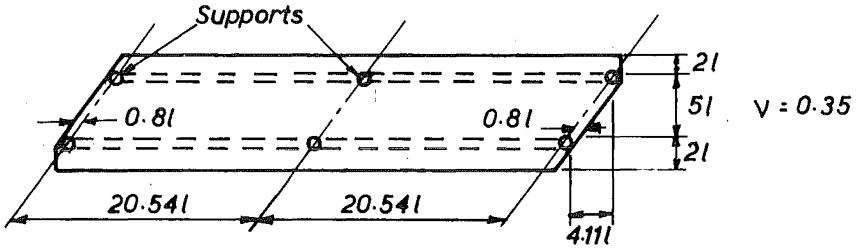

(c) PLAN OF EXPERIMENTAL MODEL

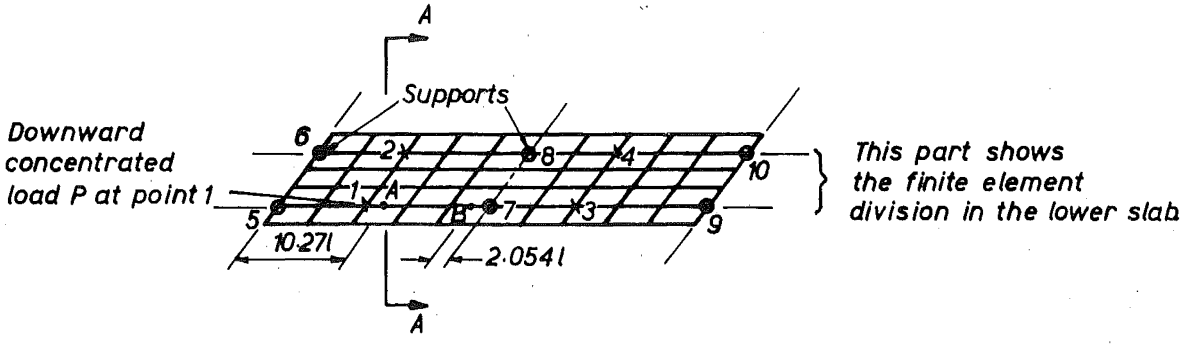

(d) IDEALISATION OF THE DECK SLAB

FIGURE IX-6.1 SKEW BOX-GIRDER BRIDGE MODEL

TABLE IX-6.1 RESULTS FROM ANALYSES OF SKEW BRIDGE MODEL

Type of analysis	Vertical displacements in terms of P/EI (positive upwards)				Strain along the span at top of web in terms of P/El^2		Reactions in terms of P					
	1*	2	3	4	A+	B	5*	6	7	8	9	10
Experimental [94]	- 60.00	- 18.50	+ 3.00	+ 7.00	- 0.662	+ 0.209	0.403	0.145	0.632	- 0.146	- 0.034	- 0.000
Finite Element Mesh A, Sisodiya et al [94]	- 51.20	- 11.19	+ 6.45	+ 4.34	- 0.637	+ 0.262	0.365	0.193	0.676	- 0.192	- 0.040	- 0.002
Finite Element Mesh A	- 49.1	- 11.7	+ 5.65	+ 3.78	- 0.680	+ 0.254	0.370	0.192	0.669	- 0.193	- 0.039	+ 0.001
Finite Element Mesh B (fine)	- 52.59	- 12.37	+ 5.32	+ 4.06	- 0.675	+ 0.248	0.366	0.198	0.667	- 0.196	- 0.033	- 0.002

* The locations of the points are shown in Fig. IX-6.1(d)

\+ This is the strain of the web element at points A and B, indicated in Fig. IX-6.1(b) and in plan in Fig. IX-6.1(d).

in the web - deck slab and web - soffit slab connections of the experimental model. Such imperfections were reported from other models of this series [92].

The experimental and theoretical strains at the midspan point A are in agreement to within 3% but there is a discrepancy of 18.6% at point B (see Fig. IX-6.1d). The difference between the theoretical and experimentally measured reactions of the piers is within 8.6% of the maximum experimental value.

The deflections, strains, and reactions computed with the Mesh A and Mesh B QMC3/CQ12 finite element idealisations agree to within 6.9%, 2.4% and 1.1% respectively, except for the reactions at points 9 and 10, but these are very small. This close agreement indicates that the results from the Mesh B idealisation of fully compatible elements have almost converged to the correct solution for the 'design structure'.

IX-7 LOBLEY HILL SOUTH OVERBRIDGE [54]

IX-7.1 Model description

A finite element analysis was performed on a 1:30 scale filled epoxy resin model of the Lobley Hill South Overbridge subjected to dead loading [54]. The bridge model was a four span curved solid slab structure, the geometry and loading details of which are shown in Fig. IX-7.1.

The elastic material properties of the filled epoxy resin were measured as; $E = 2.35 \times 10^6$ lb/in^2 (16.4 GPa), $\nu = 0.20$.

The finite element results computed with the CQ12 plate bending element are compared with those measured experimentally [54], and also the finite element results obtained by Lim and Moffatt [54] using: i) the ACM quadrilateral element, and ii) an incompatible triangular element derived by Bazely et al [6], with the same nodal parameters.

IX-7.2 Finite element idealisation

The following approximations were made to enable the model to be idealised as a two dimensional structure:-

i) the deck has a middle plane of symmetry, and a cross sectional area equal to that of the actual deck (see Fig. IX-7.2.)

ii) the superelevation and vertical curvature of the deck can be disregarded. Lim and Moffatt [54] have calculated that the effect of these assumptions on the results is generally less than 5%, by comparing

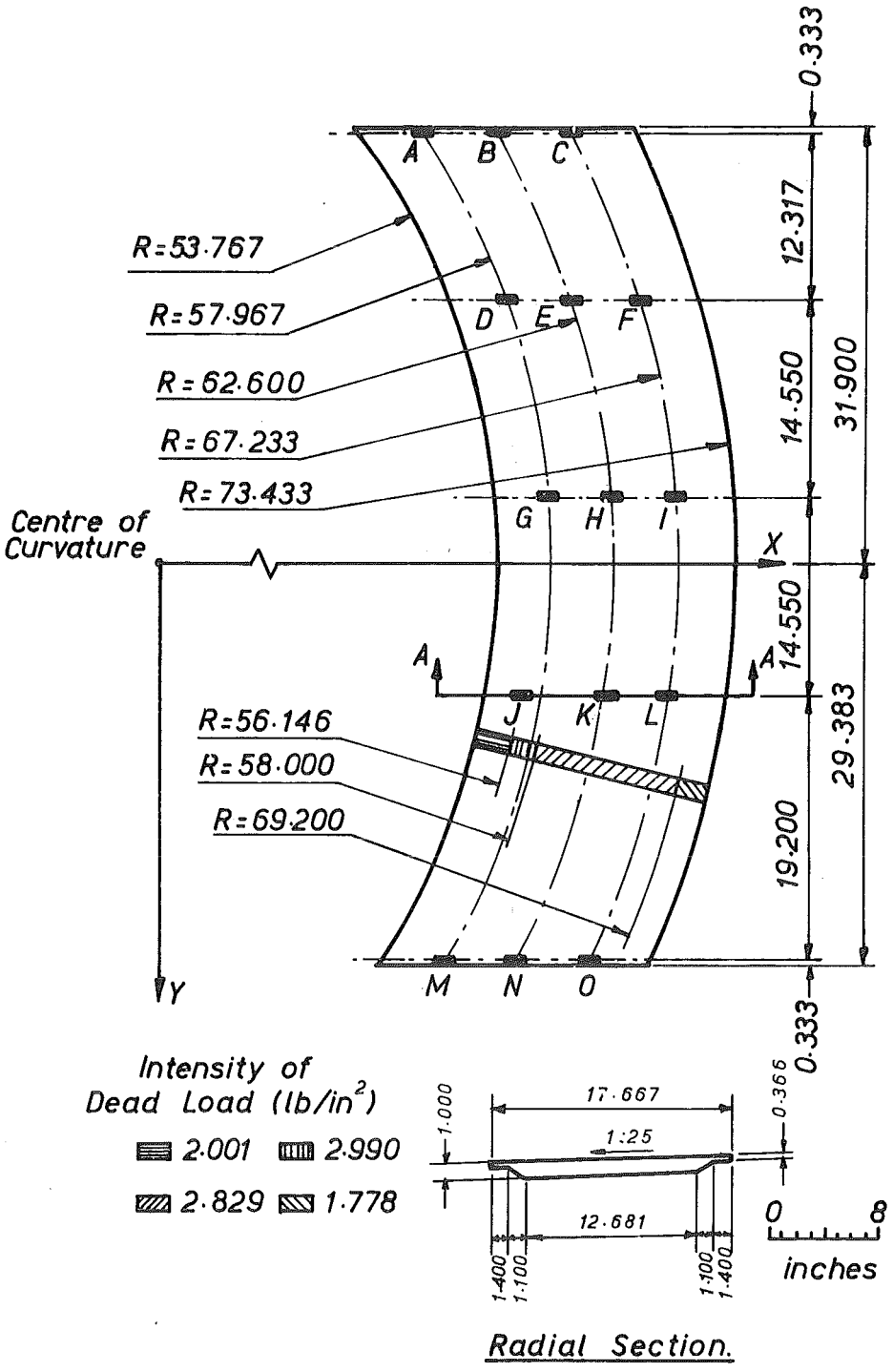

FIGURE IX-7.1 DETAILS OF LOBLEY HILL SOUTH OVERBRIDGE MODEL

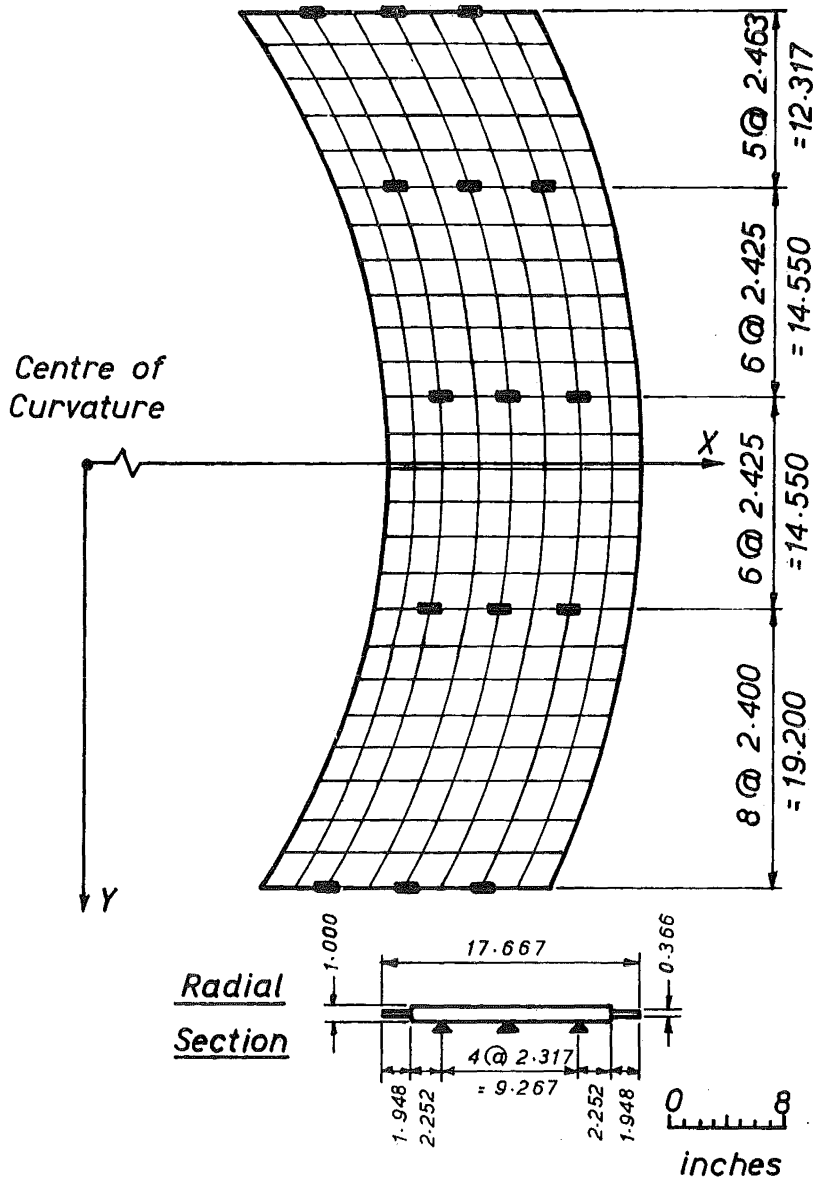

FIGURE IX-7.2 FINITE ELEMENT IDEALISATION

results obtained with and without these assumptions incorporated.

The 8 x 25 mesh shown in Fig. IX-7.2 was used to subdivide the structure into quadrilateral elements, while a finer 14 x 42 mesh was used for the triangular subdivision. Each quadrilateral element was represented for load distribution purposes by its constituent triangles so the distribution of load to the nodes would not be affected by the type of element used. Any load acting within a triangular element was replaced by a statically equivalent system of nodal forces.

The bridge deck was supported on 'hinged' piers, the locations of which are shown in Fig. IX-7.1. These piers were modelled with beam elements of negligible flexural stiffness and with axial stiffness equal to the measured values [54].

IX-7.3 Comparison of results

The agreement between the computed and experimentally measured results is excellent;

i) Deflections.

The theoretical and experimentally measured deflection profiles along the longitudinal centreline are shown in Fig. IX-7.3. The results obtained from the three finite element analyses are virtually identical, and generally agree to within 4% of the experimental deflections.

ii) Reactions.

The column reactions predicted from the three finite element analysis are listed in Fig. IX-7.4, along with those measured experimentally. The difference between the theoretical reactions computed with the CQ12 elements and the experimental reactions is within 11% of the maximum theoretical value. Some of this discrepancy may be attributed to a lack of accuracy in the values measured for the axial stiffness of the piers [54].

iii) Moments.

The distributions of experimental and theoretical longitudinal bending moments along the longitudinal centreline and across section A - A (see Fig. IX-7.1) are plotted in Figures IX-7.5 and IX-7.6 respectively. The distribution of transverse bending moments across section A - A is shown in Fig. IX-7.7. (The theoretical moments at any node were obtained by averaging the nodal moments from each element connected to that node).

The theoretical and experimental values of both longitudinal and transverse bending moments agree to within 6%, except near the supports where discrepancies of up to 34% occur because the stress concentrations above the piers cannot be reproduced accurately without

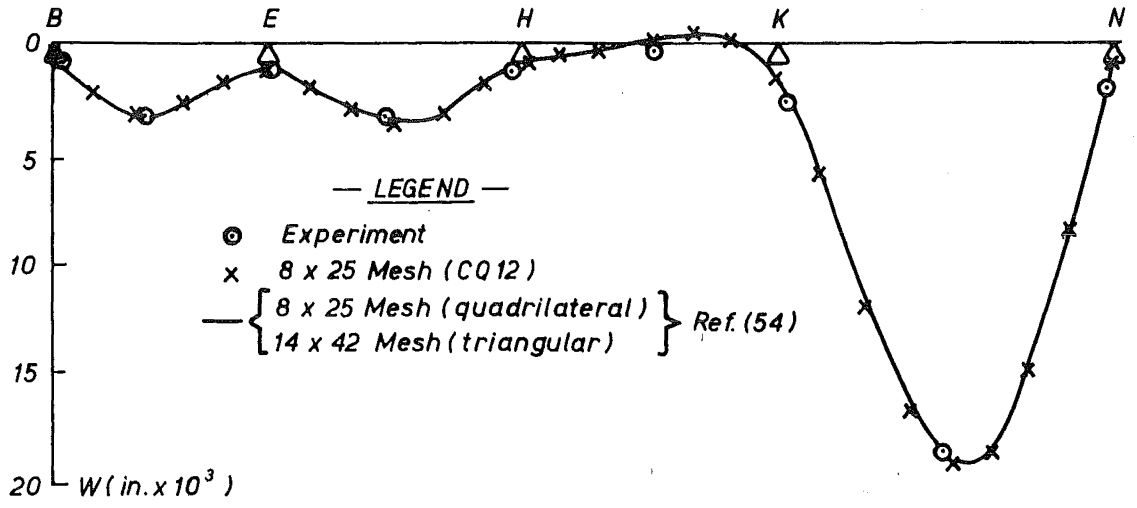

FIGURE IX-7.3 LONGITUDINAL PROFILE OF CENTRAL DEFLECTION

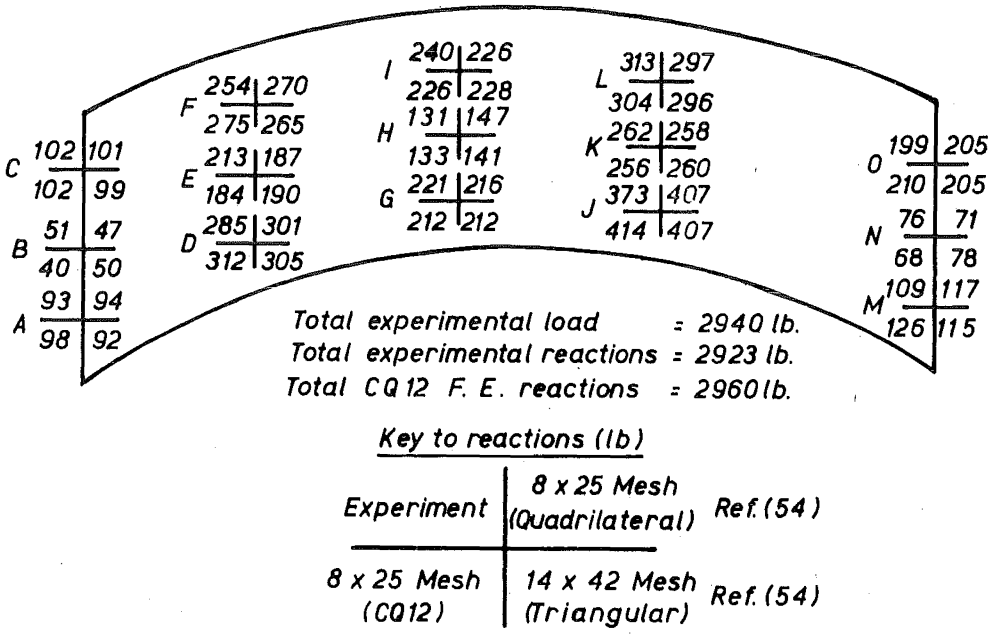

FIGURE IX-7.4 PIER REACTIONS

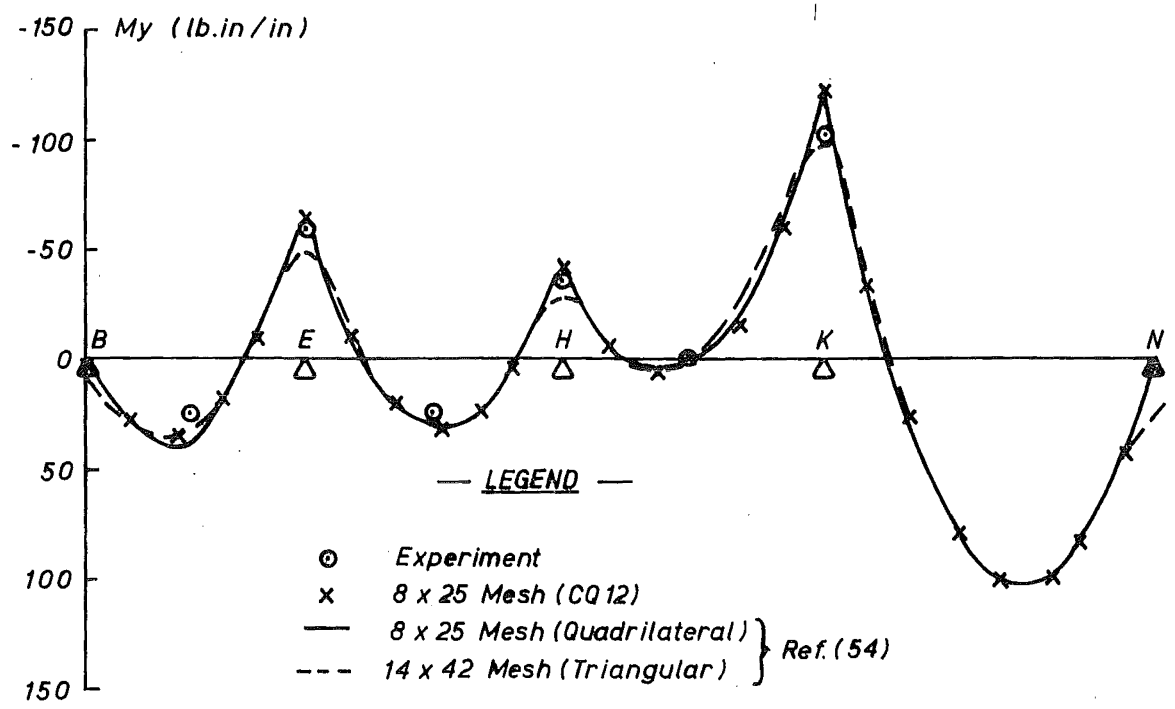

FIGURE IX-7.5 LONGITUDINAL DISTRIBUTION OF LONGITUDINAL BENDING MOMENTS

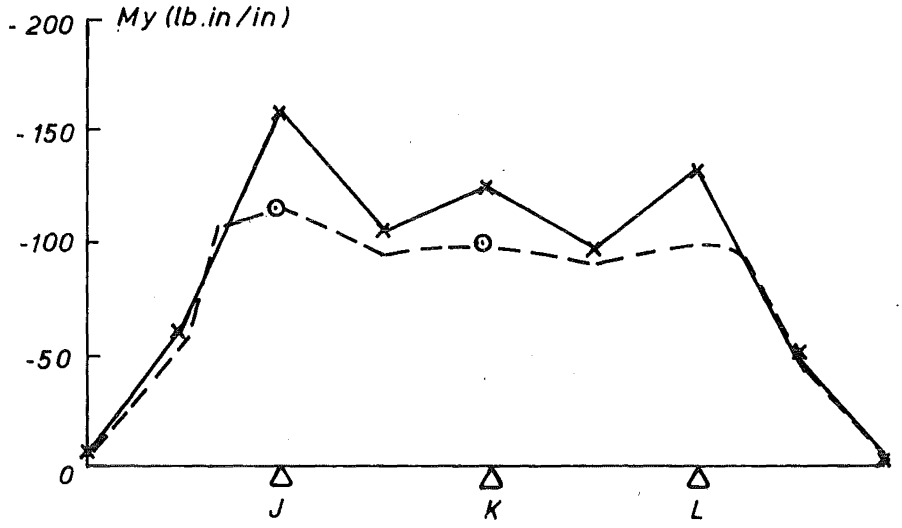

FIGURE IX-7.6 TRANSVERSE DISTRIBUTION OF LONGITUDINAL BENDING MOMENTS

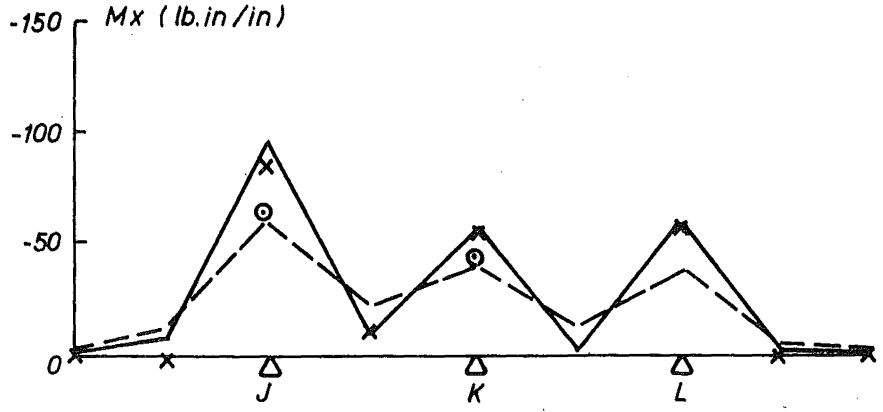

FIGURE IX-7.7 LONGITUDINAL DISTRIBUTION OF TRANSVERSE BENDING MOMENT

refining the element mesh in this region. Lim and Moffatt [54] have shown that errors in the theoretical solutions also occur here because the deck slab - pier interaction is idealised as a point load at the slab centroid, rather than as a load distributed over a circular region on the bottom surface of the deck slab.

IX-8 ASLAM AND GODDEN CURVED BOX-GIRDER BRIDGES [3]

IX-8.1 Model description

The response computed from the finite element analyses of two 1:29 scale aluminium models of curved box-girder bridges is compared with that measured experimentally [3]. The model design for both structures was a four cell box section with a total width of 356 mm (14 in) and a radius of curvature of 2.96 m (116.7 in). Model No. 1 and Model No. 2 were simply supported over spans of L = 1.52 m (60 in) and 1.14 m (45 in) respectively, and loaded at midspan over the outside web as shown in Figures IX-8.1 and IX-8.2 respectively. Poisson's ratio for the aluminium material was measured as 0.332.

IX-8.2 Finite element idealisation

i) Model No. 1

Two idealisations of the cross-section of the bridge were employed for the finite element analysis of Model No. 1;

a) Mesh A

The distribution of the finite element nodal points across a radial section is shown in Fig. IX-8.3. Only one element was employed down the depth of each web but two elements were used across the top and bottom of each cell to constitute the deck and soffit slabs respectively.

b) Mesh B

Two elements were employed down the depth of each web but only one element was used across the top and bottom of each cell. One element was used across the cantilever slab for both meshes.

The longitudinal idealisation of the bridge was the same for both meshes. A line of symmetry was assumed about the transverse centreline and half the span was divided longitudinally into thirteen elements; a mesh consisting of twelve equal length elements along the bridge was subdivided adjacent to the midspan to accommodate a row of nodes at section A - A. (See Fig. IX-8.1.) Diaphragms 6.93 mm thick

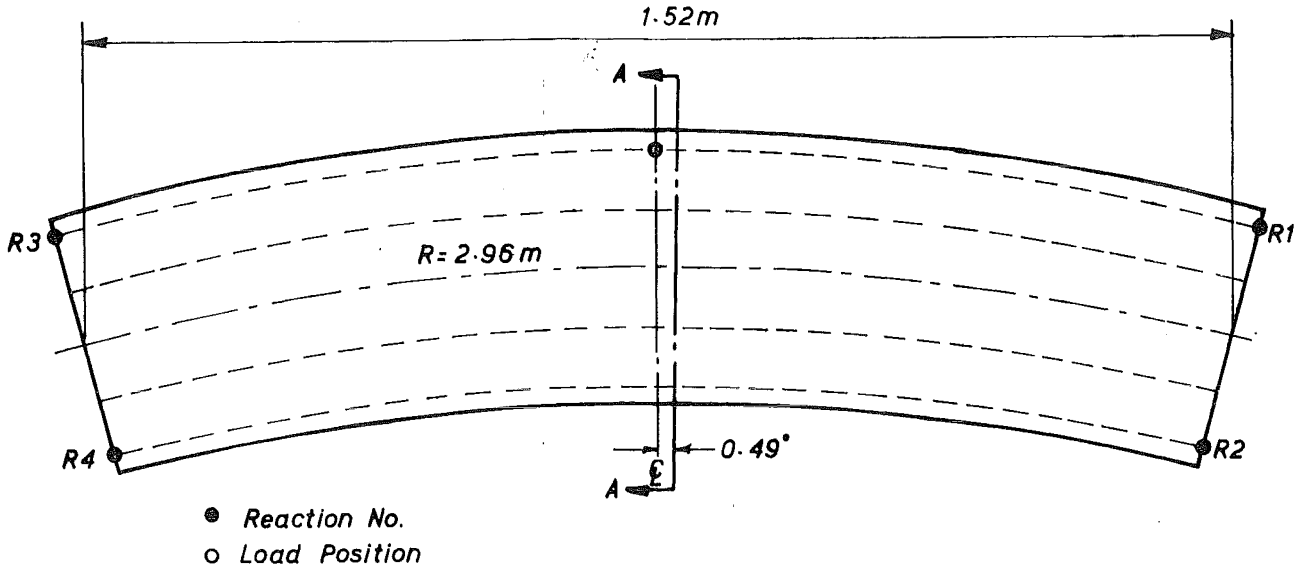

FIGURE IX-8.1 PLAN OF MODEL NO. 1

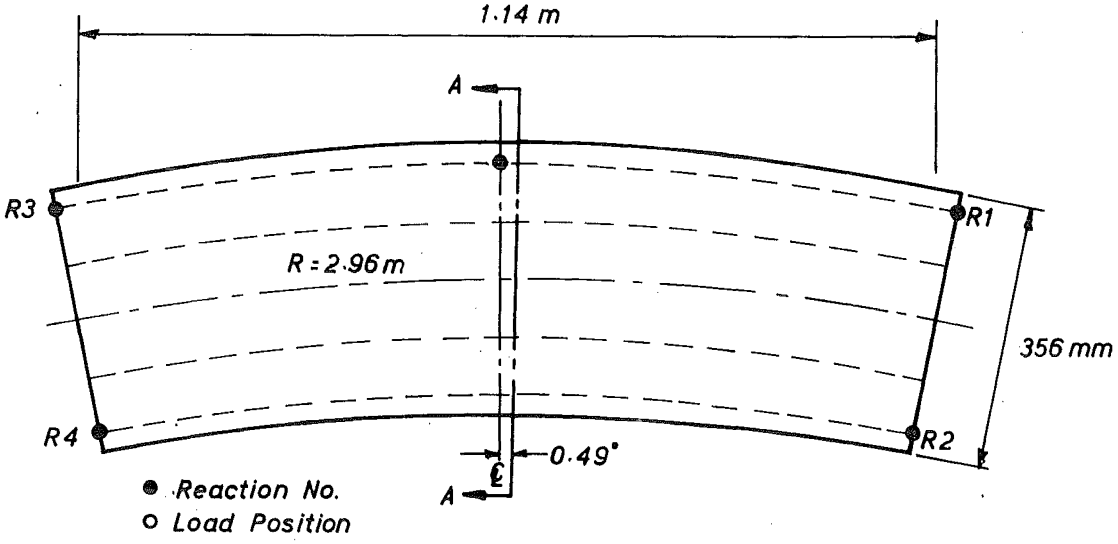

FIGURE IX-8.2 PLAN OF MODEL NO. 2

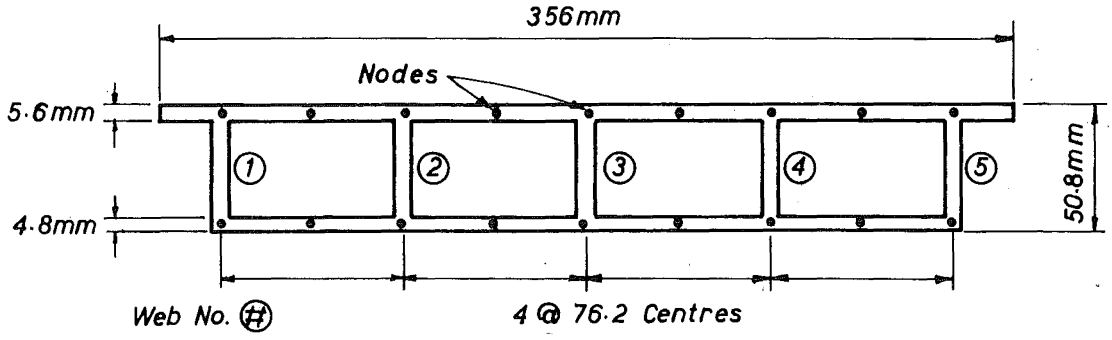

FIGURE IX-8.3 FINITE ELEMENT IDEALISATION OF RADIAL SECTION MESH A

were incorporated at the support section.

ii) Model No. 2

Model No. 2 was analysed with the Mesh A idealisation only.

The horizontal support conditions of the experimental models were such as to provide transverse restraint at supports R2 and R3 (see Figures IX-8.1 and IX-8.2) and longitudinal restraint at support R2. A line of symmetry was assumed at midspan for the finite element analyses so it was not possible to model these boundary conditions exactly; longitudinal restraint was provided across the midspan section, and transverse restraint at the top of the inside web at midspan.

IX-8.3 Static checks

Two independent static checks were applied to the finite element results obtained using Mesh A to analyse Model No. 1 (L = 1.52 m).

i) Horizontal forces.

The longitudinal (circumferential) stresses were calculated at the nodal points across section A - A, and integrated to obtain the total tensile force T and the total compressive force C . (stress distributions were assumed linear between any two adjacent nodal points). These two forces should be of equal magnitude because no external horizontal forces were applied to the bridge. The discrepancy between the forces computed by this method was only 0.1%.

ii) Bending moments.

The internal bending moment across section A - A was calculated by multiplying the average of the forces T and C by the vertical distance between the locations of the resultants of forces T and C . The external moment at section A - A was taken as the average of the "left" and "right" moment at section A - A, as computed from the applied load and the experimentally measured support reactions [3]. The discrepancy between the internal and the external moments was 4.3%, which is of acceptable magnitude since the reactions were only measured experimentally to an accuracy of $\pm$ 2% [3].

IX-8.4 Comparison of results

The theoretical and experimental distributions of the following dimensionless parameters are compared:-

i) Longitudinal membrane force per unit width (N_y L/W) across section A - A.

ii) Radial bending moment per unit width (Mx 1000/W) across section A - A

iii) The deflection (Δ EL/1000 W) at midspan, where W is the magnitude

of the applied point load.

i) Longitudinal membrane force.

Figures IX-8.4 and IX-8.5 show the distribution of longitudinal membrane force across section A - A for Model No. 1 and Model No. 2 respectively. The experimental and theoretical results generally agree to within 20% for the Mesh A solution, and to within 9% for the Mesh B solution, except for a discrepancy across the outside cantilever. The finite element solutions predict a significant shear lag here, while the longitudinal stress measured experimentally from the strain gauge located at the centre of the cantilever slab is only marginally smaller than the extrapolated value above the outside web. A more useful comparison could be made if this gauge was located at the extreme end of the cantilever slab.

ii) Radial bending moment.

The radial bending moment across the deck and soffit slabs at section A - A, and down the webs at section A - A, are plotted in Figures IX-8.6 and IX-8.7 respectively for Model No. 1, and in Figures IX-8.8 and IX-8.9 respectively for Model No. 2. There is close agreement between measured and computed moments, with the maximum discrepancy from the Mesh B solution for Model No. 1 of 20% across the deckslab, 15% across the soffit slab and 18% at the top of the loaded web. It is evident from the comparison of radial bending moments that the Mesh B solution is more accurate than the Mesh A solution, especially across the deckslab of the inner cell. The error in the theoretical moments at the top of the loaded web computed from Mesh A was 25% for Model No. 1 and 17% for Model No. 2.

iii) Deflection.

The experimental and theoretical deflection profiles across the midspan section are plotted in Fig. IX-8.10 for both Model No. 1 and Model No. 2. The maximum theoretical deflections predicted from the Mesh A solution are 8.4% and 8.3% less than the experimental deflection under the loaded web for Model No. 1 and Model No. 2 respectively. This discrepancy may be partially due to errors in the experimentally measured deflections, caused by a failure to isolate rigid body deflections due to axial shortening of the load cells upon which the structures were supported [3].

The longitudinal forces at the top and bottom of the webs, predicted from the Mesh B analysis of Model No. 1, are more accurate than those computed for Structure A and Structure B (see Sections IX-2 and IX-3 respectively) because these latter bridges have severe haunches at

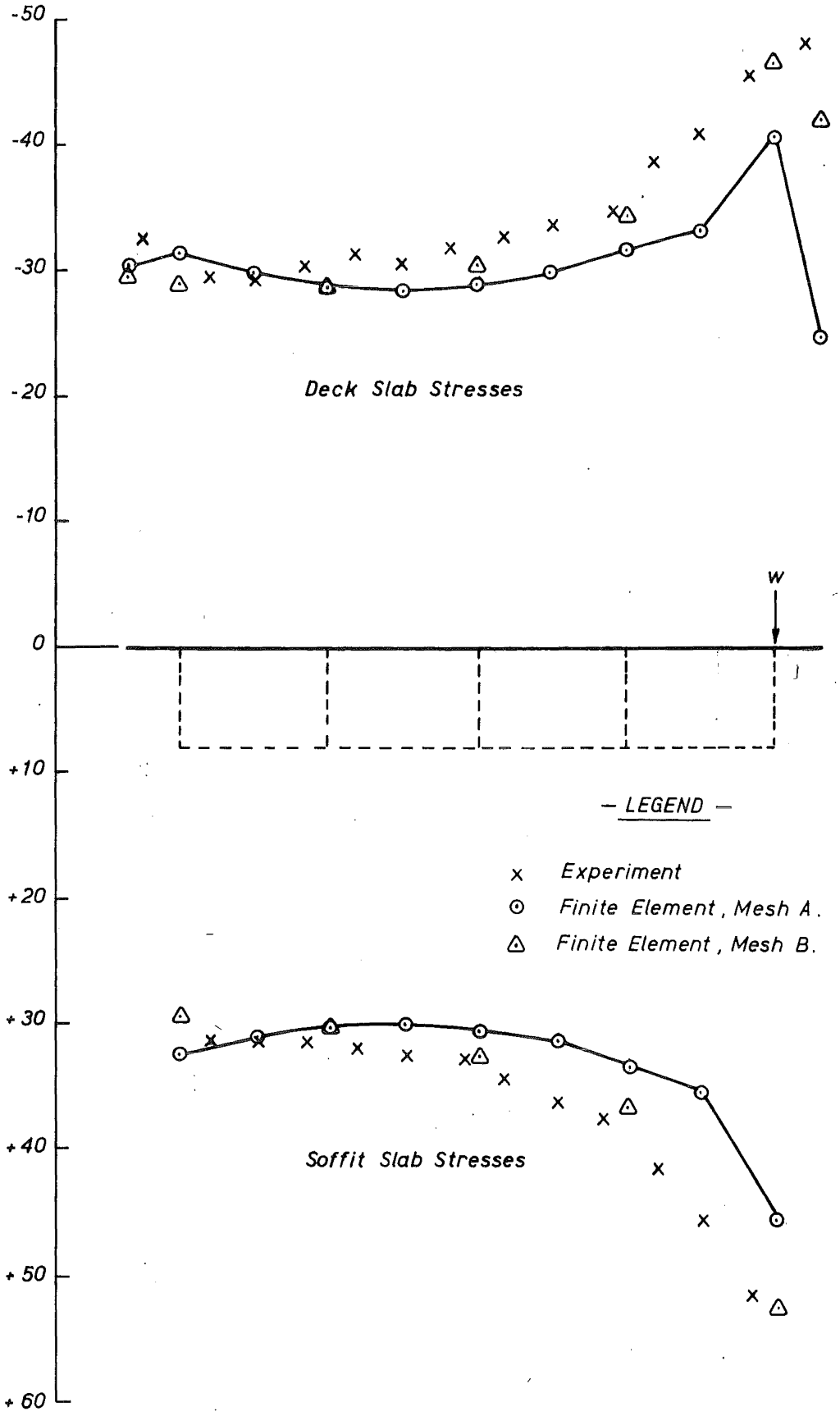

FIGURE IX-8.4 LONGITUDINAL MEMBRANE FORCE (Ny.L/W)
SECTION A-A ; MODEL NO. 1

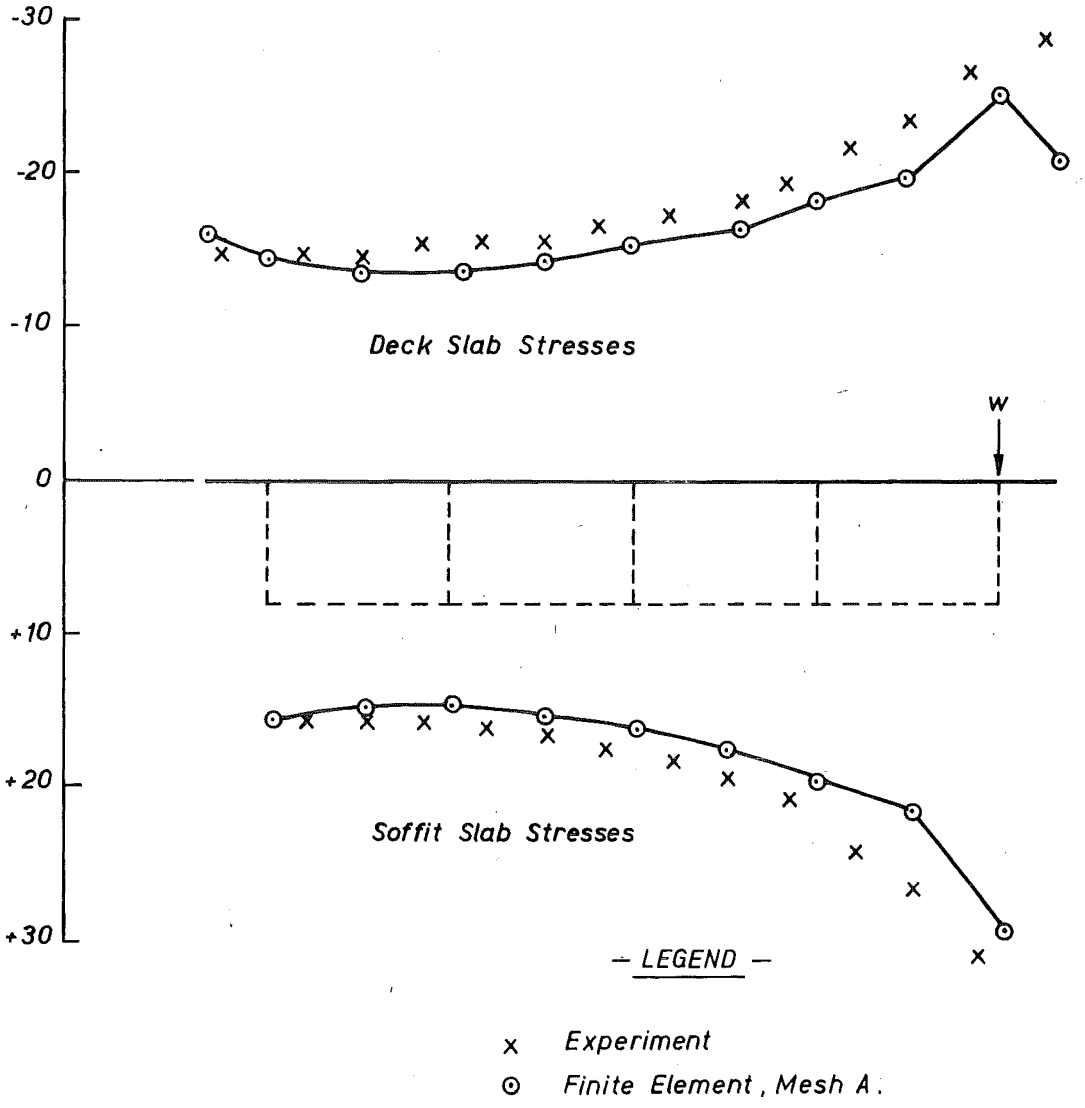

FIGURE IX-8.5 LONGITUDINAL MEMBRANE FORCE (Ny.L/W)
SECTION A-A ; MODEL NO. 2

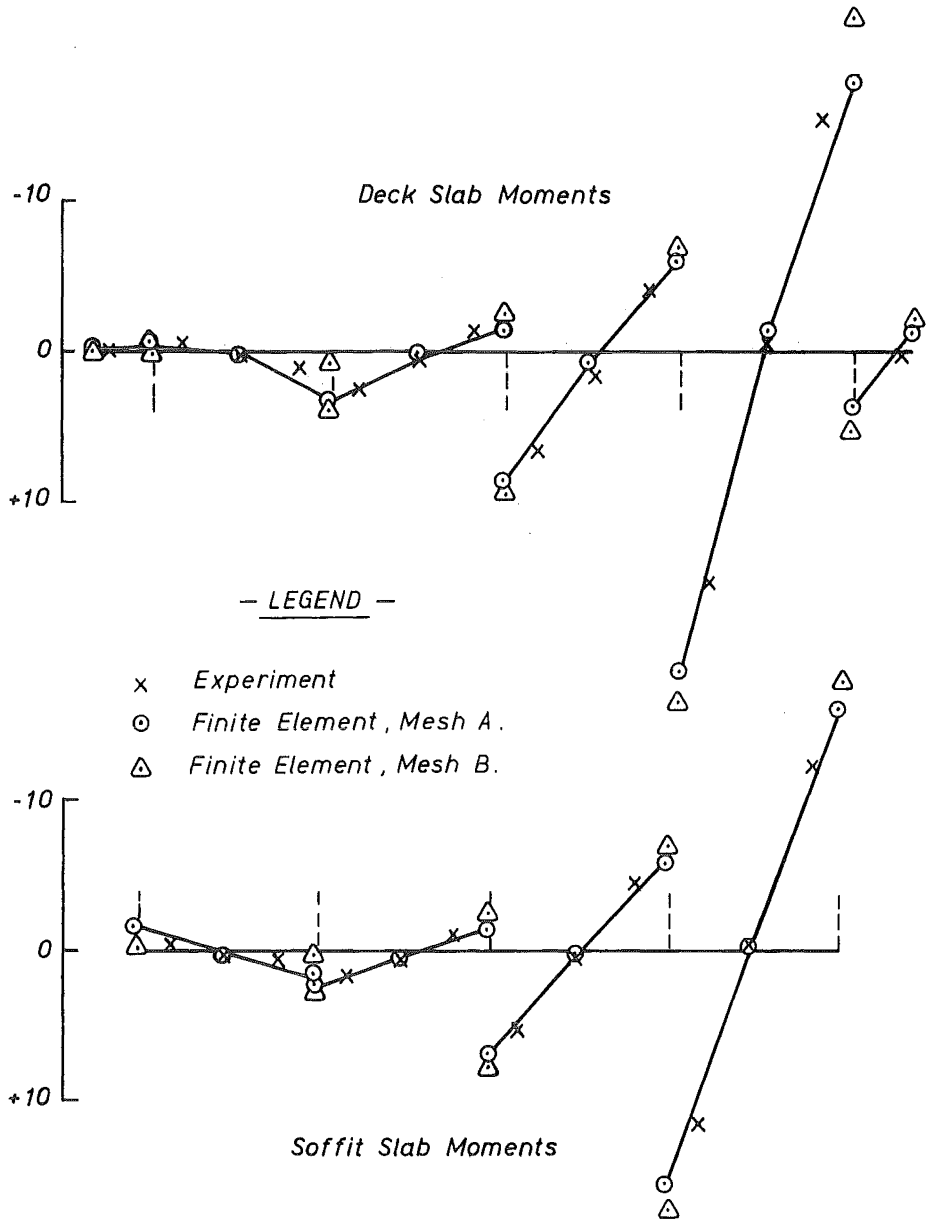

FIGURE IX-8.6 RADIAL BENDING MOMENTS (Mx.1000/W)
SECTION A-A ; MODEL NO. 1

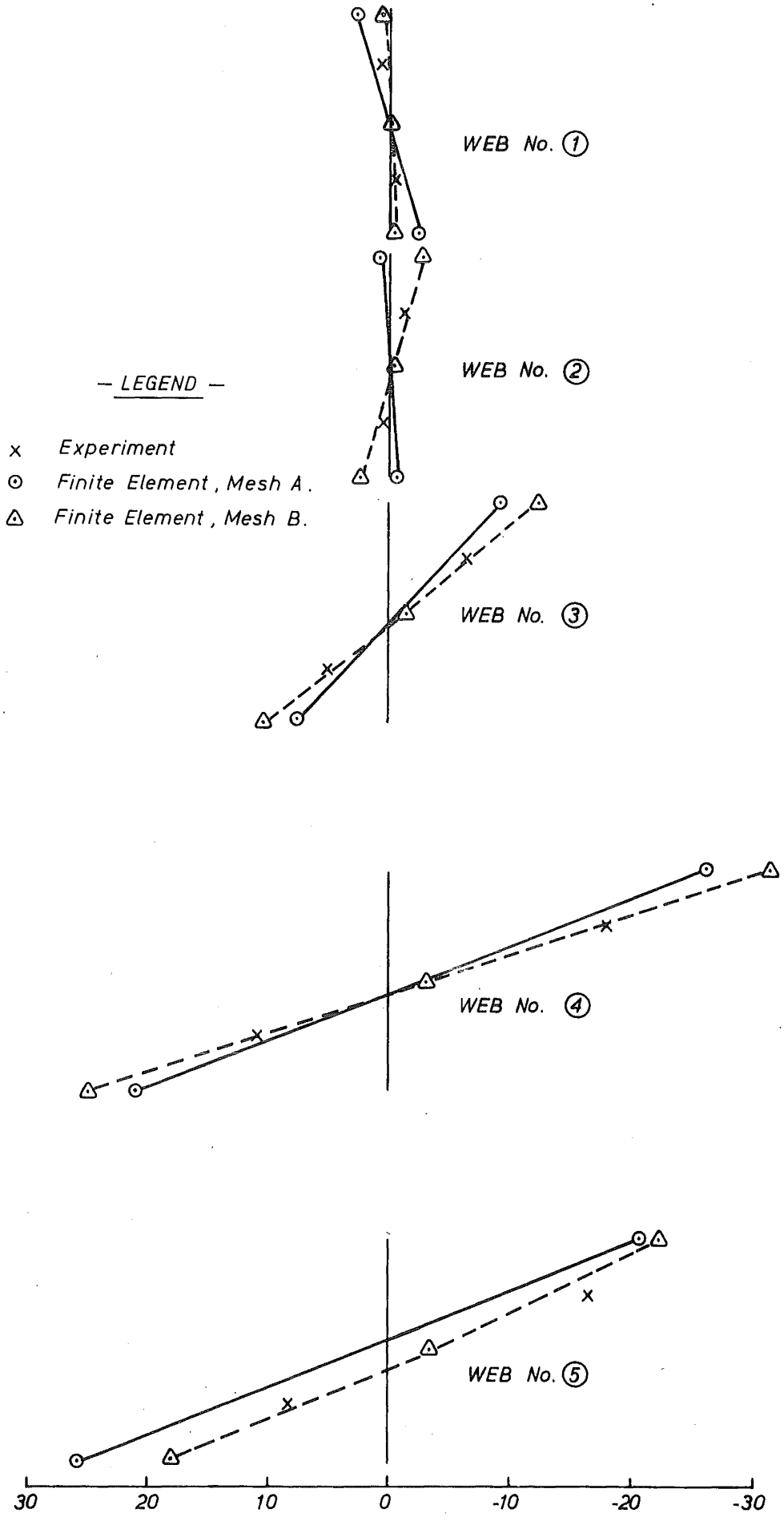

FIGURE IX-8.7 TRANSVERSE WEB MOMENTS (Mx.1000/W)
SECTION A-A ; MODEL NO. 1

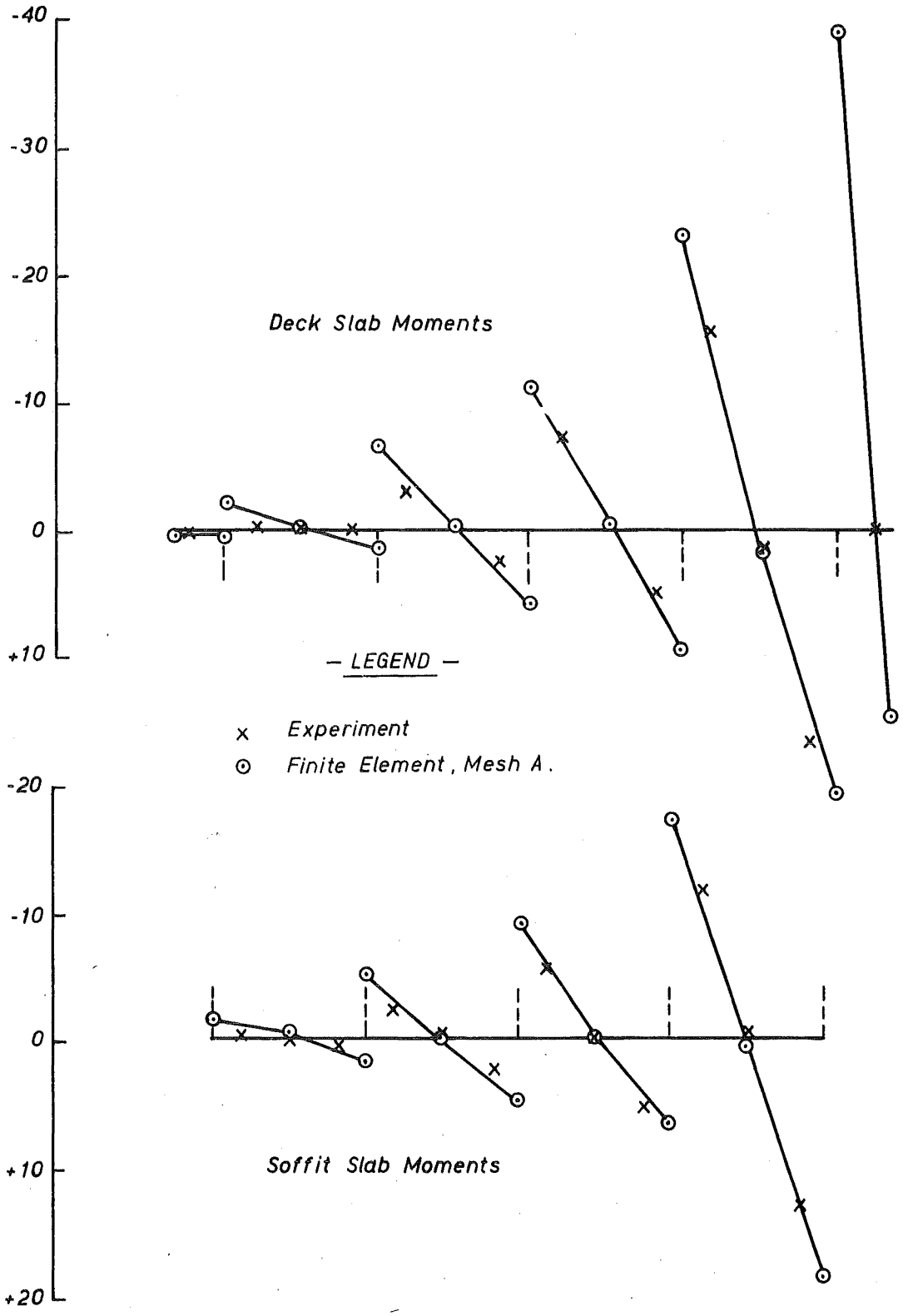

FIGURE IX-8.8 RADIAL BENDING MOMENTS (Mx.1000/W)
SECTION A-A ; MODEL NO. 2

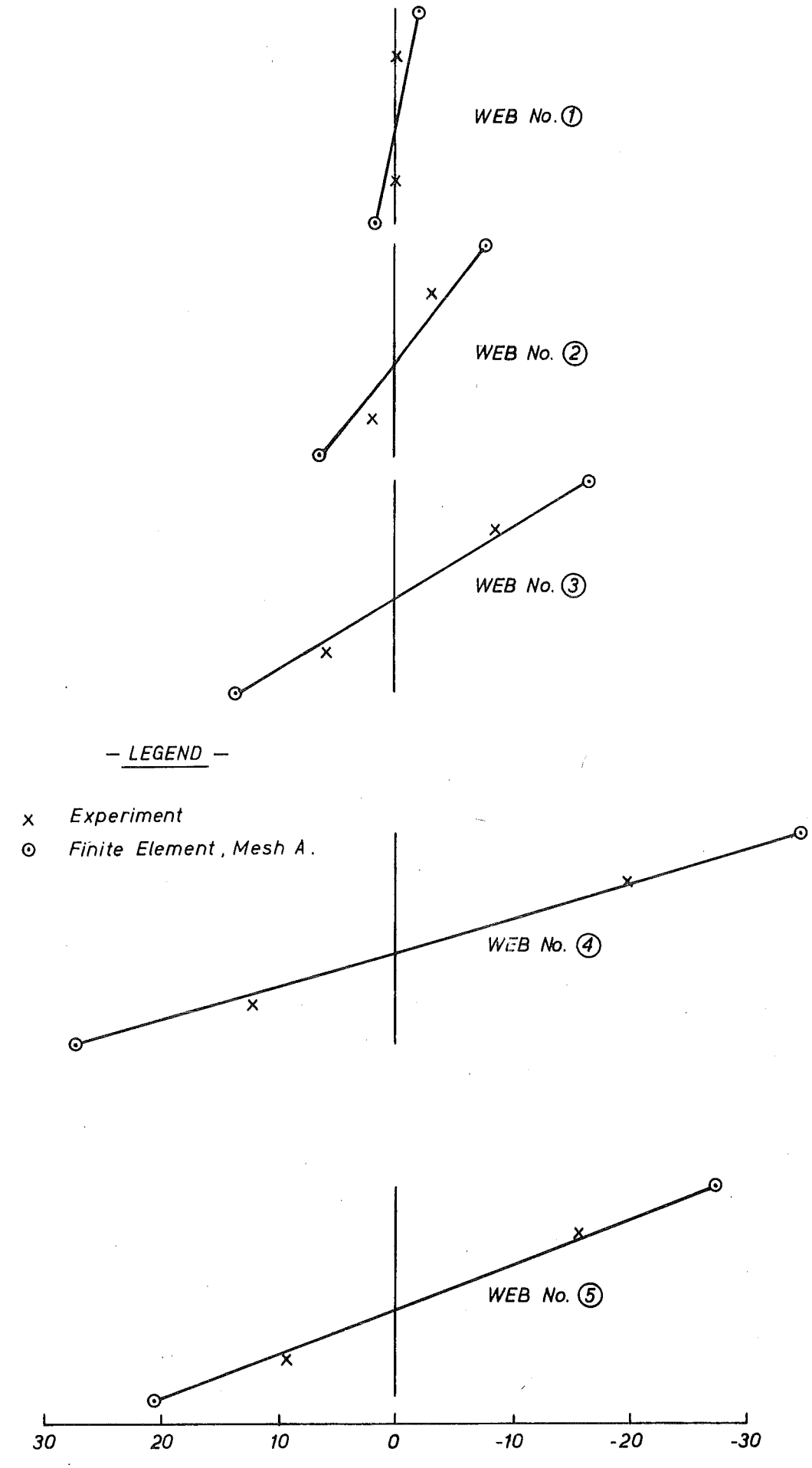

FIGURE IX-8.9 TRANSVERSE WEB MOMENT (Mx.1000/W)
SECTION A-A ; MODEL NO. 2

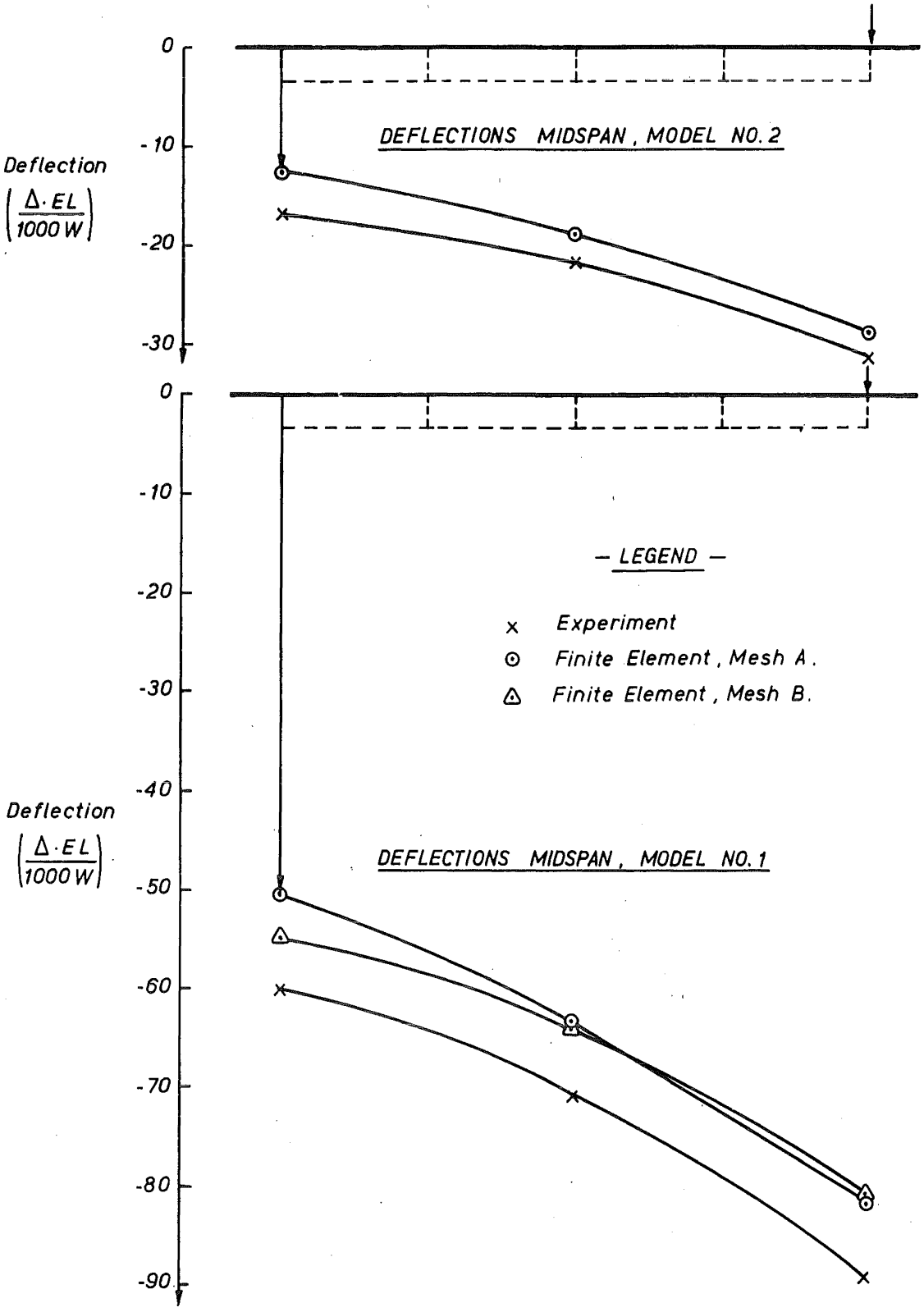

FIGURE IX-8.10 PROFILES OF DEFLECTION ACROSS MIDSPAN

the junction of the deck slab and webs, resulting in a more complex distribution of web stresses.

IX-9 STOCKTON ROAD INTERCHANGE

IX-9.1 Model description

The Stockton Road Interchange is a curved single cell multi-span box-girder bridge. Lim, Kilford and Moffatt [55] have constructed a 1:30 scale model of a segment of this prestressed concrete structure in order to investigate the transverse distribution of stresses.

The model was of a single span, with quarter span cantilevers at each end, thus enabling the effects of continuity over the supports to be investigated without the expense of constructing a multi-span model. Rigid diaphragms were incorporated at the support sections. Details of the superstructure and supports are shown in Fig. IX-9.1.

The model material was an araldite and sand mixture for which the following elastic material properties were measured; $E = 2.75 \times 10^6$ lb/in^2 (19.2 GPa), and $\nu = 0.23$

IX-9.2 Loading condition

The model was subjected to type HB truck loading [55], represented by an articulated framework which distributed the applied load of 100 lbs equally to 16 scaled rubber based steel pads, simulating the wheels of the vehicle. The truck load was centred over the outside web near quarter span, as shown in Fig. IX-9.2.

IX-9.3 Finite element idealisation

The finite element idealisation of the model is illustrated in Fig. IX-9.3, and involved the following approximations:-

i) The fillets at the junctions of the flanges and the webs were neglected.

ii) The haunched cantilever slabs were represented as tapered thickness elements with the centroid of the root of the cantilever element raised so as to coincide with the middle surface of the deck slab. The effect of these approximations produces an error of less than 1% in the second moment of inertia of the idealised cross-section [55].

A further approximation was introduced by supporting the box under the webs rather than at the actual support positions shown in Fig. IX-9.1. The effect of this approximation on the analysis of the model is considered to be negligible [55].

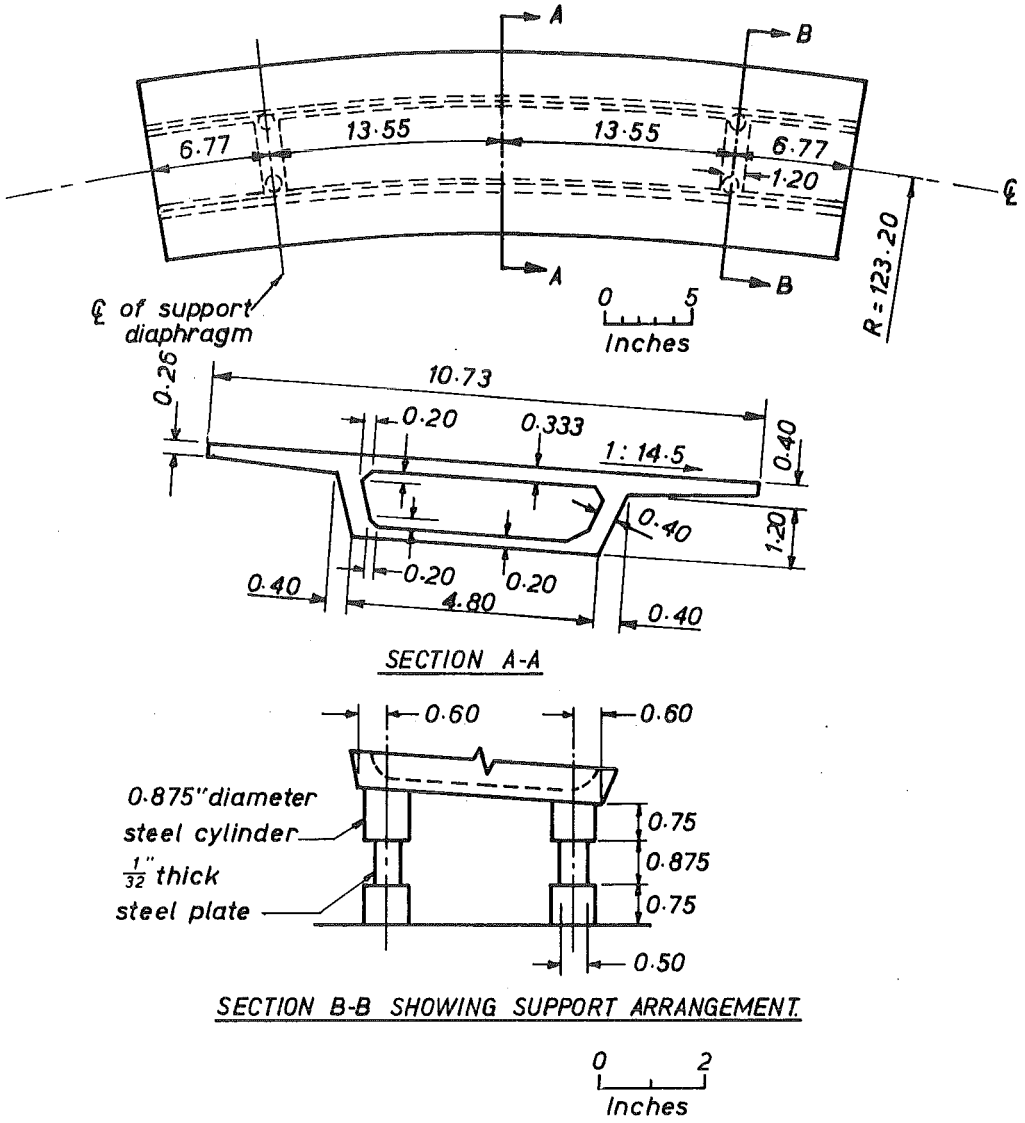

FIGURE IX-9.1 STOCKTON ROAD INTERCHANGE DETAILS OF MODEL

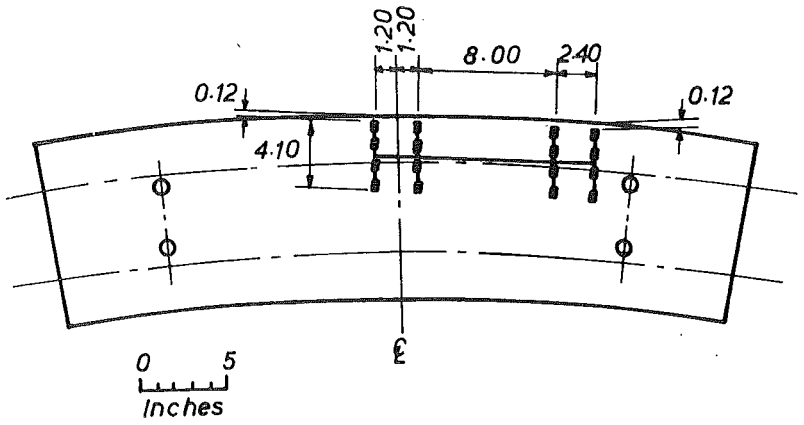

FIGURE IX-9.2 POSITION OF TRUCK LOAD

Two longitudinal subdivisions of the structure into finite elements were employed;

i) A COARSE MESH with ten elements along the length of the model, including six elements along the central span.

ii) A FINE MESH with eighteen elements along the length of the model, including twelve elements along the central span. Two elements were employed down the depth of the webs and across the cantilever slabs, and the superelevation of the structure was modelled for both idealisations. The coarse mesh finite element idealisation of the deck slab and the cross-section is illustrated in Fig. IX-9.3.

Each wheel load was approximated as a point load acting within the area of an element. To remain consistent with the procedure adopted by Lim, Kilford and Moffatt [55] when they performed a finite element analysis of this structure, a simple static distribution of each wheel load to the element nodes was employed: a quadrilateral element was divided into two triangles in two distinct ways, and half the load was distributed to the nodes of each of the triangles on which it acts.

IX-9.4 Comparison of results

The experimental and theoretical distributions of longitudinal and transverse stress are compared and are shown to be in close agreement, except for two local discrepancies.

i) Longitudinal stresses.

The distributions of longitudinal stresses across the top of the deck and soffit slabs, across the bottom of the deck and soffit slabs, and down the webs are plotted in Figures IX-9.4, IX-9.5 and IX-9.6 respectively. The agreement between the two finite element solutions and the experimental results is within 10% except: i) across the outside cantilever where the theoretical stresses are up to 42% larger. A similar discrepancy of outside cantilever stresses is evident from the finite element results presented by Lim, Kilford and Moffatt [55] who simulated the haunched cantilever slabs with a single element of uniform thickness and the same cross-sectional area. ii) the bottom surface of the deck slab near the inside wheel load where the theoretical stress from the fine mesh solution is 60% smaller. Both these discrepancies may result from local stress concentrations which occur under wheel loads and which require a refinement of mesh in their vicinity and the employment of consistent nodal loading [1] to predict the stress distribution accurately.

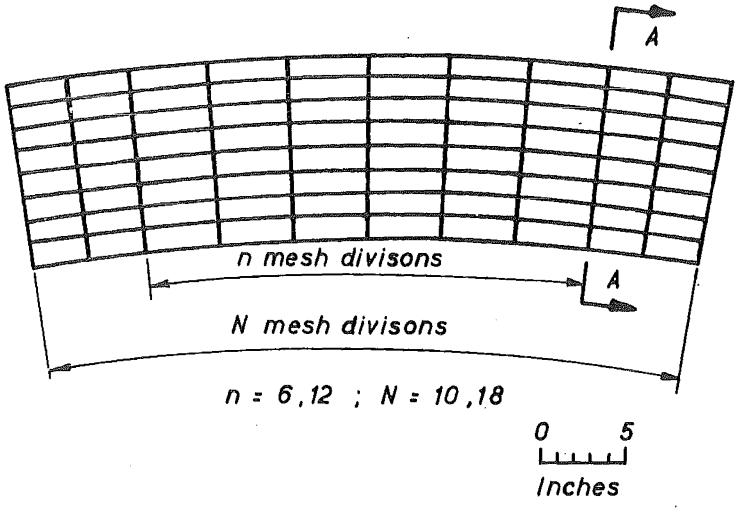

-Plan-

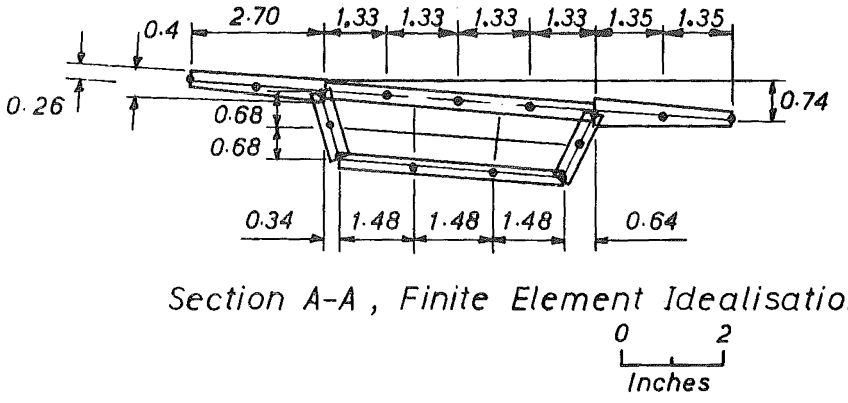

Section A-A , Finite Element Idealisation

0 2
Inches

FIGURE IX-9.3 FINITE ELEMENT IDEALISATION

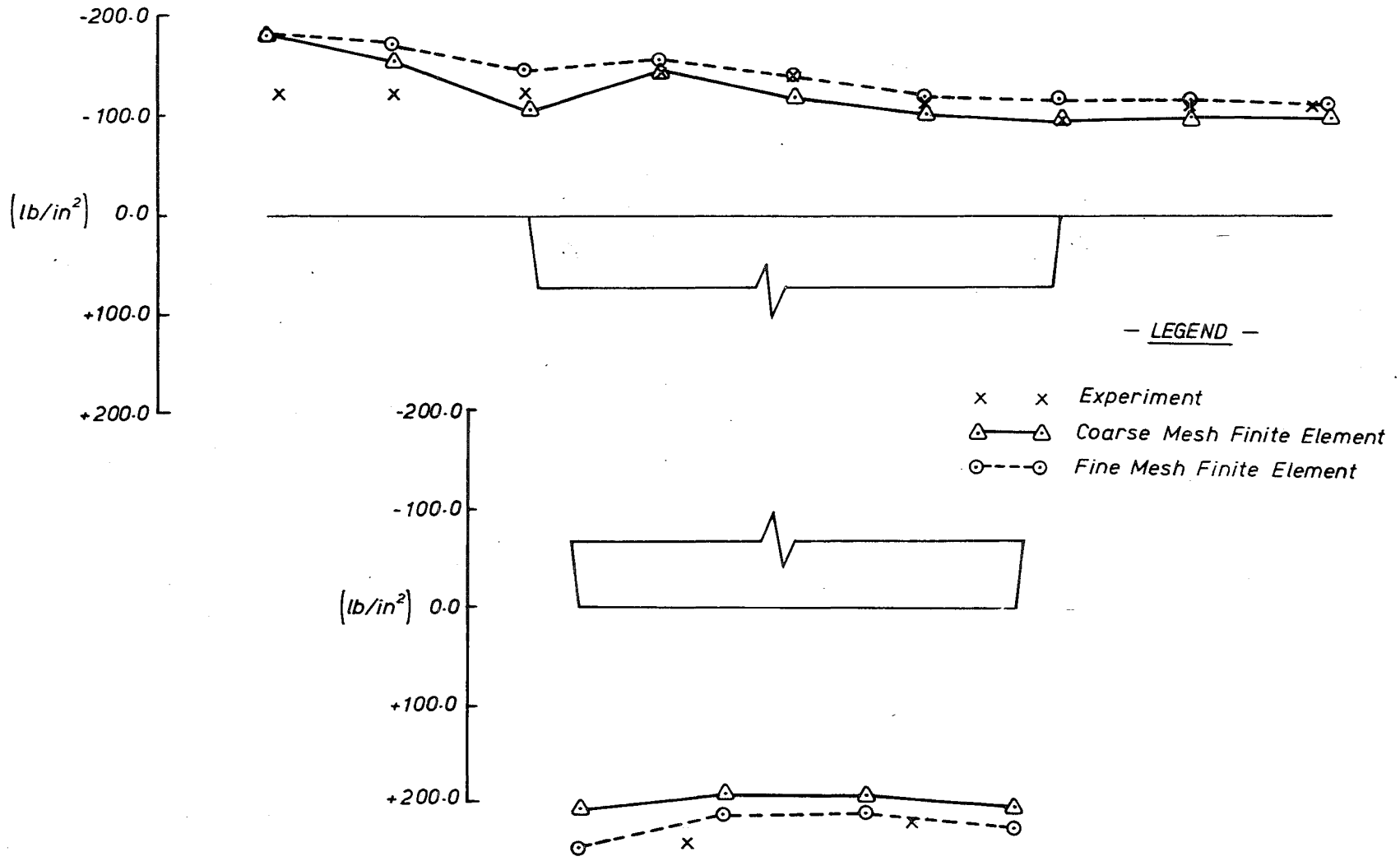

FIGURE IX-9.4 LONGITUDINAL STRESSES ALONG TOP OF DECK AND SOFFIT SLABS

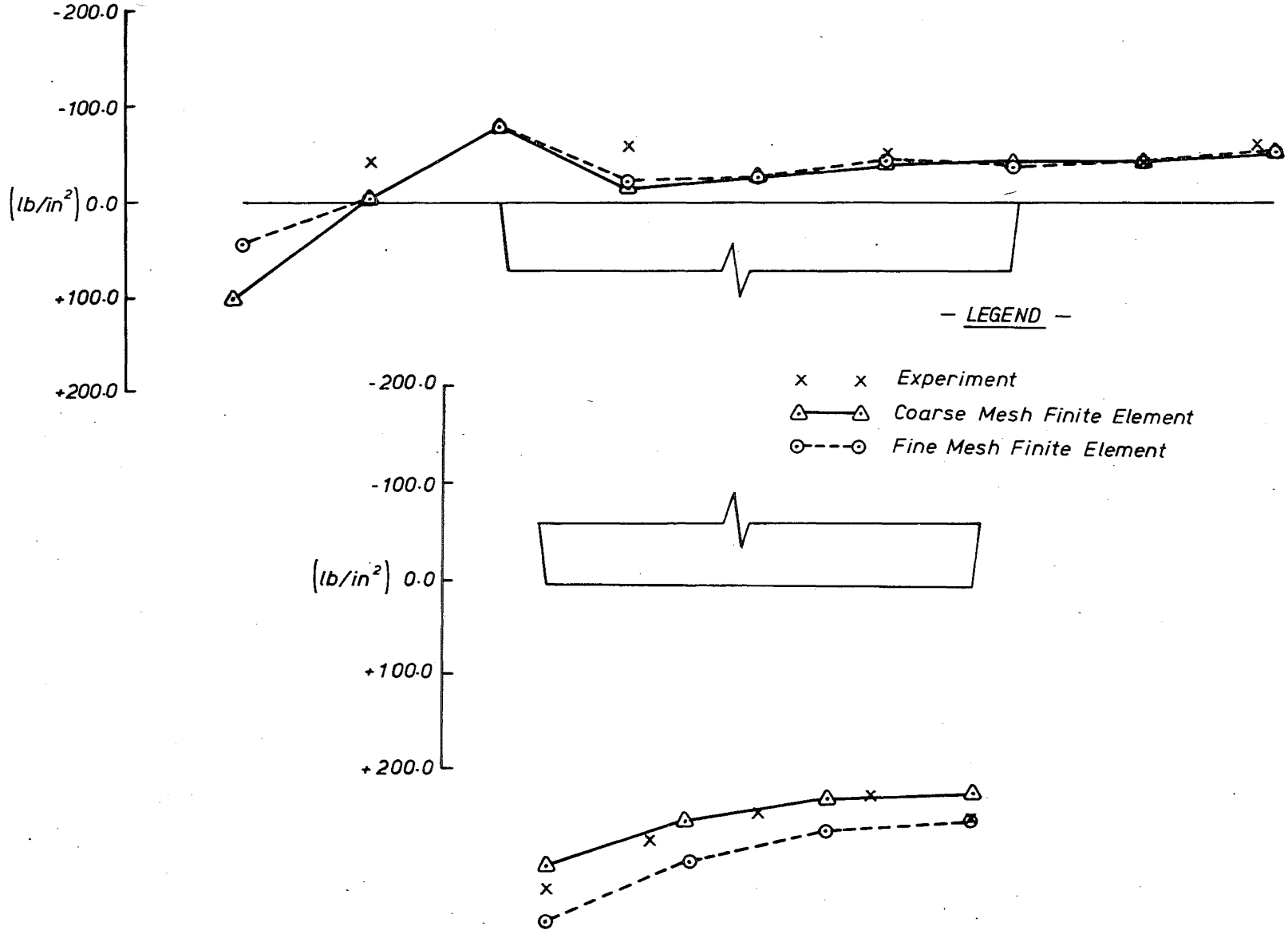

FIGURE IX-9.5 LONGITUDINAL STRESSES ALONG BOTTOM OF DECK AND SOFFIT SLABS

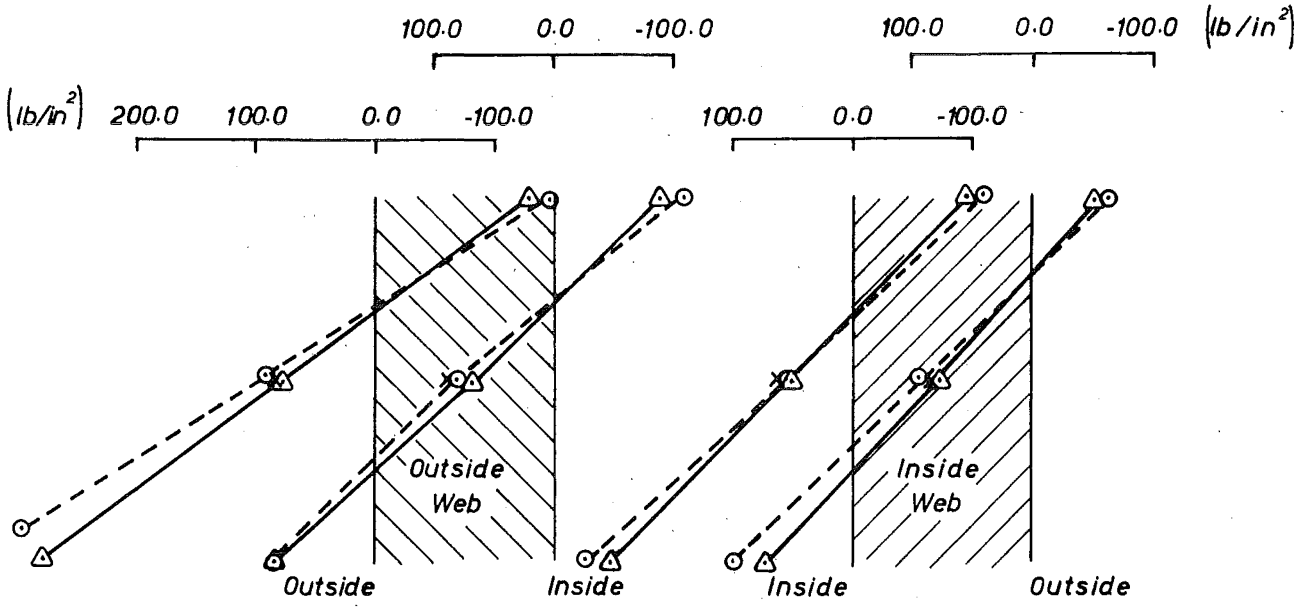

LONGITUDINAL STRESSES

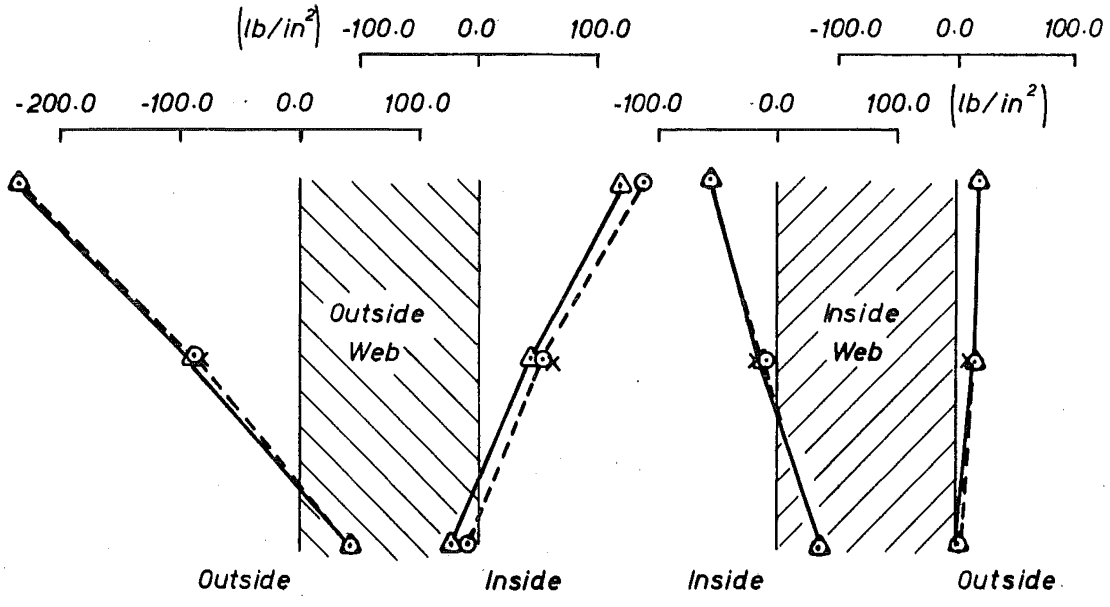

TRANSVERSE STRESSES

— LEGEND —

× × Experiment

△——△ Coarse Mesh Finite Element

⊙---⊙ Fine Mesh Finite Element

FIGURE IX-9.6 WEB STRESSES

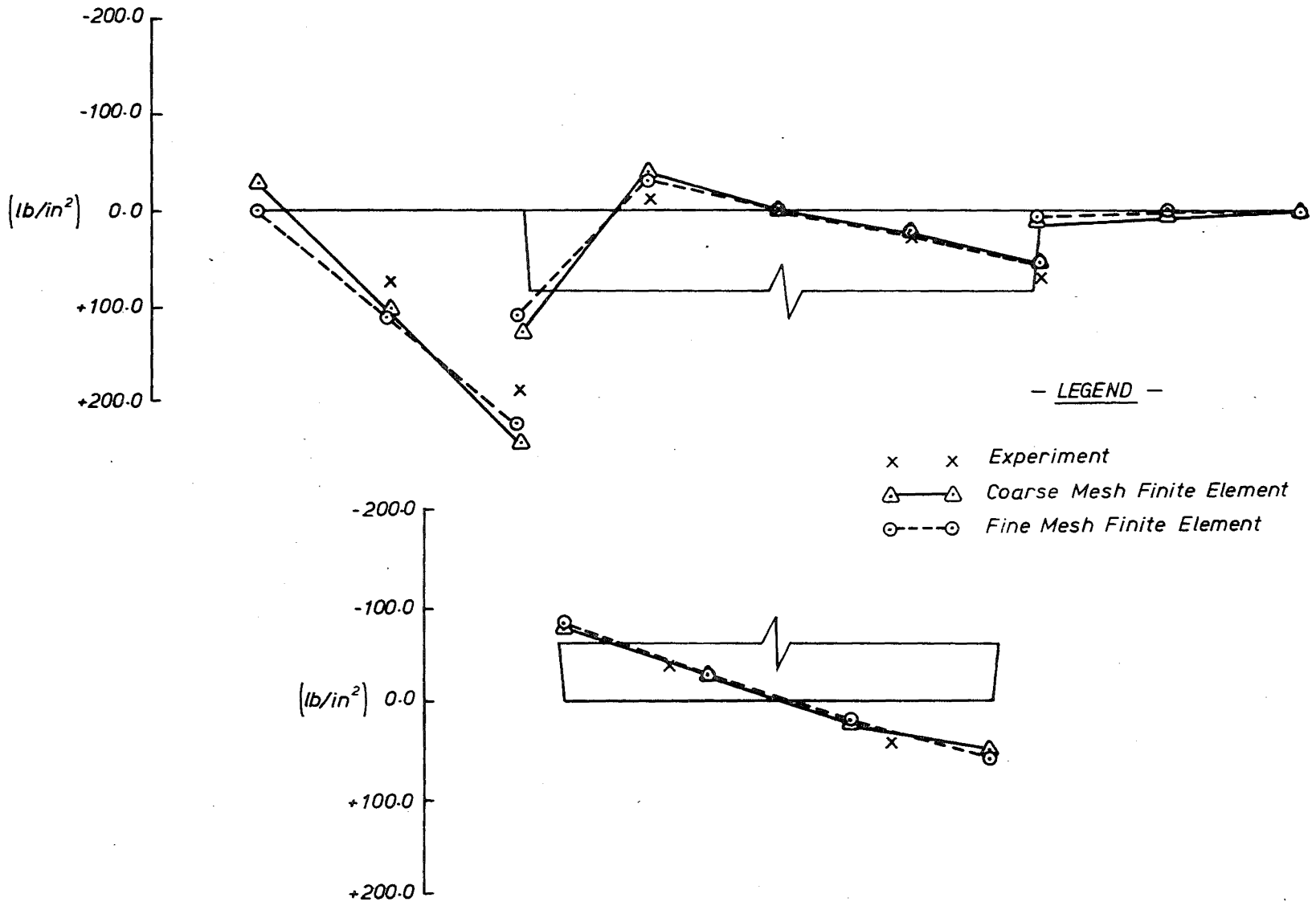

FIGURE IX-9.7 TRANSVERSE STRESSES ALONG TOP OF DECK AND SOFFIT SLABS

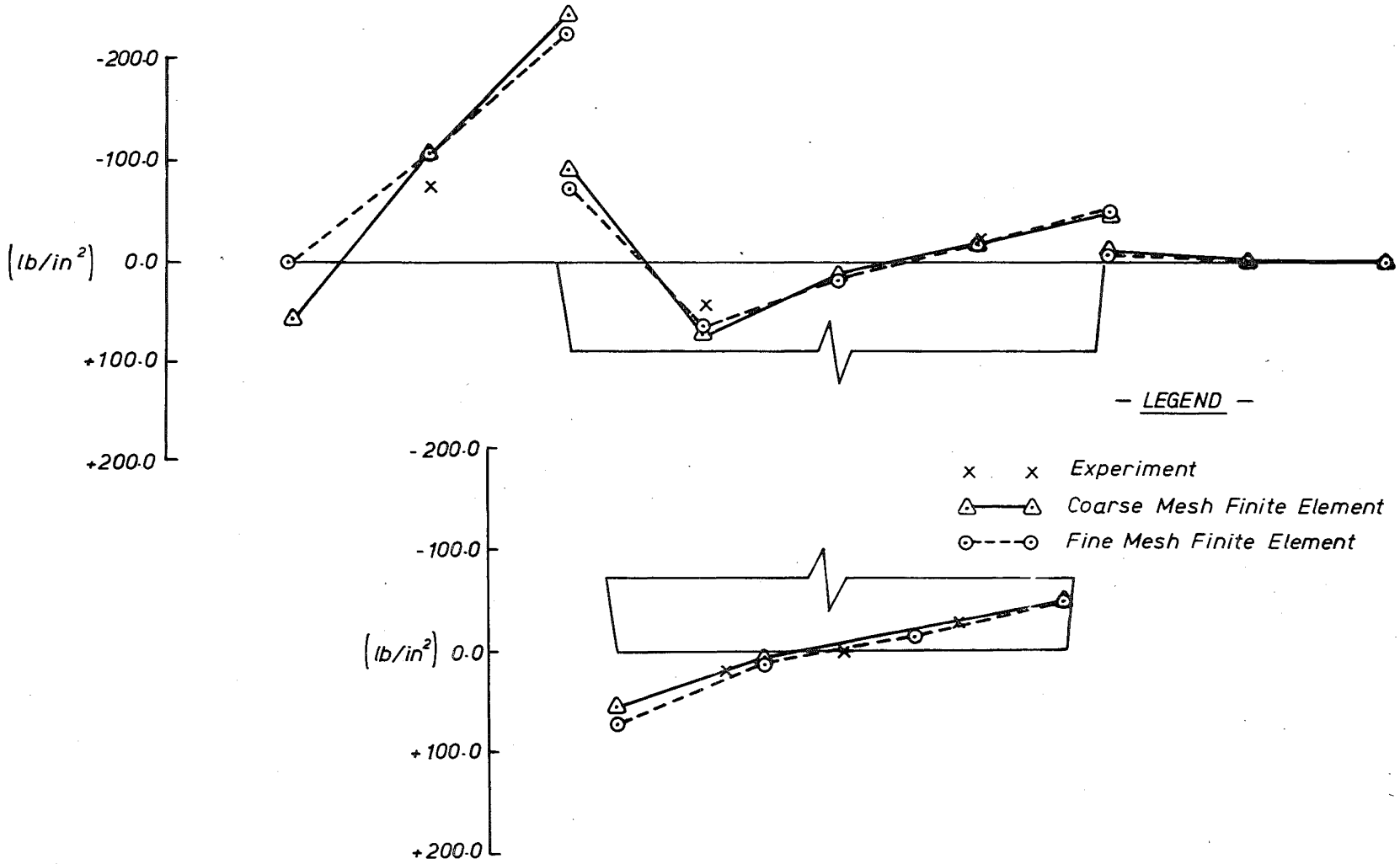

FIGURE IX-9.8 TRANSVERSE STRESSES ALONG BOTTOM OF DECK AND SOFFIT SLABS

ii) Transverse stresses.

The transverse stresses down the webs, across the top of the deck and soffit slabs,and across the bottom of the deck and soffit slabs, are plotted in Figures IX-9.6, IX-9.7 and IX-9.8 respectively. Both meshes of elements give a good representation of the transverse stresses with finite element results in agreement to within 10% of the experimental values except that a 38% maximum discrepancy is evident across the outside cantilever.

Only a marginal improvement in the accuracy of the results was obtained when the finite element mesh was refined so it is concluded that the coarse mesh idealisation provides the most suitable representation for the purposes of economical structural analysis.

IX-10 BOWEN STREET OVERPASS (BSOP)

IX-10.1 Description of structure

A plan view of the Bowen Street Overpass, which consists of both a southbound and a northbound multi-cell prestressed concrete box-girder structure, each continuous over two spans and with a small horizontal curvature, is shown in Fig. IX-10.1. Only the southbound bridge, which reduces in width to the south, is analysed here.

A typical cross-section is composed of three trapezoidal single cell spines joined by cantilever deck slab extensions, as shown in Fig. IX-10.2. However, in the vicinity of the central piers the section increases in depth and is changed in composition from three spines to a five cell single spine form by the incorporation of inclined slabs, extending from the deck slab to the soffit slab between the three existing spines, as illustrated in Fig. IX-10.3.

The following elastic material properties were assumed for the concrete:- $E = 62.5 \times 10^6$ lb/in^2 (43.5 GPa), $\nu = 0.15$.

Priestley and Miles [78] installed a number of vibrating wire strain gauges and Hewlett Packard 7 DCDT - 1000 displacement transducers across the transverse sections H - H and J - J (see Figures IX-10.4 to IX-10.6) from which they measured the strain and deflection response when the bridge was subjected to simulated truck loading. The four wheel loads of the design truck load discussed in Section IX-10.3 were represented as a number of 10 tonne blocks of concrete Kentlidge [78]. Experimental measurements were recorded for three different locations of the 'truck' across a section 96 ft (29.2 m) from the central supports, on the southern span of the southbound bridge.

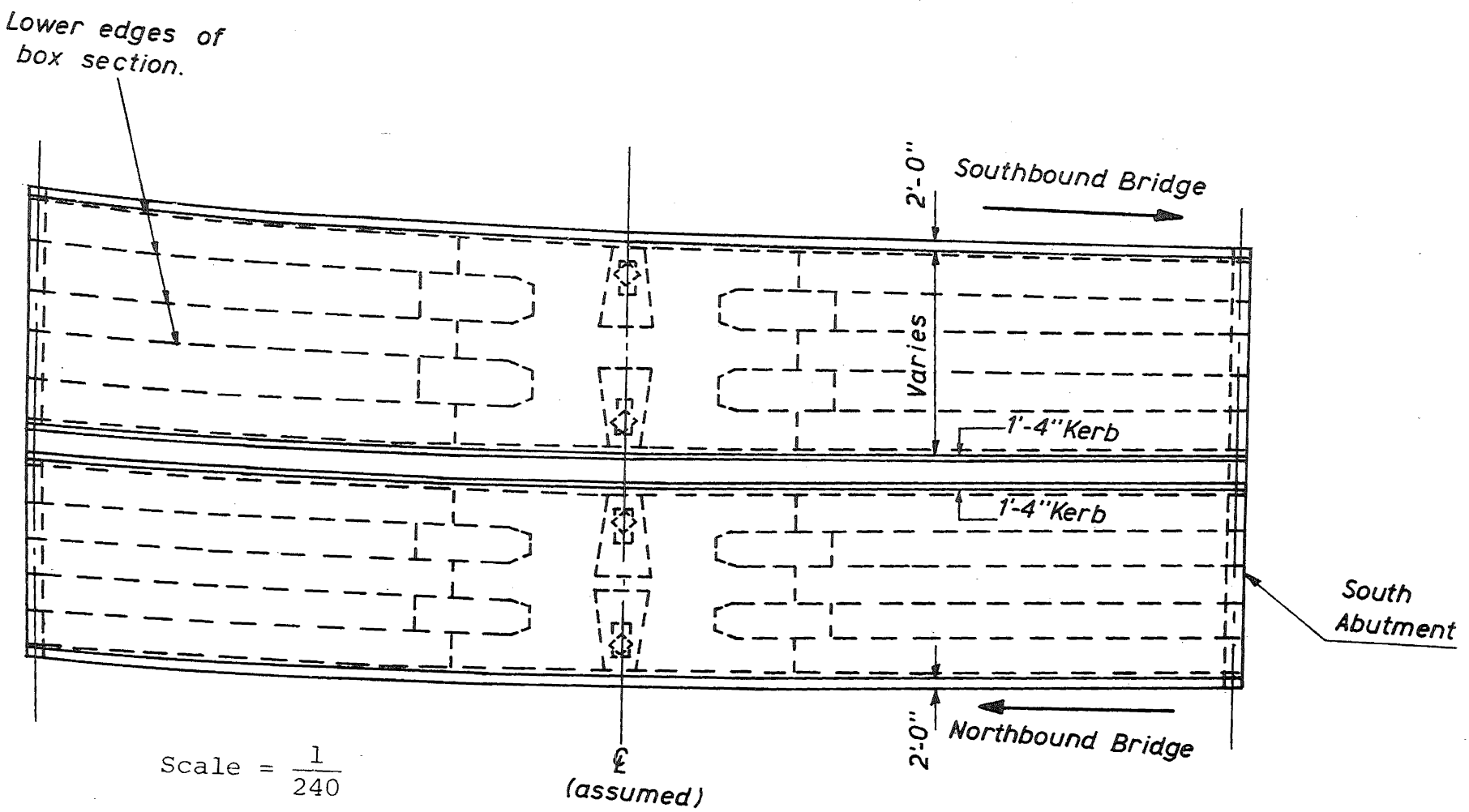

FIGURE IX-10.1 PLAN VIEW OF BOWEN STREET OVERPASS

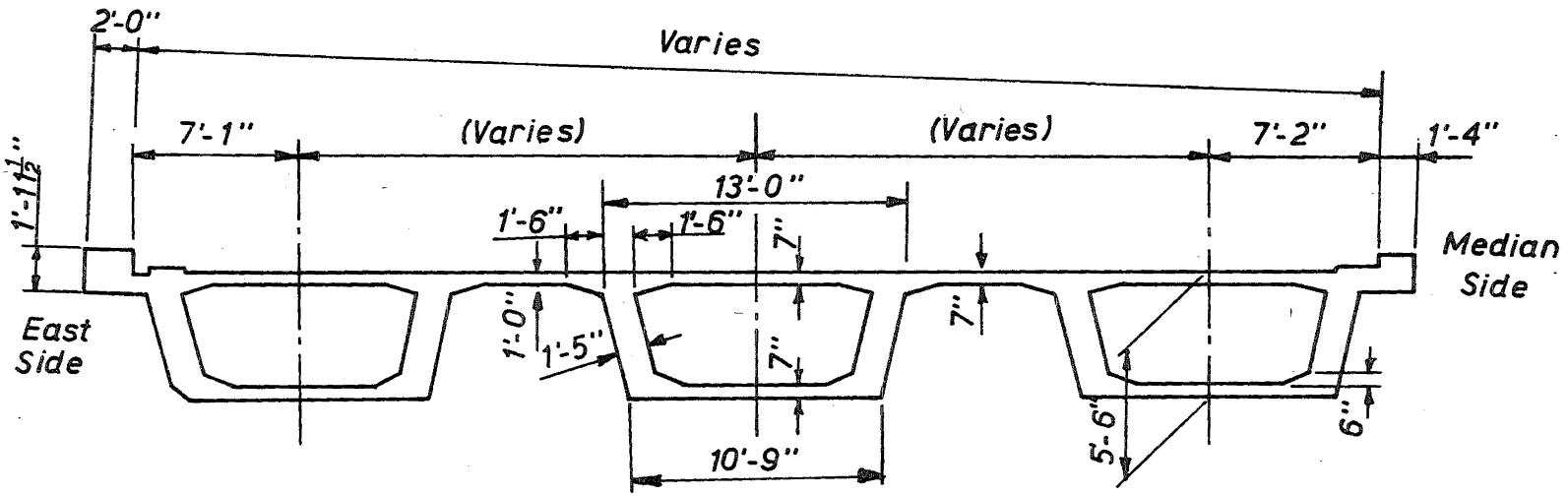

FIGURE IX-10.2 DIMENSIONS OF A TYPICAL CROSS SECTION SOUTH BOUND BRIDGE OF BSOP

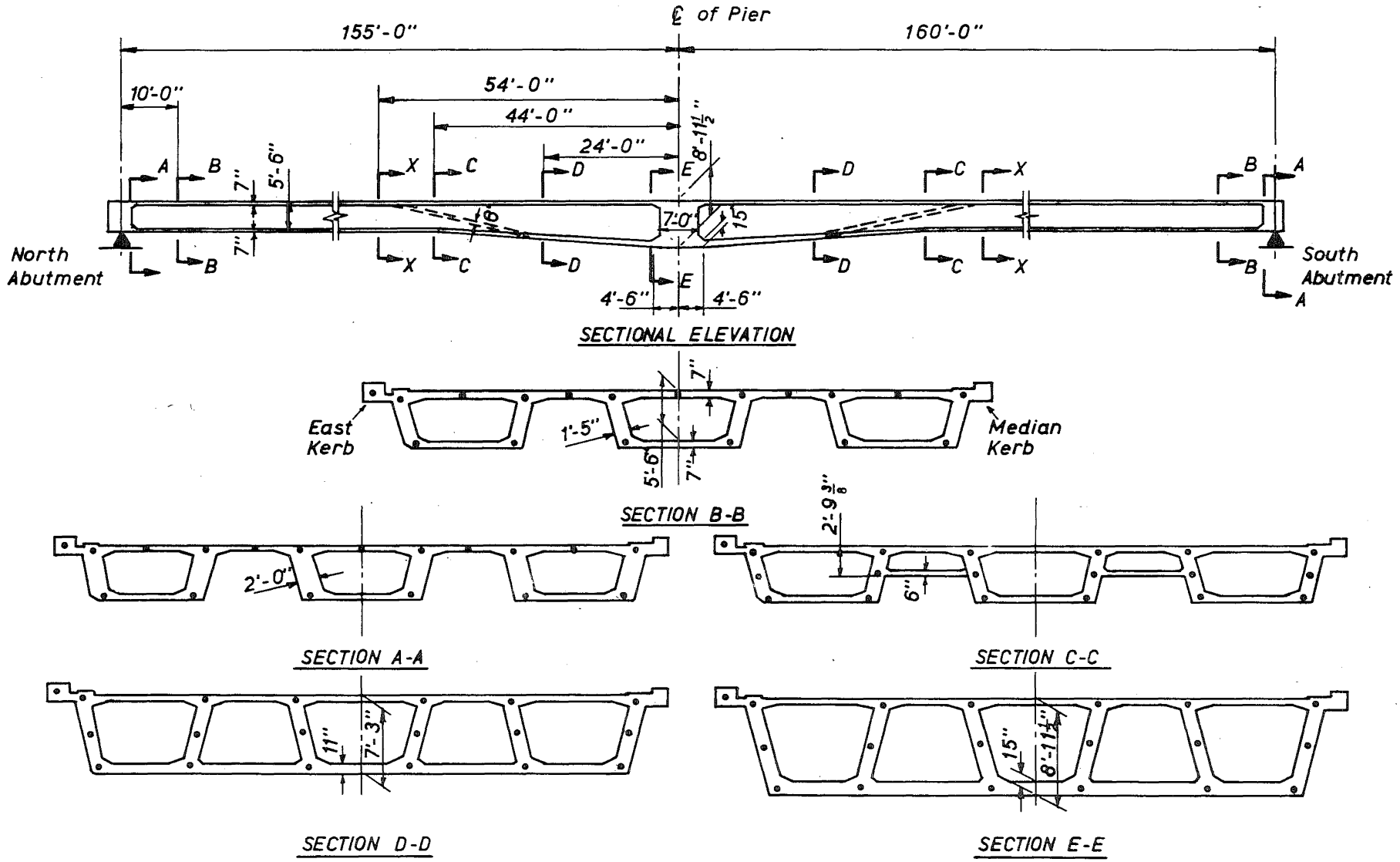

FIGURE IX-10.3 TRANSVERSE DISTRIBUTION OF FINITE ELEMENT NODES

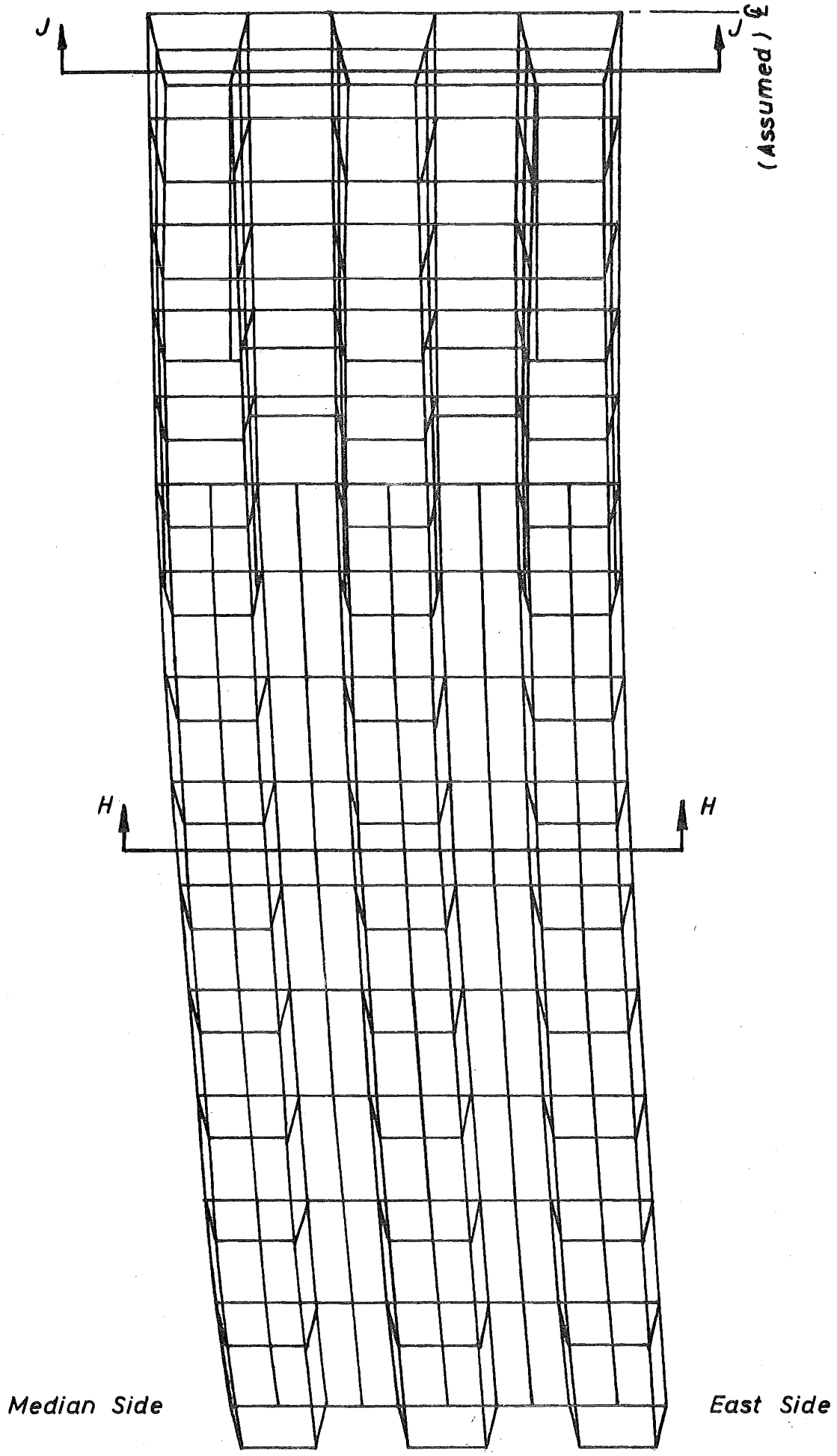

FIGURE IX-10.4 FINITE ELEMENT MESH ; SOUTHERN SPAN

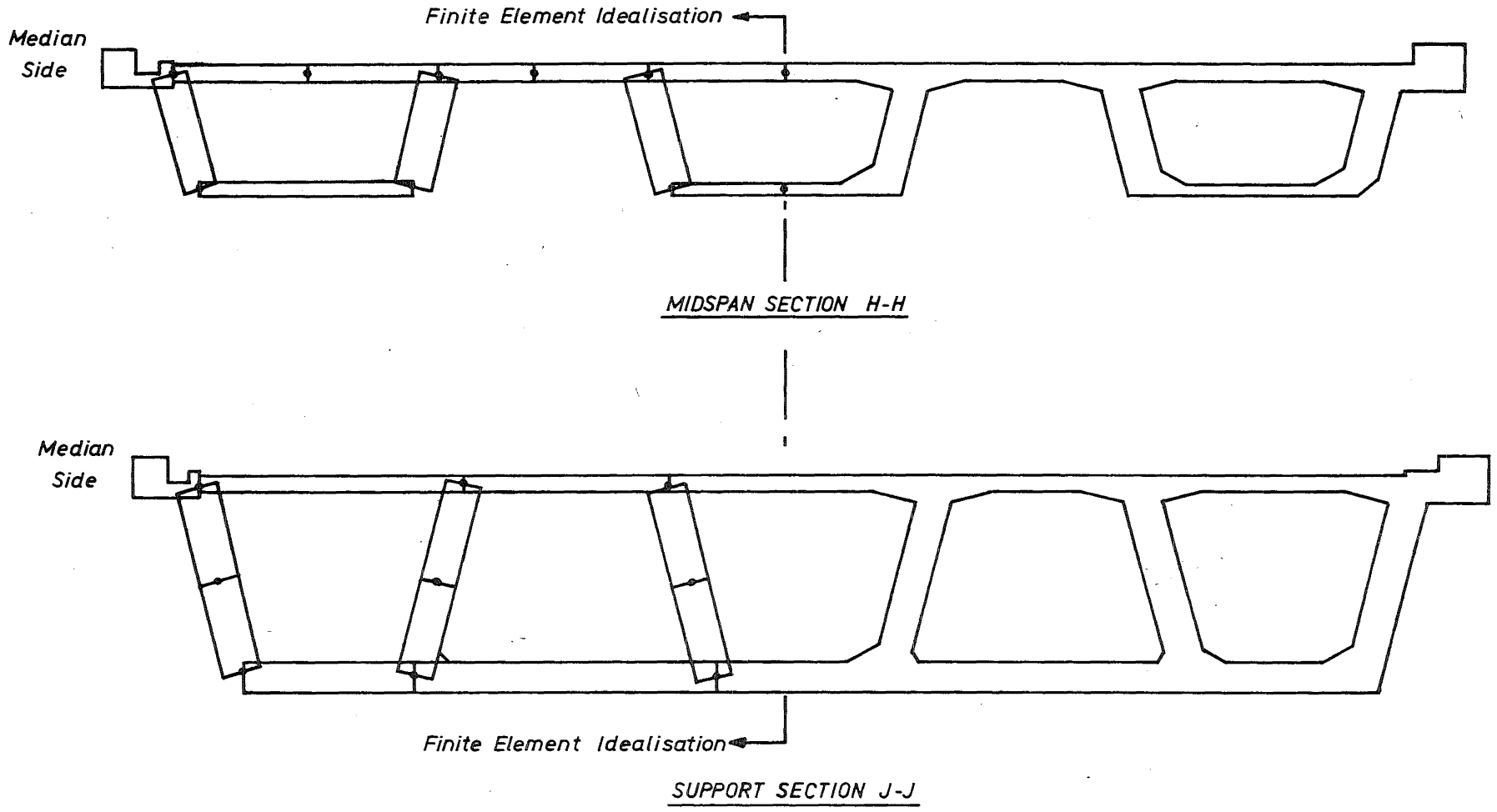

FIGURE IX-10.5 FINITE ELEMENT IDEALISATION OF TYPICAL SECTIONS

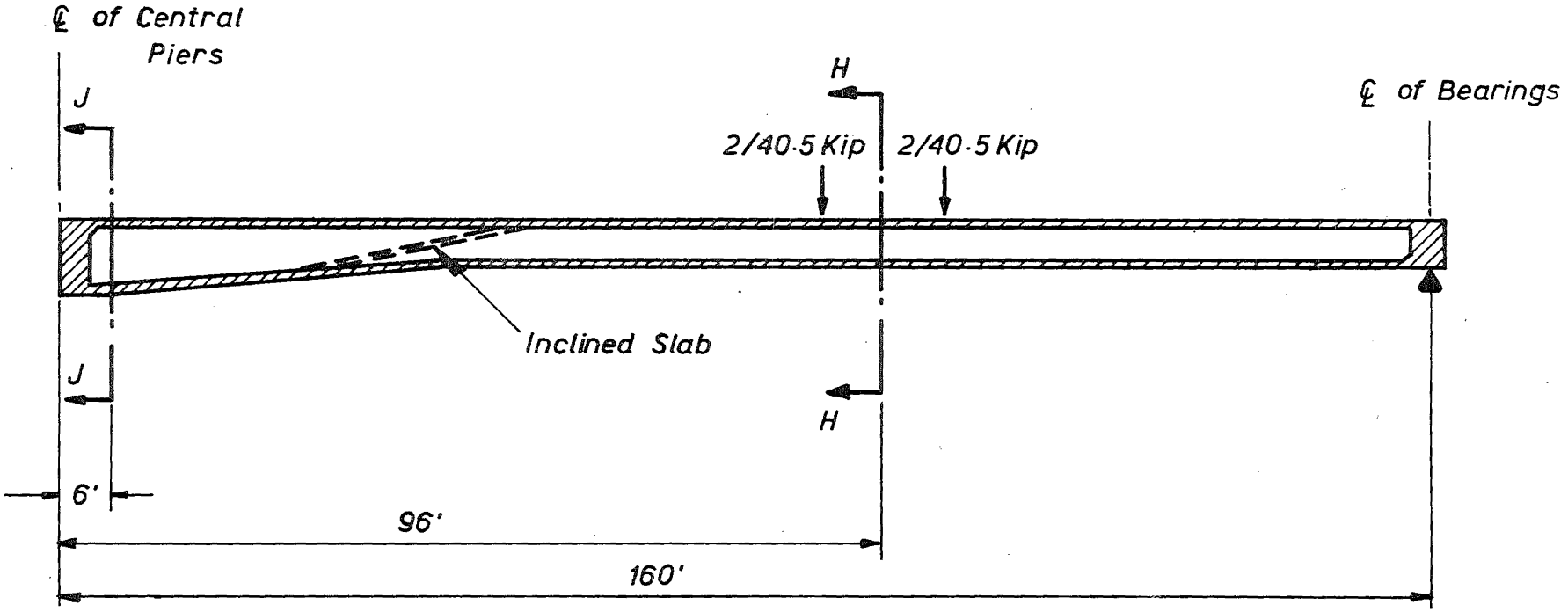

FIGURE IX-10.6 ELEVATION

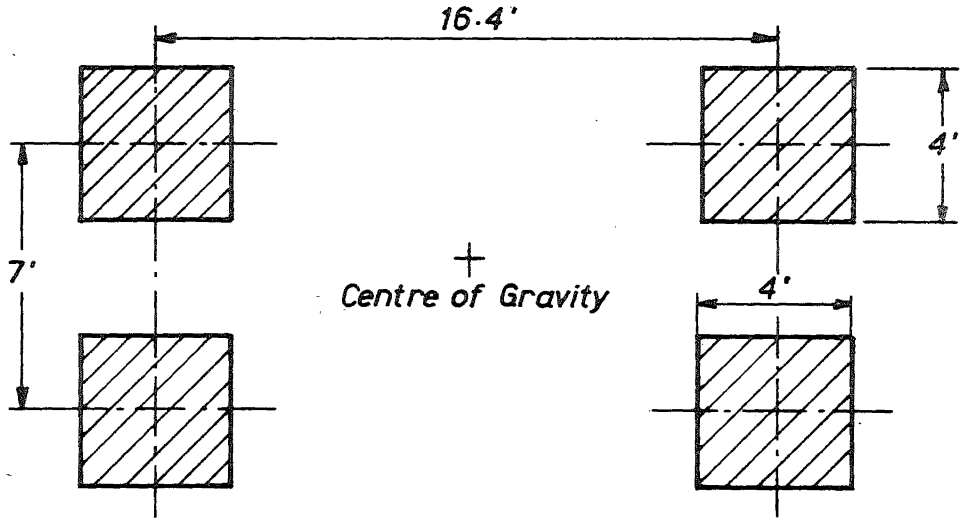

FIGURE IX-10.7 H.O. LIVE LOAD ELEMENT (4/40.5 KIP LOADS)

IX-10.2 Finite element idealisation

The experimental results are compared with those obtained from a finite element analysis using the mesh shown in Fig. IX-10.4. A line of symmetry was assumed about the line of the central supports, the truck loads resolved into symmetric and antisymmetric components, and the results superimposed. Although the width of the southbound bridge reduces slightly to the south (see Fig. IX-10.1), and the two spans have a 3% difference of length, the assumption of symmetry about the line of central support appears to have no more than a small effect upon the theoretical results because these results are in close agreement with those measured experimentally.

The transverse distribution of nodal points employed across five representative sections is illustrated in Fig. IX-10.3. The number of elements down the depth of the webs was increased from one to two at section X - X, and the number of elements across the deck slab correspondingly reduced in order to maintain a constant number of nodes across the section, and thus maintain a constant bandwidth of the structural stiffness matrix. This was achieved by employing the mesh grading technique described in Chapter V, and enabled the incorporation of a comparatively fine mesh of elements across the deck slab under the region of the truck loads, and a better simulation of the web behaviour near the central supports where the stress gradients are larger.

The finite element idealisation of two typical cross-sections is illustrated in Fig. IX-10.5. The small fillets at the junction of the flanges and the webs were neglected, but the increase in thickness of the soffit slab near the central support (see Fig. IX-10.3) was incorporated by using elements with longitudinally tapered thickness. The kerbs were represented with beam elements connected to the section via eccentric nodes.

IX-10.3 Loading conditions

The centre of gravity of each of the truck loads was located across section H - H near midspan (see Fig. IX-10.6) at the transverse positions shown in Figures IX-10.8, IX-10.9 and IX-10.10 corresponding to load cases A, B, and C respectively. The spacing and dimensions of the contact areas of the four 'wheels' were according to the M.W.D. design brief [62] and are described in Fig. IX-10.7. The magnitudes of the wheel loads were increased to 1.5 times the overload specifications (H.O.) to decrease the percentage error of the strain readings which were

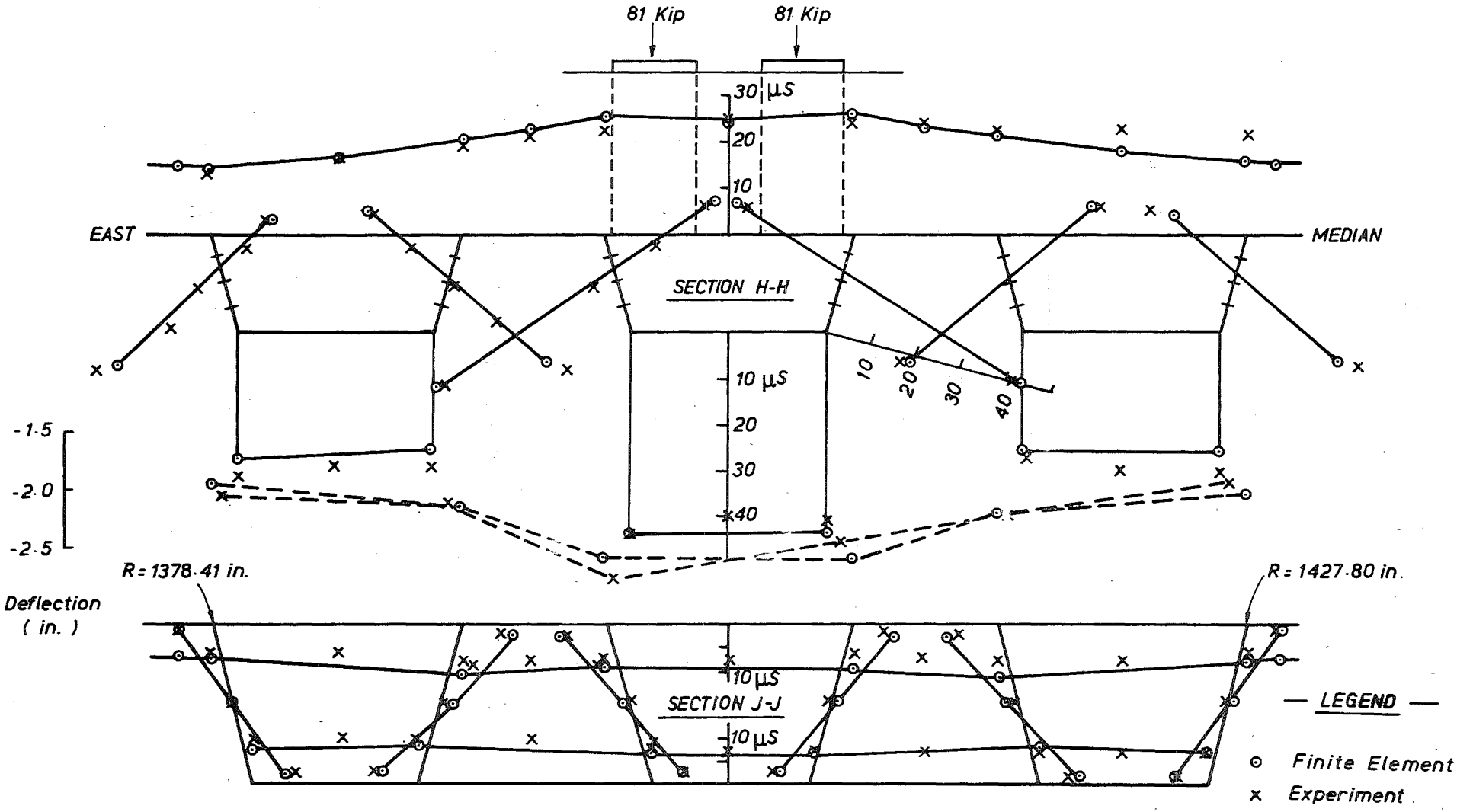

FIGURE IX-10.8 LONGITUDINAL MEMBRANE STRAINS AND DEFLECTIONS
LOAD CASE A

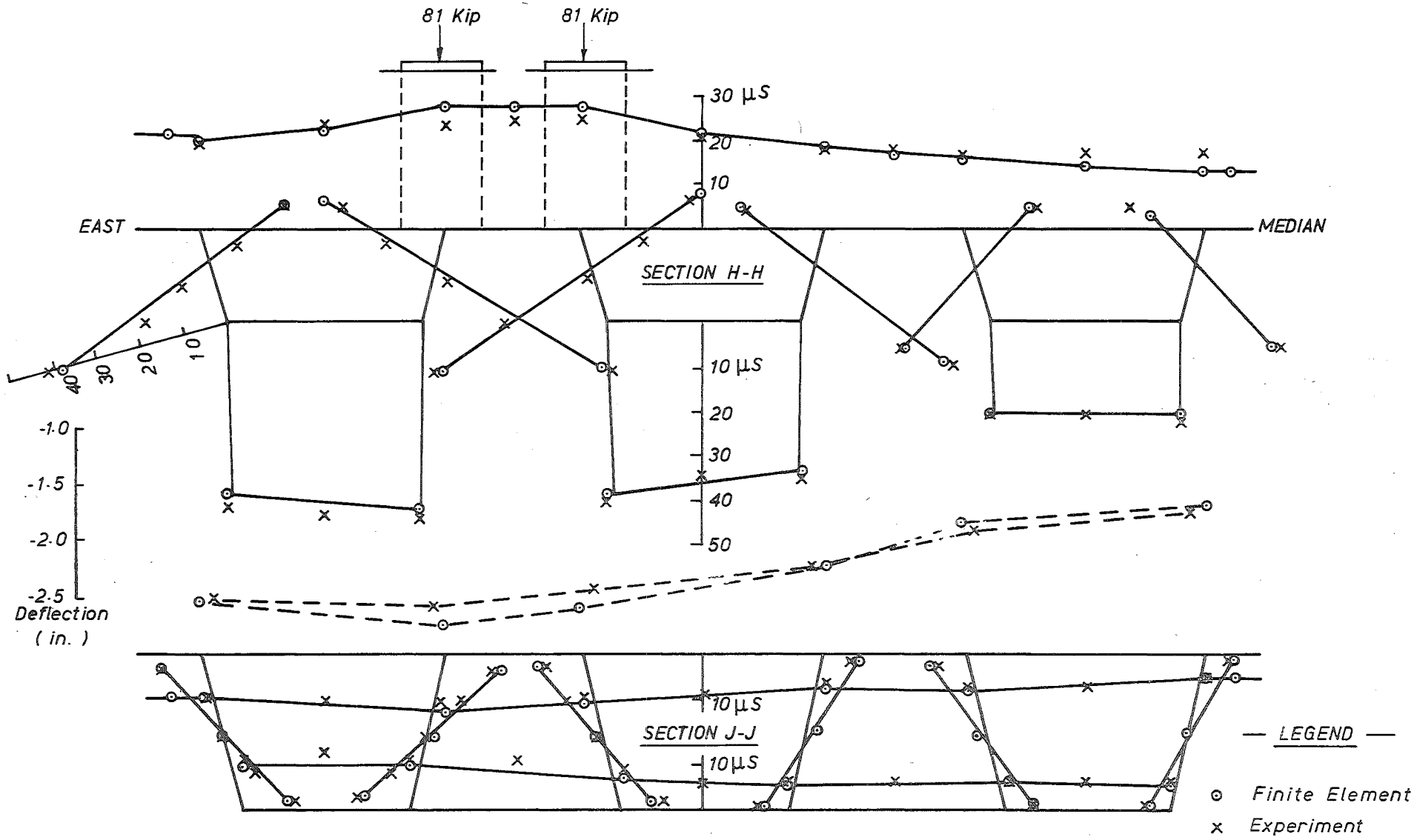

FIGURE IX-10.9 LONGITUDINAL MEMBRANE STRAINS AND DEFLECTIONS
LOAD CASE B

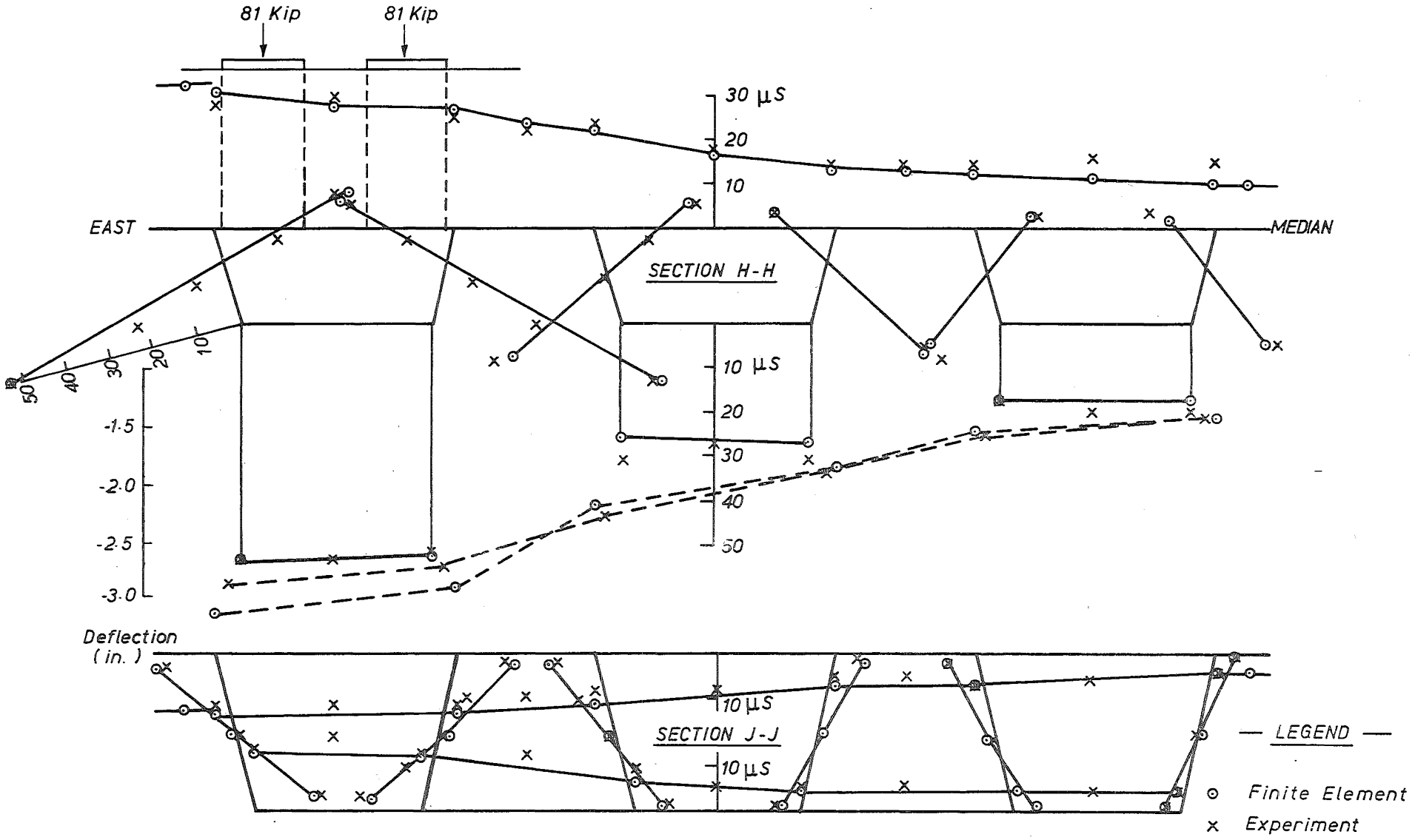

FIGURE IX-10.10 LONGITUDINAL MEMBRANE STRAINS AND DEFLECTIONS
LOAD CASE C

accurate to $\pm$ 2.0 μs (microstrains).

Each wheel load was represented by a statically equivalent system of four point loads for the finite element analyses. The equivalent nodal forces and bending moments were derived in a manner consistent with the formulation of the element stiffness matrix [1].

IX-10.4 Comparison of results

The distributions of experimental and theoretical longitudinal membrane strains and deflections across sections H - H and J - J (see Fig. IX-10.6) are plotted in Figures IX-10.8, IX-10.9, and IX-10.10 for load cases A, B, and C respectively. Agreement is excellent and although the discrepancy, expressed as a percentage, is larger across section J - J, this is to be expected because the strains along this section are small, generally less than 10 μs, and the repeatability error of the experimental results was calculated by Priestley [78] to be $\pm$ 1 μs , i.e., generally greater than $\pm$ 10%.

i) Load case A.

The experimental and theoretical longitudinal strains across section H - H agree to within 13% except across the deck slab of the western (median) cellular spine where the theoretical strains are 27% smaller. A discrepancy of this magnitude is evident for all three load cases and may be due to: i) the assumption of symmetry about the central piers. ii) local variations of Young's modulus of elasticity of the concrete material.

iii) lack of precision in the vertical location of the strain gauges.

There is also a variance between the measured and computed membrane strains across section J - J where the finite element strains are generally 20% larger across the deck slab and 10% smaller across the soffit slab. This discrepancy may be partially due to the assumption made during the finite element idealisation that the section haunch continues through to the central supports. This haunch was terminated at a distance of 6 ft. from the line of the central support for the real structure, as shown in Fig. IX-10.6.

The experimental and theoretical deflections across section H - H agree to within 5.5%.

ii) Load case B.

The experimental and theoretical longitudinal strains across section H - H agree to within 10% except:-

a) at the top of the inside web of the east cellular spine where there is a 19% discrepancy, and
b) across the deck slab of the western cellular spine, as discussed previously.

There is a maximum discrepancy between longitudinal membrane strains across section J - J of 18%, and between deflections across section H - H of 5.5%.

iii) Load case C.

The experimental and theoretical longitudinal membrane strains across section H - H agree to within 11% except across the deck slab of the western cellular spine as discussed previously.

The longitudinal membrane strains across section J - J agree to within 21%, and the maximum discrepancy between theoretical and experimental deflections across section H - H is 8%.

Young's modulus of elasticity, E, for the concrete material was calculated to be 63.5 x 10^6 lb/in^2 (43.5 GPa) by scaling an arbitrarily chosen value of E for the finite element analysis so the average computed deflections and strains corresponded with the measured response. This calculated value of Young's modulus is much larger than the value of E = 50.0 x 10^6 lb/in^2 (35.0 GPa) measured from the 28 day strength of concrete cylinder samples [78]. Therefore the modulus of concrete measured from cylinder samples during the construction of this structure does not represent the modulus of the reinforced concrete when it is cast "en masse".

IX-11 CUMBERLAND STREET OVERPASS

IX-11.1 Description of structure

An oblique view of the finite element mesh used for the analyses of the Cumberland Street Overpass (CSOP) is shown in Fig. IX-11.1. This bridge, which trifurcates at one end and bifurcates at the other, is to be constructed as a prestressed concrete box-girder structure for the Dunedin City Corporation, and is to span the Dunedin railway yard.

The bridge is supported on four rows of bearing pads which provide vertical restraint only, except for the two central rows at sections C - C and E - E where transverse restraint is also provided by the bearings. The longitudinal restraint of the bridge was assumed to be applied at section C - C for the finite element analyses.

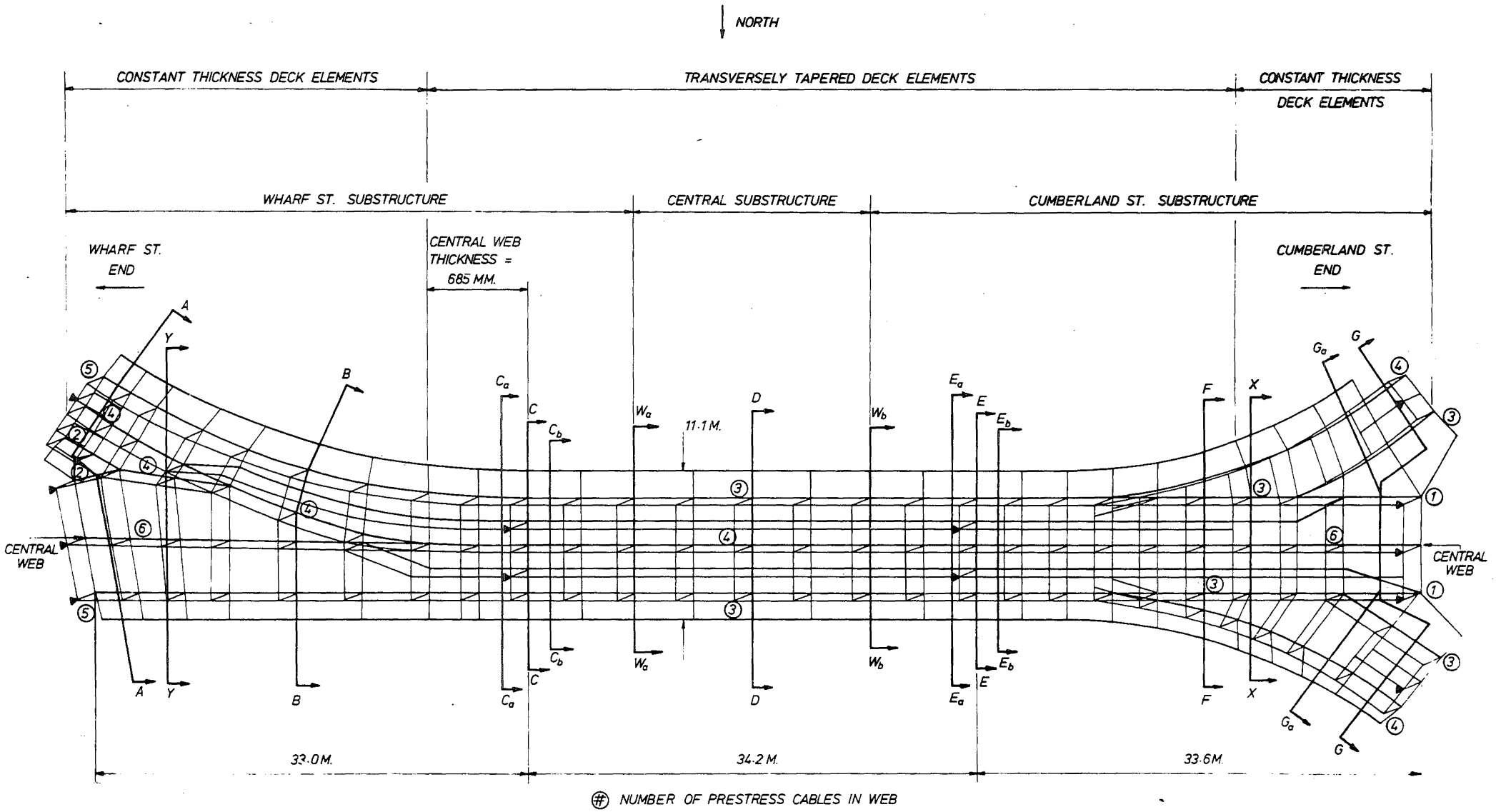

FIGURE IX-11.1 FINITE ELEMENT MESH ; CUMBERLAND STREET OVERPASS

Diaphragms, 910 mm thick, are incorporated at each of the four support sections, and the thickness of the central web is increased from 178 mm to 685 mm for a distance east of section C - C to where this web bifurcates, as shown in Fig. IX-11.1.

The following elastic material properties were assumed for the concrete; $E = 33.0$ GPa, $\nu = 0.15$.

IX-11.2 Finite element idealisation

The finite element idealisations employed for three typical cross-sections; sections X - X, D - D, and Y - Y are illustrated in Figures IX-11.2a, IX-11.2b, and IX-11.2c respectively. Tapered elements with thickness varying transversely from 178 mm to 295 mm were used to represent the tapered cantilever slabs and haunched deck slabs, except over a region of the end spans (see Fig. IX-11.1) where only one element was used to span across the top and bottom of each cell. Constant thickness elements of the same cross-sectional area were used to represent the deck slabs here, and small haunches were neglected. The cross-sectional area of the idealised sections X - X, D - D, and Y - Y are in error by only + 2.4%, + 1%, and - 0.2% respectively, and the second moments of inertia of these idealised sections are in error by + 0.3%, + 4.5%, and + 1.2% respectively. The 152 mm transverse variation of soffit levels was neglected for the finite element idealisation of the bridge.

The two outside boxes at the trifurcating Cumberland St. end of the structure (see Fig. IX-11.1) are to be continued as multispan off-ramp structures via a pin-jointed connection. The effect of this continuity was simulated in the finite element analysis by supporting these boxes on 354 mm square strut elements of 4.7 m and 5.1 m length for the south and north boxes respectively. These dimensions were calculated to provide the same vertical stiffness as the off-ramp structure.

Each wheel load was assumed to act as a single point load and was represented as a set of nodal loads for the finite element analyses, using a distribution consistent with the formulation of the element stiffness matrix [1].

Uniformly distributed dead loading across an element was represented as a set of nodal loads by dividing the quadrilateral element along both diagonals to form two sets of two triangles and half the load on each triangle distributed equally to its three nodes.

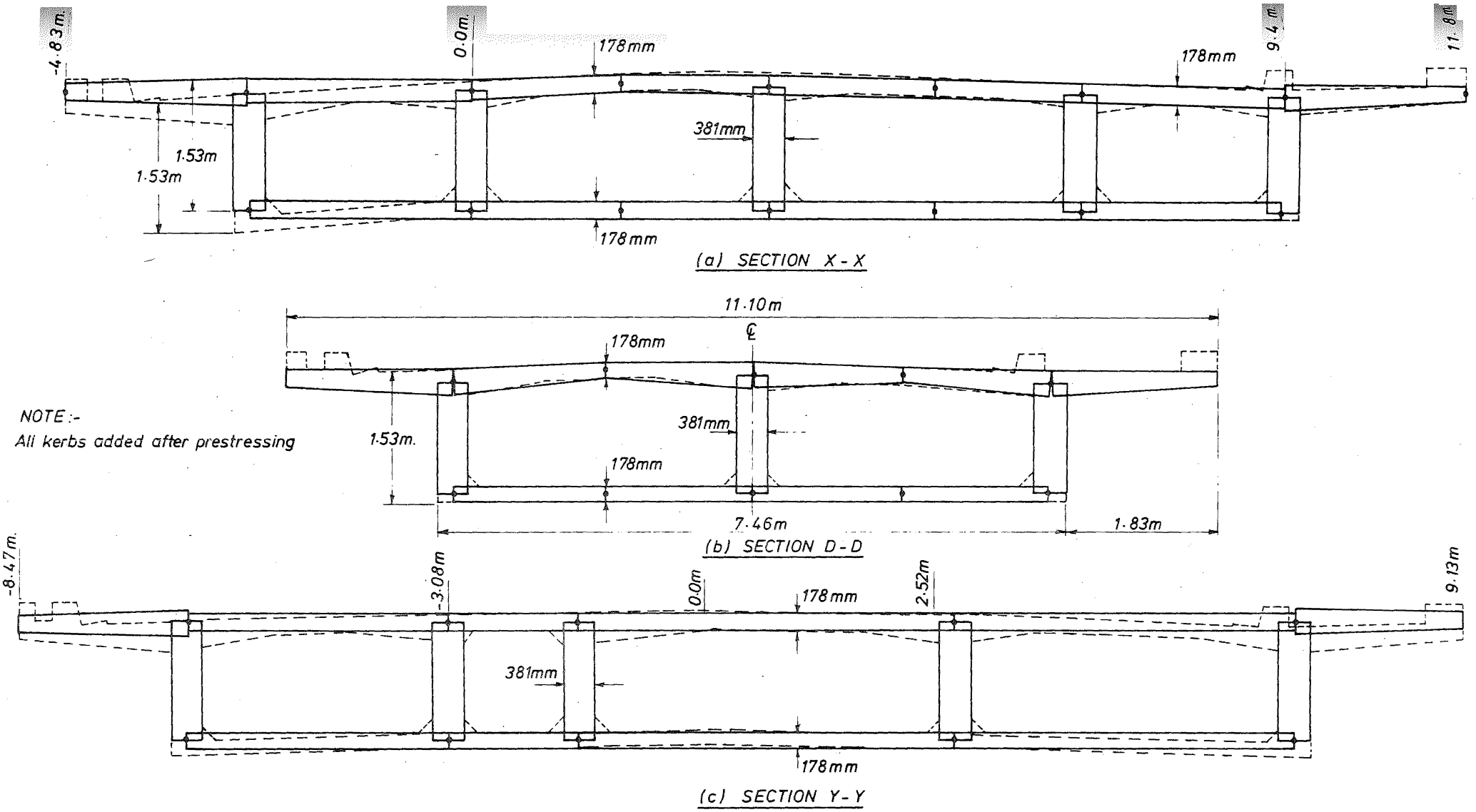

FIGURE IX-11.2 FINITE ELEMENT IDEALISATION OF TYPICAL SECTIONS

IX-11.3 Loading conditions

The bridge is to be constructed as three substructures, separated at sections Wa - Wa and Wb - Wb (see Fig. IX-11.1) and made continuous by passing prestressing cables through these sections. Thus the load cases considered were:-

i) Dead loading of Wharf Street Substructure.

ii) Dead loading of Cumberland Street Substructure.

iii) Dead loading of Central Substructure.
(The three substructures were then joined via 'pin' connections).

iv) Half of the dead load of the Central Substructure acting as a cantilever load on Wharf Street Substructure.

v) Half of the dead load of the Central Substructure acting as a cantilever load on Cumberland Street Substructure.
(Complete continuity between the three substructures was then achieved by prestressing).

vi) Prestressing of the total structure, CSOP. The system of prestressing cables was designed to balance dead load.

vii) Dead load of CSOP. The weight of the structural concrete only was considered to act as dead load and the density of the concrete was assumed to be 24.4 kN/m^3.

viii) Temperature effects. A vertical temperature gradient with a sixth power distribution from 40°C at the top surface of the deck slab to 10°C at the bottom surface of the soffit slab, according to the Ministry of Works and Development design brief [62] was approximated as follows; A linear distribution from 10°C at the bottom of the webs to 16°C at the top of the webs was assumed, and the gradient of the linear temperature distribution assumed through the deck slab was adjusted according to the slab thickness so as to provide the correct extreme fibre temperatures. The concrete was assumed to have a coefficient of thermal expansion of $10.8 \times 10^{-6}/°C$.

ix) Live load. Four 60 kN wheel loads (per Ministry of Works and Development design brief [62])were centred above the south web at the centre of the Wharf Street end span. The spacing and contact areas of the design loads are shown in Fig. IX-10.7.

The analyses of these structures were performed with the additional purpose of providing the designers with an extensive knowledge of the theoretical behaviour of the bridge, so a large number of loading

cases were considered. The results from three further live load cases are not presented here, for reasons of brevity.

IX-11.4 Results

Finite element results are presented in the form of longitudinal distributions of deflection and extreme fibre longitudinal stresses along the central web (except for the live load case where the distributions are plotted along the loaded web), and the transverse distributions of deflection, longitudinal stress, and transverse stress across the midspan sections B - B, D - D, F - F, and the support sections of the bridge. Longitudinal stresses predicted from a grid analysis, performed by the Dunedin City Corporation in the course of a preliminary design, are included for comparison. These latter results are presented for substructure dead loading and temperature loading, and were derived using a technique where the bridge is simulated as a grid of beam elements, having degrees of freedom w, θx, and θy at each node [79], with a row of nodes located along the line of each web.

The legend used to present these results is described in Table IX-11.1 which folds out from page 213 for easy reference.

i) Dead loading of Wharf St. Substructure.

Figure IX-11.3a shows the computed longitudinal distributions of deflection and extreme fibre longitudinal stresses along the central web (the configuration of the central web is defined in Fig. IX-11.1). The distributions are of a similar form to those predicted from simple beam theory for a simply supported prismatic structure, except that a degree of rotational constraint exists at the Wharf St. end due to the influence of the bifurcation of the bridge. This constraint results in a complex stress distribution in this region which could only be represented accurately by refining the element idealisation here.

The transverse distributions of deflection and longitudinal stress across sections B - B and Cb - Cb are plotted in Figures IX-11.4a and IX-11.5a respectively, and the distributions of transverse stress across these sections are plotted in Figures IX-11.6a and IX-11.7a respectively. The extreme fibre longitudinal stresses across section B - B calculated from the grid analysis are also plotted in Fig. IX-11.4a. The average longitudinal stresses across the top of the deck slab, predicted from the two theories, agree to within 10%, while across the bottom of the soffit slab there is a discrepancy of less than 5% of the average longitudinal stress.

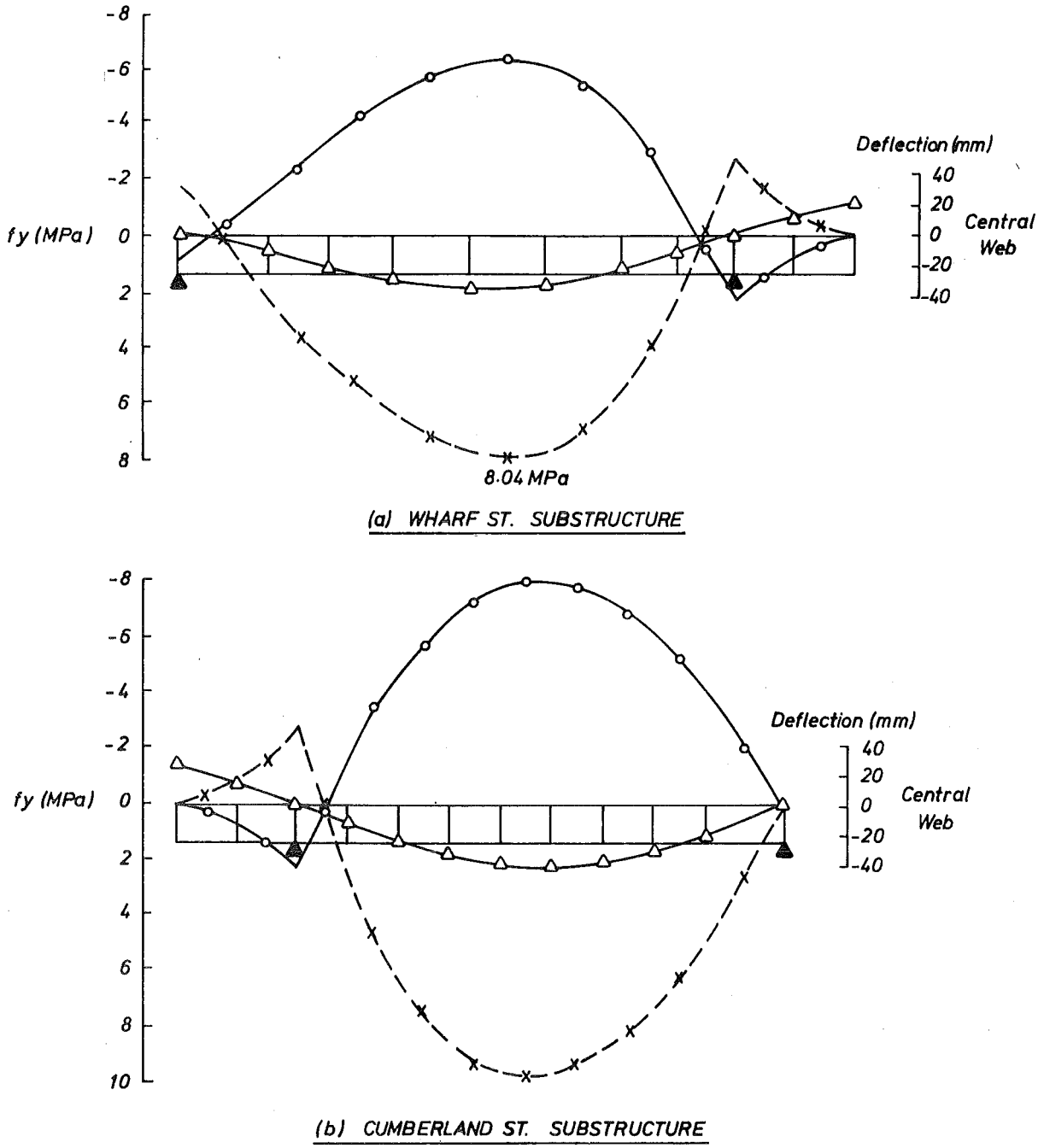

FIGURE IX-11.3 SUBSTRUCTURE DEAD LOADING
LONGITUDINAL DISTRIBUTION OF LONGITUDINAL STRESS AND DEFLECTION

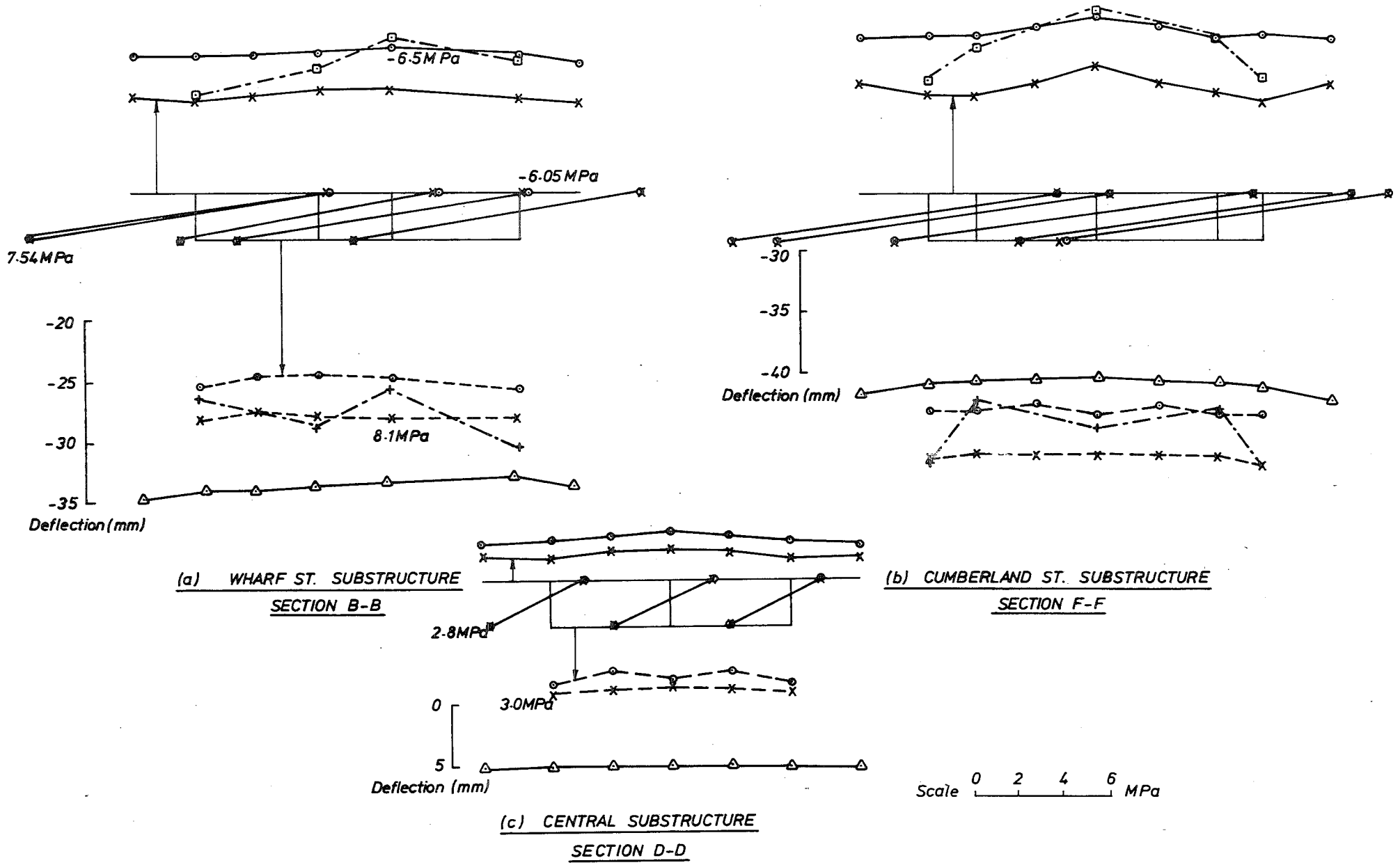

FIGURE IX-11.4 SUBSTRUCTURE DEAD LOADING
LONGITUDINAL STRESS AND DEFLECTION ACROSS MIDSPAN SECTIONS

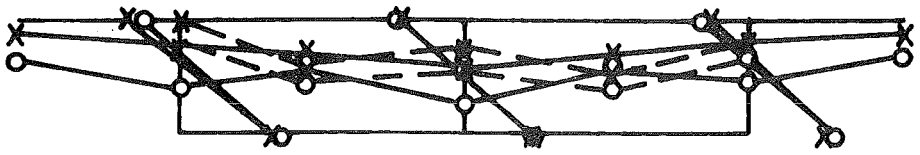

(a) WHARF ST. SUBSTRUCTURE

SECTION C_b-C_b

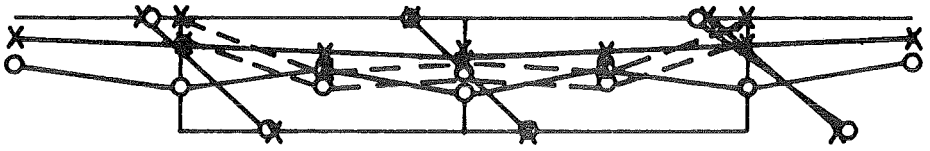

(b) CUMBERLAND ST. SUBSTRUCTURE

SECTION E_a-E_a

Scale 0 2 4 6 MPa

FIGURE IX-11.5 SUBSTRUCTURE DEAD LOADING
LONGITUDINAL STRESS ACROSS SECTIONS NEAR CANTILEVER ROOT

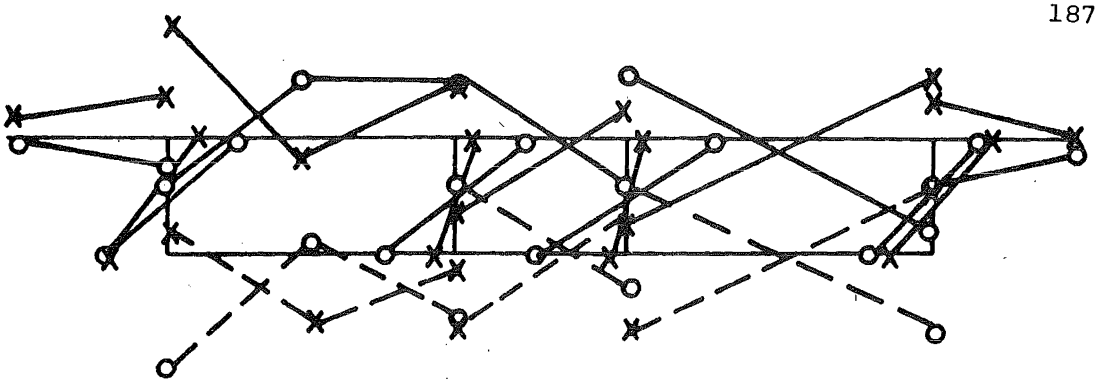

(a) WHARF ST. SUBSTRUCTURE

SECTION B-B

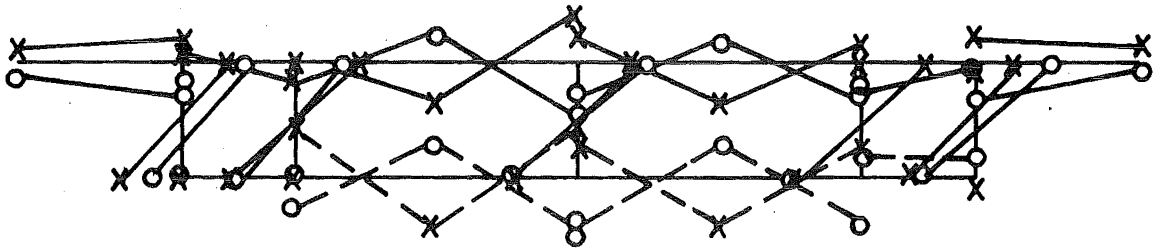

(b) CUMBERLAND ST. SUBSTRUCTURE

SECTION F-F

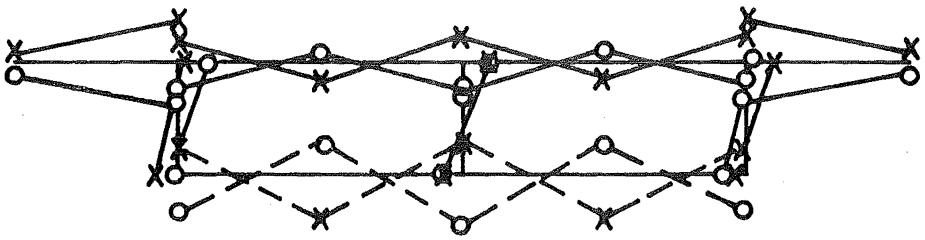

(c) CENTRAL SUBSTRUCTURE

SECTION D-D

Scale 0 2 4 6 MPa

FIGURE IX-11.6 SUBSTRUCTURE DEAD LOADING TRANSVERSE STRESS ACROSS MIDSPAN SECTIONS

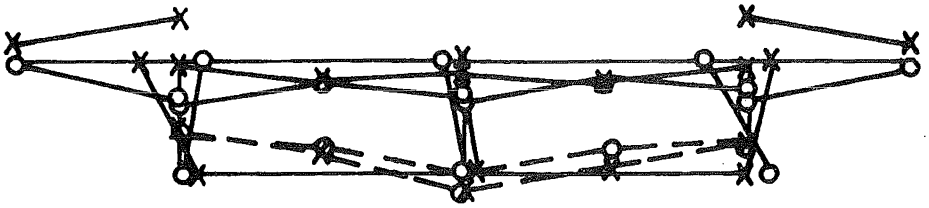

(a) WHARF ST. SUBSTRUCTURE

SECTION C_b-C_b

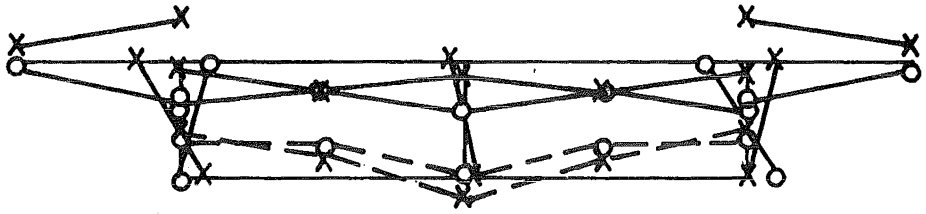

(b) CUMBERLAND ST. SUBSTRUCTURE

SECTION E_a-E_a

Scale 0 2 4 6 MPa

FIGURE IX-11.7 SUBSTRUCTURE DEAD LOADING
TRANSVERSE STRESSES ACROSS SECTIONS NEAR CANTILEVER ROOT

Simple beam theory predicts an average longitudinal tension stress across the top of the deck slab at Section Cb - Cb of 1.0 MPa, and an average compression stress across the bottom of the soffit slab of -1.4 MPa. These stresses are based on the calculated cross-sectional area of the idealised cantilever section of 6.0 m^2, second moment of inertia of 1.9 m^4, and neutral axis 0.83 m above the centroid of the soffit slab. The finite element stresses computed across section Cb - Cb (see Fig. IX-11.5a) correspond closely with the average stresses predicted from simple beam theory.

ii) Dead loading of Cumberland St. Substructure

The computed longitudinal distribution of deflection and extreme fibre longitudinal stresses along the central web are plotted in Fig. IX-11.3b. They correspond closely with the distributions for the Wharf St. Substructure shown in Fig. IX-11.3a.

The transverse distributions of deflection and longitudinal stress across sections F - F and Ea - Ea are plotted in Figures IX-11.4b and IX-11.5b respectively, and the distributions of transverse stress across these sections are plotted in Figures IX-11.6b and IX-11.7b respectively. The extreme fibre longitudinal stresses across section F - F, calculated from the grid analysis, are also plotted in Fig. IX-11.4b. These stresses agree closely with those predicted from the finite element analysis, apart from a 27% discrepancy of deck slab stresses above the outside webs, and a 24% discrepancy of soffit slab stresses below the adjacent inner webs. The transverse distribution of the finite element stresses is more realistically uniform compared with those calculated from the grid analysis.

The stresses computed at section Ea - Ea of the Cumberland St. Substructure (see Figures IX-11.5 and IX-11.7) are virtually identical to those computed at section Cb - Cb of the Wharf St. Substructure except that a small discrepancy of the longitudinal stresses, due to the nonsymmetric support provided to the Wharf St. Substructure cantilever, is evident from a comparison of Figures IX-11.5a and IX-11.5b.

iii) Dead loading of Central Substructure

The distributions of longitudinal stress and deflection and the distribution of the transverse stress, across section D - D of this simply supported, single span, prismatic substructure, are plotted in Figures IX-11.4c and IX-11.6c respectively. The average extreme fibre longitudinal stresses across the midspan section D - D predicted from simple beam theory are -2.1 MPa compression for the top of the deck slab, and 2.9 MPa

tension for the bottom of the soffit slab. The longitudinal stresses shown in Fig. IX-11.4c from the finite element analysis correspond closely with these average beam theory stresses.

iv) Cantilever load, Wharf St. Substructure

The effect of half the self-weight of the Central Substructure distributed across the cantilever end of the Wharf St. Substructure is analysed. This load arises when the Central Substructure is joined to the rest of the bridge via 'pin' connections and temporary supports removed.

The longitudinal profiles of deflection and extreme fibre longitudinal stresses along the central web are illustrated in Fig. IX-11.8a, and the distributions of longitudinal stress and deflection across sections B - B and Cb - Cb are plotted in Figures IX-11.9a and IX-11.10a respectively. Simple beam theory predicts an average longitudinal tension across the top of the deck slab of 2.85 MPa at section Cb - Cb, and an average compression of -4.0 MPa across the bottom of the soffit slab. These average stresses correspond closely with the finite element stresses shown in Fig. IX-11.10a.

The computed distribution of transverse stresses across these sections was uniform, with a maximum value of 0.35 MPa tension across the top of the deck slab, and 0.56 MPa compression across the bottom of the soffit slab at section Cb - Cb.

v) Cantilever load, Cumberland St. Substructure

The longitudinal profiles of deflection and extreme fibre longitudinal stresses along the central web are illustrated in Fig. IX-11.8b, and the distributions of longitudinal stress and deflection across sections F - F and Ea - Ea are plotted in Figures IX-11.9b and IX-11.10b respectively.

The results computed for the Cumberland St. Substructure are virtually identical to the results obtained at the corresponding locations of the Wharf St. Substructure when it was subjected to a transverse line load at the end of the cantilever.

vi) Prestressing

Prestress cables were positioned in the three substructures separately, and additional continuity cables employed to connect these substructures to form the total composite structure (CSOP). The cable forces and profiles were designed by the Dunedin City Corporation with the objective of balancing dead load.

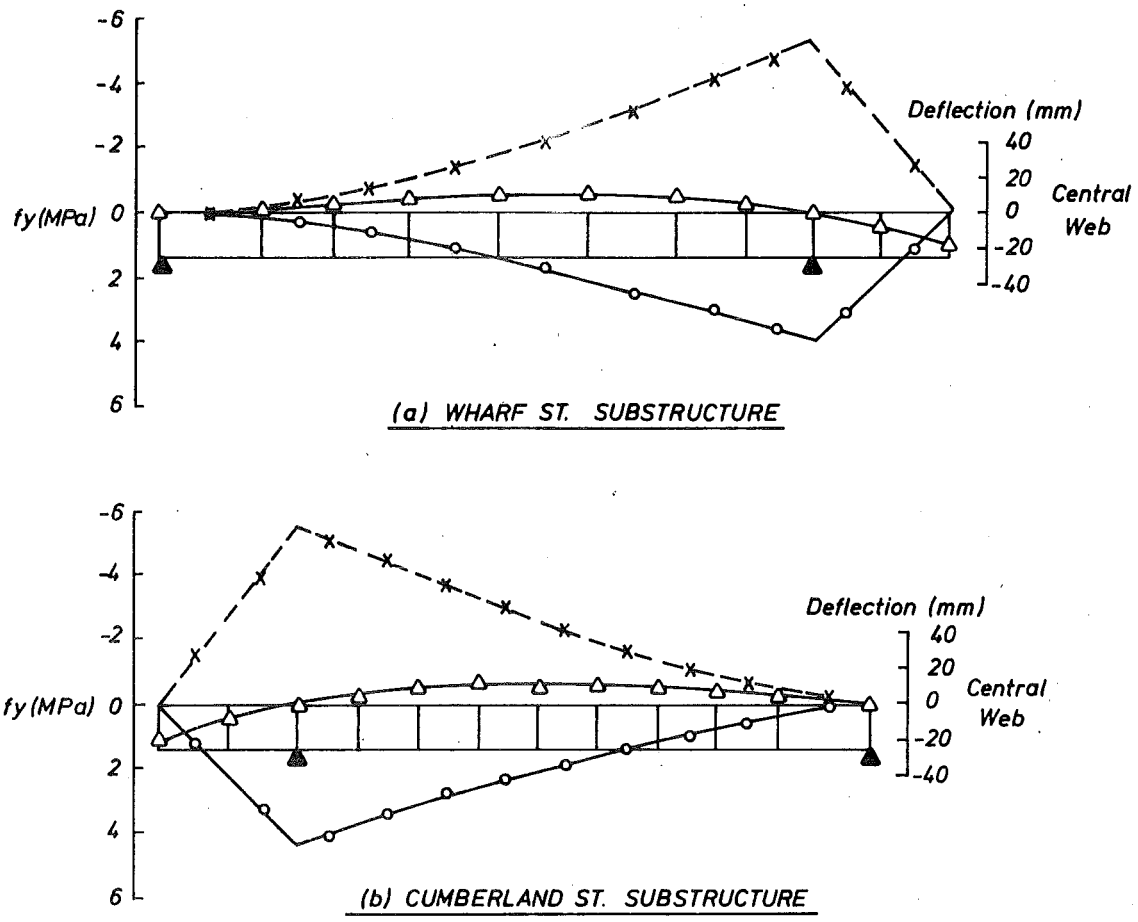

FIGURE IX-11.8 CANTILEVER LOADING OF THE SUBSTRUCTURES
LONGITUDINAL DISTRIBUTIONS OF LONGITUDINAL STRESS AND DEFLECTION

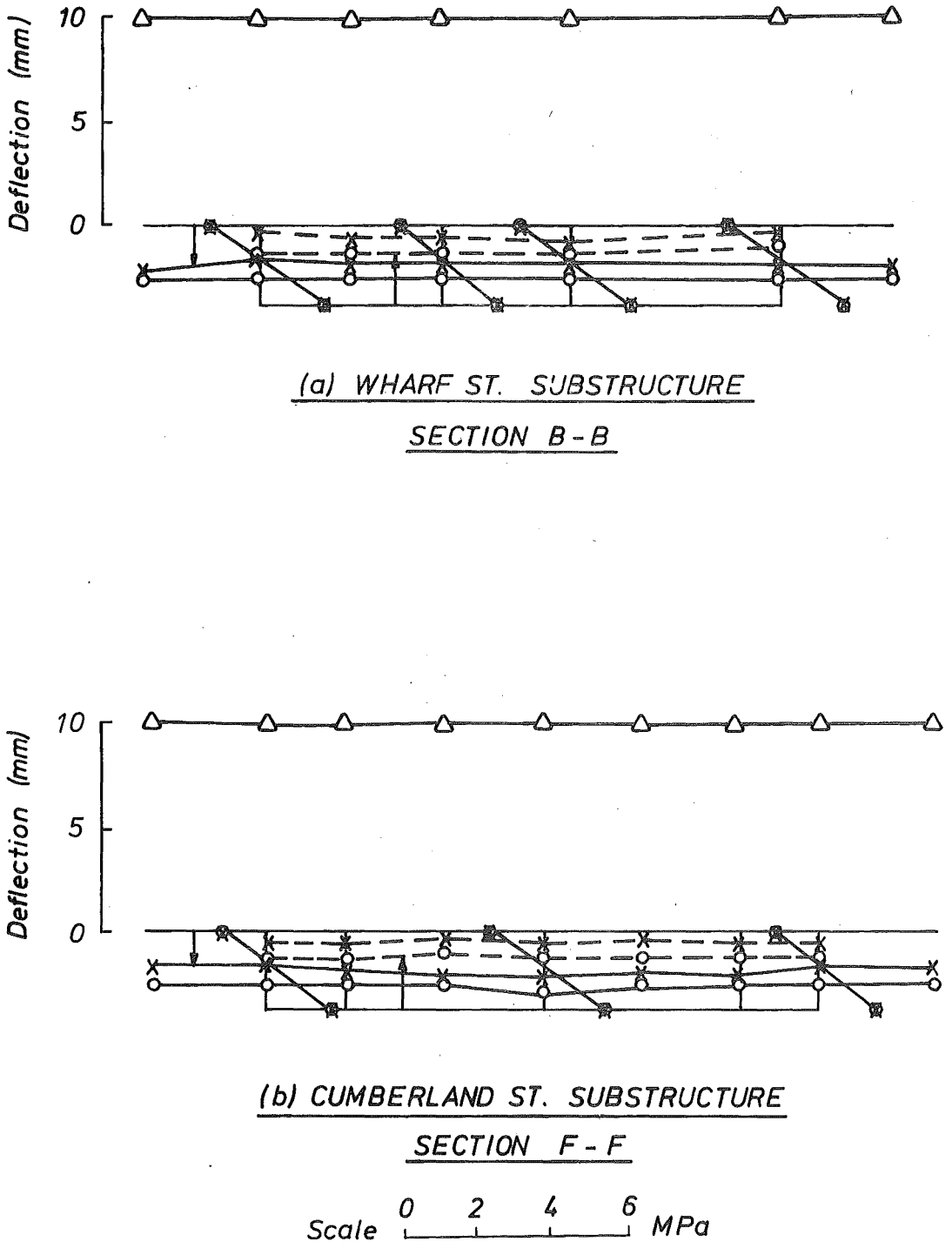

FIGURE IX-11.9 CANTILEVER LOADING OF THE SUBSTRUCTURES LONGITUDINAL STRESS AND DEFLECTION ACROSS MIDSPAN SECTIONS

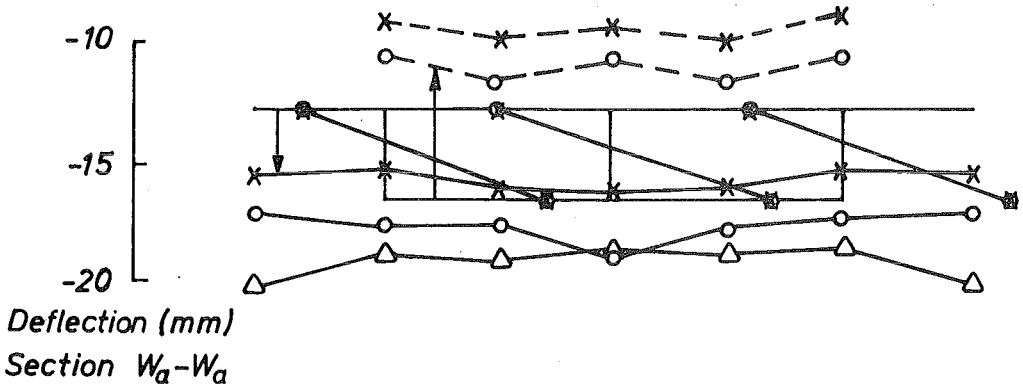

(a) WHARF ST. SUBSTRUCTURE

SECTION C_b-C_b

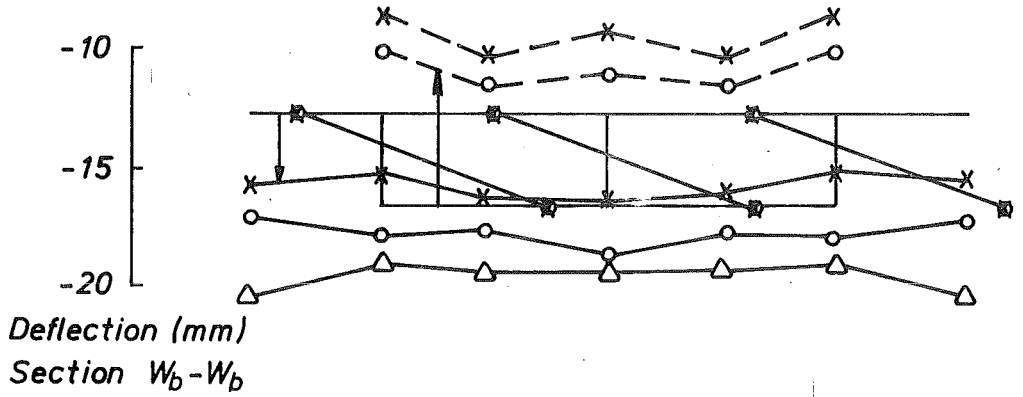

(b) CUMBERLAND ST. SUBSTRUCTURE

SECTION E_a-E_a

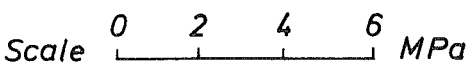

FIGURE IX-11.10 CANTILEVER LOADING OF SUBSTRUCTURES
LONGITUDINAL STRESS ACROSS SECTIONS NEAR CANTILEVER ROOT

The anchorage forces were distributed to the finite element nodes above and below the web anchorage sites so as to provide the correct applied axial force and bending moment about the neutral axis of the member. The uniformly distributed vertical forces due to vertical cable drape, which were calculated from the formulae of Park [69], and the transverse and longitudinal uniformly distributed forces due to horizontal curvature of the cables (which generally follow the web alignments) were applied as statically equivalent nodal forces.

The computed longitudinal distributions of deflection and extreme fibre longitudinal stresses along the central web are plotted in Fig. IX-11.11. A discontinuity of longitudinal stress occurs at the ends of the two substructure cantilevers (sections Wa - Wa and Wb - Wb) because a large percentage of the cables are anchored off here. Smaller discontinuities will also occur near 'minor' anchorage sites and these appear as kinks in the plotted longitudinal stress profiles.

The distributions of longitudinal stress and deflection across sections A - A, B - B, Ca - Ca, D - D, Eb - Eb, F - F, and G - G are plotted in Figures IX-11.12 to IX-11.18 respectively. Maximum stresses of up to -16.5 MPa are predicted across the top of the deck slab at the support sections Ca - Ca and Eb - Eb, and across the bottom of the soffit slab at the midspan sections B - B and F - F. The maximum longitudinal stresses always occur on the south edge of the sections, while a minimum longitudinal stress of -1.1 MPa (compression) is predicted at the bottom of the north edge of the soffit slab at the support section Ca - Ca. Although the magnitude of this stress is small, nett tension is not likely to accumulate over this region because a finite element analysis of the structure subjected to dead loading predicts a compression stress of -6.65 MPa along the bottom of the soffit slab at section Ca - Ca (see Fig. IX-11.22).

The large transverse variation of longitudinal stress across the bridge sections is a consequence of imperfect balancing of the prestress cables about the section centroids, resulting in a bending moment about the vertical axis. The achievement of perfect cable balance is difficult for a bridge of this configuration but the cable profiles have since been modified to reduce this eccentricity of longitudinal stress and the associated local stress peaks in the region of the interior supports; Peak local compression stresses are evident across the soffit slab above the south support at section Ca - Ca, and to a lesser extent at section Eb - Eb, accompanied by tension stresses

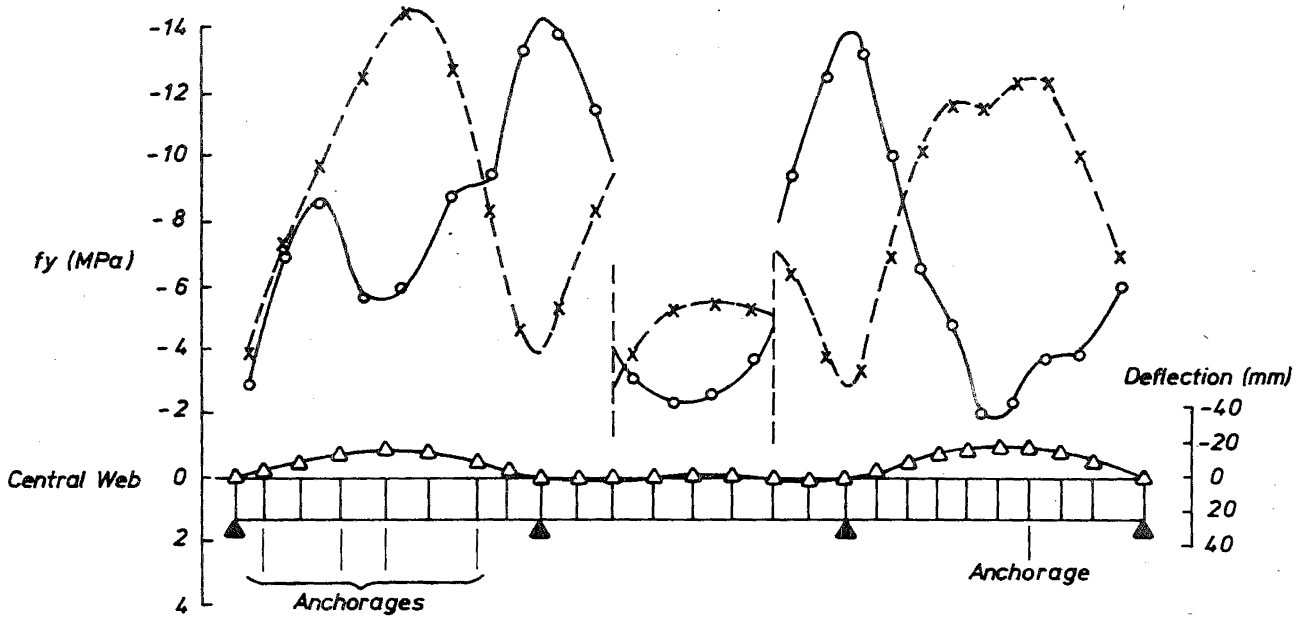

FIGURE IX-11.11 PRESTRESS LOAD
LONGITUDINAL DISTRIBUTION OF LONGITUDINAL STRESS AND DEFLECTION

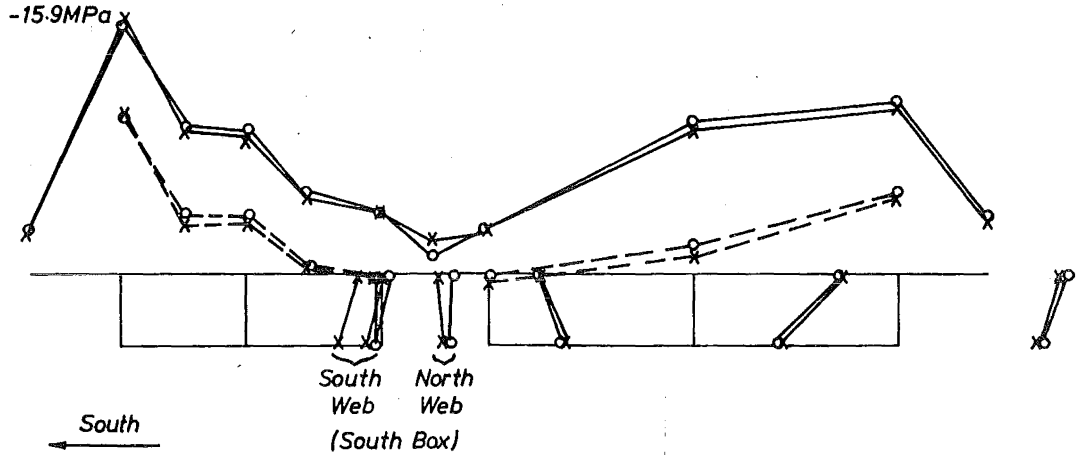

SECTION A-A

FIGURE IX-11.12 PRESTRESS LOAD ; LONGITUDINAL STRESS

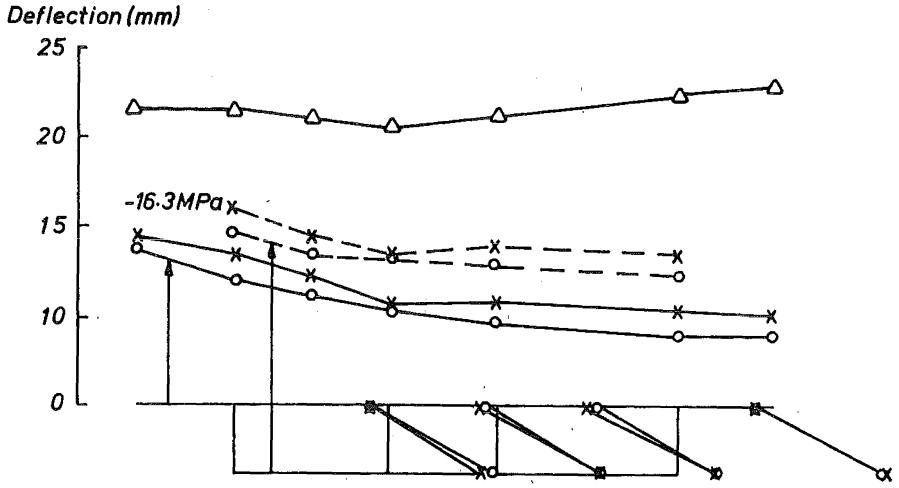

SECTION B-B

FIGURE IX-11.13 PRESTRESS LOAD ; LONGITUDINAL STRESS AND DEFLECTION

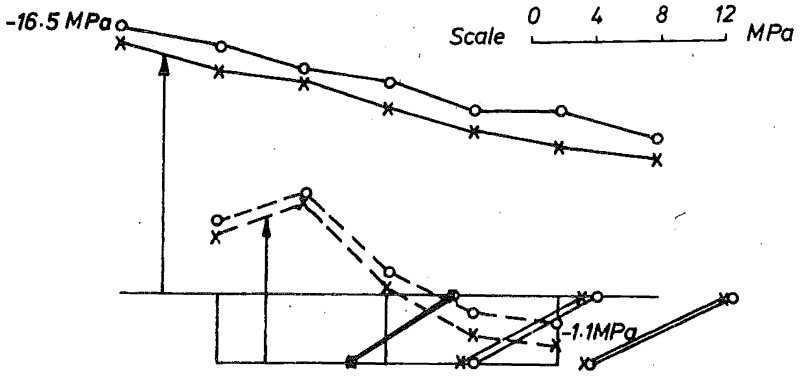

SECTION Ca-Ca

FIGURE IX-11.14 PRESTRESS LOAD ; LONGITUDINAL STRESS

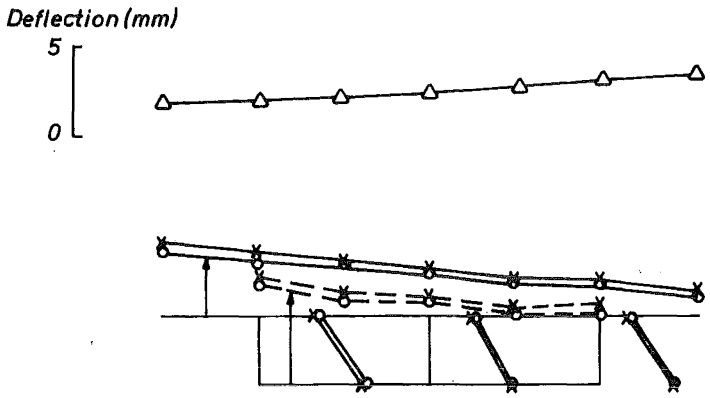

SECTION D-D

FIGURE IX-11.15 PRESTRESS LOAD ; LONGITUDINAL STRESS AND DEFLECTION

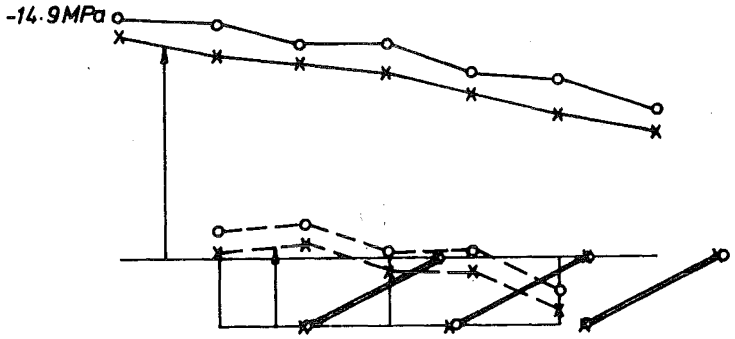

SECTION Eb-Eb

FIGURE IX-11.16 PRESTRESS LOAD ; LONGITUDINAL STRESS

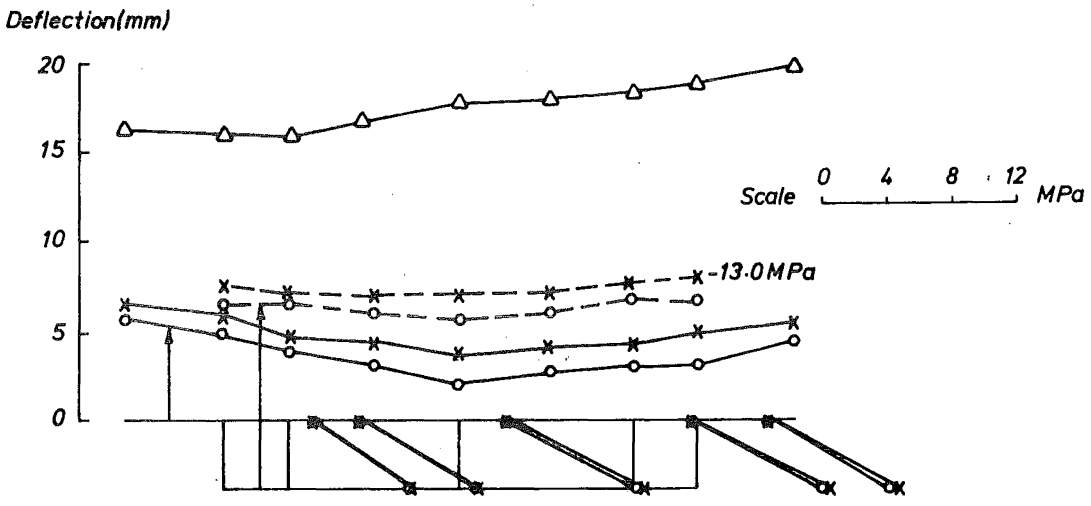

SECTION F-F

FIGURE IX-11.17 PRESTRESS LOAD ; LONGITUDINAL STRESS AND DEFLECTION

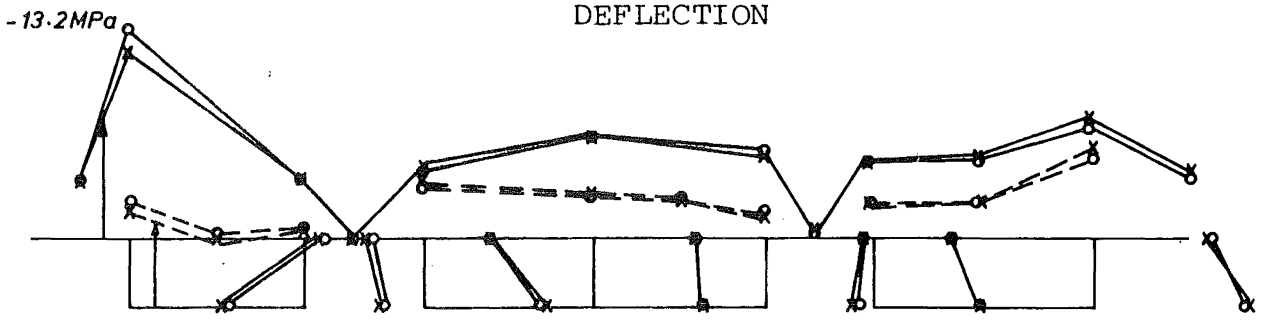

SECTION G-G

FIGURE IX-11.18 PRESTRESS LOAD ; LONGITUDINAL STRESS

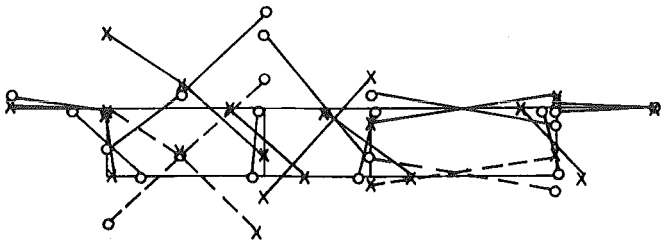

(a) SECTION B-B

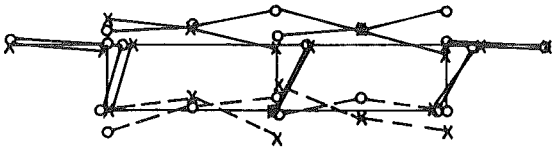

(b) SECTION C_a-C_a

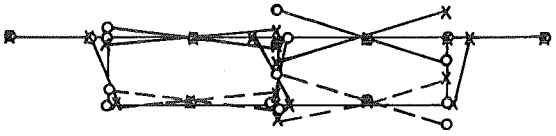

(c) SECTION D-D

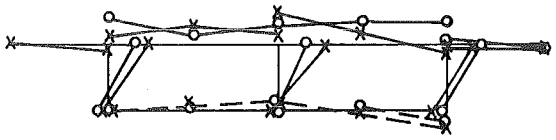

(d) SECTION E_b-E_b

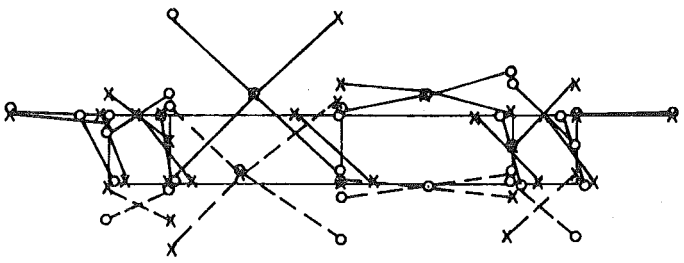

(e) SECTION F-F

Scale 0 2 4 6 MPa

FIGURE IX-11.19 TRANSVERSE STRESSES
PRESTRESS LOAD

above the north supports (see Figures IX-11.14 and IX-11.16). This results from the application of a lateral bending moment to a 'cantilever' fixed at only two discrete points.

The distributions of transverse stress across sections B - B, Ca - Ca, D - D, Eb - Eb, and F - F are plotted in Figures IX-11.19a to IX-11.19e respectively, from which it is evident that small transverse compression stresses (generally less than 0.7 MPa) are induced across the deck slab due to Poisson's ratio effect. Also, larger transverse tension stresses of up to 2.8 MPa occur in the deck and soffit slabs at sections B - B and F - F due to the transfer of shear from the south web to the central webs at section B - B, and from the central web to the south webs at section F - F.

vii) Dead loading of Cumberland St. Overpass

The computed distributions of deflection and extreme fibre longitudinal stresses along the central web are shown in Fig. IX-11.20. These distributions are similar, but of opposite sense, to those produced by the prestress loading (see Fig. IX-11.11), except that the latter load case results in an additional average longitudinal compression stress throughout each section of approximately -8.4 MPa along the two end spans, and -4.2 MPa along the central span.

The distributions of longitudinal stress and deflection across sections B - B, Ca - Ca, D - D, Eb - Eb, and F - F are plotted in Figure IX-11.21 to IX-11.25 respectively. A maximum tension stress of 7.7 MPa is predicted along the bottom of the soffit slab at section F - F, and is balanced by a compression stress of -12.6 MPa from the prestress cables. A peak compression stress of -8.0 MPa occurs along the bottom of the soffit slab, below the outside webs at section Eb - Eb.

The distributions of(extreme fibre)transverse stress across sections B - B, Ca - Ca, D - D, Eb - Eb, and F - F are plotted in Figure IX-11.26a to IX-11.26e respectively. The magnitudes of these stresses are less than 1.4 MPa at all sections. The largest tension stresses occur at the roots of the cantilevers and, for the midspan sections, along the top of the deck and soffit slabs where they intersect the central web. The local transverse bending stresses across the deck and soffit slabs, due to dead load forces acting between the webs, will not be predicted accurately because the finite element mesh employed here is too coarse to simulate the stress distribution correctly, and the uniform loading was represented as nodal forces which are statically equivalent in the global sense only.

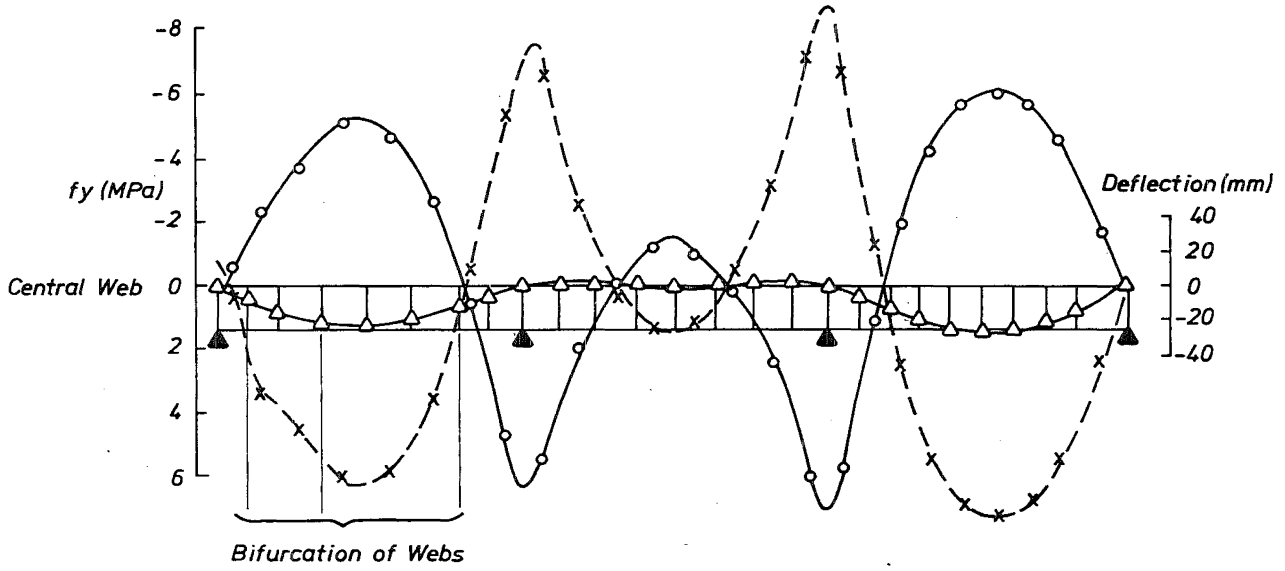

FIGURE IX-11.20 DEAD LOADING
LONGITUDINAL DISTRIBUTION OF LONGITUDINAL STRESS AND DEFLECTION

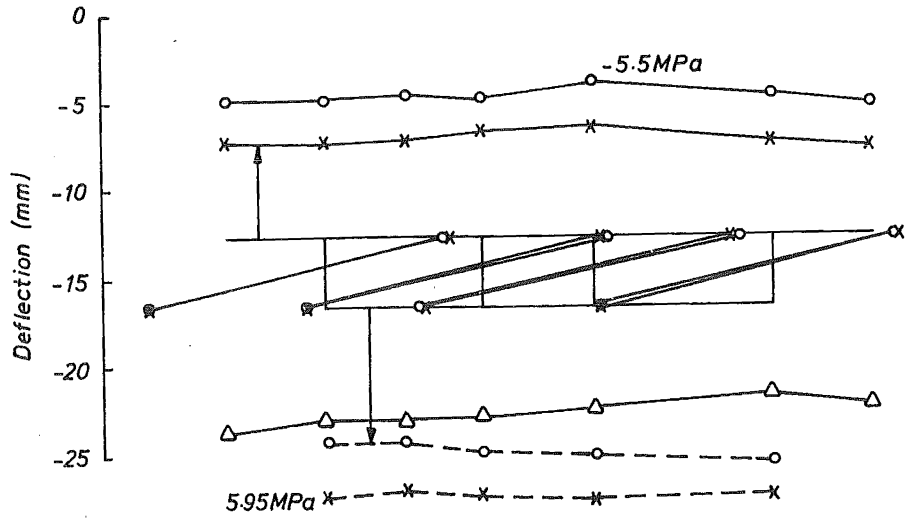

SECTION B-B

FIGURE IX-11.21 DEAD LOADING ; LONGITUDINAL STRESS AND DEFLECTION

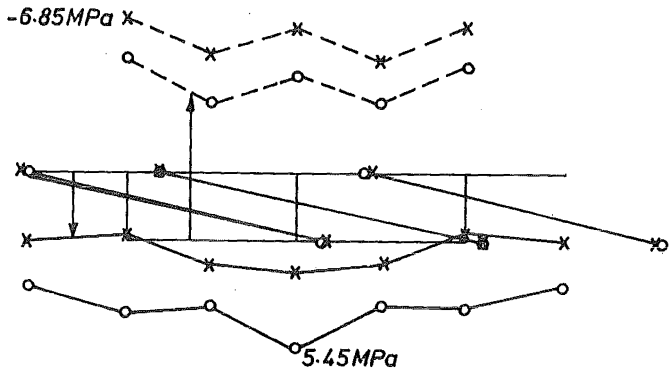

SECTION Ca-Ca

FIGURE IX-11.22 DEAD LOADING ; LONGITUDINAL STRESS

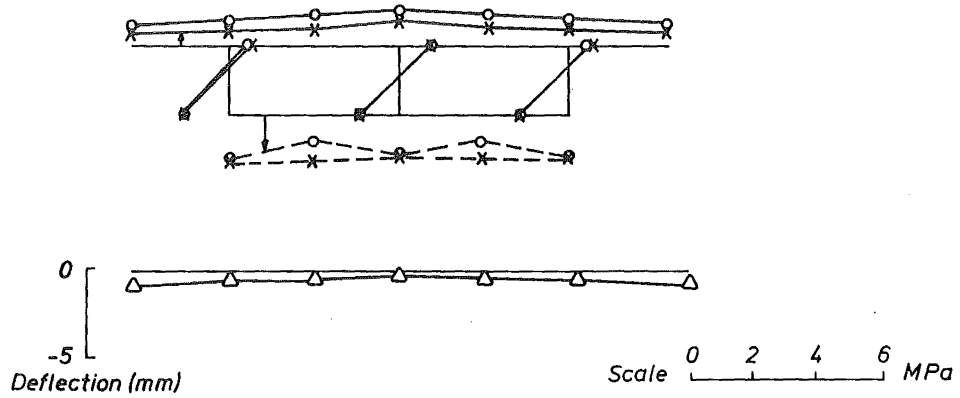

SECTION D-D

FIGURE IX-11.23 DEAD LOADING ; LONGITUDINAL STRESS AND DEFLECTION

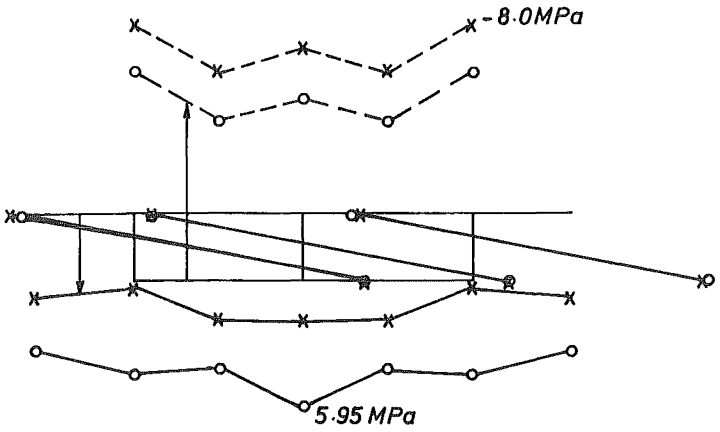

SECTION Eb-Eb

FIGURE IX-11.24 DEAD LOADING ; LONGITUDINAL STRESS

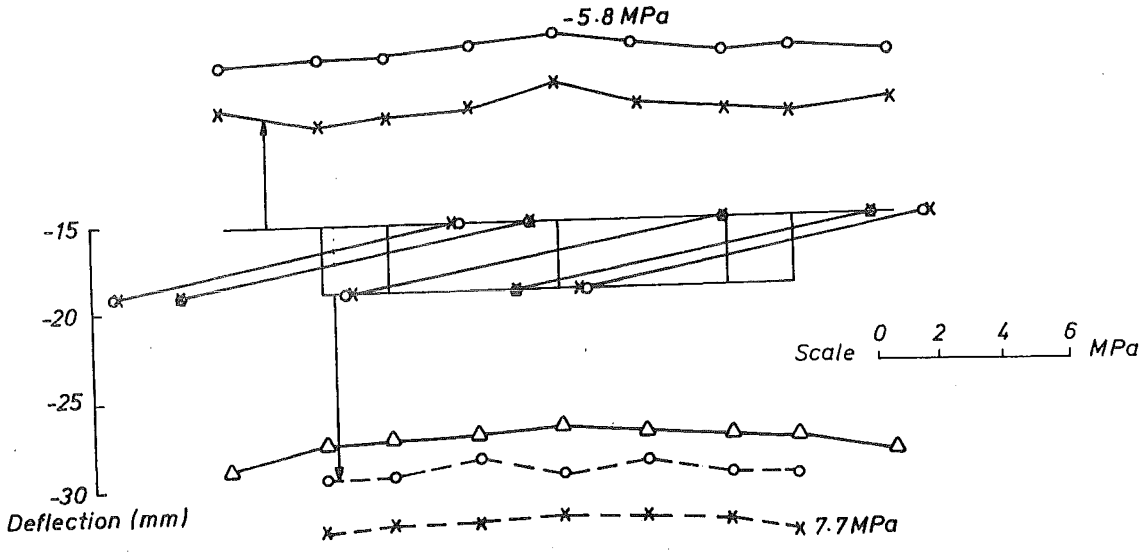

SECTION F-F

FIGURE IX-11.25 DEAD LOADING ; LONGITUDINAL STRESS AND DEFLECTION

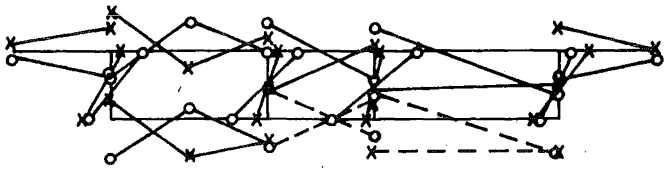

(a) SECTION B-B

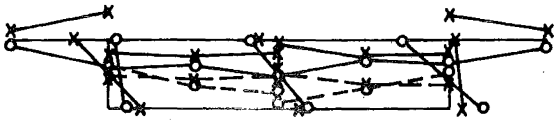

(b) SECTION C_a-C_a

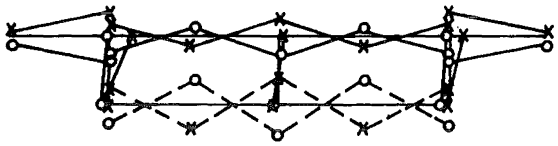

(c) SECTION D-D

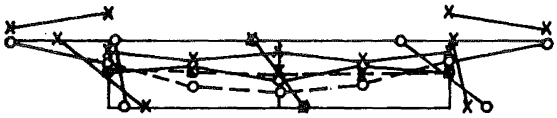

(d) SECTION E_b-E_b

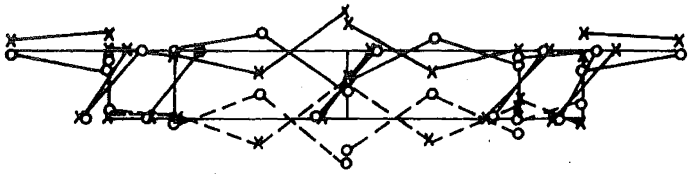

(e) SECTION F-F

Scale 0 2 4 6 MPa

FIGURE IX-11.26 DEAD LOADING ; TRANSVERSE STRESSES

viii) Vertical temperature gradient

A finite element analysis was performed on the Cumberland Street Overpass subjected to a bilinear approximation of a sixth power vertical temperature distribution, with a temperature difference of 30°C from the top of the deck slab to the bottom of the soffit slab.

The distributions of deflection, extreme fibre longitudinal stresses, and longitudinal stress at the top and bottom of the webs are plotted in Fig. IX-11.27.

The restraint provided to the hogging action by the intermediate supports has the effect of decreasing the longitudinal tension stress at the top of the web from that produced by the temperature gradient on a single span structure (see Fig. VIII-2), but induces a larger longitudinal tension stress along the soffit slab. Thus a longitudinal tension stress of 4.9 MPa is predicted along the central span soffit slab, but along the top of the central web of the central span the tension stress is only 0.85 MPa.

The distributions of deflection and longitudinal stress across sections A - A, B - B, Cb - Cb, D - D, Ea - Ea, F - F, and Ga - Ga are plotted in Figures IX-11.28 to IX-11.34 respectively. Longitudinal tension stresses of between 2.8 MPa and 3.64 MPa occur at the Wharf Street end (section A - A) along the bottom surface of the cantilever slabs, and along the bottom of the deck slab in the region between the bifurcating boxes. A similar pattern is evident at the Cumberland Street end (section Ga - Ga), but the magnitudes of these tension stresses are smaller (1.95 - 2.3 MPa).

The extreme fibre longitudinal stresses across sections Cb - Cb and F - F, calculated from the grid analysis, are also plotted in Figures IX-11.30 and IX-11.33 respectively. The agreement between the longitudinal stresses predicted from the two theories is good except that a discrepancy of 23% and 24% is evident above the central web at sections Cb - Cb and F - F respectively. Also, the highly non-uniform longitudinal stress distribution predicted by the grid analysis across the soffit slab of section F - F is not a realistic response to this load case where the temperature is constant on horizontal lines across the width of the bridge.

The distribution of transverse stress across sections A - A, B - B, Cb - Cb, D - D, Ea - Ea, F - F, and Ga - Ga are plotted in Figures IX-11.35 to IX-11.41 respectively. Transverse tension stresses, generally of the order of 3.0 MPa, are predicted along the bottom of the deck slab in the vicinity of the central web. These stresses result from the

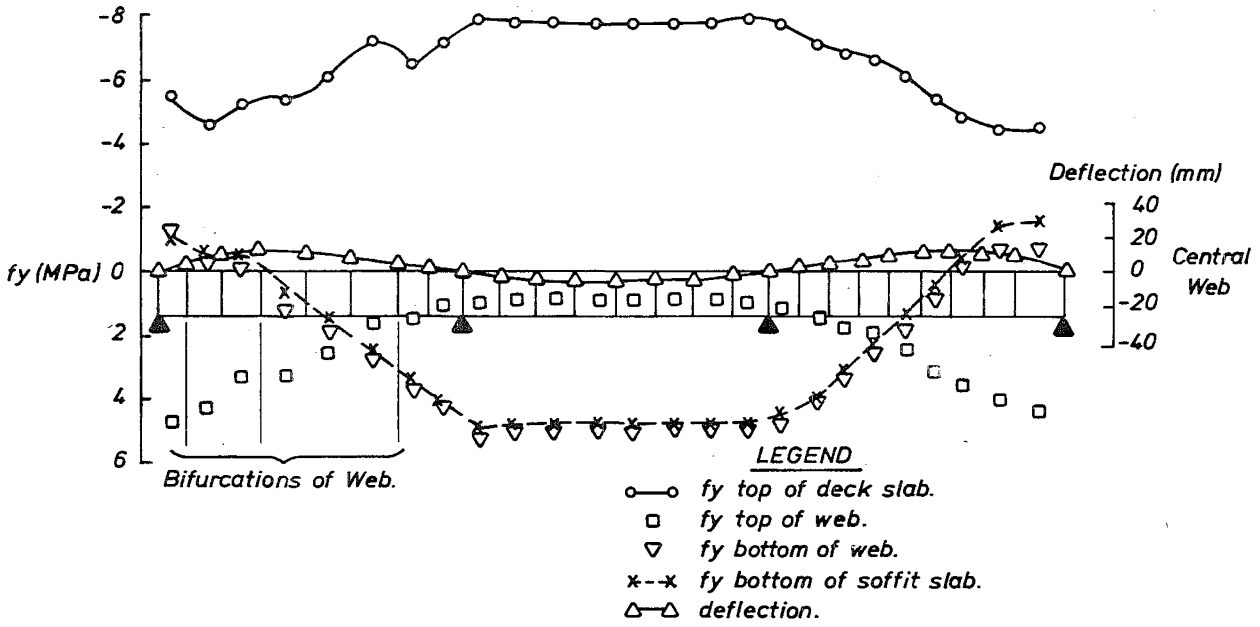

FIGURE IX-11.27 TEMPERATURE LOAD
LONGITUDINAL DISTRIBUTION OF LONGITUDINAL STRESS AND DEFLECTION

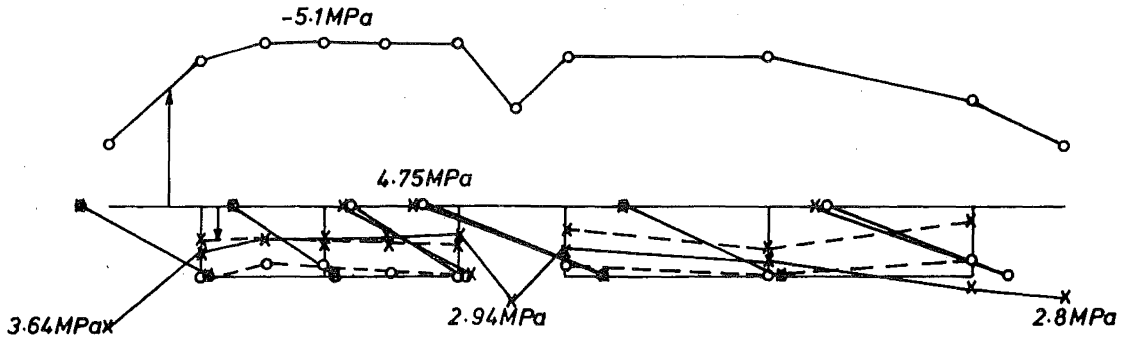

SECTION A-A

FIGURE IX-11.28 TEMPERATURE LOAD ; LONGITUDINAL STRESS

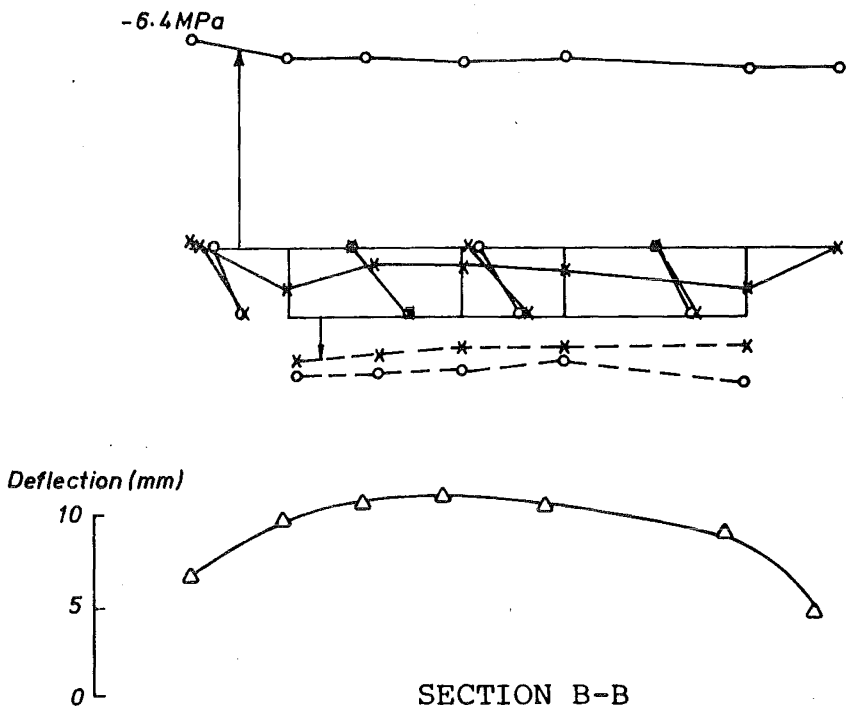

SECTION B-B

FIGURE IX-11.29 TEMPERATURE LOAD ; LONGITUDINAL STRESS AND DEFLECTION

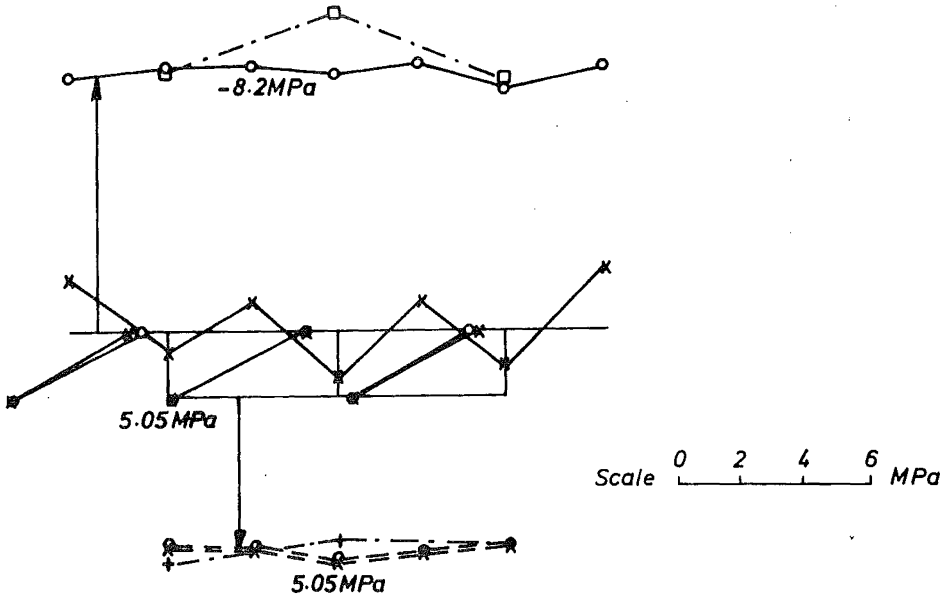

SECTION Cb-Cb

FIGURE IX-11.30 TEMPERATURE LOAD : LONGITUDINAL STRESS

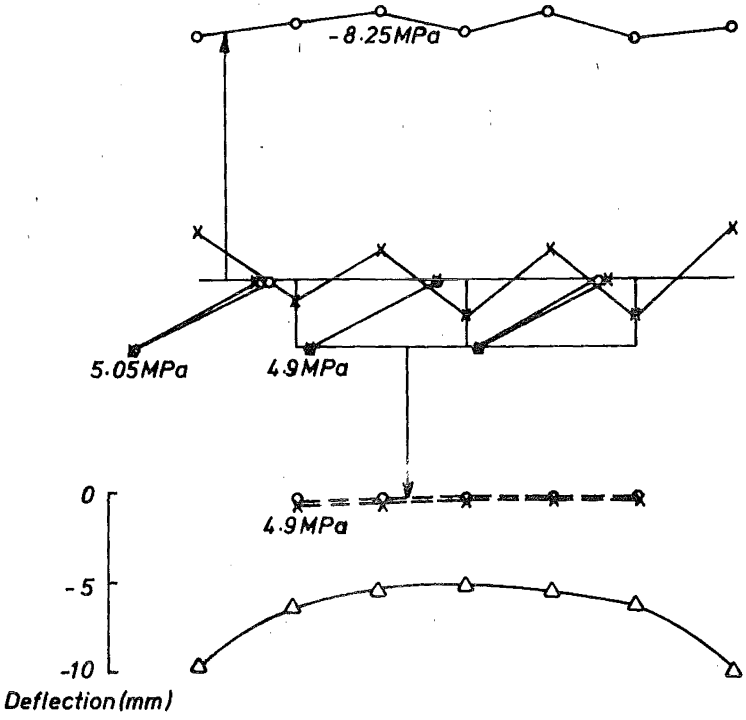

SECTION D-D

FIGURE IX-11.31 TEMPERATURE LOAD ; LONGITUDINAL STRESS AND DEFLECTION

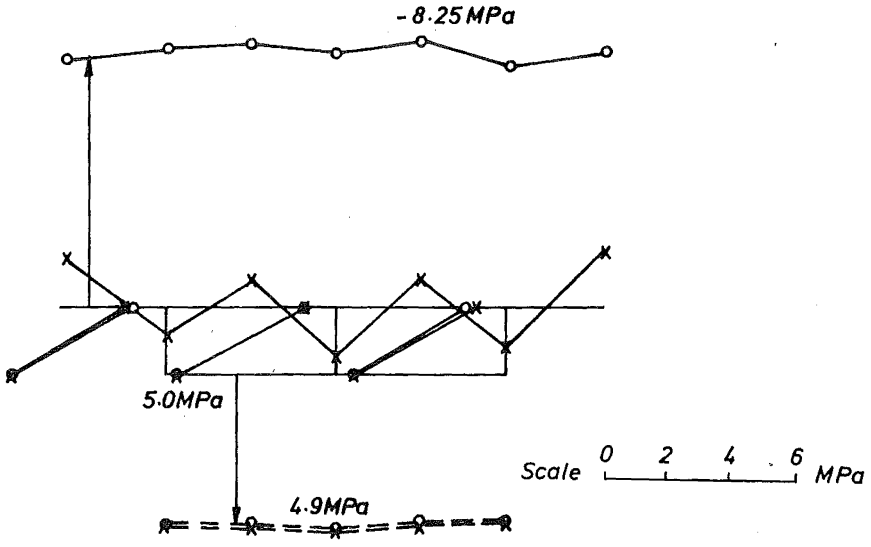

SECTION Ea-Ea

FIGURE IX-11.32 TEMPERATURE LOAD ; LONGITUDINAL STRESS

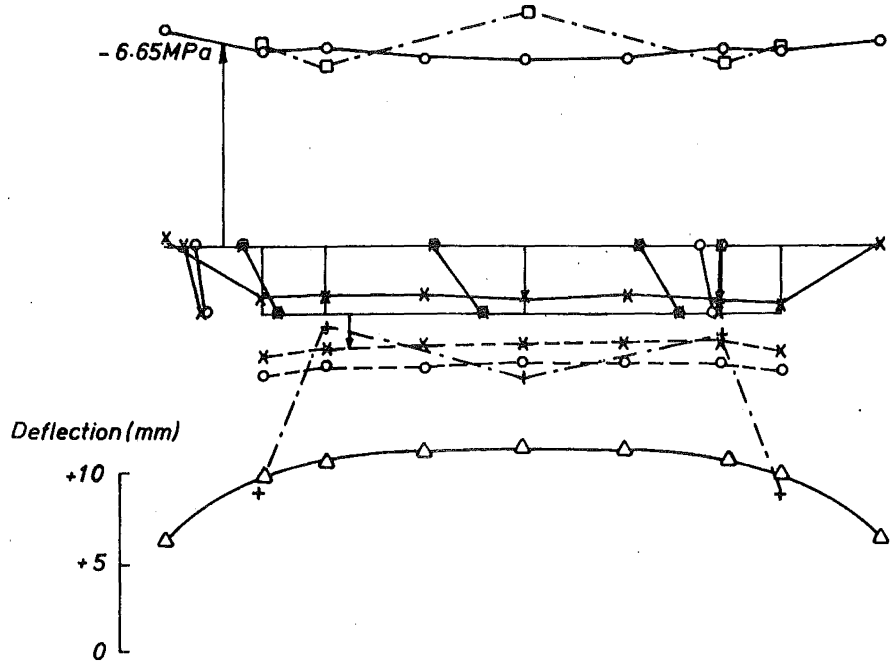

SECTION F-F

FIGURE IX-11.33 TEMPERATURE LOAD ; LONGITUDINAL STRESS AND DEFLECTION

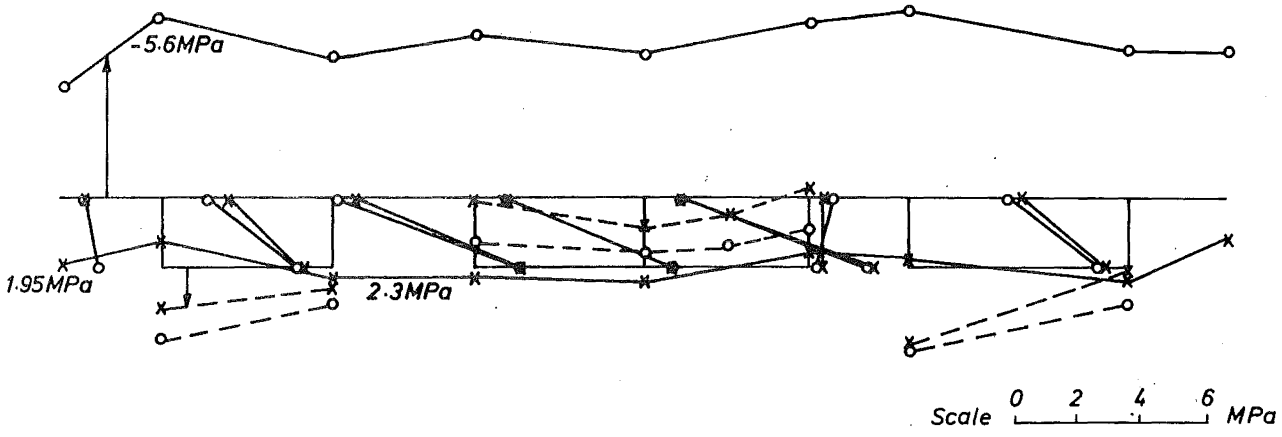

SECTION G-G

FIGURE IX-11.34 TEMPERATURE LOAD ; LONGITUDINAL STRESS

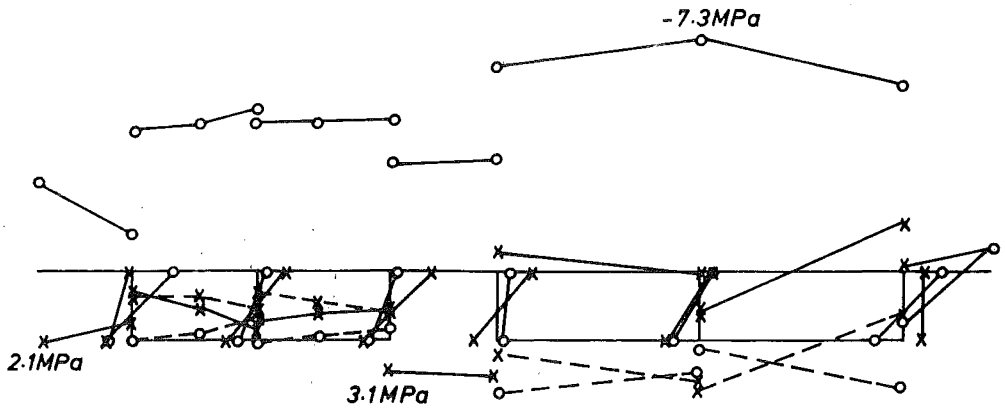

SECTION A-A

FIGURE IX-11.35 TEMPERATURE LOAD ; TRANSVERSE STRESS

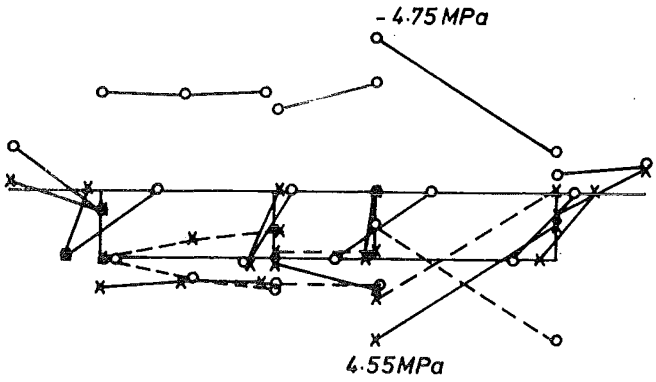

SECTION B-B

FIGURE IX-11.36 TEMPERATURE LOAD ; TRANSVERSE STRESS

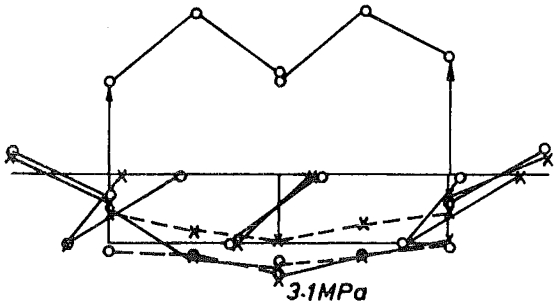

SECTION Cb-Cb

FIGURE IX-11.37 TEMPERATURE LOAD ; TRANSVERSE STRESS

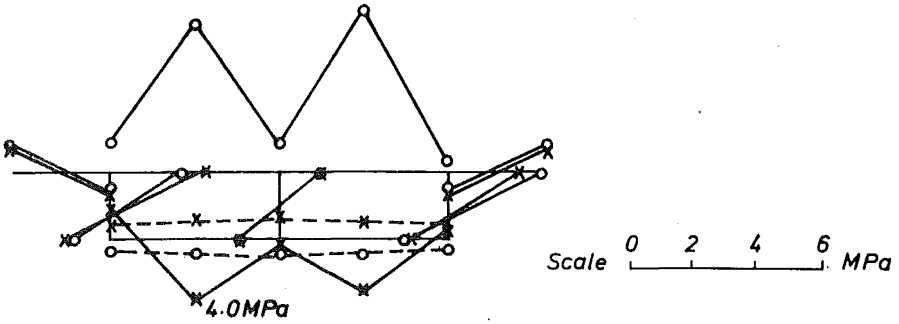

SECTION D-D

FIGURE IX-11.38 TEMPERATURE LOAD ; TRANSVERSE STRESS

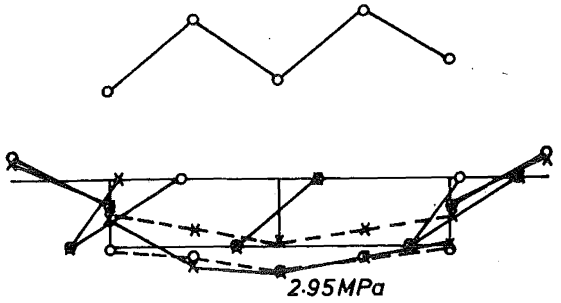

SECTION Ea-Ea

FIGURE IX-11.39 TEMPERATURE LOAD ; TRANSVERSE STRESS

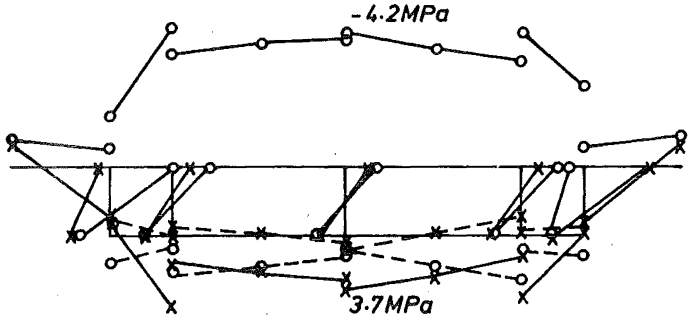

SECTION F-F

FIGURE IX-11.40 TEMPERATURE LOAD : TRANSVERSE STRESS

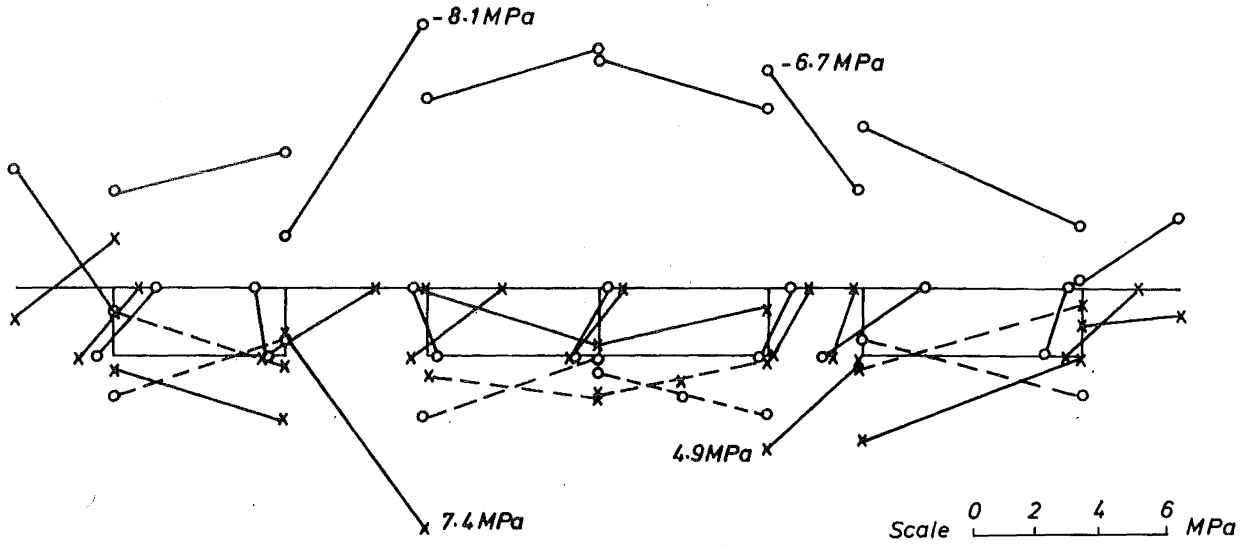

SECTION Ga-Ga

FIGURE IX-11.41 TEMPERATURE LOAD ; TRANSVERSE STRESS

restraint applied to the deck slab by the central web to prevent transverse hogging. Very large transverse tension stresses (between 4.9 MPa and 7.4 MPa) are evident from Fig. IX-11.41, at the bottom of the deck slabs in the two regions between the trifurcating boxes at the Cumberland Street end (section Ga - Ga).

ix) Live load

Four 60 kN wheel loads were centred above the south web at the centre of the Wharf Street end span. The longitudinal position of these wheel loads, and the longitudinal distributions of the resulting deflection and extreme fibre longitudinal stresses along the south web, are shown in Fig. IX-11.42a.

The distributions of longitudinal stress and deflection across section B - B are plotted in Fig. IX-11.42b, and the distribution of transverse stress across this section in Fig. IX-11.42c. The computed live load stresses are small, with a maximum tension stress of approximately 0.85 MPa in both the transverse and longitudinal directions across the soffit slab of the south box.

The finite element mesh employed here is too coarse to simulate the local stress peaks in the deck slab under the individual wheel loads.

IX-12 CONCLUSIONS

IX-12.1 Straight bridges

A comparison of theoretical and experimental results indicated that the finite element approach adopted here provides an accurate representation of the structural behaviour of both Structure A and Structure B. The simulation of the deck slab,with the use of beam elements to represent the kerbs and tapered thickness thin plate elements to model the haunches, was excellent. However, when the deck slab is severely haunched above the webs of a box-girder the distribution of stresses down the depth of the webs is complex and three or more elements are required for an accurate idealisation here.

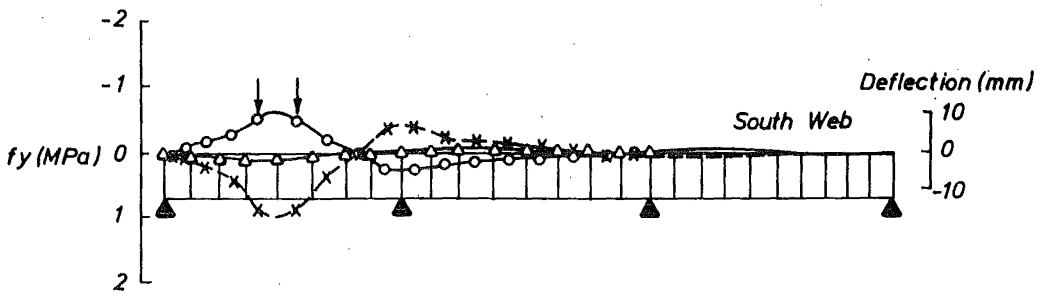

(a) LONGITUDINAL DISTRIBUTION OF LONGITUDINAL STRESS AND DEFLECTION.

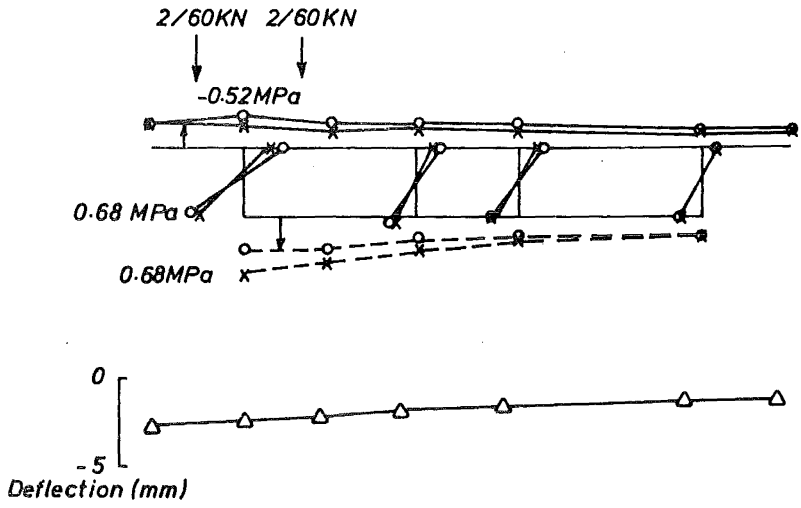

(b) LONGITUDINAL STRESS AND DEFLECTION

SECTION B-B

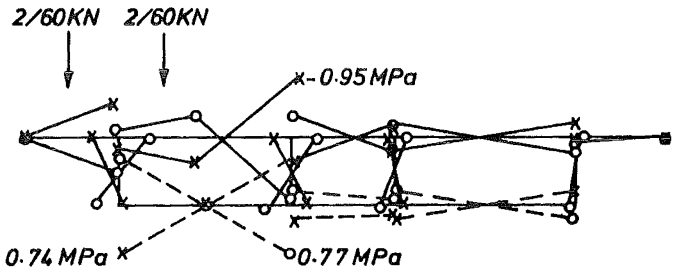

(c) TRANSVERSE STRESS

SECTION B-B

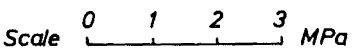

FIGURE IX-11.42 LIVE LOAD : CUMBERLAND STREET OVERPASS

LONGITUDINAL DISTRIBUTION ALONG WEB

Longitudinal stress, top of deck slab (MPa)

Longitudinal stress, bottom of soffit slab

Deflection (mm)

TRANSVERSE DISTRIBUTION ACROSS SECTION

FINITE ELEMENT RESULTS

Stress along top of deck slab or L.H.S. of web (MPa)

Stress along bottom of deck slab or R.H.S. of web

Stress along top of soffit slab

Stress along bottom of soffit slab

Deflection (mm)

GRID ANALYSIS RESULTS

Longitudinal stress along top of deck slab

Longitudinal stress along bottom of soffit slab

SIGN CONVENTION

Positive Deflection upwards

Positive Stresses tension

TABLE IX-11-1 LEGEND.

IX-12.2 Skew bridges

Comparisons of the finite element results obtained from analysing a 45° skew slab, a 30° skew cellular bridge, and a 45° skew two span box-girder with those measured experimentally and those presented from alternative numerical solutions indicates that no significant deterioration occurs in the performance of the CQ12 plate bending element or the QMC3 plane stress element when they are transformed to a parallelogram shape. The finite element results generally agree closely with those measured experimentally except in the region of stress concentrations.

There are very few experimental studies of skew box-girder bridges reported in the literature and the experimental results published for the three skew structures studied here are not sufficiently extensive to enable the structural behaviour of such structures to be described fully.

IX-12.3 Curved bridges

Comparisons of the theoretical and experimental results measured from the Lobley Hill South Overbridge model, Aslam & Godden's curved box-girder, and a model of the Stockton Rd. Interchange indicate that the finite elements perform well when transformed to midly distorted quadrilateral shapes and that the small violations of compatibility along the element boundaries due to the non-unique definition of the nodal parameter θz_i (discussed in Chapter III) produce no significant deterioration of accuracy. The agreement between experimental and theoretical results obtained with refined element meshes is excellent, except above supports and under wheel loads where local stress concentrations occur and a grading of the mesh is required to enable an accurate representation of these concentrations to be achieved.

The accuracy of the theoretical stresses deteriorates slightly when only one element is employed through the depth of the webs during the structural idealisation but the simulation of box-girder behaviour is still adequate for design purposes.

IX-12.4 Bowen Street Overpass

The presence of severe longitudinal haunching near the central supports of this two span structure introduces additional complexity to the simulation of the structural behaviour, but the computed longitudinal strains and deflections correspond closely to the response measured

experimentally from the full scale structure.

The employment of the mesh grading technique has enabled good results to be obtained at a relatively low cost by using a fine mesh of elements over regions where the stress distribution is more complex.

The computed longitudinal web strains are more accurate than the web stresses predicted from finite element analyses of Structures A and B because the Bowen Street Overpass does not have severe transverse haunching of the deck slab above the webs.

The accuracy of the finite element idealisation used to analyse this structure indicates that linear elastic thin plate theory may be employed to construct a realistic mathematical model of mildly cracked prestressed concrete box-girder bridge superstructures.

IX-12.5 Cumberland Street Overpass

The finite element results presented for the Cumberland Street Overpass are considered to provide an accurate representation of the structural behaviour because:-

i) The finite element mesh, shown in Fig. IX-11.1, was plotted automatically from the nodal coordinates and the specifications of the element connectivity, and therefore provides a check of the finite element data.

ii) The finite element method employed here has been shown to produce results which are in close agreement with the measured performance of a wide variety of box-girder structures (see Sections IX-2 to IX-10).

iii) The computed results for the nine load cases are compatible with the structural behaviour which may be anticipated from considerations of simple beam theory and thin plate theory.

iv) The longitudinal stresses, computed for the three substructures subjected to dead loading, correspond with the average longitudinal stresses across the deck and soffit slabs at sections Cb - Cb, D - D, and Ea - Ea, predicted from simple beam theory.

v) The longitudinal dead load stresses computed for the Wharf Street Substructure across section B - B, and for the Cumberland Street Substructure across section F - F, and the longitudinal temperature stresses across section Ca - Ca and F - F agree closely with those predicted from a grid analysis.

The following undesirable structural behaviour was predicted from the finite element analyses:-

i) A large transverse gradient of longitudinal stress occurs along the central span of the structure because the horizontal prestress forces were not balanced about the centroid of every cross section. The cable profiles have since been modified to reduce this gradient.

ii) The vertical temperature gradient produces longitudinal tensile stresses of 4.9 MPa along the central span soffit slab, which will act along with dead load tension stresses of 1.4 MPa. These stresses must be counteracted by the effect of the prestress cables, which result in compression stresses of between 4.9 MPa and 6.6 MPa across the soffit slab at section D - D. Therefore, additional prestress cables are to be employed over the central span.

iii) Large transverse tension stresses are produced across i) the midspan sections B - B and F - F from the prestressing load. These stresses are caused by the transfer of shear from webs with a larger vertical cable force to those with smaller cable forces, and may also be partially due to the effect of concentrating the uniformly distributed prestressing forces at the element nodes. ii) the end support sections A - A and Ga - Ga when the structure is subjected to the vertical temperature. This is caused by the end supports restraining transverse hogging.

It has been demonstrated that finite element analyses of complex box-girder bridges may be performed on a production basis to present reliable and informative results to the designers of such structures.

CHAPTER X

GEOMETRIC NONLINEARITY

X-1 INTRODUCTION

Geometric nonlinearity arises when loading causes the configuration of a structure to change so as to affect the stiffness of the structure significantly. A finite element approach is developed which is capable of determining the large deflection elastic response, including the nonlinear postbuckling behaviour, of stiffened spatial plate structures such as box-girder bridges.

The nonlinear equilibrium equations are solved with an approximate incremental method but errors are prevented from accumulating by the application of a self-correcting initial value scheme and, at selected load levels, equilibrium is restored by incorporating Newton-Raphson iteration.

The linear elastic contribution to the incremental stiffness matrix of the plate element employed in this work was obtained by combining the previously derived stiffness matrices of the PMC3 plane stress and the CQ12 plate bending elements but, for a more convenient formulation of the nonlinear contributions, the displacement function of the ACM plate bending element was used to evaluate the second order strain components. The resulting planar shell element has all three translational and rotational cartesian degrees of freedom at each node so is amenable to the geometrically nonlinear analysis of box-girder bridges, and the incorporation of three dimensional stiffener elements presents no difficulties.

The performance of this finite element approach was tested by analysing a range of structures and comparing results with analytical solutions and experimental measurements where these are available.

X-2 INSTABILITY PHENOMENA

The geometrically nonlinear response of a structure may be associated with a bifurcation point on the load-deflection curve corresponding to the classical buckling load, although this point is only well defined when the geometric imperfections of the structure are very small. Continued application of the load past this point may result in a stiffening post-buckling response (e.g. compressed plates).

Alternatively, the load - deflection curve may descend after reaching a maximum load, termed the limit point. This load corresponds to the classical buckling load for perfect structures but is reduced when the structure possesses geometric imperfections (e.g. compressed thin-walled cylinders with appropriate boundary conditions). A limit point may also occur for structures which do not exhibit bifurcating load-deflection behaviour. This buckling phenomenon is termed snap through (e.g. circular arches).

When two or more different equilibrium configurations are available to the structure at a particular load level the computed response may follow an unstable branch, direct from the first configuration to the second, as illustrated in Fig. X-1. The method used to solve the nonlinear equilibrium equations of the structure must therefore be chosen judiciously to avoid problems at limit points, and the following of unstable branches.

X-3 THE CLASSICAL APPROACH

The classical approach to problems associated with geometric nonlinearity is based on the assumption that the level of membrane stress within a structure is a linear function of the applied load. The critical (buckling) load, P_{cr} is defined as the magnitude of the applied load that causes the effective flexural stiffness to become negligible. Thus the bifurcation point of the perfect structure is sought as an eigenvalue solution [44,47,117].

When the influence of imperfections is of consequence and the solution is path dependent, or a knowledge of the ultimate load is required, this approach must be abandonded and the complete load-deflection path traced.

X-4 VON KARMAN THEORY OF LARGE DISPLACEMENTS [38,107]

The Kirchhoff strain-displacement equations are based on the assumptions that the displacement gradients are much smaller than one and the transverse displacements of a plate are of the order of one third the plate thickness. A theory is sought which extends the scope of the analysis beyond this range.

Two approaches have been commonly employed to simulate the large displacement nonlinear response of spatial plate structures;

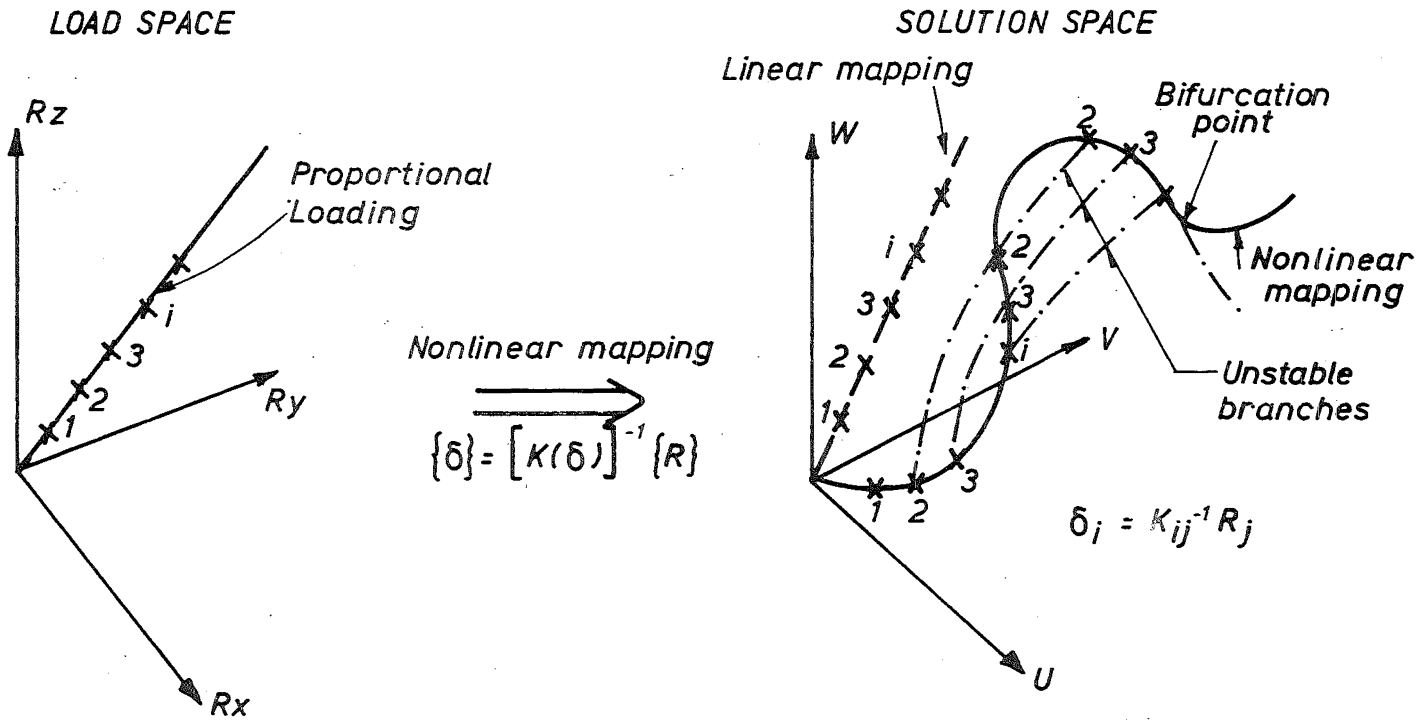

FIGURE X-1 INSTABILITY PHENOMENA

i) Updated Lagrangian Formulation

Kirchoff's strain-displacement relationships may be employed to determine the geometrically nonlinear response of structures provided the element deformations are referred to a set of local axes which translate and rotate with the element [5].

Bathe et al [5] have demomstrated that if the variations of Cauchy's infinitesimal strain tensor and the Cauchy stress tensor [38], which are always referred to the configuration in which they occur, are used to establish the equations of virtual work, and thus provide a rigorous generalised basis for the Updated Lagrangian Formulation, then the results obtained from an assembly of elements capable of representing the deformed geometry exactly will be identical to those obtained from the second approach, and converge to the correct solution with mesh refinement.

The deformed configuration of a plate structure will usually take the form of a doubly curved surface which cannot be represented with an assembly of planar four-sided elements without introducing additional approximations. The second approach (the Total Lagrangian Formulation), for which the deformations are referred to the undeformed geometry, was therefore preferred for this work. However, results from research performed by Horrigmoe at the University of Trondheim indicate that these approximations do not introduce significant errors for many problems.

ii) The Total Lagrangian Formulation

It is possible to use a general definition of strains which is valid whether the displacements are large or small. Such a definition was introduced by Green and St. Venant and is known as the Green's strain tensor [38]. Let the components of the displacement of a particle located initially at (x,y,z) be denoted by U_x, U_y, U_z. In the Lagrangian description the components of Green's strain tensor, referred to the initial undeformed configuration, are

$$E_{xx} = \frac{\partial U_x}{\partial x} + \frac{1}{2}\left[\left(\frac{\partial U_x}{\partial x}\right)^2 + \left(\frac{\partial U_y}{\partial x}\right)^2 + \left(\frac{\partial U_z}{\partial x}\right)^2\right]$$

$$E_{yy} = \frac{\partial U_y}{\partial y} + \frac{1}{2}\left[\left(\frac{\partial U_x}{\partial y}\right)^2 + \left(\frac{\partial U_y}{\partial y}\right)^2 + \left(\frac{\partial U_z}{\partial y}\right)^2\right]$$

$$E_{xy} = \tfrac{1}{2}\left[\frac{\partial U_x}{\partial y} + \frac{\partial U_y}{\partial x} + \frac{\partial U_x}{\partial x}\cdot\frac{\partial U_x}{\partial y} + \frac{\partial U_y}{\partial x}\cdot\frac{\partial U_y}{\partial y} + \frac{\partial U_z}{\partial x}\cdot\frac{\partial U_z}{\partial y}\right] \quad \ldots(X\text{-}1)$$

The assumption is made during the derivation of these relationships and the subsequent formulation that:

(A1) The displacement gradients U_z,x and U_z,y (which imply rotation about the y and x axes respectively) may become of such a magnitude that the product of these quantities is of the same order as the engineering strains but must be small compared with unity because the approximations

$$-\sin\Theta y \doteq U_z,x \qquad \cos\Theta y \doteq 1$$

$$\sin\Theta x \doteq U_z,y \qquad \cos\Theta x \doteq 1$$

in which Θx and Θy are the rotations of the middle surface, must remain valid [64].

The following assumptions associated with classical thin plate theory are also made;

(A2) The plate thickness is small compared with the typical plate dimension so transverse shear effects may be neglected.

(A3) All strain components are small. Hooke's law holds.

(A4) Kirchoff's hypotheses hold; i.e., normal stresses on surfaces parallel to the middle surface are negligble and strains vary linearly across the plate thickness.

It follows from assumption (A4) that

$$U_x = u(x,y) - z\frac{\partial w}{\partial x}, \quad U_y = v(x,y) - z\frac{\partial w}{\partial y}, \quad U_z = w(x,y)$$

The Von Karman theory, which is adopted here, makes the additional assumption:

(A5) The tangential displacements u,v are infinitesimal. Only those nonlinear terms which depend on $\frac{\partial w}{\partial x}$, $\frac{\partial w}{\partial y}$ are retained in the strain-displacement equations.

Thus,

$$E_{xx} = u,x - z\,w,xx + \tfrac{1}{2}(w,x)^2$$

$$E_{yy} = v,y - z\,w,yy + \tfrac{1}{2}(w,y)^2$$

$$E_{xy} = \tfrac{1}{2}[u,y + v,x - 2zw,xy + w,x.w,y]$$

The 2nd Piola-Kirchhoff stress tensor T_{ij} [5] can be used in conjunction with Green's strain tensor to define the strain energy of an element referred to the Lagrangian coordinate system [38] and is assumed to be related to E_{ij} through Hooke's law (A3). It is

convenient to separate the generalised strains and stresses into membrane components (e_{ij} , s_{ij}) and flexural components (X_{ij} , M_{ij}) at this stage.

$$e_{xx} = u,x + \tfrac{1}{2} w,x^2 \qquad X_{xx} = - w,xx$$

$$e_{yy} = v,y + \tfrac{1}{2} w,y^2 \qquad X_{yy} = - w,yy$$

$$e_{xy} = u,y + v,x + w,x\, w,y \qquad X_{xy} = 2w,xy \quad \ldots \text{(X-2)}$$

The flexural and membrane components of the generalised stresses are illustrated in Fig. X-2. The strain energy of an element may thus be written

$$U = \frac{1}{2} \int_{vol} \{E\}^T . \{T\} \, dvol$$

where vol refers to the undeformed volume of the element.

If the thickness t of the element is constant

$$U = \frac{1}{2} \int_{Area} \begin{Bmatrix} e \\ X \end{Bmatrix}^T . \begin{Bmatrix} S \\ M \end{Bmatrix} t \, dxdy \qquad \ldots \text{(X-3)}$$

where the integration in the direction normal to the plate has been performed explicitly to enable the variable z to be removed from the integrand. This is easily accomplished because in Lagrangian coordinates the plate surfaces are always designated as $z = \pm t/2$. Equation (X-3) may be expressed more concisely as

$$U = \frac{1}{2} \int_{vol} \{\varepsilon\}^T . \{\sigma\} \, dvol \qquad \ldots \text{(X-4)}$$

where $\{\varepsilon\}^T = < e_{ij}, X_{ij} >$ and $\{\sigma\}^T = < S_{ij}, M_{ij} > \ldots$ (X-5)

It should be noted that it is necessary to employ the Updated Lagrandian Formulation exclusively when analysing structures which respond to load with very large displacements. This is because rotations do not transform as vectors for large displacements, as assumed during the Total Lagrangian formulation

X-5 FORMULATION OF NONLINEAR EQUILIBRIUM EQUATIONS

The principle of stationary total potential energy is valid whether displacements are large or small. Thus, for an equilibrium configuration

$$\frac{\partial V}{\partial \{\delta\}} = \frac{\partial U}{\partial \{\delta\}} - \{R\} = \{0\} \qquad \ldots \text{(X-6)}$$

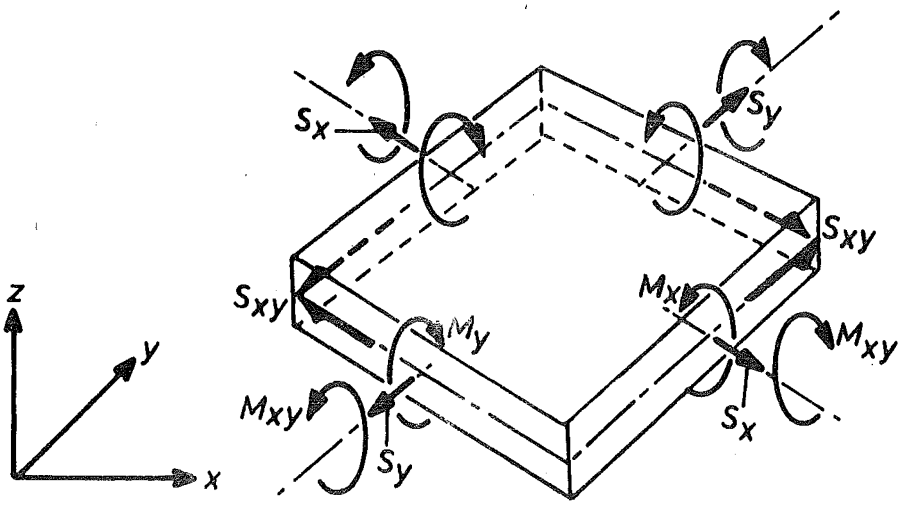

(a) BENDING MOMENTS AND MEMBRANE STRESSES.

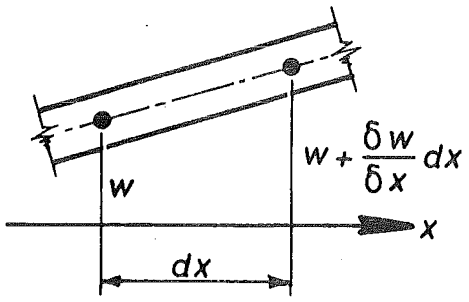

(b) EXTENSION DUE TO TRANSVERSE DISPLACEMENT.

FIGURE X-2 BENDING MOMENTS AND MEMBRANE STRESSES

where V is the total potential energy and U is the strain energy (see Chapter I).

$$\text{Let } \frac{\partial U}{\partial \{\delta\}} = [K_s(\delta)]\{\delta\} \qquad \ldots \quad (X\text{-}7)$$

where $[K_s(\delta)]$ is defined as the secant stiffness, and is a function of the nodal displacement parameters $\{\delta\}$ when a nonlinear strain-displacement relation is employed during the formulation. The derivation of various forms of the secant stiffness of a plate element is described in Appendix B. Many authors [41,100] choose to employ a pseudo force vector rather than a nonlinear stiffness matrix, for which it is convenient to separate the strain energy into two components.

$$U = U_o + U_N$$

where U_o is the contribution due to the linear terms in the strain-displacement relation of equation (X-2), and yields a quadratic expression in terms of the generalised displacements.

$$\frac{\partial U_o}{\partial \{\delta\}} = [K_o]\{\delta\} \qquad \ldots \quad (X\text{-}8)$$

where $[K_o]$ is the linear elastic stiffness matrix obtained previously.

U_N is the contribution due to nonlinear terms in the strain-displacement relation. Let

$$\frac{\partial U_N}{\partial \{\delta\}} = \{R^*(\delta)\} \qquad \ldots \quad (X\text{-}9)$$

where $\{R^*(\delta)\}$ are a set of pseudo forces due to the nonlinearity.

The equations of equilibrium may then be expressed

$$[K_o]\{\delta\} = \{R\} - \{R^*(\delta)\} \qquad \ldots \quad (X\text{-}10)$$

A force imbalance vector $\{f\}$ is defined as a measure of the deviation from a true state of equilibrium

$$\{f\} = \{R\} - [K_o]\{\delta\} - \{R^*(\delta)\} \qquad \ldots \quad (X\text{-}11)$$

which may be related to the nonlinear secant stiffness

$$\{f\} = \{R\} - [K_s(\delta)]\{\delta\} \qquad \ldots \quad (X\text{-}12)$$

To obtain a detailed knowledge of the structural response the load must be applied incrementally. The total load at any point may then be represented as a function of a load parameter, $\bar{P}$, and a normalised load vector $\{\bar{R}\}$, i.e.,

$$\{R\} = \bar{P}\,\{\bar{R}\} \qquad \ldots \quad (X\text{-}13)$$

If this expression is substituted into equation (X-11), which in turn is differentiated with respect to the load parameter $\bar{P}$,

$$\{\dot{f}\} = \{\bar{R}\} - [K_o]\,\{\dot{\delta}\} - \{\dot{R}^*\} \qquad \ldots \quad (X\text{-}14)$$

where the dot denotes differentiation with respect to $\bar{P}$.

The formulation may proceed in terms of a nonlinear stiffness matrix by using the chain rule of partial differentiation to expand the pseudo force vector of equation (X-14)

$$\dot{R}^*_i = d\,R^*_i/d\,\bar{P} = [d\,R^*_i/d\,\delta_j]\,d\,\delta_j/d\,\bar{P}$$

$$\text{i.e.} \quad \{\dot{R}^*\} = [K^*]\{\dot{\delta}\} \qquad \ldots \quad (X\text{-}15)$$

The tangent stiffness matrix $[K_t(\delta)]$ is defined by the expression

$$[K_t(\delta)] = [K_o] + [K^*]$$

$$= \left[\frac{\partial^2 (U_o + U_N)}{\partial \delta_i \partial \delta_j}\right] \qquad \ldots \quad (X\text{-}16)$$

where the summation of indices is implied.

Equation (X-14) may now be written

$$\{\dot{f}\} = \{\bar{R}\} - [K_t(\delta)]\{\dot{\delta}\} \qquad \ldots \quad (X\text{-}17)$$

The incremental solution techniques employed in geometrically nonlinear analyses may be classified according to whether they are based on equation (X-11) or (X-14), setting $\{f\} = 0$ or $\{\dot{f}\} = 0$ respectively.

X-6 SOLUTION OF NONLINEAR EQUATIONS

X-6.1 Solution procedures

There is no one method for solving the class of equilibrium equations associated with the nonlinear response of structures. The solution procedure must be selected according to the type of problem, the degree of nonlinearity involved, and the accuracy desired. The incremental schemes employed by researchers investigating problems of geometric nonlinearity may be separated into two categories;

i) Methods which are based on linearised incremental procedures and therefore tend to drift from the equilibrium path.

ii) Methods which are self-correcting and tend to stay on the true equilibrium path.

X-6.2 Linearised incremental methods

The load is applied as a sequence of sufficiently small increments so the structure can be assumed to respond linearly during each increment.

a) PURE INCREMENTAL STIFFNESS PROCEDURE

The solution procedure for the pure incremental method may be expressed as follows: Assume that a solution $\{\delta\}_n$ is known at load $\{R\}_n$ and that a solution $\{\delta\}_n + \{\Delta\delta\}_n$ is desired at load $\{R\}_n + \{\Delta R\}_n$. Substituting into the equilibrium equation (X-10)

$$[K_o](\{\delta\}_n + \{\Delta\delta\}_n) = \{R\}_n + \{\Delta R\}_n - \{R^*(\delta_n + \Delta\delta_n)\} \quad \ldots \text{(X-18)}$$

Using a first-order Taylor series expansion of the term $\{R^*\}$ yields

$$\{R^*(\delta_n + \Delta\delta_n\} = \{R^*(\delta_n)\} + \left[\frac{\partial^2 U_N(\delta_n)}{\partial\delta_i \partial\delta_j}\right]\{\Delta\delta\}_n \quad \ldots \text{(X-19)}$$

$$= \{R^*(\delta_n)\} + [K^*(\delta_n)]\{\Delta\delta\}_n$$

which, after substituting into the equilibrium equation (X-18) and rearranging, leads to

$$([K_o] + [K^*(\delta_n)])\{\Delta\delta\}_n = \{\Delta R\}_n + \{f(\delta_n)\} \quad \ldots \text{(X-20)}$$

where $\{f(\delta_n)\} = \{R\} - [K_o(\delta_n)]\{\delta\}_n - \{R^*(\delta_n)\}$

represents the out of balance forces, which are zero for a true equilibrium position $\{\delta\}_n$. Consequently, equation (X-20) reduces to

$$[K_t(\delta_n)]\{\Delta\delta\}_n = \{\Delta R\}_n \quad \ldots \text{(X-21)}$$

where $$\{\delta\}_{n+1} = \{\delta\}_n + \{\Delta\delta\}_n \quad \ldots \text{(X-22)}$$

These equations enable a solution to be obtained one load step beyond that at which a solution is already known. The response of a hypothetical one degree of freedom structure computed from the pure incremental stiffness method is illustrated in Fig. X-3a.

b) INITIAL VALUE FORMULATION

The nonlinear equilibrium equations (X-17) may be transformed into first-order ordinary differential equations by assuming that the first derivative of the force imbalance with respect to the load parameter $\overline{P}$ is zero. Thus,

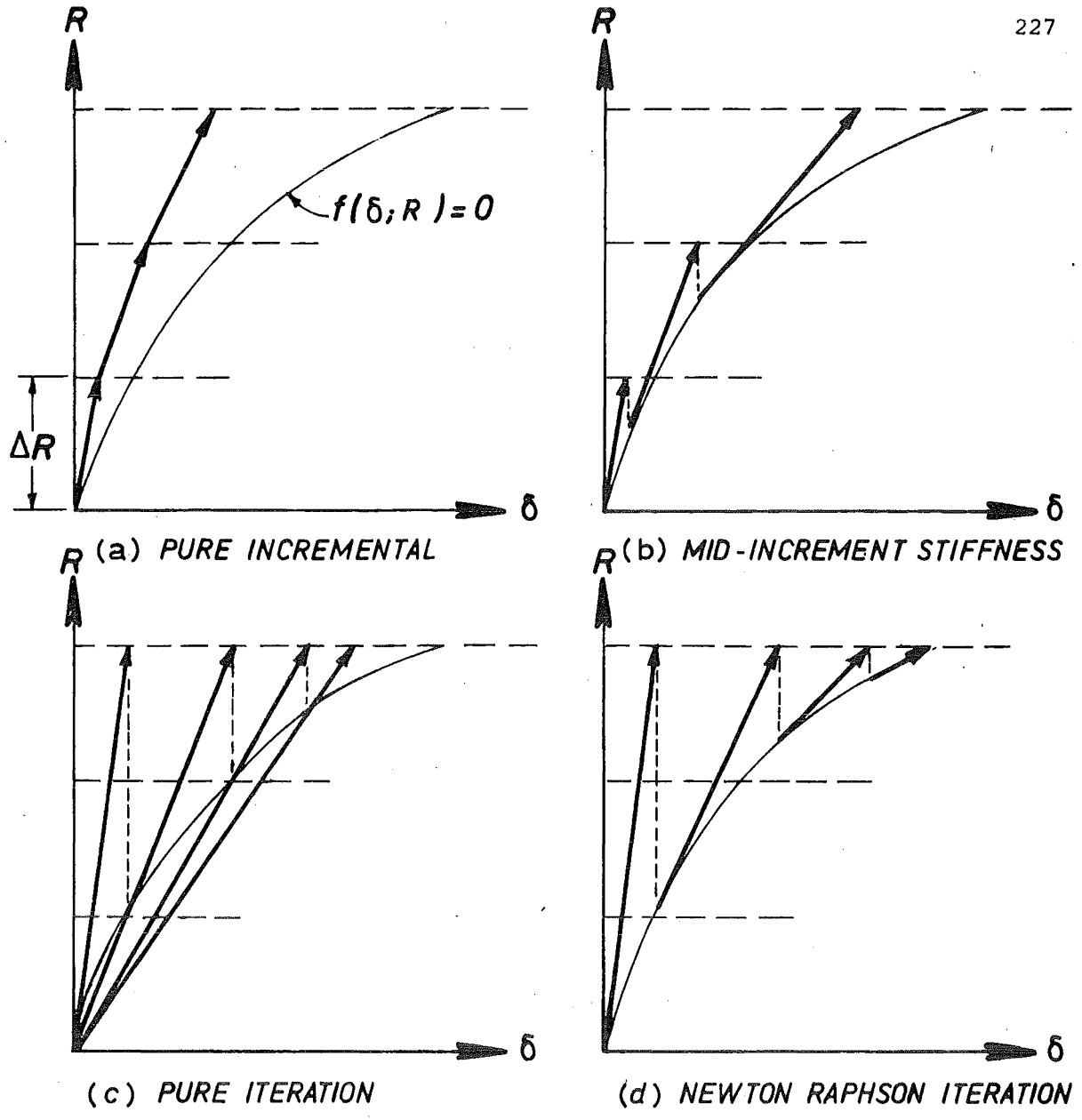

FIGURE X-3 NUMERICAL SOLUTION OF NONLINEAR EQUATIONS

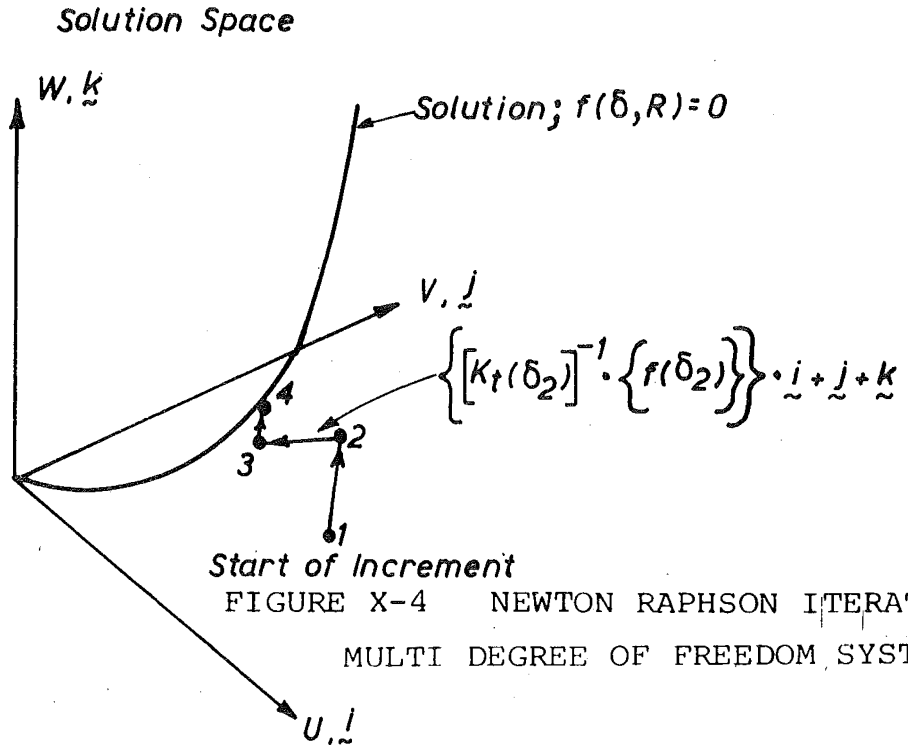

FIGURE X-4 NEWTON RAPHSON ITERATION
MULTI DEGREE OF FREEDOM SYSTEM

$$[K_t(\delta)]\{\dot{\delta}\} = \{\bar{R}\} \qquad \ldots \quad (X\text{-}23)$$

i) If the Euler-Cauchy forward difference approximation [13] of the displacement derivative,

$$\{\dot{\delta}\}_n = \{\frac{1}{\Delta\bar{P}}\}\ (\{\delta\}_{n+1} - \{\delta\}_n)$$

is substituted into equation (X-23), the linearised equation (X-21) of the pure incremental method result. The drifting from the equilibrium solution associated with this method may be reduced by using more accurate integration schemes, such as the Runge-Kutta or predictor corrector method [13].

ii) If the improved polygonal scheme of the second order Runge-Kutta method [13] is used to approximate the displacement derivative,

I.e. $$(\{\delta\}_{n+1} - \{\delta\}_n) = \Delta\bar{P}\{\dot{\delta}\}_{n+\frac{1}{2}}$$

where $$\{\dot{\delta}\}_{n+\frac{1}{2}} = \frac{\{R\}}{[K_t]_{n+\frac{1}{2}}}$$

is substituted into equation (X-23) the equation defining the MID-INCREMENT STIFFNESS METHOD [83,113] result.

$$[K_t\ (\delta_{n+\frac{1}{2}})]\ \{\Delta\delta\}_n = \{\Delta R\}_n \qquad \ldots \quad (X\text{-}24)$$

where $[K_t\ (\delta_{n+\frac{1}{2}})]$ represents the tangent stiffness evaluated mid-way along the increment $\Delta\bar{P}_n$. However, the configuration at this load is unknown so the assumption is made that the anticipated response will be of the same magnitude as the response from the previous load increment,

$$\{\Delta\delta\}_n = \beta_n\{\Delta\delta\}_{n-1} \text{ where } \beta_n = \Delta\bar{P}_n/\Delta\bar{P}_{n-1}$$

is the ratio of the magnitude of the load parameters from the previous and present load increment. Then

$$\{\delta\}_{n+\frac{1}{2}} = \{\delta\}_n + \tfrac{1}{2}\,\beta_n\{\Delta\delta\}_{n-1} \qquad \ldots \quad (X\text{-}25)$$

Although the mid-increment stiffness method will generally achieve solutions of the same accuracy as the pure incremental method while employing fewer load increments, the assumption defined in equation (X-25) will not be accurate for highly nonlinear problems.

c) STATIC PERTURBATION METHOD [41]

This method seeks the displacement corresponding to the value of the load parameter $\bar{P} + \Delta\bar{P}$ by using a Taylor sener expansion about the known point $\bar{P}$.

$$\{\delta\}_{n+1} = \{\delta\}_n + \{\Delta\dot{\delta}\}_n \Delta\bar{P} + \tfrac{1}{2}\{\Delta\ddot{\delta}\}_n \Delta\bar{P}^2 + \frac{1}{6}\{\Delta\dddot{\delta}\}_n \Delta\bar{P}^3 \quad ..(X\text{-}26)$$

where the dot denotes the derivative with respect to the load parameter $\bar{P}$. The path derivatives $\{\Delta\dot{\delta}\}_n$, $\{\Delta\ddot{\delta}\}_n$, $\{\Delta\dddot{\delta}\}_n$ etc. are defined from the solution of the sets of equilibrium equations $\{\dot{f}\} = 0$, $\{\ddot{f}\} = 0$, $\{\dddot{f}\} = 0$ etc. equal in number to the number of terms retained in the Taylor series expansion [41] . When the displacements have been defined at a particular load value the whole process is repeated to obtain the displacements corresponding to the next load value. However, errors will tend to accumulate and the amount of drift from the true equilibrium path is dependent on the load step size and the number of terms retained in the series expansion. Therefore, corrective measures such as Newton Raphson iteration must be employed to obtain accurate results for highly nonlinear problems [41]. Also, the method may become time consuming for problems involving a large number of degrees of freedom because of the numerous evaluations of derivatives required.

X-6.3 Self-correcting methods

These methods incorporate procedures where the drift associated with incremental methods is prevented from accumulating and, in the case of iterative procedures, is eliminated to within prescribed limits.

a) SELF-CORRECTING INITIAL VALUE METHODS [41,58]

These methods are significantly more accurate and stable than the linearised incremental methods because a corrective term is added to the incremental equation at each load step to ensure that the response will follow the equilibrium path closely.

i) The first order self-correcting procedures are characterised by the relation $\{\dot{f}\} + z\{f\} = 0$ ... (X-27)
where the quantity z is a scale amplification factor applied to the force imbalance vector $\{f\}$ to reduce the drift. The self-correcting nature of this formulation becomes evident when the exact solution to equation (X-27) is considered. This may be expressed as

$$f_i = C_o e^{-z\bar{P}}$$

Thus, as the value of the load parameter $\bar{P}$ is increased the magnitude of the force imbalance will tend to decrease exponentially.

Substitution of equations (X-12) and (X-17) into equation (X-27) yields the set of self-correcting first order differential equations

$$[K_t]\{\dot{\delta}\} = (1 + z\bar{P})\{\bar{R}\} - z([K_o]\{\delta\} + \{R^*(\delta)\}) \quad \ldots \quad (X\text{-}28)$$

These equations can be solved by a number of integration procedures [13] such as the Euler-Cauchy forward difference equations

$$\{\dot{\delta}\}_n = \frac{1}{\Delta\bar{P}}(\{\delta\}_{n+1} - \{\delta_n\}) \quad \ldots \quad (X\text{-}29)$$

If the amplification factor is set equal to $\frac{1}{\Delta\bar{P}}$ i.e.

$$z\,\Delta\bar{P} = 1.0 \quad \ldots \quad (X\text{-}30)$$

and equations (X-29) and (X-30) are substituted into equation (X-28)

$$[K_t]\{\dot{\delta}\} = \{\bar{R}\} + \frac{1}{\Delta\bar{P}}(\{R\} - [K_o]\{\delta\} - \{R^*(\delta)\}) \quad \ldots \quad (X\text{-}31)$$

which may be expressed

$$[K_t(\delta_n)]\{\Delta\delta\}_n = \{\Delta R\}_n + (\{R\} - [K_o]\{\delta\}_n - \{R^*(\delta_n)\}) \quad \ldots \quad (X\text{-}32)$$

where $\{\delta\}_{n+1} = \{\delta\}_n + \{\Delta\delta\}_n$

These equations define the SELF CORRECTING INCREMENTAL APPROACH [40, 41, 58] which is equivalent to the pure incremental procedure with a one-step Newton-Raphson corrector term added. I.e., the out of balance forces $\{f(\delta_n)\}$ are included in equation (X-21).

The response of a hypothetical structure with only one degree of freedom, computed with the self correcting incremental approach, is represented graphically in Figure X-3b.

This method tends to produce results which oscillate about the true solution in regions where the load deflection curve exhibits an inflection point [41, 58]. This oscillation is associated with the phase lag effect when the imbalance of forces is calculated from the previous step. However, Haisler et al [41] and Massett et al [58] have shown that the results obtained with the self-correcting scheme are generally of significantly greater accuracy than those computed with the pure incremental method using the same loading procedure, while the computational effort is only marginally increased. Also,

the deviation from the true solution which occurs in the vicinity of an inflection point is rapidly corrected when further load increments are applied.

A logical argument for using value of $z.\Delta\overline{P}$ greater than 1.0 lies in the fact that the force imbalance $\{f(\delta_n)\}$ is calculated at the start of each load increment so it is conceivable that the quantity may be varied from 1.0 to about 1.3 to increase the accuracy of the response. However, the oscillations in the vicinity of inflection points will be amplified unless these points can be anticipated and the value reduced locally.

ii) A second order self-correcting procedure may be developed by considering the second order differential equations

$$\{\ddot{f}\} + C\{\dot{f}\} + z\{f\} = \{0\} \qquad \cdots \quad (X\text{-}33)$$

where z and C are scalar amplifying factors to control the effect of the added terms. This equation can be solved by substituting expressions for $\{f\}$, $\{\dot{f}\}$, and $\{\ddot{f}\}$ into equation (X-33) and approximating the displacement derivatives by using backwards difference formulae [58]. The displacement response obtained with this solution procedure (numerical integration) has also exhibited a tendency to oscillate about the true solution in geometrically nonlinear applications.

The oscillatory nature of the displacement response is significantly reduced if exact integration of equation (X-33) is employed over each load step [56]. The solution is that of damped vibratory motion

$$\{f(s)\} = e^{-cs/2}\,(\{A\}\cos\omega s + \{B\}\sin\omega s)$$

where

$$\omega = \tfrac{1}{4}\sqrt{4z - C^2}$$

The value s is a variable for the load increment such that $\{f(s=0)\} = \{f\}_n$ and $\{f(\Delta\overline{P})\} = \{f\}_{n+1}$. $\{A\}$ and $\{B\}$ are constants which are evaluated at each load increment using the boundary conditions $\{f\}_n$ and $\{\dot{f}\}_n$. i.e.,

$$\{f(s=0)\} = \{A\} = \{f\}_n = -[K_o]\{\delta\}_n + \overline{P}_n\{\overline{R}\} - \{R^*\}_n$$

and

$$\{\dot{f}(s=0)\} = -\tfrac{C}{2}\{A\} + \omega\{B\} = \{\dot{f}\}_n = -[K_o]\{\dot{\delta}\}_n + \{\overline{R}\}$$

$$\{f\}_{n+1} = \{f(s=\Delta\overline{P})\}$$

The displacement at the end of the increment is then obtained by rearranging equation (X-11) to yield

$$\{\delta\}_{n+1} = [K_o]^{-1} \left(\bar{P}_{n+1} \{\bar{R}\} - \{R^*\}_n - \{f\}_{n+1}\right) \quad \ldots \quad (X\text{-}34)$$

where it has been assumed that the pseudo forces $\{R^*\}$ at the end of the load step may be approximated by the value at the start of the load step.

A majority of results obtained with this procedure [56] have reflected the selection of the parameter z as

$$z = \frac{5.0}{\Delta\bar{P}\sqrt{\bar{P}.\Delta\bar{P}}} \qquad \bar{P} \in [0,100] \text{ and } C = 0, \text{ or } C = \tfrac{1}{2} z^{0.2}$$

It was observed by Massett and Stricklin [58] that a small positive value of C can be used for some problems to increase the stability. However, this causes the load-displacement curve to be sluggish in response.

The advantages of this method are best realised for problems of a highly nonlinear nature and for systems with many degrees of freedom because the computational efficiency arises from the fact that the stiffness matrix is inverted (or decomposed in practice) only once for the entire analysis.

b) PURE ITERATION (successive substitution)

This method is characterised by the recursion relation

$$[K_o]\{\delta\}_{n+1} = \{R\} - \{R^*(\delta_n)\} \quad \ldots \quad (X\text{-}35)$$

Starting with an initial estimate to the displacement solution, the nonlinear effects are estimated and a set of linearised equations is solved to obtain an improved solution. This solution is back-substituted into equation (X-35) and the iteration continued until convergence of successive iterations is achieved.

For geometrically nonlinear analysis this method is severely limited by its inability to converge for problems exhibiting a significant degree of nonlinearity [100], and is not applicable to structures for which the response is path dependent.

c) NEWTON-RAPHSON ITERATION

This procedure is extremely accurate and usually converges quite rapidly, even for highly nonlinear problems, provided realistic initial estimates of the solution are made.

The ith component of the out of balance forces for an initial estimate of the displacement vector $\{\delta\}$ at a given load $\{R\}$ may be written

$$f_i(\delta) = R_i - K_{o_{ij}} \delta_j - R_i^*(\delta) \qquad \ldots \quad (X\text{-}36)$$

where the summation of index j is implied.

A Taylor series expansion of the force imbalance about the point $\{\delta\}$ yields the following expression for the out-of-balance force at an adjacent displacement state $\{\delta + \Delta\delta\}$

$$f_i(\delta + \Delta\delta) = f_i(\delta) + (\partial f_i(\delta)/\partial\delta_j)\Delta\delta_j + O[\Delta\delta^2]$$

Equating this force imbalance to zero and retaining only the first two terms in the Taylor series expansion leads to

$$-(\partial f_i(\delta)/\partial\delta_j)\Delta\delta_j = f_i(\delta)$$

which may be written

$$K_t(\delta)_{ij}\,\Delta\delta_j = f_i(\delta)$$

After assembling all the equations the Newton-Raphson procedure may be expressed

$$[K_t(\delta_n)]\{\Delta\delta\}_n = \{f(\delta_n)\}$$

The correction $\{\Delta\delta\}_n$ is added to the approximate solution $\{\delta\}_n$ to obtain a more correct (n+1)th approximate solution

$$\{\delta\}_{n+1} = \{\delta\}_n + \{\Delta\delta\}_n$$

The process is continued until $\{\Delta\delta\}_n$ is sufficiently small.

Convergence was tested during this work by comparing the Euclidean norm of each of the cartesian components of the displacement correction vector with the Euclidean norm of the corresponding vector of the total displacements. However, Bergan and Clough [7] have derived more effective convergence criteria for the displacement corrections and have noted that for some applications it may be more convenient to use

the out-of-balance forces $\{f\}$ or the element stresses as a measurement. Convergence to the correct solution is guaranteed provided:

i) $\partial f_i / \partial \delta_j$ is continuous in the neighbourhood of the root;

ii) the determinant of the tangent stiffness is not zero at the root;

iii) the initial estimate $\{\delta\}_o$ is sufficiently near the root [13].

The responses of a hypothetical structure with one degree of freedom, computed using pure iteration (successive substitution) and Newton-Raphson iteration procedures, are represented graphically in Figures X-3c and X-3d respectively. The translational response of node i of a multi-degree of freedom system, computed with the Newton-Raphson iteration scheme, may be portrayed as shown in Fig. X-4.

To obtain a knowledge of the load-deflection history an incremental/iterative method may be employed, (and indeed is essential for path dependent problems) where the load is applied in increments and Newton-Raphson iteration incorporated at each load stop. However, the 'inversion' of the tangent stiffness during each cycle of iteration may become time consuming. To reduce the amount of computational effort a MODIFIED NEWTON-RAPHSON PROCEDURE may be adopted where the tangent stiffness is held constant for several iterations and is only updated when the rate of convergence begins to deteriorate. However, the use of the procedure places some burden upon the user in deciding when the tangent stiffness should be updated because the procedure may diverge if the stiffness is not updated often enough.

X-6.4 Adopted solution procedure

Brebbin and Conner [9] have suggested that more economical solutions to many problems of geometric nonlinearity may be obtained by carrying out iteration at only, for example, every third increment. Thus the accumulated drift is eliminated intermittently and solutions of reasonable accuracy may be obtained at intermediate increments.

When confronted with machine time constraints during this work a policy of applying the load in increments, of smaller magnitude where the response is highly nonlinear, and using the self-correcting incremental scheme with intermittent Newton-Raphson iteration for a limited number of cycles was adopted. This procedure has a disadvantage however in that a prior knowledge of the degree of nonlinearity associated

with the problem is necessary to enable a selection of a suitable increment size and iteration spacing, although this selection could be made automatically within the program.

X-6.5 Limit points

Precautionary measures must be taken in the vicinity of a limit point where the determinant of the tangent stiffness is zero and consequently the system of equilibrium equations does not possess a unique solution. If a pure incremental solution procedure is employed this difficulty can be overcome by applying the loads in the form of displacement increments. In the case of incremental/iterative procedures the following method, which is illustrated graphically in Fig. X-5 for a one degree of freedom system, may be adopted.

i) Test the sign of the external work done ($\Delta^2 w$) during the application of the load increment before commencing iteration

$$\Delta^2 w = \{\Delta\delta\}^T [K_t(\delta)]\{\Delta\delta\}$$
$$= \{\Delta\delta\}^T . \{\Delta R\}$$

ii) If the sign of $\Delta^2 w$ hasn't changed but the iteration procedure fails to converge after a limited number of cycles the structural configuration is approaching a limit point so reduce the increment size.

iii) If the sign of $\Delta^2 w$ has changed (at point b of Fig X-5) do not iterate but unload to the previous load level $\{R\}_{n-1}$.

iv) If the sign of $\Delta^2 w$ is still changed (at point c of Fig. X-5) there is a limit point between the initial configuration obtained at load $\{R\}_{n-1}$ (point a) and the configuration where the change was first noted (point b)

$$\bar{p}_a < \bar{p}_{cr} < \bar{p}_b$$

v) The iteration process may be resumed at point c but it is safer to unload one extra step to point d' before starting iterations.

vi) The process of applying negative load increments and iterating continues up to the next limit point when the convergence rate will again reduce.

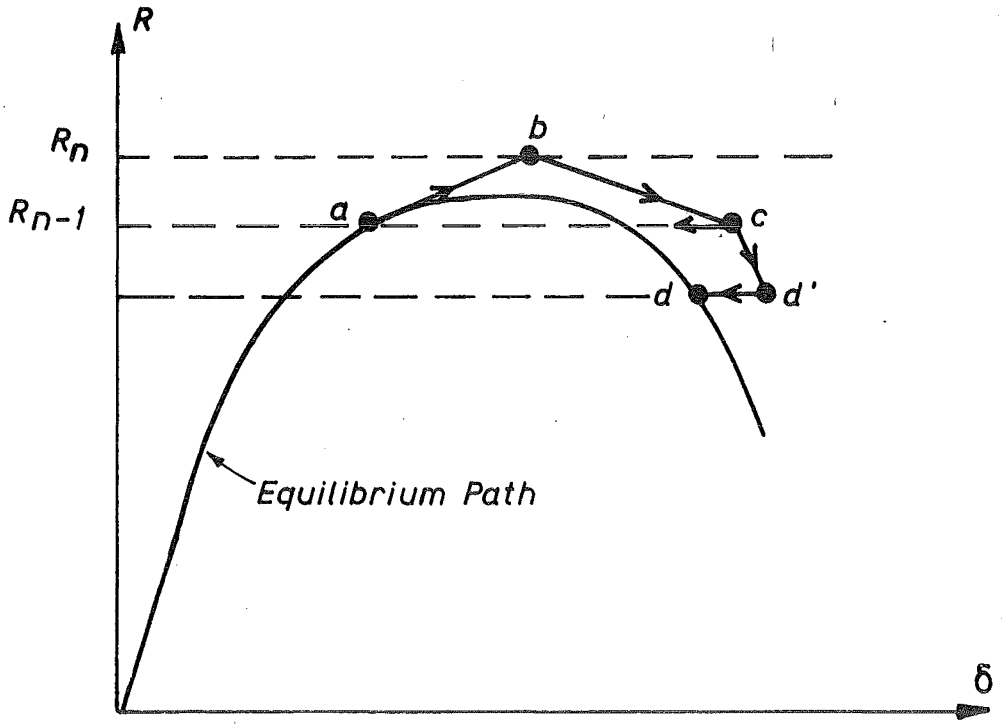

FIGURE X-5 LIMIT POINT PROCEDURE

X-7 SELECTION OF FINITE ELEMENTS

It is desirable to use higher order in-plane displacement functions when the Total Lagrangian Formulation is employed to analyse geometrically nonlinear problems because, in contrast to linear analysis, the Euler equations of the total potential energy function imply a higher order representation for membrane action than for flexural behaviour [40,57]. Also, Yang [113] concluded from numerical studies of the compression buckling of flat plates that the linear in-plane displacement functions of the QLC2 plane stress element do not couple efficiently with the third order transverse displacement functions of the twelve degree of freedom plate bending elements. The fully compatible rectangular plane stress element PMC3 is therefore preferred to the QMC3 element for geometrically nonlinear analyses because it has a higher order displacement function. However, it is necessary to use the QMC3 element to analyse nonprismatic structures because the PMC3 element is not fully compatible with a general quadrilateral shape. Although the PMC3 element permits a more complex variation of displacement in the longitudinal direction this lack of isotropy does not have any detrimental effect upon the numerical results obtained for problems associated with the large deflections of square plates, as demonstrated in section X-11.

The fully compatible CQ12 element was used to compute the linear component of the flexural stiffness but the more simply defined cubic displacement function of the ACM plate bending element was employed to evaluate the nonlinear stiffness terms, thus reducing the amount of computational effort required here. Although the ACM displacement function is not compatible in normal slope it may be argued that the boundedness requirement of interelement compatibility is not violated because if the strain energy is a function of the n^{th} derivative of the displacements then continuity of only the $(n-1)^{th}$ derivative need be satisfied between elements [20,117]. The nonlinear strain terms are a function of the first derivative of the transverse displacement only (see equation X-2).

Oden et al [66] have demonstrated that the use of a lower order displacement function to evaluate the contribution of the nonlinear terms may reduce the rate of convergence to the correct solution and a larger number of elements may be required for this inconsistent model to obtain comparable accuracy with the consistent model. A thin planar

shell element could be derived by using the simple transverse displacement function

$$w = \sum_{i=1}^{4} \tfrac{1}{4}(1 + ss_i)(1 + tt_i)w_i$$

to evaluate the nonlinear terms of the stiffness matrix. However, a rigid body rotation of this element will induce straining and thus its application is limited to small rotations [100]. Consequently, although it has been shown that the element may give satisfactory results with a coarse subdivision of the structure, the results do not necessarily converge to the correct solution with mesh refinement [24].

X-8 REDUCED ORDER OF INTEGRATION

The large amount of computational effort required to evaluate the nonlinear stiffness terms may be reduced by employing the minimum necessary number of numerical integration points. Reducing the number of integration points also has the effect of reducing the stiffness of displacement elements [118] and, provided sufficient points are used to evaluate the strain energy associated with constant strain states exactly, convergence to the correct solution with mesh refinement is guaranteed [70]. However, if too few integration points are used deformation modes may exist for which zero strains result at these points. The integration scheme will interpret these deformations as non-straining modes and may result in a singular stiffness matrix for the assembled structure. This difficulty is circumvented in the present application by using a sufficient number of points during the evaluation of the linear stiffness terms to perform the integration exactly.

A 7 x 7 Gauss-Legendre integration scheme is sufficient to integrate exactly [13] the highest order nonlinear terms of the strain energy gradient

$$\frac{\partial}{\partial\{\delta\}} \int (w,x)^4 \, dxdy \quad \text{etc}$$

because the ACM element has a cubically varying displacement function. However, a 3 x 3 integration scheme was found to produce virtually identical results for the problem of a uniaxially compressed plate, modelled with a 2 x 2 mesh of elements (see section X-11.4). Also, a 2 x 2 integration scheme produced results with a discrepancy of central transverse deflection of -3.5% at a load of $p = p_{cr}$ and of -5.6% at a load of $p = 1.6\, p_{cr}$.

The reason the accuracy of the results does not deteriorate significantly when a reduced order of integration is employed with a coarse mesh is that numerically integrated nonlinear stiffness matrices derived from cubically varying transverse displacement functions will effectively be based on lower order polynomials if the order of quadrature is sufficiently low [26], and the simple linear plate bending displacement function discussed in section (X-7) has been shown to perform satisfactorily in this context for coarse mesh idealisations [24]. Therefore, the worst consequence is not unacceptable.

However, the use of reduced integration does imply some risks and further experience will help to guide the decision as to when and by what order the integration may be reduced.

X-9 IMPERFECTIONS DUE TO FABRICATION

A perfectly flat plate subjected to in-plane compression or shear forces will not deform transversely during response, so it is necessary to perturb the system by instigating an initial out of flatness (w_o) in order to carry out a realistic nonlinear finite element analysis [117]. The solution procedure will then predict the "least energy" symmetric or antisymmetric buckling made according to whether the applied perturbation results in a symmetric or antisymmetric mode of initial out-of-flatness [24,64,84].

In reality, perfectly flat plates do not exist. Imperfections arise during fabrication due to rolling of the material and from residual stresses locked in plate elements when they are welded to other structural components. The performance of imperfect plate structures could be simulated with the finite element approach by instigating an initial out-of-flatness within the element idealisation, having the same magnitude of imperfection (w_o) as measured from the real plate, and with a mode corresponding to the critical buckling mode of the plate determined from classical theory [104]. This mode is likely to be more relevant than the measured initial shape because it will be associated with the smallest buckling load.

Plates with initial imperfections which do not correspond to the lowest buckling mode were observed, during the experimental testing of the series of plate girders described in section X-11.8, to snap-through to it during loading.

Snap-through may be caused by bending moments along the edge of the plate which arise during the distribution of the applied load among the various structural members, and are often sensitively affected by imperfections of fabrication, loading, and support conditions. However, it is not usually possible to measure these imperfections with sufficient accuracy to enable an accurate theoretical prediction of the snap-through characteristics.

The accuracy of theoretical solutions to the problem of predicting the geometrically nonlinear behaviour of thin welded plates may be improved considerably if a realistic distribution of the locked-in forces due to welding could be estimated. Few attempts have been made to measure these residual forces however.

When the measured initial out-of-flatness of a plate is small ($w_o^{max} < t/3$) a policy was adopted of applying an initial perturbation to the finite element model in the form of a small transverse point load, located so as to produce the required magnitude and mode of initial imperfection. If the measured imperfection is larger the finite element model would respond nonlinearly to the "large" perturbation load required to produce this imperfection, significant initial stresses would result, and a number of cycles of iteration would need to be performed before the equilibrium response to the initial perturbation was obtained. Therefore, plates with a large initial out-of-flatness were idealised with doubly curved surfaces constructed as an assembly of "best fit" planar elements, using topological transformations with the direction cosines of the elements based on the average of the slopes of the two transverse or longitudinal sides. This approach has the disadvantage that interelement compatibility is now violated when four sided elements are used and additional computational effort is required to implement these transformations during each increment.

Compatibility could be maintained when idealising plates with a large initial imperfection by using doubly curved shell elements rather than planar elements, with strain-displacement equations defined from a suitable shell theory. Unfortunately the inclusion of all rigid body and constant strain states now presents difficulties when a formulation based on the principle of stationary potential energy is employed and unless these difficulties can be overcome convergence to the correct solution with mesh refinement is not guaranteed.

Roberts and Ashwell [84] have used Marguerre's shallow shell theory [83] to adapt the flat rectangular QLC2/ACM finite element with the purpose of studying the buckling of imperfect plates. The strain-displacement relationships associated with this theory are,

$$\varepsilon_x = u,x + \tfrac{1}{2}(w,x)^2 + w_o,x.w,x$$

$$\varepsilon_y = v,y + \tfrac{1}{2}(w,y)^2 + w_o,y.w,y$$

$$\varepsilon_{xy} = u,y + v,x + w,x.w,y + w_o,x.w,y + w_o,y.w,x$$

where $w_o(x,y)$ represent the initial out of flatness, and the transverse deflection w is measured relative to this datum. This theory is valid provided w_o,x and $w_o,y < \tfrac{1}{8}$. [83]. The results obtained by Roberts and Ashwell for a compressed plate with an initial out of flatness $w_o^{max} = 0.1t$, idealised with an 8 x 8 mesh of QLC2/ACM elements, were virtually identical to an alternative analytical solution [84].

X-10 THREE DIMENSIONAL STIFFENER ELEMENTS

Stiffeners and frame diaphragms are often incorporated in thin-walled box-girder bridges and other thin plate structures to control buckling and transverse bending.

Harris and Bifko [44] have used only the linear component of the stiffness of beam elements to perform finite element analyses of stiffened rectangular plates with the purpose of determining the classical buckling load. However, it is important that the nonlinear terms of the beam element stiffness should also be included for a complete geometrically nonlinear analysis of thin plate structures which are controlled by slender stiffeners. The Total Lagrangian formulation was employed to evaluate these terms with the strain-displacement relationships defined by Green's strain tensors [10,38,117].

The computational effort required to derive the nonlinear terms of the stiffness matrices was reduced by neglecting shear deformations here. This assumption is justifiable for slender members because shear deformations are negligible in this case, while for non-slender members the nonlinear terms of the element stiffness matrices will be very small compared with the linear terms and thus of no consequence.

Several researchers [4,28] have preferred to use a displacement function incorporating a cubic rather than a linear variation of

twisting rotation ($\Theta y = w,x$) along the element, in order to facilitate the analysis of problems associated with torsional buckling. This may be achieved by including the curvature $\Theta y,y = w,xy$ as an additional nodal parameter, but now 'excessive continuity' is enforced between plate elements [117]. A linear variation of twisting rotation was assumed along the length of the beam element employed in this work, which has the three translational and rotational cartesian degrees of freedom at each node.

The derivation of the nonlinear element stiffness matrices according to this approach is described in Appendix B-3.

X-11 NUMERICAL EXAMPLES

X-11.1 Large deflections of a transversely loaded plate

A clamped square plate of side 2a and thickness t was modelled with both a 4 x 4 and an 8 x 8 mesh of elements. The plate was subjected to a uniform normal pressure q and the nonlinear equilibrium equations solved using both the self-correcting incremental scheme, with a load increment of $\bar{p} = qa^4/Dt = 25$; $[D = Et^3/12(1-\nu^2)]$, and the Newton Raphson incremental/iterative method with a larger load increment of $\bar{p} = 75$, for which only 2 or 3 cycles of iteration were required to achieve convergence.

The analyses were repeated using both the ACM displacement function with 25 Gauss-Legendre integration points, and the CQ12 displacement function with 28 integration points of the Hammer scheme (see chapter VI) to evaluate the nonlinear terms of the element stiffness matrices. The results were identical and since the ACM displacement function is computationally more convenient this function was used exclusively to evaluate the nonlinear terms for all subsequent examples.

The variations of the central transverse plate deflection with load, computed from the two finite element solution procedures and from the analytical theories of Timoshenko [104], Way [109] and Levy [53] are plotted in Fig. X-6. The deflections computed with the 8 x 8 mesh of elements agree to within 2% of the analytical solution obtained by Timoshenko [104].

The variations of the central membrane stress, bending stress, and total stress with load, computed from the two finite element procedures and the analytical theories of Way [109] and Levy [53], are plotted in Fig. X-7. The displacement functions of the PMC3 element

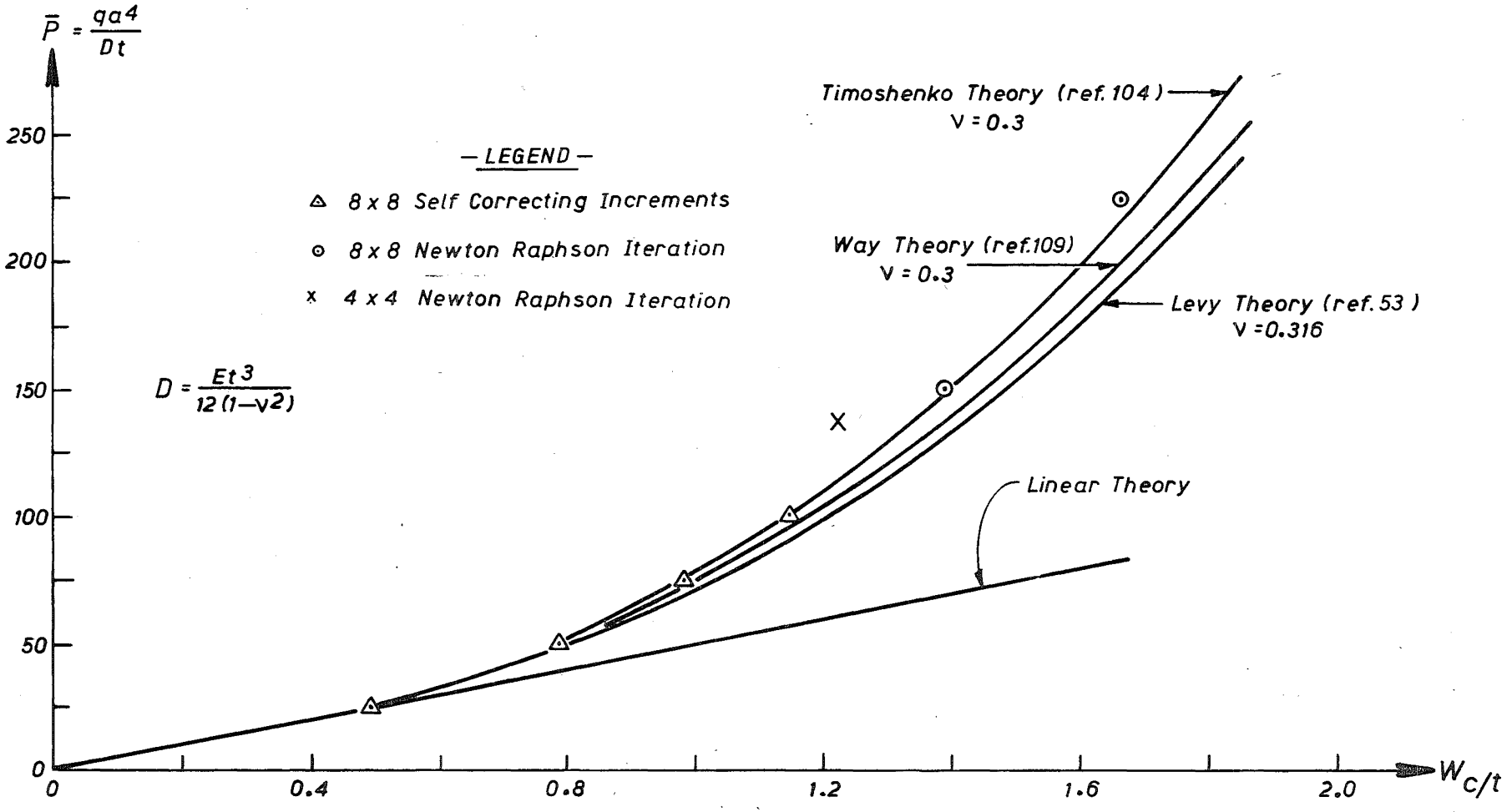

FIGURE X-6 CENTRAL DEFLECTION OF A TRANSVERSELY LOADED CLAMPED PLATE

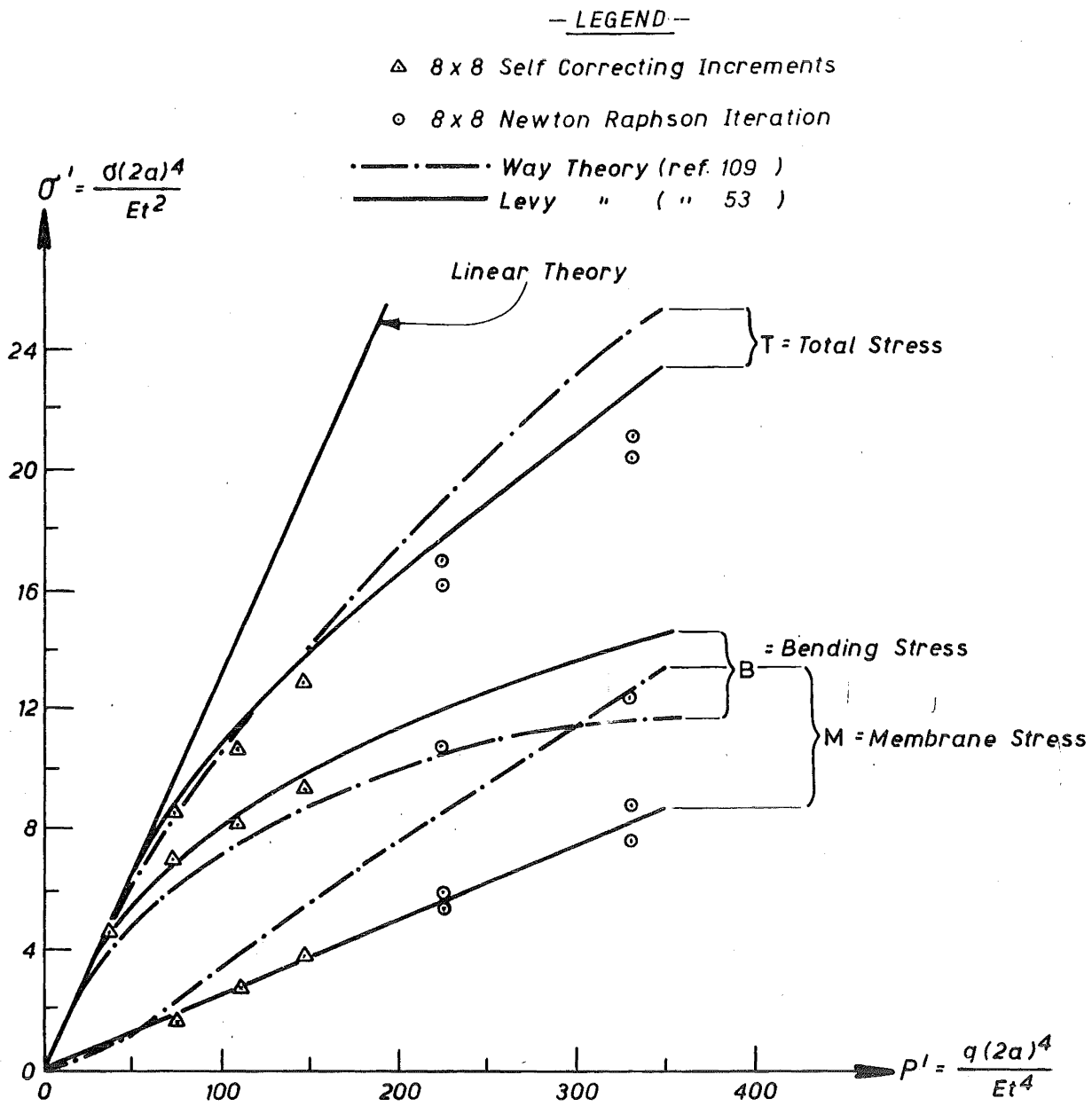

FIGURE X-7 VARIATION OF CENTRAL PLATE STRESSES

are not isotropic so membrane stresses are presented for both the longitudinal and transverse directions. The averaged membrane stresses predicted from the finite element solution agree to within 6% of the stresses obtained by Levy, but the bending stresses, although following the Levy solution during initial loading, transmute to agree to within 7% of the Way solution at larger loads. The Way solution is based upon a polynomial representation of the plate displacement field whereas Levy employs a truncated Fourier series.

X-11.2 Uni-axially compressed plate

A finite element model of a simply supported square plate with a sinusoidal initial out-of-flatness of $w_o^{max} = 0.1t$, subjected to a uniform distribution of membrane forces in the x-direction, was analysed with the loaded edges constrained to remain straight and the other edges free, as shown in Fig. X-8.

The initial out-of-flatness of the plate was simulated by applying a central transverse perturbation load of sufficient magnitude to cause a central deflection of 0.1t. The in-plane loading was then applied in increments of 0.4 Pcr and Newton-Raphson iteration employed at each step, requiring only three or four cycles of iteration to achieve convergence.

Coan [23] has presented an analytical solution to this problem using Fourier series to represent the displaced configuration.

The computed variations of central deflection with the ratio of applied load/critical load for a perfectly flat plate are plotted in Fig. X-8. The finite element results converge to within 4% of Coan's analytical solution [23] as the element subdivision is refined from a 2 x 2 mesh with 9 Gauss-Legendre integration points producing identical results to those obtained with a 49 point scheme, through a 4 x 4 mesh with 16 quadrature points, to an 8 x 8 mesh with 25 quadrature points.

Figures X-9a, X-9b, and X-9c show the variations of median fibre membrane strain ratios in both the x and y directions at;

a) the centre of the plate,

b) the midpoint of the loaded edge; and

c) the central extreme fibre bending strain, and bending strain difference from the concave to the convex side, in the direction of the loading. These strain ratios are defined as the ratio of

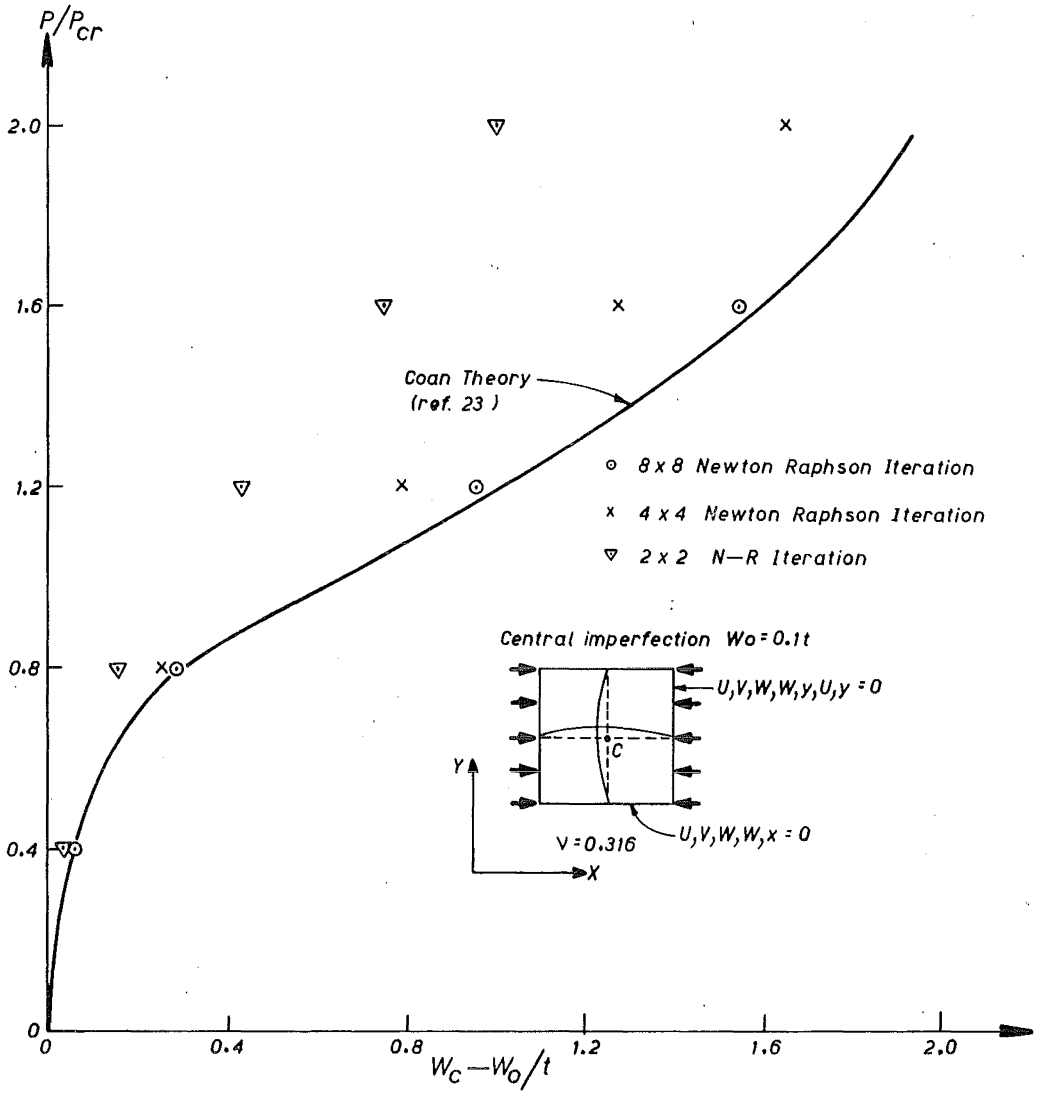

FIGURE X-8 CENTRAL DEFLECTION OF COMPRESSED PLATE

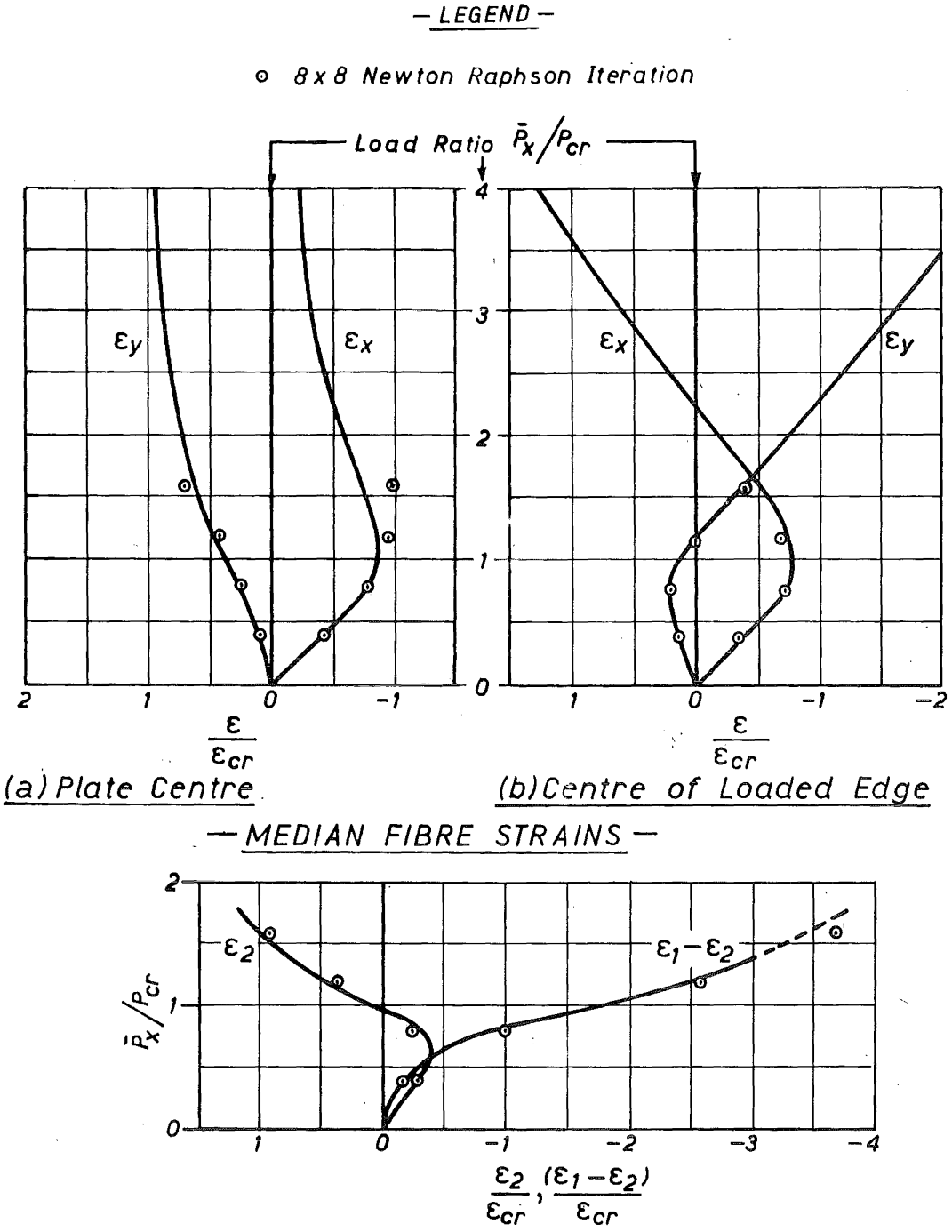

FIGURE X-9 VARIATION OF LOAD V STRAIN FOR COMPRESSED PLATE

computed strain/critical strain for a perfectly flat plate, where the computed strains are defined from Von Karman's theory of large deflections (see equation X-2) and are measured with respect to the undeformed geometry.

The finite element strains from the fine mesh solution agree to within 10% of Coan's analytical solution except for the postbuckling membrane strain ε_x, for which discrepancies of 24% and 26% are evident at the centre and mid-side of the plate respectively when $\bar{p}_x = 1.6$ Pcr. These discrepancies may be reduced by employing a higher order displacement function for the plane stress element, or refining the element mesh.

X-11.3 Flexural buckling of an imperfect column

To test the performance of the three dimensional beam element, designed to model the stiffeners of box-girder bridges and the flanges of plate girders, a slender axially compressed strut having a small initial bow (w_o^{max} = 0.1 in.) was simulated with 8 beam elements and loaded in increments of 0.1 Pcr. Newton-Raphson iteration was performed after each load increment.

The following properties were assumed for the strut: length = 40 in., cross-sectional area = 1.225 in^2, moment of inertia = 0.153 in^4, and Young's modulus of elasticity = 10^7 lb/in^2.

The computed variations of central deflection (w_c) and end shortening with axial load are plotted in Figures X-10a and X-10b respectively, along with an analytical solution presented by Roberts and Ashwell [84] who assume a sinusoidal distribution of initial out-of-flatness. Agreement is generally within 10% but the finite element model predicts a larger response near the critical load. This discrepancy may be due to the use of different assumptions in the formulation of the nonlinear stiffness matrices.

X-11.4 Flexural-torsional buckling of a universal beam

Three dimensional beam elements were used to simulate the flexural-torsional buckling of a simply supported 24 WF 76 universal beam 24 ft in length, subjected to an axial load and end moments about the major axis. These bending moments were of equal magnitude and opposite sense so as to produce single curvature.

The section of the universal beam was modelled with a deep beam element representing the web, connected to two wide beam elements representing the top and bottom flanges via an eccentric node located

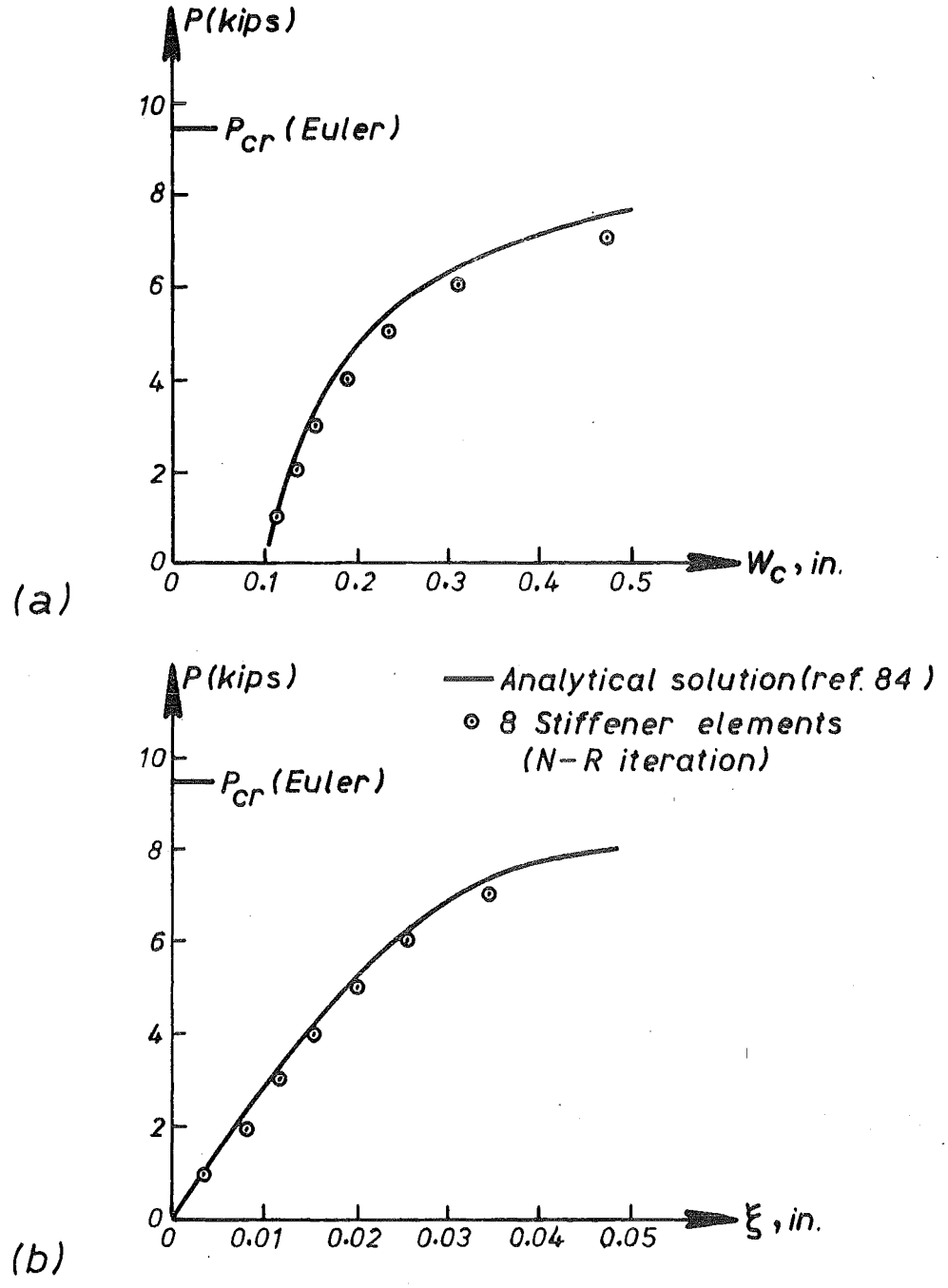

FIGURE X-10 VARIATION OF CENTRAL DEFLECTION (a) & END SHORTENING (b) FOR IMPERFECT STRUT

at the centroid of the web element. The universal beam was idealised longitudinally with 8 sets of elements.

McGuire has performed a classical eigenvalue analysis of this problem (page 536 or ref [59]) and has shown that flexural-torsional buckling will occur at an axial load of 160 kips (Pcr) with a bending moment about the major axis of 200 kip-ft (Mcr). If this mode is restrained flexural buckling will occur about the minor axis at an axial load of 257 kips.

Because the classical problem involves two loading modes, i.e., axial compression and end moments about the major axis, it is difficult to resolve this problem with an incremental approach. An assumption that the end moments result from an eccentricity of the axial load was made here. The load was applied to the finite element model in increments of 0.1 Pcr and 0.1 Mcr after a small initial perturbation moment of 2 kip-ft had been applied about the longitudinal axis to induce a torsional response. Newton-Raphson iteration was performed after each load increment.

Both the transverse displacement perpendicular to the plane of the web (Δ), and the twist about the longitudinal axis (Θ), increase rapidly over the region of the classical buckling load, as shown in Figures X-11. However, the finite element model has a reserve of strength at loads larger than the critical value, in contrast to the response exhibited during the flexural buckling of the slender strut discussed in section X-11.3. This discrepancy may be caused by the assumption of a linear variation of twist (Θ) along each element, resulting in an element which is torsionally over-stiff compared with the flexural rigidity, as discussed in section X-10.

The computed end shortening does not deviate significantly from the linear solution, as shown in Fig. X-11b, because the deflection of the beam in the plane of the web, the response of which is virtually linear, is much larger than the deflection (Δ) perpendicular to this plane. Therefore, the nonlinear axial shortening associated with the latter deflection (Δ) is negligible compared with the linear axial shortening associated with the deflection of the beam in the plane of the web.

X-11.5 Snap-through buckling of an arch

The snap-through response of a centrally loaded two hinged circular arch was analysed using two finite element idealisations, with

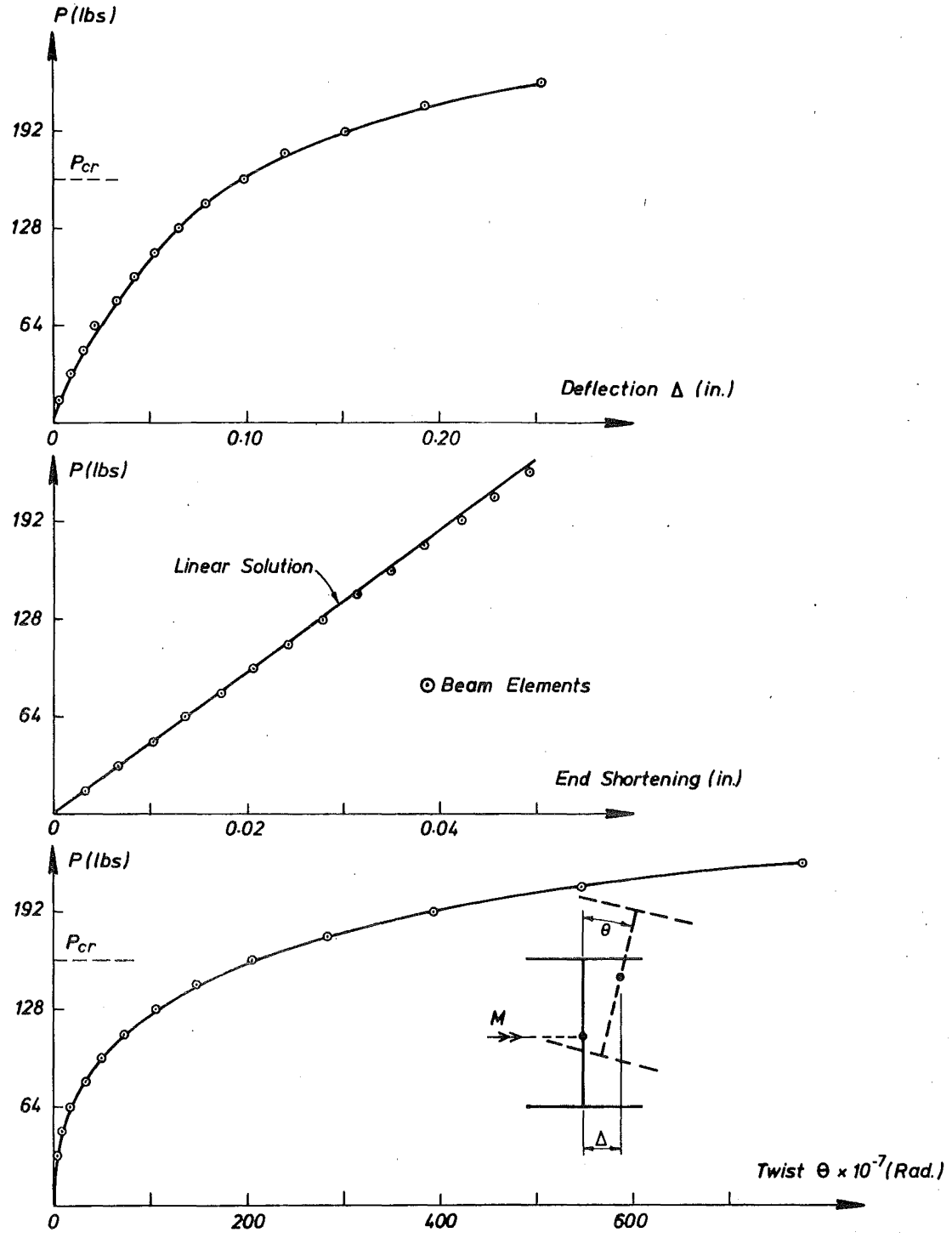

FIGURE X-11 FLEXURAL-TORSIONAL BUCKLING OF A UNIVERSAL BEAM

14 thin plate elements and 14 beam elements respectively.

The following properties were assumed for the arch:

Span L = 100 in., rise h = 3.11 in., radius R = 400 in., cross-sectional area A = 1.0 in^2., moment of inertia I = 1.0 in^4., Young's modulus of elasticity E = 10 x 10^6 lb/in^2.

A pure incremental solution procedure, with the load applied as displacement increments of 0.1 h, was employed to determine the response.

An alternative finite element solution to this problem has been presented by Argyris [2] who used 20 beam elements to idealise the arch and applied displacement increments of 0.05h to the crown of the arch. An analytical solution has been presented by Sabir and Lock [87].

The variations of the crown deflection with applied load, computed from the three finite element solutions and the analytical solution, are plotted in Fig. X-12. The finite element solutions predict the limit point phenomenon but tend to drift from the analytical solution in the characteristic manner associated with pure incremental schemes. To eliminate this drift the solution procedure must be modified as described in section X-6.5, to incorporate iteration.

The discrepancies between the three numerical solutions is due to the different idealisations employed; Argyris [2] employed an Updated Lagragain formulation while the geometric stiffness of the thin plate elements were derived with the assumption of a uniform membrane stress distribution within each element. The solution from the three dimensional beam elements was obtained with all the second order terms [38] included in the strain-displacement equations.

X-11.6 Large deflection response of a transversely loaded cylindrical Shell

A plot of the computed variation of the central deflection of a cylindrical shell with clamped edges, subjected to a uniform normal pressure, is shown in Fig. X-13, along with three alternative finite element solutions presented by Brebbin, Rodriguez and Prato [9]. An 8 x 8 finite element grid was used to model the shell and the Newton-Raphson incremental/iterative procedure employed for all solutions except that due to Prato, who used a 12 x 12 mesh of triangular elements and a mixed formulation to derive the stiffness matrices [9]. Brebbia

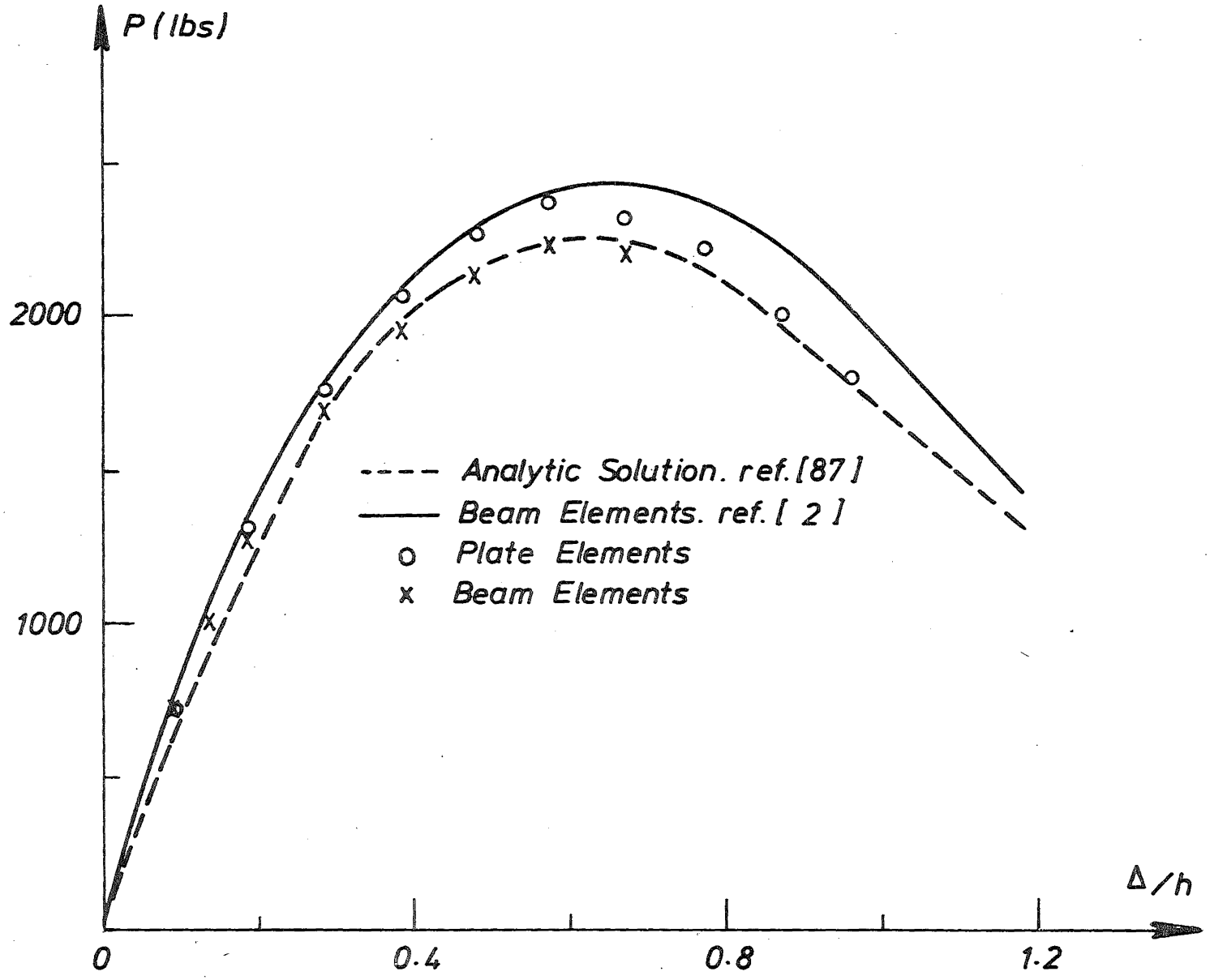

FIGURE X-12 SNAP-THROUGH OF A CIRCULAR ARCH
CROWN DEFLECTIONS

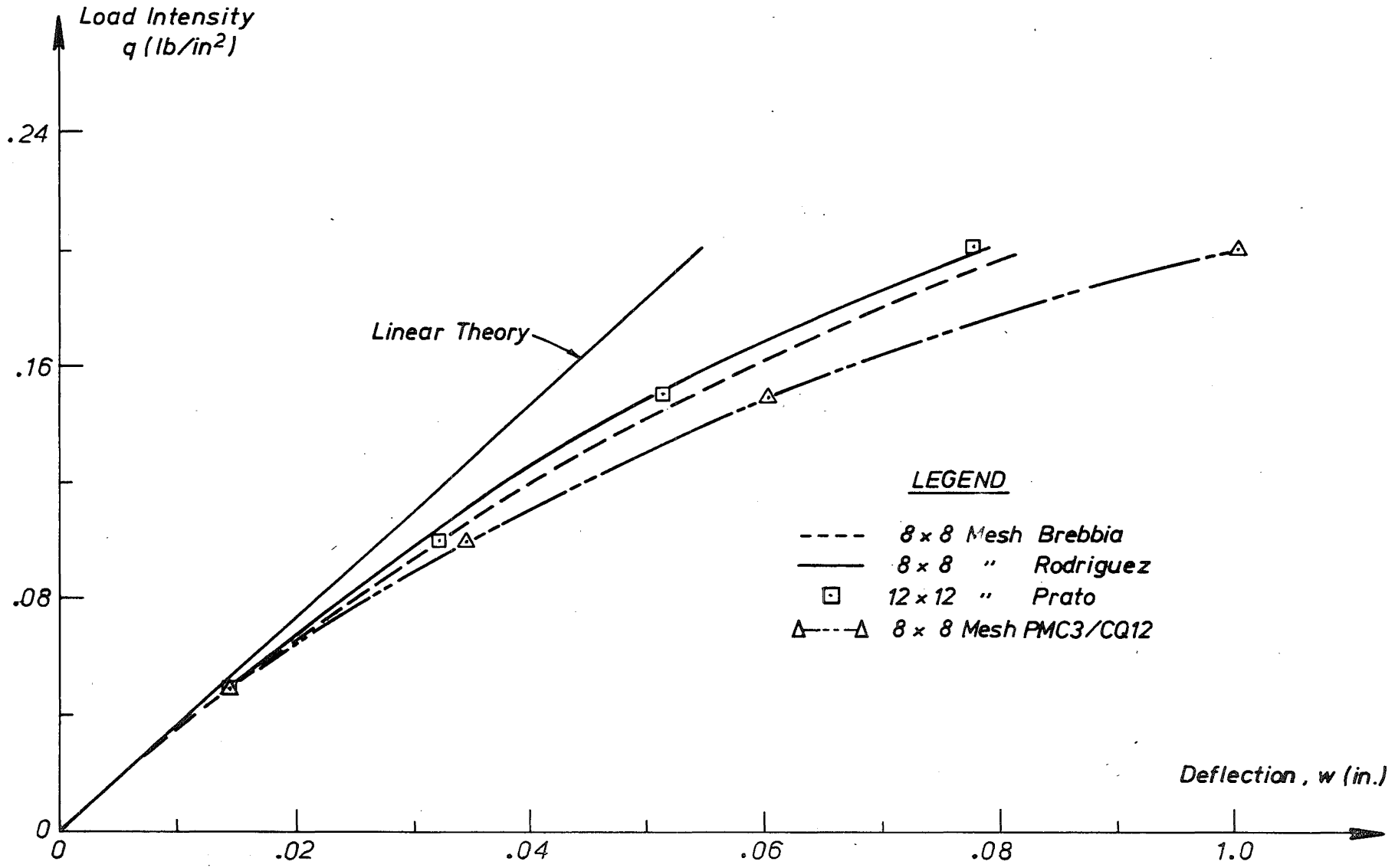

FIGURE X-13 CENTRAL DEFLECTION OF A CYLINDRICAL SHELL

idealised the shell with a mesh of rectangular elements while Rodriguez used nonconforming triangular elements, both derived from a displacement formulation.

The following dimensions and material properties were assumed for the cylindrical shell:

Length $L = 20$ in., width $b = 20$ in., radius $R = 100$ in., thickness $t = 0.125$ in., Young's modulus of elasticity $E = 450000$ lb/in^2; Poisson's ratio $\nu = 0.3$.

The finite element solution presented here, for which 16 Gauss-Legendre integration points were used over each element, predicts a variation of central deflection with the same trend as obtained from the alternative finite element models but the magnitude of the response is larger, with a maximum discrepancy of 20%. However, the geometric stiffnesses of these alternative models were derived with the assumption of a uniform membrane stress within each element [9, 106]. Virtually identical results to those presented by Prato were obtained when this assumption was incorporated into the present approach.

X-11.7 Shear buckling of an imperfect plate

A finite element model of a simply supported rectangular plate with an aspect ratio of 1.5, thickness 0.316 in., and a small sinusoidal initial out-of-flatness ($w_o^{max} = 0.01$ in.,) was loaded with the system of self-equilibrating membrane shear forces shown in Fig. X-14.

A small transverse perturbation load was applied at the centre of the plate model to simulate the initial out-of-flatness. The in-plane load was then applied in increments, with the step size reduced in the vicinity of the classical buckling load (Ncr = 0.83 Tons/in.), as portrayed in Fig. X-14. The self-correcting incremental scheme was used to solve the nonlinear equilibrium equations, with an additional cycle of Newton-Raphson iteration incorporated at loads of 0.7, 0.9, and 1.2 Tons/in.

The plate was idealised with both an 8 x 8 mesh of finite elements, with 4 Gauss-Legendre integration points used to evaluate the nonlinear terms of the element stiffness, and a 4 x 4 mesh of elements, for which solutions are presented from schemes of 4 and 9 quadrature points. Three cycles of Newton-Raphson iteration were performed for the coarse mesh solutions.

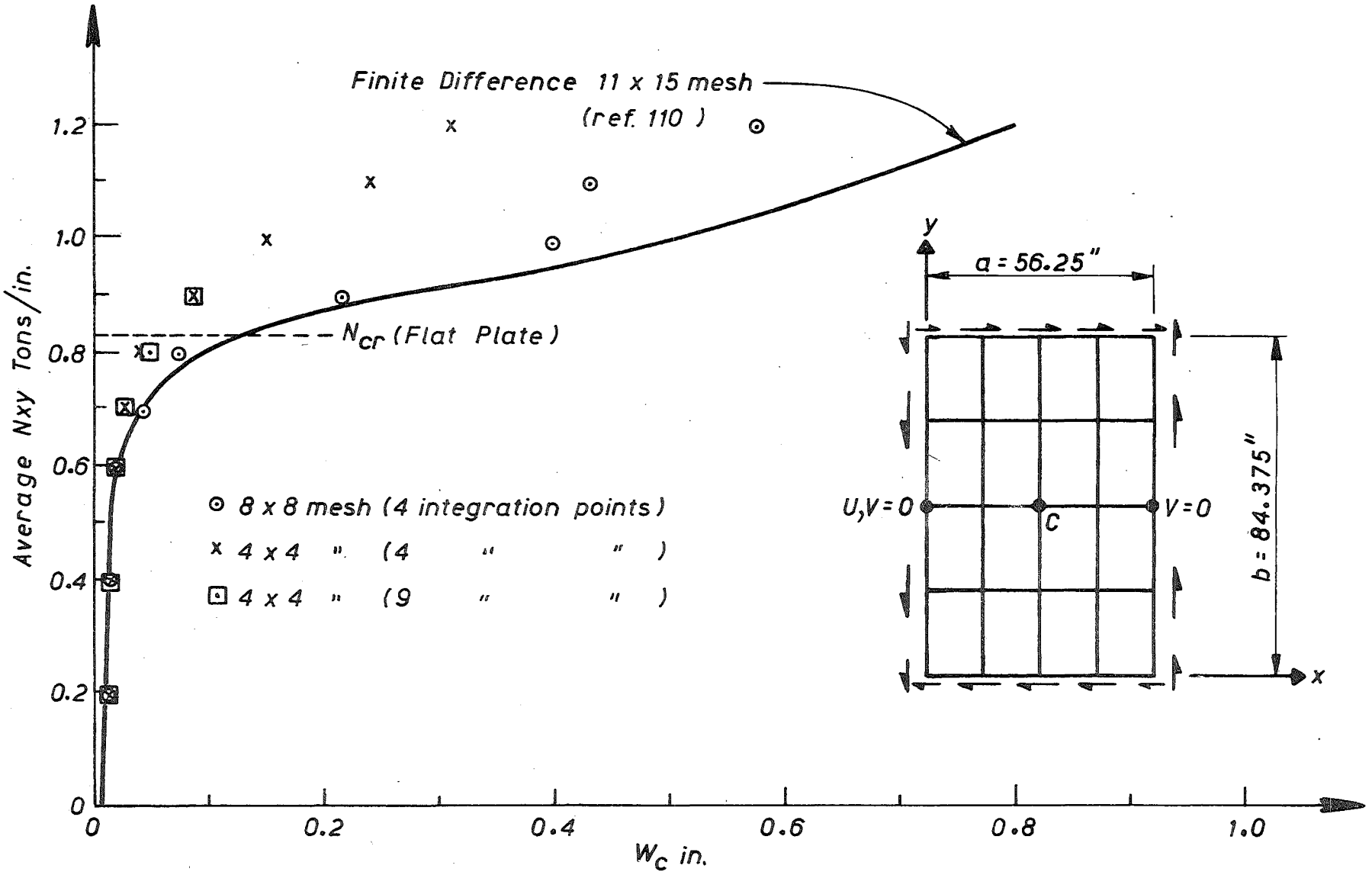

FIGURE X-14 VARIATION OF CENTRAL DEFLECTION WITH APPLIED SHEAR FOR IMPERFECT RECTANGULAR PLATE

The variations of computed central deflection with applied load are plotted in Fig. X-14, along with an alternative numerical solution presented by Williams [110] who employed a dynamic relaxation technique to solve the first order finite difference approximations to the equilibrium equations, which were derived from an 11 x 15 mesh. The finite element results obtained with the more refined 8 x 8 mesh idealisation agree to within 16% of the finite difference solution, except at loads of 1.1 Tons/in, and 1.2 Tons/in, where an oscillatory response is predicted due to the presence of an inflection point on the load-deflection curve (see section X-6.3). It is necessary to perform several cycles of iteration after each load increment in this region to obtain a solution which satisfies the equilibrium equations.

The same trend is evident from Fig. X-15 where the computed variations of the equivalent stress, S_{eq}, at the centre of the plate, with applied load are plotted. [$S_{eq} = (T_x^2 + T_y^2 - 2T_x T_y + 3T_{xy}^2)^{\frac{1}{2}}$ is the measure of the Hencky-Von Mises yield criterion, and T_x, T_y, T_{xy} are the sum of the membrane and bending stress components corresponding to the 2nd Piola-Kirchhoff stress tensor]. The 8 x 8 mesh finite element solution agrees to within 10% of the finite difference solution except at loads of 1.1 Tons/in^2 and 1.2 Tons/in^2 where there is a discrepancy of 20%. Also, convergence of the computed results with mesh refinement is slower than that achieved from the finite element analyses of uni-axially compressed plates (see section 11-6.2). This is because a shear buckle occurs over a more localised region and therefore more complex displacement functions are required to represent the deformed configuration. This trend is also evident when the accuracy of classical eigenvalue solutions to the shear and compression buckling problem are compared for a range of mesh idealisations [47].

However, the computed responses of both central deflection and equivalent stress exhibit bifurcation points in the vicinity of the classical buckling load and the stresses computed from the refined mesh are of acceptable accuracy for design purposes.

X-11.8 Shear buckling of plate girders

A number of small scale steel plate girders have been tested experimentally by Moss and Cooke [63]. Finite element analyses were performed upon two of these girders (designation number 3B and 17). The computed variations of central web deformation and stress with applied load are compared with those measured experimentally, and

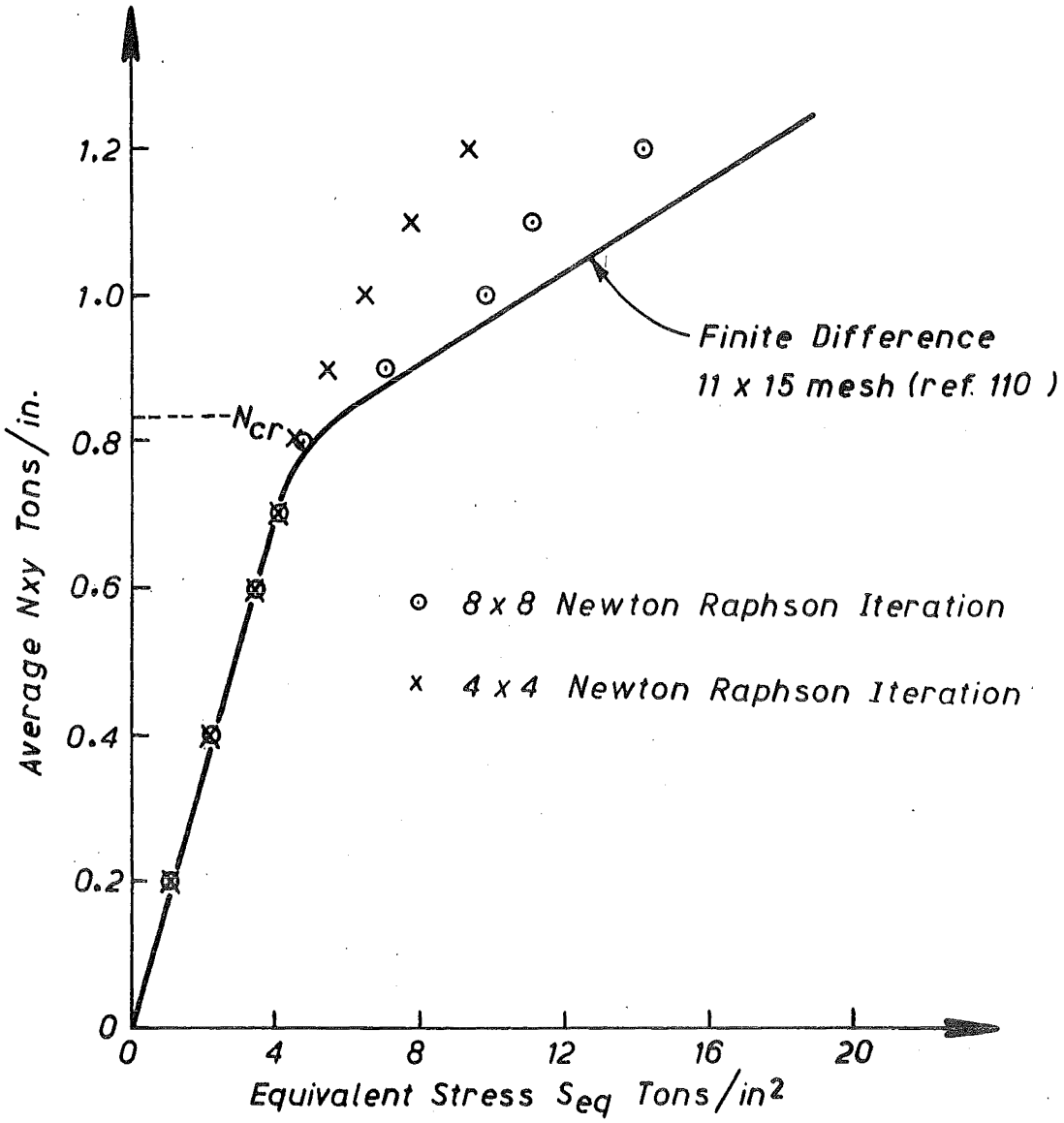

FIGURE X-15 VARIATION OF MAXIMUM SURFACE STRESSES WITH APPLIED SHEAR

related to the classical buckling load of a simply supported web panel loaded in pure shear, and to the ultimate load predicted from the theory of Rocky and Skaloud [85].

Both girders were simply supported over a span of 900 mm and loaded with two symmetrically located point loads to produce constant bending moment over the central region (see Fig. X-16)

A typical cross-section of the plate girders is shown in Fig. X-16a; the angles which join the flanges and the stiffeners to the web were 12 mm by 12 mm by 20 S.W.G. mild steel sheet, and were connected with a steel-steel "Araldite" glue for girder 17. The size of these angles was reduced for girder 3B to 6 mm by 6 mm 20 S.W.G. mild steel sheet and were connected by spot welding [63].

The webs and stiffeners for both girders were constructed from mild steel sheet with a thickness of 1.0 mm. The flanges were made from one thickness of 16 S.W.G. sheet (1.54 mm x 100 mm) for girder 17, and from two thicknesses of 16 S.W.G. (3.12 mm x 90 mm) for girder 3B. The stiffeners were designed as load bearing stiffeners according to the N.Z.S.S. 1900 Chapter 9 Clause 9.4.27.

The girder and web panel dimensions, the arrangement of stiffeners, the loading systems, and the finite element idealisations are illustrated in Figures X-16b and X-16c for specimens 17 and 3B respectively. Only one half of the girders were modelled during the finite element analyses (see Figures X-16b and X-16c) with the longitudinal in-plane displacements, the transverse flexural displacements, and the in-plane rotations restrained across the assumed centreline at midspan. Although girder 3B was not constructed with a symmetric arrangement of stiffeners (see Fig. X-16c) the assumed boundary conditions at midspan were not violated; strain gauges were located at the neutral axis and 6 mm below the compression flange, on both sides of the web across the assumed centreline, and no longitudinal flexural strains were measured at either of these stations throughout the loading.

A 6 x 6 mesh of thin plate elements was used to model the larger web panels with 4 Gauss-Legendre integration points employed to evaluate the nonlinear terms of the element stiffness. Nonlinear stiffener (beam) elements were used to represent the flanges and the stiffeners.

The maximum out-of-flatness of the web of specimen 3B was measured as 3.6 mm (3.6 times the thickness). This large imperfection was caused by residual stresses, locked into the girder during the spot

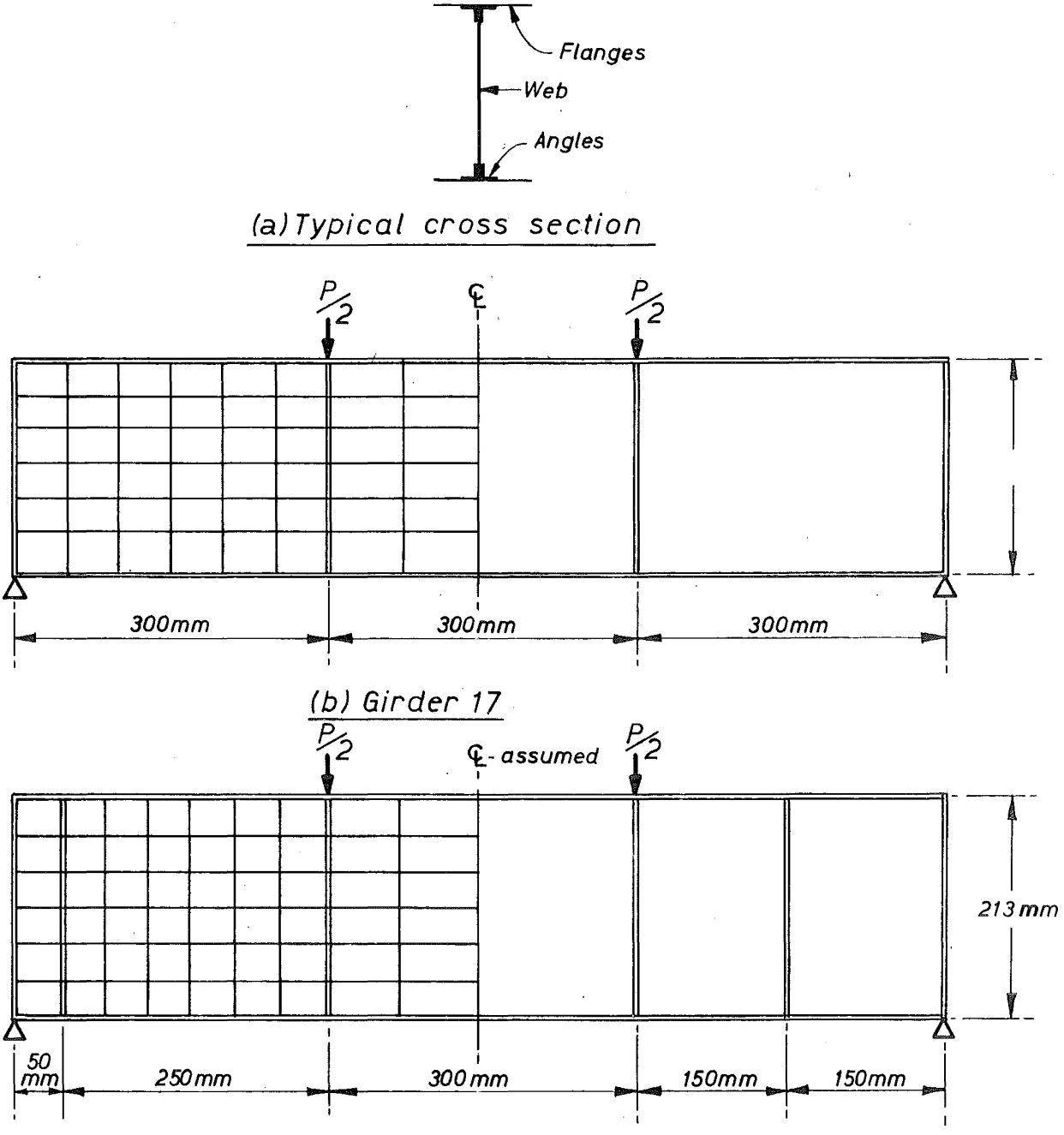

FIGURE X-16 FINITE ELEMENT MESH FOR PLATE GIRDERS

welding process, and was simulated by topologically transforming the flat plate elements so the nodes of the large web panel passed through a sinusoidal surface of central amplitude equal to 3.6 mm. The element direction cosines used in the transformation process were assumed as the average slopes of the two sides in the corresponding direction.

The out of flatness of the large web panels of the glued specimen 17 was too small to measure accurately but was assumed to have a maximum value of $w_o^{max} = 0.2$ mm for the finite element analysis, and was simulated by applying a transverse perturbation to the centre of the large web panel before loading commenced.

The load P was applied in increments to produce a loading sequence of 6 kN, 12, 16, 19, 22, 25 and 28 kN for both specimens. (The classical buckling load is approximately 13 kN). The nonlinear equilibrium equations were solved by using the self correcting incremental scheme and incorporating two additional cycles of Newton-Raphson iteration after all but the first two load steps.

The variations of transverse deflection at the centre of the web panel, computed from the finite element models of the two specimens, are plotted in Fig. X-17 along with the deflections measured experimentally from girder 3B (the deflections of girder 17 were not measured). The correlation between computed and experimental deflections is not good. However, the finite element results do follow the trend computed by Williams [110], who used a finite difference scheme to study the influence the magnitude of the initial imperfections has upon the deflection response: The nonlinear response commences near the classical buckling load (Pcr = 12.5 kN and 13.4 kN for girders 3B and 17 respectively) but this parameter assumes less significance as the magnitude of the imperfections is increased.

Considerable discrepancy (typically 25% in the vicinity of the classical buckling load) is also evident between the theoretical and experimental variations of equivalent stress (S_{eq}) with the applied loading of girder 3B, which are plotted in Fig. X-18. This discrepancy arises because the large residual stresses, locked into the girder during the welding process, caused it to yield prematurely.

Residual stresses were not present in girder 17 and agreement between the theoretical and experimentally measured equivalent stress at the centre of the left hand side web panel (side A) is to within 5% at all load steps, as shown in Fig. X-19.

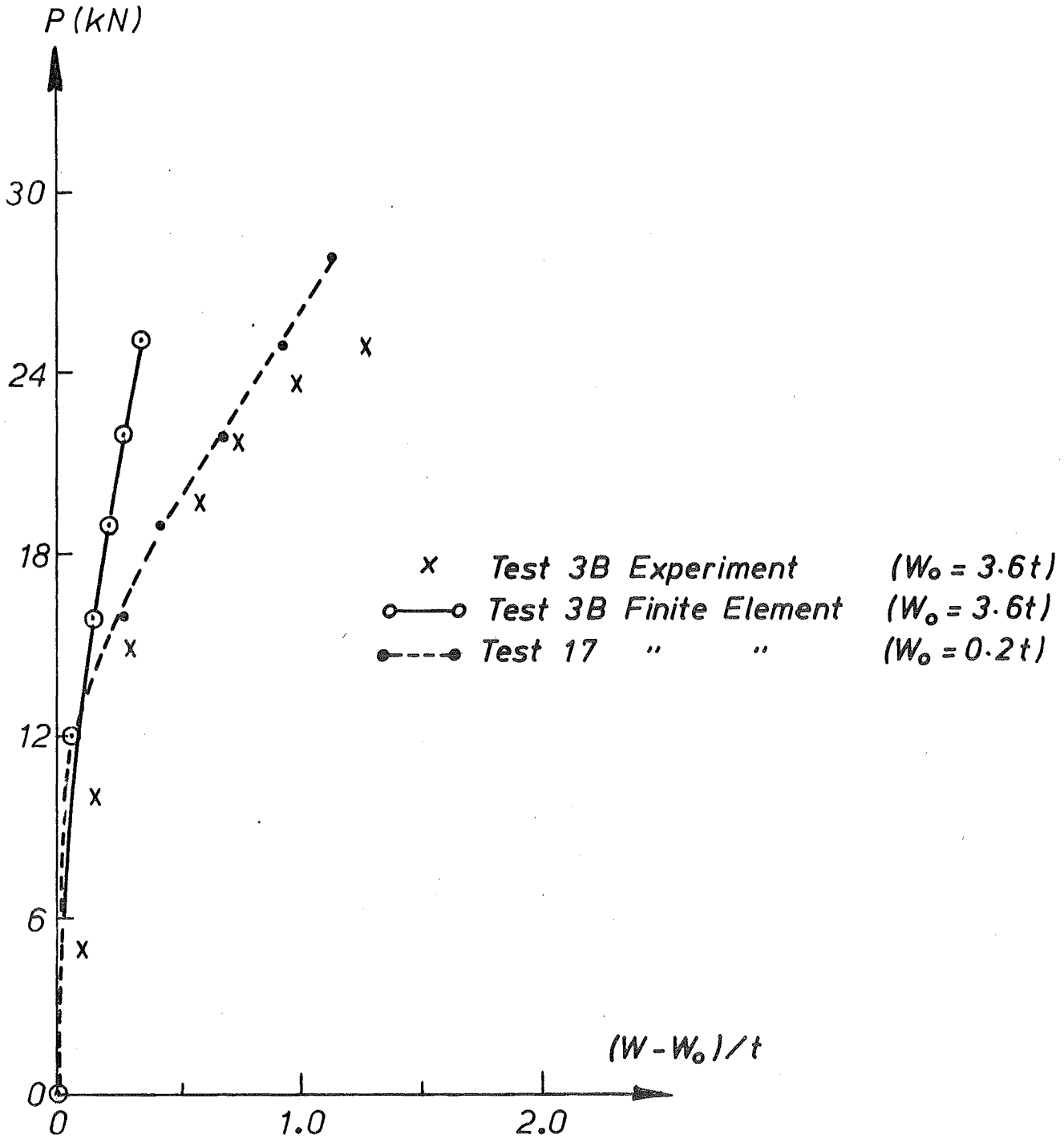

FIGURE X-17 CENTRAL TRANSVERSE WEB DEFLECTION OF PLATE GIRDERS

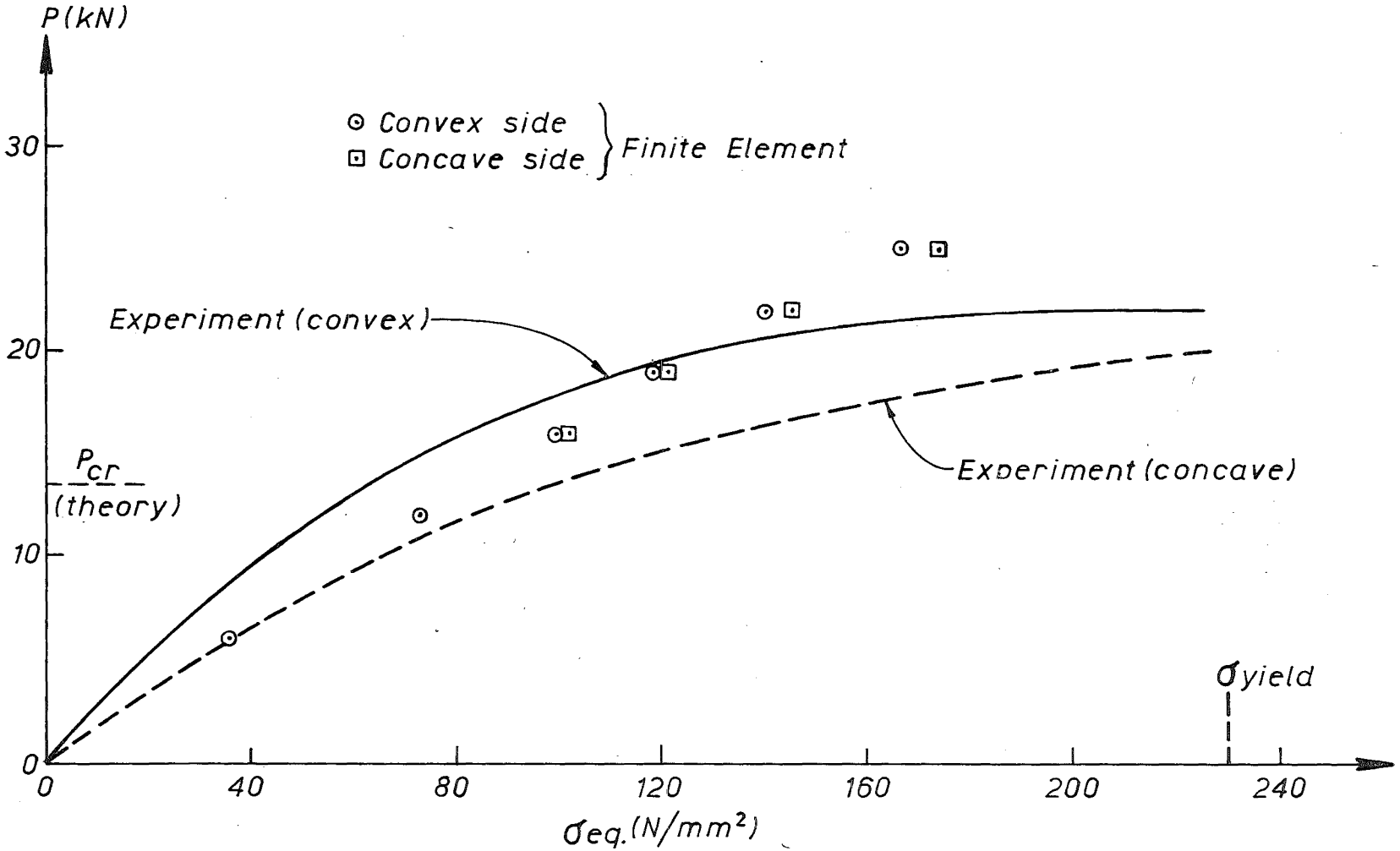

FIGURE X-18 VARIATION OF EQUIVALENT STRESS
CENTRE OF PANEL, GIRDER 3B

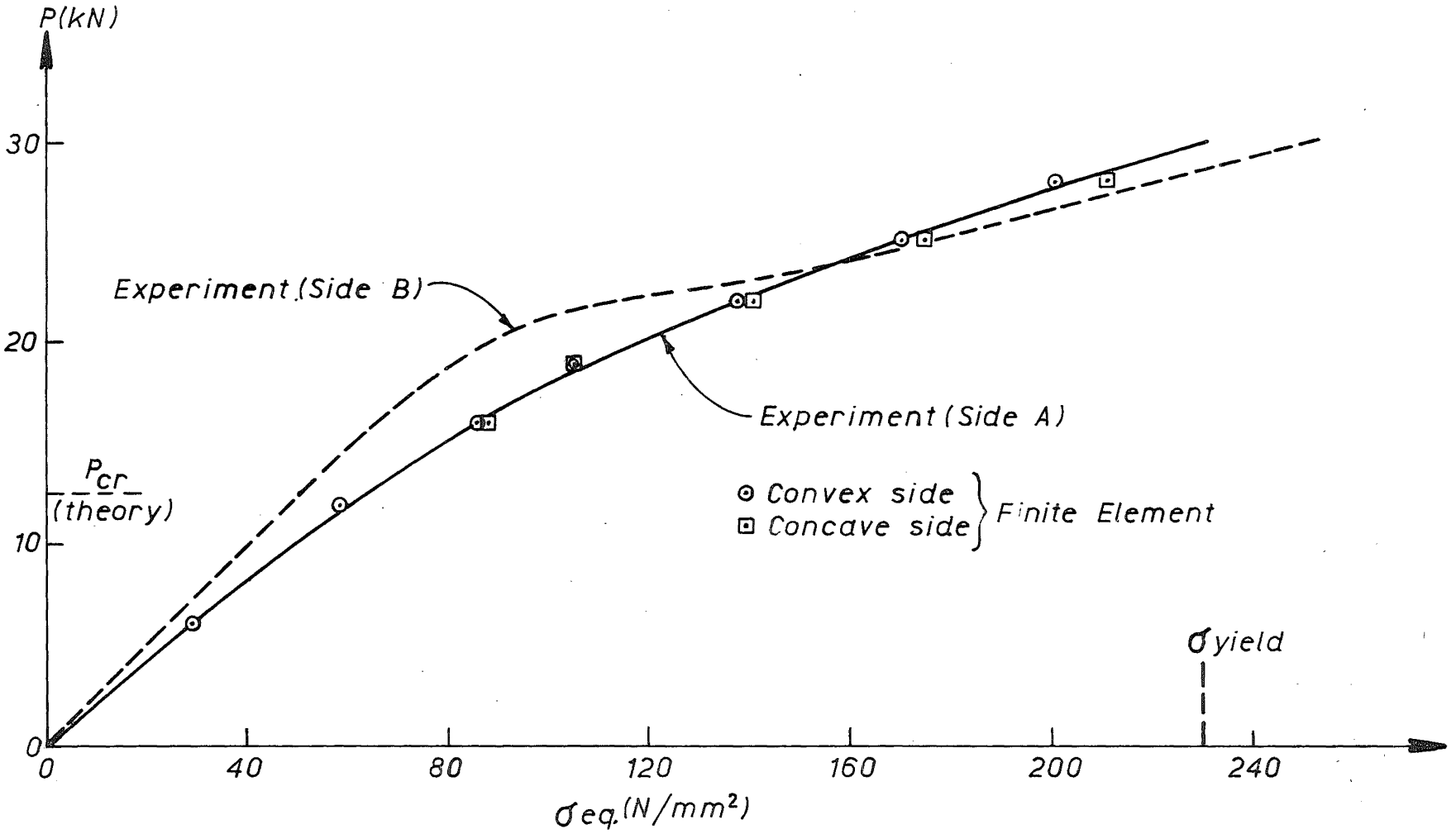

FIGURE X-19 VARIATION OF EQUIVALENT STRESS
CENTRE OF PANEL, GIRDER 17

The theoretical and experimental stresses begin to diverge near the ultimate load however, because the finite element solution presented here is based on the assumption of linear elastic material properties. Also, agreement with the stresses measured at the centre of the right hand side web panel (side B) is inferior (a maximum discrepancy of 30%) because this panel yielded at a load considerably lower than for the left hand side panel due to local imperfections, as shown photographically in Fig. X-20.

Contours of web panel deflections, computed from the finite element model of girder 17, are plotted in Fig. X-21. The form of the diagonal buckle is evident and the pattern is similar to that measured by Kerensky, Flint and Brown [48] from similar plate girder tests. It can be seen that the buckle forms more severely at the support end of the web panel, due to the more flexible panel boundary at this end and, to a lesser extent, the influence of the longitudinal compressive stresses which occur above the neutral axis of the web as a result of longitudinal bending.

X-12 CONCLUSIONS

i) The PMC3 in-plane displacement functions have been shown to perform adequately when coupled with a cubic transverse displacement function to represent geometrically nonlinear deformations. The PMC3 displacement functions are preferred to higher order in-plane displacement functions, which require additional nodal parameters, because the resulting thin planar shell element may be conveniently applied to box-girder bridge analysis without enforcing undesirable strain continuities along the element boundaries, or introducing computationally inefficient midside nodes. Also, three dimensional stiffness elements are easily incorporated.

ii) Computational effort may be reduced by employing a reduced order of integration to evaluate the geometrically nonlinear terms of the element stiffness matrices. Results which converge to the correct solution with mesh refinement may be achieved provided;

1) The linear terms of the stiffness matrix are evaluated correctly so that 'zero energy straining modes' are avoided. These may occur if insufficient integration points are used [70].

2) Sufficient integration points are used to represent the constant strain modes exactly.

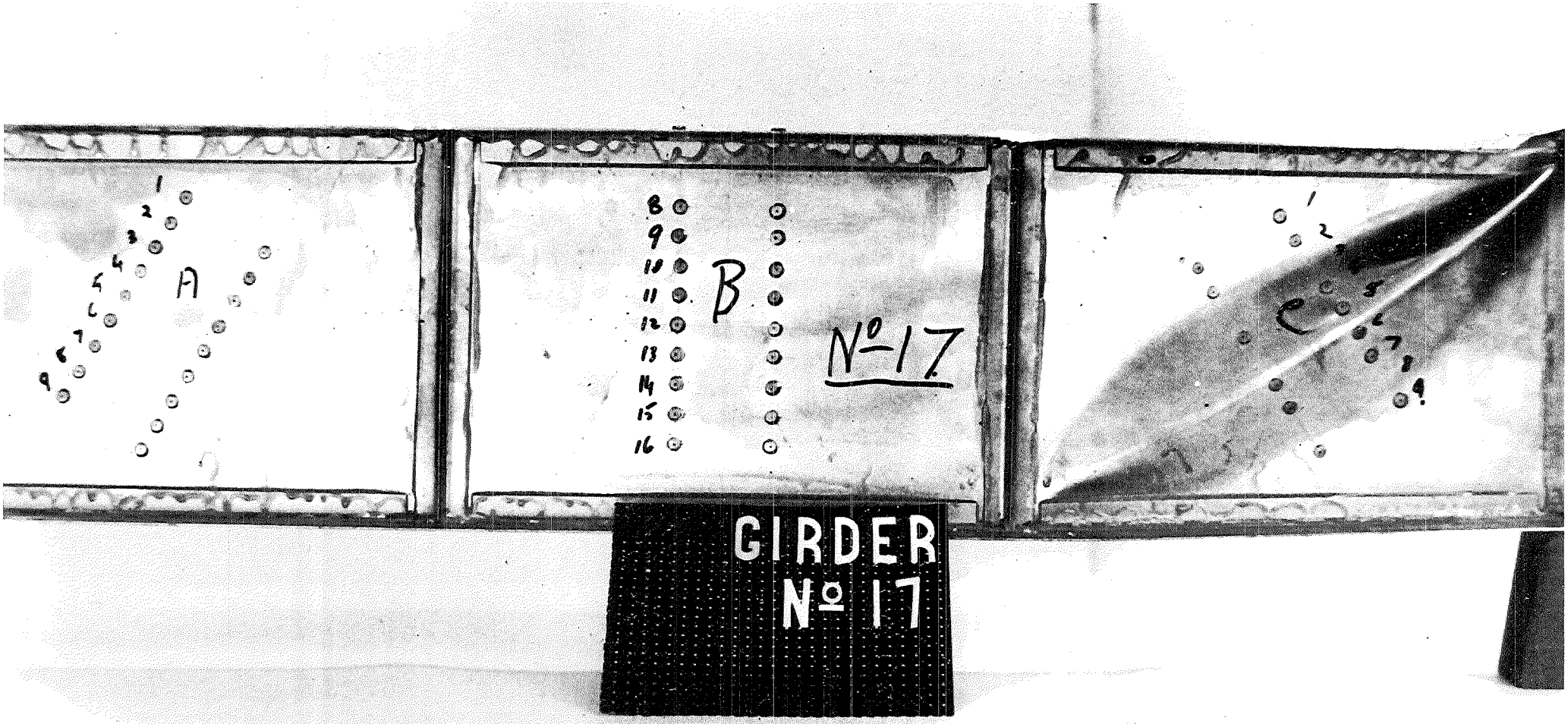

FIGURE X-20 PHOTOGRAPH OF GIRDER 17
POST ELASTIC RESPONSE

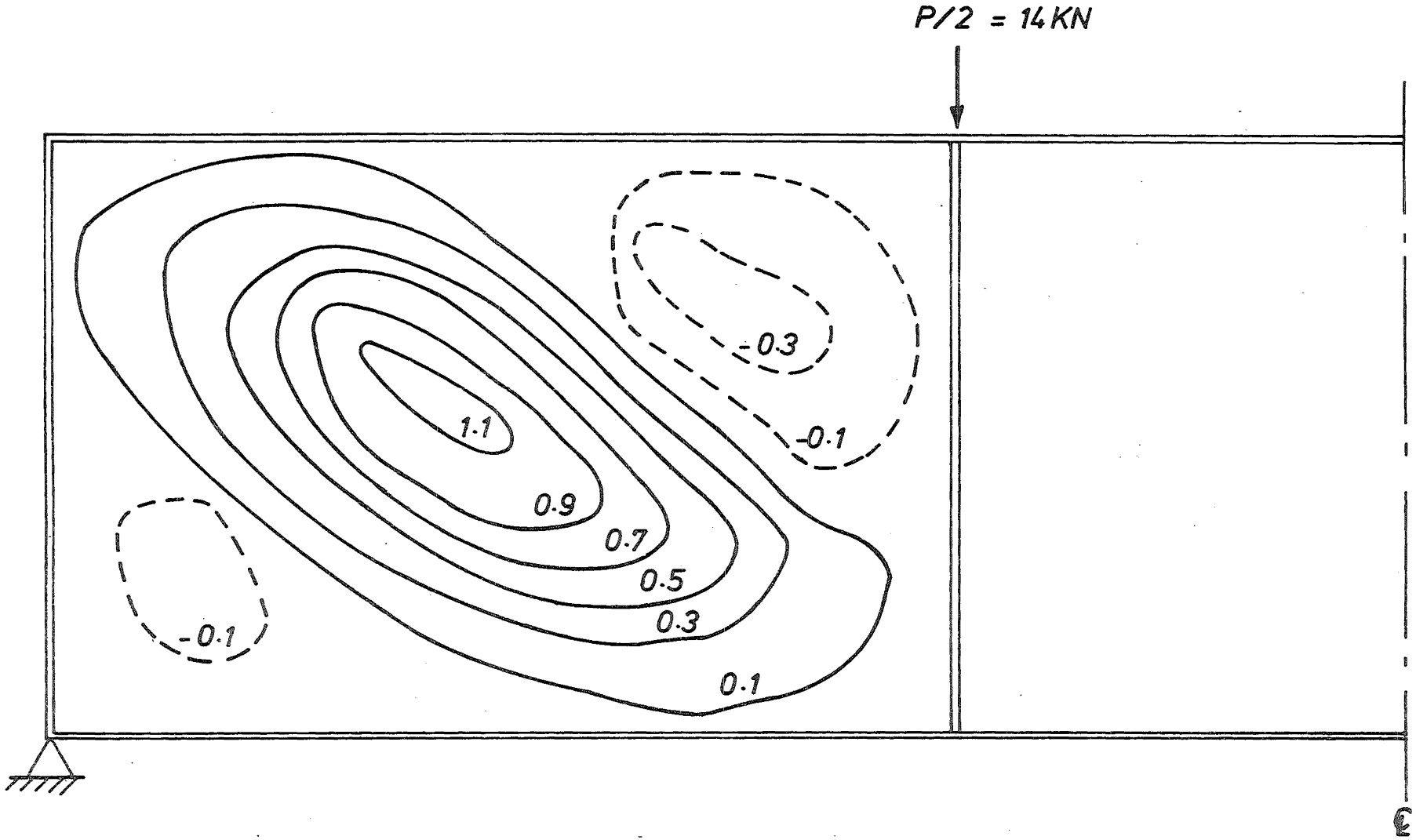

FIGURE X-21 COMPUTED DEFLECTION CONTOURS (MM) GIRDER 17

In this respect a larger number of quadrature points may be necessary for elements with a variable thickness or non-rectangular geometry. The use of a 3 x 3 Gauss-Legendre scheme to evaluate the geometrically nonlinear terms of the stiffness matrices was found to produce identical results to those obtained from an exact (7 x 7) scheme when analysing a compressed plate represented by a 2 x 2 mesh of square elements. A 2 x 2 integration scheme produced results with less than 6% discrepancy for this problem and achieved adequate results when applied to a finite model of a plate subjected to membrane shear, represented by an 8 x 8 mesh of elements.

iii) A finer mesh of finite elements is required to model the shear buckling of thin plates than to model compression buckling because shear buckling occurs over a more localised region along the plate diagonal, and is therefore associated with larger stress gradients. Antisymmetric buckling modes were not investigated here but the analysis procedure is similar except that a more refined mesh of elements will be required to achieve the same accuracy as for symmetric modes.

iv) Small initial plate out-of-flatness may be conveniently represented by applying transverse perturbation loads, but for larger imperfections ($w_o^{max} > 0.3t$) an alternative method is sought. Providing the constant strain and rigid body modes are represented correctly the shallow shell theory of Marguerre [83] may prove satisfactory in this respect because moderately large imperfections may be simulated without violating interelement compatibility or inducing initial stresses, in contrast to the methods of assembling planar four-sided elements to form a doubly curved surface, or applying large perturbation loads.

v) The equilibrium equations defining the geometrically nonlinear response of a finite element model may be solved economically by employing the self-correcting incremental scheme and incorporating Newton-Raphson iteration after selected load increments. However, the second order self-correcting initial value procedures may be even more successful and research into their performance for an extensive range of structures is warranted.

CHAPTER XI

SUMMARY AND SUGGESTIONS FOR FUTURE RESEARCH

XI-1 LINEAR ELASTIC ANALYSIS OF BOX-GIRDER BRIDGES

XI-1.1 Modelling of bridge structures

Box-girder bridges were represented in this thesis as an assemblage of thin planar finite elements, with the flexural deformations of each element governed by thin plate theory, and the in-plane behaviour by the plane stress specalisation of two-dimensional elasticity.

Analytical solutions to problems of structural and continuum mechanics can only be obtained for certain simplified geometry and boundary conditions so a numerical method which provides approximate but acceptable solutions to the real problem is preferred. The finite element method not only accommodates complex geometry and boundary conditions efficiently but it is capable of representing various types of complicated material properties that are difficult to incorporate into other numerical methods, and was therefore selected as the most suitable approach for modelling the structural behaviour of box-girder bridges of arbitrary plan and variable cross-section.

The assumption that multi-cell, multi-span, skew, curved and branching box-girder bridges behave as thin spatial plate structures was shown to be realistic, except in the vicinity of thick transverse deck slab haunches where stresses may be induced normal to the plane of the slab. However, the error associated with using thin plate theory to model this three dimensional stress state has only a local influence and is therefore acceptable when the overall behaviour of the bridge is being modelled.

XI-1.2 Finite element idealisation

THIN PLANAR SHELL ELEMENT:

The quadrilateral QMC3/CQ12 thin planar displacement element was used for this work because;

i) It has the invariant set of three translational and three rotational degrees of freedom at each node which facilitates the transformation from local to global coordinates.

ii) The displacement functions are fully compatible except for a small violation of compatibility when the longitudinal sides of adjacent elements, connected end to end, are not colinear.

iii) The plane stress component of the element has a biased beam-like behaviour so the number of elements required to represent the behaviour of the webs is minimised.

iv) The performance of the element compares favourably with other elements when employed with a large aspect ratio (1:5) so bridges of larger span can be idealised without resort to additional mesh refinement in the longitudinal direction. However, there are commendatory reports on the performance of hybrid stress and hybrid displacement elements [25, 112] so future research could be directed towards testing the suitability of these types of elements for spatial plate analysis.

THREE DIMENSIONAL BEAM ELEMENT:

Three dimensional beam elements with eccentric nodes were incorporated to model the kerbs and piers of bridge structures, the former application resulting in a significant reduction of the bandwidth of the structural stiffness matrix compared with that for a plate element representation.

TAPERED THICKNESS SHELL ELEMENT:

The use of transversely tapered elements to simulate the structural behaviour of haunched deck slabs was successful except that the stress state within thick haunches can only be represented accurately by employing a three dimensional theory. Also, modelling the webs with elements which span from the middle plane of the thick haunch to the middle plane of the soffit slab may introduce significant errors. Therefore, future research could be aimed at investigating the possibility of employing a thin-thick shell element which is tapered in the transverse direction with the deformations governed by thin plate theory along the thin edge, and by thick shell theory or three dimensional theory along the opposite thick edge, where it would be necessary to incorporate nodes at the top and bottom extreme fibres. This would eliminate the overlapping of the webs and haunched deck slab elements and the consequent inaccurate modelling of the transverse stiffness of the webs.

ELEMENT MESH:

The finite element representation of the structural behaviour of the box-girders analysed in this thesis was improved when the number of elements employed down the depth of the webs was increased from one to two, especially for those bridges constructed with thick transverse deck slab haunches, but the results obtained with the single element model were generally of sufficient accuracy for design purposes. It was shown that a longitudinal subdivision of the structure into 6 - 8 finite elements

per span provides an accurate idealisation of the structural behaviour, except that a refinement of the mesh was required in the vicinity of concentrated loads to achieve a good representation of local stress concentrations.

It was demonstrated that it is advantageous to use the mesh grading technique during the finite element analysis of complex box-girder bridges. The advantages are that firstly it facilitates local refinement of the element mesh, and thus enables a better representation of stress concentrations in the immediate vicinity of the refined mesh to be achieved without substantial additional computational effort, and secondly it alleviates the geometric restrictions previously associated with an assembly of four sided elements. However, the efficiency of the technique, when use to grade a mesh of CQ12 plate bending elements, is reduced compared with that reported for the same graded mesh of CQ16 elements [97].

Future research could be directed at establishing whether this reduction of efficiency is eliminated when the normal slope is included as a midside nodal parameter on those sides of the CQ12 element to which the mesh grading technique is to be applied.

ECONOMIZING PROCEDURES:

The analyses of regular shaped box-girder bridges may be economically performed by employing a uniform mesh idealisation so only a few element stiffness matrices need be evaluated. However, if the bridge is of irregular geometry, the deflections are large, or the material properties are inelastic, the stiffness matrix of each element will generally be different and must be evaluated separately, often requiring a large percentage of the computational effort for the complete analysis. Therefore it may be necessary to employ a reduced order of integration in order to comply with machine time constraints when such structures are idealised with a large number of element. However, although criteria have been established for selecting the minimum number of integration points necessary to ensure convergence to the correct solution with mesh refinement [70,118], an extensive programme of testing is required before the effect the

use of a reduced order of integration has upon the accuracy of solutions obtained with coarse mesh idealisation can be established.

XI-1.3 Performance of the model

The modelling of filled epoxy and aluminium box-girder bridges as linear elastic spatial plate structures was shown to be accurate for a wide range of geometric forms. Also, the transverse distributions of longitudinal membrane strain computed from the finite element idealisation of the longitudinally prestressed Bowen Street Overpass are in excellent agreement with the strain distributions measured across the cracked concrete structure. Therefore, it is concluded that design methods based upon thin plate theory will provide an accurate analysis of linear elastic and even mildly cracked reinforced concrete box-girder bridges, but it should be noted that the theory has not been verified for severely skewed box-girders or curved bridges of small radius due to the lack of suitable experimental data. Future research could be directed at achieving this verification, and also at including the effects of stiffness degradation due to concrete cracking, creep and shrinkage of the concrete,and the dynamic nature of vehicle and seismic loading within the analysis.

The longitudinal temperature stresses computed from linear elastic finite element analyses of box-girder bridges subjected to bilinear and trilinear approximations of a realistic sixth power vertical distribution of temperature are of the same order of magnitude as those induced by the self-weight of the bridge, and therefore must be considered when designing these structures. However, it is important that a range of bridges be instrumented to enable the temperature stresses to be measured experimentally and thus establish their significance.

XI-2 GEOMETRICALLY NONLINEAR ANALYSIS

XI-2.1 Physical requirements

A finite element method which is suitable for determining the geometrically nonlinear response of spatial structures, including thin walled box-girder bridges, was developed. However, the large deflection response of real structures can only be simulated accurately if the initial geometry (including the out-of-flatness of individual plate

panels), the boundary conditions, the material properties, and the initial stresses due to rolling and welding etc. are measured precisely. Also, access to a large computer is necessary in order to perform the large number of computations associated with formulating and solving the equilibrium equations of an assembled structure. These requirements are often difficult to satisfy but useful results may still be obtained when simplifying assumptions are introduced to the analysis.

XI-2.2 Total Lagrangian versus Updated Lagrangian formulation

Before performing a geometrically nonlinear finite element analysis it was necessary to choose between using a Total Lagrangian formulation or an Updated Lagrangian formulation of the equilibrium equations. The Total Lagrangian formulation was used for this work but it's application is limited to problems for which the rotational response of the structural elements is not too large, and higher order in-plane displacement functions must be used with this formulation to achieve the same accuracy as that obtained with the Updated Lagrangian formulation [40, 57]. However, this formulation has an advantage in that the effort required to implement a nonlinear constitutive relation can be less than in the Updated Lagrangian formulation [5].

XI-2.3 Finite element idealisation

The PMC3 in-plane displacement functions were used and have been shown to couple efficiently with a cubic out-of-plane element displacement function to represent the geometrically nonlinear response of a range of structures. However, it was observed that the membrane strains computed for a uniaxially compressed plate loaded in the postbuckling range were not as accurate as the computed flexural strains. The PMC3 in-plane displacement functions were preferred to higher order functions which require additional nodal parameters because firstly the assembled thin shell element may be conveniently applied to box-girder bridge analysis without enforcing undesirable strain continuity across element interfaces or introducing computationally inefficient midside nodes, and secondly, three dimensional beam elements are easily incorporated.

The procedure of using the CQ12 and ACM plate bending displacement functions separately to evaluate the linear and nonlinear contributions to the element stiffness matrix respectively is computationally efficient and was shown to have no detrimental effects upon the accuracy of the solution.

Geometrically nonlinear analyses require a more refined mesh of finite elements than linear elastic analyses because the deformations are more complex. It is necessary to use a more refined element idealisation to model shear buckling than to model compression buckling because the former phenomenon occurs over a more localised region.

XI-2.4 Initial out-of-flatness

A decision must be made as to whether to represent the initial out-of-flatness of each individual panel of a plate structure, as well as the assembled structure, as a symmetric mode, an antisymmetric mode, or possibly a combination, and how to achieve this representation.

The form of the initial out-of-flatness may be selected to correspond with that measured from the structure being simulated, or if this is not practical may be chosen to correspond with the lowest critical buckling mode as determined from a classical eigenvalue solution.

Small initial imperfections were successfully instigated within the finite element idealisation by applying small transverse perturbation loads at appropriate locations, but for larger imperfections it is necessary to use an alternative method because the application of a large perturbation load may itself result in a nonlinear large deflection response and will induce significant initial flexural stresses. The procedure used in this work was to represent the initial doubly curved surface of an imperfect plate with an assembly of four-sided planar elements, which required that transformations be applied to the stiffness matrix of each element. This procedure is computationally expensive, and interelement compatibility is violated when four-sided elements are used. Future research could be directed at testing the suitability of the shallow shell theory of Marguerre for this purpose [23, 84] because this theory enables a moderately large out-of-flatness to be simulated without violting interelement compatibility or inducing initial stresses.

XI-2.5 Solution of nonlinear equilibrium equations

The final step was to select a procedure for solving the nonlinear equilibrium equations defining the response of the structure, for which the load was applied incrementally in order to trace the load-deflection path. Pure incremental methods are associated with drifting from the true equilibrium path but this was controlled or eliminated by using self-correcting initial value or iterative procedures respectively.

The Newton-Raphson incremental/iterative procedure was concluded to be the most accurate method available for analysing geometrically nonlinear problems but it's application requires considerable computational effort because the tangent stiffness matrix must be updated and decomposed for each cycle of iteration. Also, this procedure is not generally applicable to materially nonlinear path-dependent problems. The second order self-correcting initial value procedures have been shown [41, 58] to provide results approaching the same accuracy, except in the vicinity of inflection points on the load-deflection path, but require much less computational effort than the Newton-Raphson method because it is only necessary to decompose the stiffness matrix once in the entire analysis. This is particularly advantageous when analysing structures idealised with a large number of degrees of freedom.

When confronted with machine-time constraints during this work a policy of using a first order self-correcting initial value procedure with intermittent Newton-Raphson iteration was adopted. However, because of these constraints it was only possible to use a limited number of cycles of iteration, and consequently inaccurate results were still obtained in the vicinity of inflection points on the load-deflection path.

There is a need for further research into the relative merits of the numerous solution procedures which are available, including a second order self-correcting initial value procedure with Modified Newton-Raphson iteration employed intermittently and automatically when a suitably defined measure of the drift from equilibrium exhibits significant amplification. Routines whereby reduction of increment size in the vicinity of highly nonlinear response, discriminate updating of the stiffness matrix during iteration, application of extrapolation and relaxation techniques to improve the rate of convergence of the iteration procedure [41] are included automatically within the program will also be the subject of continuing research.

It should be noted that special precautionary measures must be taken to trace the load-deflection path up to and past limit points. At the limit point the determinant of the stiffness matrix is zero so the sign of the determinant should be calculated after each load increment and having established in this way that a limit point has been negotiated, during which iteration should be dispersed with, the direction of the applied load increments must be reversed for proceeding steps until the next limit point is encountered.

XI-2.6 Substructure analysis

Relatively inexpensive solutions to the problem of local buckling may be obtained by analysing individual panels of the structure separately, using boundary conditions obtained from a linear analysis of the total structure. The effect of the redistribution of stresses due to changes in the structural configuration which may occur during loading will now be neglected, but results obtained by Langdon [52] using this approach to analyse complex large scale plate girders indicate that this may not be too serious for these types of structures.

XI-3 FUTURE RESEARCH

XI-3.1 Geometrically linear analysis of box-girder bridges

Future research into geometrically linear analysis of the structural behaviour of box-girder bridges could be aimed at:

i) testing the suitability of hybrid stress and hybrid displacement finite elements for the purpose of analysing these structures.

ii) investigating the possibility of employing a thin-thick shell element with a linear variation of thickness in one direction to simulate the structural behaviour of haunched deck slabs.

iii) investigating the desirability of including the normal slope as a midside nodal parameter on those sides of the CQ12 element to which the mesh grading technique is to be applied.

iv) constructing physical models of, and testing the accuracy of linear elastic thin plate finite element models of severely skewed box-girders and curved bridges of small radius.

v) incorporating the capability to analyse the effects of stiffness degradation due to concrete cracking, creep and shrinkage of the concrete, and the dynamic nature of vehicle and seismic loading within a finite element program.

vi) instrumenting a range of bridges to enable the stresses due to temperature gradients to be measured experimentally and thus establish their significance.

XI-3.2 Geometrically nonlinear analysis

The results presented in Chapter X indicate that the geometrically nonlinear response of thin spatial plate structures may be adequately simulated using the finite element method, so future research could be directed at:

i) establishing the relative merits of the Total Lagrangian and Updated Lagrangian formulations.

ii) testing the most promising of the nonlinear equation solving techniques and presenting qualitative and quantitative comparisons of their relative efficiency for a wide range of problems.

iii) designing or adapting displacement or hybrid elements specifically for the purpose of geometrically nonlinear analysis where, if the Total Lagrangian formulation is employed, it is desirable to use higher order in-plane displacement and stress functions relative to the bending functions. The invariant set of three translational and three rotational degrees of freedom should be retained as nodal parameters.

iv) testing the suitability of the shallow shell theory of Marguerre for the purpose of modelling the structural behaviour of thin plate structures with large initial out-of-flatness.

v) performing numerical and analytical studies to determine the efficiency of, and to present guidelines for using a reduced order of numerical integration to reduce the computational effort required to evaluate the nonlinear terms of the equilibrium equations.

vi) performing numerical studies to establish the refinement of mesh necessary to accurately simulate antisymmetric and higher buckling modes, and also the interaction of deformations across stiffness between adjacent panels. Some preliminary work on these subjects has been reported by Murray and Wilson [64] and by Langdon [51].

vii) incorporating the effects of material nonlinearity within the analysis using, for example, the Von Mises yield criterion.

viii) establishing the effect the magnitude of the initial imperfections of spatial plate structures has upon the structural response in relation to the strength of the structure.

ix) performing experimental studies to investigate the effect encouraging noncritical buckling modes (eg. antisymmetric mode for a square plate) has upon the ultimate strength of plate structures.

x) establishing the magnitude of initial stresses induced by rolling and welding of the panels of thin rolled steel plate structures.

xi) Investigating the accuracy of design formulae used for establishing the working and ultimate load of thin plate structures subjected to in-plane loading. In contrast to the assumption made during the derivation of these formulae, finite element analyses indicate that there is not a sudden, but a gradual transition from substantial to negligible flexural stiffness of thin plate structures as the magnitude of the applied load is increased.

xii) It is essential that experimental studies be performed to test the theories developed for describing the geometrically nonlinear response of thin plate structures.

REFERENCES

1. Archer, J.S., "Consistent Mass Matrix for Distributed Systems", *Journal of the Structural Division*, ASCE, Vol. 89, ST4, 1963, pp.161-173.
2. Argyris, J.H., "Continua and Discontinua", *Proceedings of the Conference on Matrix Mathods in Structural Mechanics*, W.P.A.F.B., Dayton Ohio, 1965, pp.11-190.
3. Aslam, M. and Godden, W.G., "Model Studies of Curved Box-Girder Bridges", *U.C. SESEM Report*, University of California, Berkeley, Report No. 73-5, 1973.
4. Barsoum, R.S. and Gallagher, R.H., "Finite Element Analysis of Torsional and Torsional-Flexural Stability Problems", *Int. J. Num. Methods in Eng.*, Vol. 2, 1970, pp.335-352.
5. Bathe, K., Ramm, E., and Wilson, E.L., "Finite Element Formulations for Large Deflections", *Int. J. Num. Methods in Eng.*, Vol. 19, 1975, pp. 353-386.
6. Bazely, G.P., Cheung, Y.K., Irons B.M., and Zienkiewicz, O.C., "Triangular Elements in Plate Bending-Conforming and Non-Conforming Solutions", *Proceedings of the Conference on Matrix Methods in Structural Mechanics*, W.P.A.F.B., Dayton Ohio, 1965, pp. 547-576.
7. Bergan, P.G., and Clough, R.W., "Convergence Criteria for Iterative Processes", *AIAA-JOURNAL*, Vol. 10, No. 8, 1972, pp. 1107-1108.
8. Birkhoff, G., and Garabedean, H.L., "Smooth Surface Interpolation", *J. Math, Phys. 39*, 1960, pp. 353-368.
9. Brebbia, C., and Conner, J., "Geometrically Non-Linear Finite Element Analysis", *Journal of the Engineering Mechanics Division*,ASCE, Vol. 95, No. EM2, pp. 463-483, 1969.
10. Brebbia, C., "Plane Stress-Plane Strain", Chapter 3 of *Finite Element Techniques in Structural Mechanics*", Edited by Tottenham and Brebbia. Proceedings of a Seminar at the University of Southampton, April, 1970.
11. Buckle, I.G., and Lannigan, A.G., "Transient Thermal Response of Box-Girder Bridge Decks", 3rd Australasian Conference on the Mechanics of Structures and Materials", Auckland, New Zealand, August, 1971.

12. Butlin, G.A., and McMillan, C.M., "An Improved Finite Element Analysis of Plane Coupled Shear Walls", *Civil Engineering and Public Works Review*, Dec., 1971, pp. 1299-1303.

13. Carnahan, B., Luther, H.A., and Wilkies, J.O., *"Applied Numerical Methods"*, Wiley & Son, Chapter 6, 1969, pp.362.

14. Cantin, G., and Clough, R.W., "A Curved Cylindrical Shell Finite Element", *AIAA Journal*, Vol. 6, No. 6, pp. 1057-1062 June 1968.

15. Carr, A.J., "A Refined Finite Element Analysis of Thin Shell Structures Including Dynamic Loadings", Ph. D. Dissertation *U.C. SESM Report*, University of California, Berkeley, Report No. 67-9, 1967.

16. Chan, Y.K., and Kabaila, A.P., "A Conforming Quadrilateral Element for Buckling Analysis of Stiffened Plates", *UNICIV Report* No. R-121, University of N.S.W., Dec. 1973.

17. Chapman, J.C., Dowling, P.J., Lim, P.T.K., and Billington, C.J., "The Structural Behaviour of Steel and Concrete Box-Girder Bridges", *Structural Engineer*, Vol. 49, No. 3, March, 1971.

18. Cheng, F.Y., "Dynamic Response of Nonlinear Space Frames by Finite Element Method", Proc. 1971 IASS Pacific Symposium, Part II, on *Tension Structures and Space Frames*, Tokyo and Kyoto, Paper No. 9-5, 1972, Architectural Institute of Japan, pp. 817-826.

19. Clough, R.W., and Tocher, J.L., "Finite Element Stiffness Matrices for Analysis of Plate Bending", *Proceedings of the Conference on Matrix Methods in Structural Mechanics*, W.P.A.F.B., Dayton Ohio, 1965, pp.515-546.

20. Clough, R.W., "The Finite Element Method in Structural Mechanics", Chapter 7 of *Stress Analysis*, ed. Zienkiewicz, O.C. and Holister, G.S., J. Wiley, 1965.

21. Clough, R.W., and Felippa, C.A., "A Refined Quadrilateral Element for the Analysis of Plate Bending", *Proc. 2nd Conf. Matrix Methods in Structural Mechanics*, W.P.A.F.B., Dayton Ohio, 1968.

22. Clough, R.W., and Johnson, C.P., "A Finite Element Approximation for the Analysis of Thin Shells", *Int. J. Solids and Structures*, Vol. 4, 1968, pp. 43-60.

23. Coan, J.M., "Large Deflection Theory for Plates with Small Initial Curvature Loaded in Edge Compression", *Journal of Applied Mechanics*, June, 1951, pp. 143-151.

24. Colville, J., Becker, E.B., and Furlong, R.W., "Large Displacement Analysis of Thin Plates", *Journal of the Structural Division*, ASCE, Vol. 99, No. ST3, 1973, pp. 349-364.

25. Cook, R.D., "Improved Two-Dimensional Finite Element", *Journal of the Structural Division*, ASCE, Vol. 100, No. ST9, Sept., 1974.

26. Cook, R.D., "Finite Element Buckling Analysis of Homogeneous and Sandwich Plates", *Int. J. Numerical Methods in Eng.*, Vol. 9, 1975, pp. 39-50.

27. Cowper, G.R., Lindberg, G.M., and Olson, M.D., "A Shallow Shell Finite Element of Triangular Shape", *Int. J. of Solids and Structures*, Vol. 6, 1970, pp. 1133-1156.

28. Davidson, B.J., Medland, I.C., "A Finite Element Approach to Stability Analysis in Frames", *Proceedings of Conference on Finite Element Methods in Engineering*, University of New South Wales, 1974, pp. 621.

29. Davies, J.D., Somerville, I.J., and Zienkiewicz, O.C., "Analysis of Various Types of Bridges by the Finite Element Method", *Developments in Bridge Design and Construction*, Ed. by Rockey, K.C., Bannister, J.L., and Evans, H.R., University College, Cardiff, Crosby Lockwood & Son Ltd, 1971, pp. 217-236.

30. Deak, A.L., and Pian, T.H.H., "The Application of a Smooth Surface Interpolation Technique to the Finite Element Analysis of Thin Plates", *M.I.T. Aeroelastic and Structures Research Laboratory, Report No. TR 136-2*, August, 1966.

31. Felippa, C.A., Discussion of "Incremental Finite Element Matrices" [82], *Journal of the Structural Division*, ASCE, ST12, Dec., 1974.

32. Fox, L., *"An Introduction to Numerical Linear Algebra"*, Clarendon Press, Oxford, 1964.

33. Fraeijs de Veubeke, B., "Displacement and Equilibrium Models in the Finite Element Method", Chapter 9 of *Stress Analysis* Edited by Zienkiewicz, O.C. and Holister, G.S., J. Wiley, 1965.

34. Fraeijs de Veubeke, B., "Bending and Stretching of Plates, Special Models for Upper and Lower Bounds", *Proceedings of the Conference on Matrix Methods in Structural Mechanics*, W.P.A.F.B., Dayton, Ohio, 1965, pp. 863-886.

35. Fraeijs de Veubeke, B., "A Conforming Finite Element for Plate Bending", *Int. J. Solids and Structures*, Vol. 4, 1968, pp. 95-108.

36. Fraeijs de Veubeke, B., and Sander, G., "An Equilibrium Model for Plate Bending", *Int. J. Solids and Structures*, Vol. 4, 1968, pp. 447-468.

37. Fried, I., "Accuracy of Complex Finite Elements", *AIAA Journal*, Vol. 10, No. 3, March, 1972, pp. 347-348.

38. Fund, Y.C., *"Foundations of Solid Mechanics"*, Prentice Hall, 1965.

39. Gallagher, R.H., "Analysis of Plate and Shell Structures", Proceedings of the Symposium on *Application of Finite Element Methods in Civil Engineering*, Vanderbilt University, Nashville, Tennessee, Nov. 1969, pp. 155-206.

40. Gallagher, R.H., "The Finite Element Method in Plate and Shell Instability Analysis", *Proceedings of the 4th Australasian Conference on Mechanics of Structures and Materials*, Brisbane, August, 1973, pp. 77-86.

41. Haisler, W.E., Stricklin, J.A., and Stebbins, F.J., "Development and Evaluation of Solution Procedures for Geometrically Nonlinear Structural Analysis", *AIAA-Journal*, Vol. 10, No. 3, March 1972, pp. 264-272.

42. Hammer, P.C., Marlowe, O.P., and Stroud, A.H., "Numerical Integration Over Simplexes and Cones", *Math. Tables Aid Comp.*, Vol. 10, 1956, pp. 130-137.

43. Hansteen, O.C., "Finite Element Methods as Applications of Variational Principles", Chapter 16 of Proceedings of a *Course on Finite Element Methods in Stress Analysis*, ed. Holand, I., and Bell, K., Trondheim Tech. University, 1969.

44. Harris, H.G., and Pifko, A.B., "Elastic-Plastic Buckling of Stiffened Rectangular Plates", *Proceedings of the Symposium on Application of Finite Element Methods in Civil Engineering*, Vanderbilt University, Nashville, Tennessee, Nov. 1969, pp. 207-254.

45. Irons, B.M., and Razzague, A., "Introduction of Shear Deformations into a Thin Plate Displacement Formulation", *AIAA Journal*, Vol. 11, No. 10, Oct., 1973, pp. 1438-1441.

46. Jones, R.F., "Shell and Plate Analysis by Finite Elements", *Journal of the Structural Division*, ASCE, Vol. 99, No. ST5, May, 1973.

47. Kapur, K.K., and Hartz, B.J., "Stability of Plates Using the Finite Element Method", *Journal of the Engineering Mechanics Division*, ASCE, Vol. 92, No. EM2, April, 1966.

48. Kerensky, O.A., Flint, A.R., and Brown, C.B., "The Basis for Design of Beams and Plate Girders in the Revised British Standard 153", *I.C.E.*, Part III, Vol. 5, 1956, pp. 396-521.

49. Kopal, Z., *"Numerical Analysis"*, 2nd Ed., Chapman and Hall, London, 1961.

50. Krahula, J.L., and Polhemus, J.F., "Use of Fourier Series in the Finite Element Method", *AIAA, Journal*, Vol. 6, No. 4, 1967.

51. Krylov, V.I., *"Approximate Calculation of Integrals"*, McMillan, N.Y. Translated by Stroud A.H., 1962.

52. Langdon, D.W.W., "The Buckling and Ultimate Load Behaviour of Plate Girders Loaded Under Combined Shear and Bending", M.E. Dissertation, *Report No. 75-6, University of Canterbury*, School of Engineering, 1975.

53. Levy, S., "Bending of Rectangular Plates with Large Deflections", *NACA Report No. TR 740*, 1942.

54. Lim, P.T.K., and Moffatt,K.R., "Finite Element Analysis of Curved Slab Bridges with Special Reference to Local Stresses", Proceedings of the Conference on *Developments in Bridge Design and Construction*, Ed. by Rockey, K.C., Bannister, J.L., and Evans, H.R., University College, Cardiff, Crosby Lockwood and Son Ltd, 1971, pp. 27-52.

55. Lim, P.T.K., Kilford, J.T., and Moffatt,K.R., "Finite Element Analysis of Curved Box Girder Bridges", Proceedings of the conference on *Developments in Bridge Design and Construction*, Ed. by Rockey, K.C., Bannister, J.L., and Evans, H.R., University College Cardiff, Crosby Lockwood and Son Ltd., 1971, pp. 264-286.

56. Maisel, B.I., Rowe, R.E., and Swann, R.H., "Concrete Box-Girder Bridges' *Structural Engineer*, Vol. 51, Oct., 1973, pp. 363-376.

57. Mallet, R.H., "A Mathematical Programming Approach to Nonlinear Structural Analysis", Case Inst. of Tech., Cleveland, Ohio, *EDC Report 2-65-10*, 1965.

58. Massett,D.A., and Stricklin, J.A., "Self-Correcting Incremental Approach in Non-Linear Structural Mechanics", *AIAA-Journal*, Vol. 9, 1971, pp. 2469-2466.

59. McGuire, W., *"Steel Structures"*, Prentice-Hall International Series in Theoretical and Applied Mechanics, 1968.

60. McLeod, I.A., "New Rectangular Finite Element for Shear Wall Analysis", *Journal of the Structural Division*, ASCE, Vol. 95, ST3, March 1969.

61. Ministry of Works and Development, New Zealand, Civil Engineering Division, *"Bridge Design-Temperature Gradient"*, 1970.

62. Ministry of Works and Development, New Zealand, Civil Engineering Division, *"Highway Bridge Design Brief"*, Issue C, July 1973.

63. Moss, P.J., and Cooke, N., "The Use of Small Experimental Girders to Predict the Shear Buckling and Ultimate Strength of Plate Girders", *Conference on Metal Structures and the Practising Engineer*, Inst. of Engineers, Australia, National Conference Publication No. 7416, Nov. 1974.

64. Murray, D.W., and Wilson, E.L., "Finite Element Large Deflection Analysis of Plates", *Journal of the Engineering Mechanics Division*, ASCE, Vol. 95, No. EM1, Feb., 1969, pp. 143-166.

65. Murray, D.W., and Wilson, E.L., "Finite Element Post Buckling Analysis of Thin Elastic Plates", *AIAA-Journal*, Vol. 7, No. 10, Oct., 1969, pp. 1915-1920.

66. Oden, J.T., Akay, H.U., and Johnson, C.P., "Effect of Higher Order Terms in Certain Nonlinear Finite Element Modes", *AIAA-Journal*, Vol. 11, No. 11, Nov. 1973.

67. Oliveira, E.R. de Arantes, "Theoretical Foundations of the Finite Element Method", *Int. J. Solids and Structures*, Vol. 4, 1968, pp. 929-952.

68. Palacol, E.L., and Stanton, E.L., "Anisotropic Parametric Plate Discrete Elements", *Int. J. Numerical Methods*, Vol. 6, 1973, pp. 412-425.

69. Park, R., "Design of Prestressed Concrete Structures", Vol. I, *Theory of Prestressed Concrete*, for a seminar arranged by the Department of Civil Engineering and Extension Studies, University of Canterbury, 1972.

70. Pawsley, S.F., and Clough, R.W., "Improved Numerical Integration of Thick Shell Finite Elements", *Int. J. Num. Methods in Engineering*, Vol. 3, No. 4, 1971, pp. 575-586.

71. Pian, T.H.H., "Derivation of Element Stiffness Matrices", *AIAA-Journal*, Vol. 2, No. 3, March 1964, pp. 576-577.

72. Pian, T.H.H., and Tong Ping, "The Convergence of the Finite Element Method in Solving Linear Elastic Problems", *Int. J. Solids and Structures*, Vol. 3, 1967, pp. 865-880.

73. Pian, T.H.H., and Deak, A.L., "Application of Smooth-Surface Interpolation to the Finite Element Analysis", Technical Notes, *AIAA-Journal*, Vol. 5, No. 1, Jan. 1967, pp. 187-189.

74. Pole, G.M., and Felippa, C.A., Discussion of "Rectangular Finite Elements For Shear Wall Analysis" [60], *Journal of the Structural Division*, ASCE, Vol. 96, No. ST1, January, 1970.

75. Priestley, M.J.N., "Bowen Street Overpass Prototype Test Proposal", *Central Laboratories Report No. 410*, Ministry of Works and Development, New Zealand, January, 1972.

76. Priestley, M.J.N., "Design and Research in Concrete Box-Girder Bridges in New Zealand", *Central Laboratories Report No. 411*, Ministry of Works and Development, New Zealand, 1972.

77. Priestley, M.J.N., "Thermal Gradients in Bridges - Some Design Considerations", *New Zealand Engineering*, Vol. 27, No. 7, July, 1972, pp. 228-233.

78. Priestley, M.J.N., and Miles, J.W., "Prototype Investigation of a Complex Box-Girder Bridge", Preprint, *7th ARRB Conference*, Adelaide, 1974, paper No. A52.

79. Priestley, M.J.N., "Testing a Single Cell Box-Girder Model", National Roads Board, *RRU Bulletin No. 25*, New Zealand, 1974.

80. Priestley, M.J.N., "Testing and Analysis of a Twin Spine Single Span Box-Girder Model", *Central Laboratories Report No. 491*, Ministry of Works and Development, New Zealand, Feb., 1975.

81. Przemieniecki, J.S., *"Theory of Matrix Structural Analysis"*, McGraw-Hill, 1968.

82. Rajasekaran, S., and Murray, D.W., "Incremental Finite Element Matrices", *Journal of the Structural Division*, ASCE, Vol. 99, No. ST12, Dec., 1973.

83. Reissner, E., "On Some Aspects of the Theory of Thin Elastic Shells", *J. Boston Society of Civil Engineers*, 1955, pp. 100-133.

84. Roberts, T.M., and Ashwell, D.G., "The Use of Finite Element Mid-Increment Stiffness Matrices in the Post-Buckling Analysis of Imperfect Structures", *Int. J. Solids and Structures*, Vol. 7, 1971, pp. 805-823.

85. Rockey, K.C., and Skaloud, M., "The Ultimate Load Behaviour of Plate Girders Loaded in Shear", *Structural Engineer*, Vol. 50, No. 1, January, 1972, pp. 29-47.

86. Robinson, K.E., "Cement and Concrete Research", *Research Report No. 8*, Nov. 1959.

87. Sabir, A.B., and Lock, A.C., "Analytical Solution for Snap-Through Buckling of an Arch", *Int. J. Mechanical Sciences*, Vol. 15, No. 1, January, 1973, pp. 37-48.

88. Sawko, F., and Cope, R.J., Discussion of "Finite Element Methods for the Analysis of Multicellular Structures", Crisfield, M.A., *ICE, No. 7373*, Jan., 1972, pp. 159-165.

89. Scordelis, A.C., and Lo, K.S., "Computer Analysis of Cylindrical Shells", *Journal A.C.I.*, Proc., Vol. 61, No. 5, May, 1964.

90. Scordelis, A.C., "Analysis of Continuous Box-Girder Bridges", *Structural Engineering and Structural Mechanics Report*, Department of Civil Engineering, University of California, Berkeley, Report No. 67-25, Nov., 1967.

91. Scordelis, A.C., "Analytical Solutions for Box Girder Bridges", *Developments in Bridge Design and Construction*, Ed. by Rockey, K.C., Bannister, J.L., and Evans, H.R., University College, Cardiff, Crosby Lockwood and Son Ltd., 1971, pp. 200-216.

92. Sisodiya, R.G., Cheung, Y.K., and Ghali, A., "Finite Element Analysis of Skew Curved Box-Girder Bridges", *IABSE, 30-II*, 1970, pp. 191-199.

93. Sisodiya, R.G., and Cheung, Y.K., "A Higher Order Inplane Parallelogram Element and its Application to Skewed Curved Box Girder Bridges", *Developments in Bridge Design and Construction*, Ed. by Rockey, K.C., Bannister, J.L., and Evans, H.R., University College, Cardiff, Crosby Lockwood and Son Ltd., 1971, pp. 287-303.

94. Sisodiya, R.G., Cheung, Y.K., and Ghali, A., "New Finite Elements with Application to Box Girder Bridges", *Supplement No. 74795, ICE*, 1972, pp. 207-223.

95. Sisodiya, R.G., Ghali, A., and Cheung, Y.K., "Diaphragms in Single and Double Cell Box Girder Bridges with Varying Angles of Skew", *ACI Journal*, Title No. 69-37, July, 1972, pp. 415-419.

96. Skjolingstad, L., "Three Dimensional Stress Analysis and Field Problems by the Finite Element Method", *M. Sc. Thesis*, University of Calgary, 1970.

97. Sommervaille, I.J., "A General Procedure for Grading the Mesh in Arrays of Finite Elements", *UNICIV Report No. R-85*, University of New South Wales, School of Engineering, 1971.

98. Squire, W., *"Integration for Engineers and Scientists"*, Elsevier, 1970.

99. Stegun, I.A., and Abramowitz, M., *"Handbook of Mathematical Functions with Formulae, Graphs, and Mathematical Tables"*, N.Y., Dover Publications, 1965.

100. Stricklin, J.A., Haisler, W.E., and Von Riesemann, W.A., "Geometrically Nonlinear Structural Analysis by the Direct Stiffness Method", *Journal of the Structural Division*, ASCE, Vol. 97, No. ST9, September, 1971, pp. 2299-2313.

101. Swann, R.A., "A Feature Survey of Concrete Box Spine-Beam Bridges", *Cement and Concrete Association*, Technical Report 42.469, June, 1972.

102. Taylor, R.L., "On Completeness of Shape Functions for Finite Element Analysis", *Int. J. Numerical Methods*, Vol. 4, 1972, pp. 17-22.

103. Timoshenko, S.P., and Goodier, J.N., *"Theory of Elasticity"*, 2nd Edition, McGraw-Hill,1951.

104. Timoshenko, S.P., and Woinowsky-Kreiger, S., *"Theory of Plates and Shells"*, 2nd Edition, McGraw-Hill, New York, 1959.

105. Tottenham, H., "Basic Principles", Chapter 1 of *Finite Element Techniques in Structural Mechanics*, Southampton University Press, 1971.

106. Tottenham, H., and Brebbia, C., "Shells", Chapter 6 of *Finite Element Techniques in Structural Mechanics*, Southampton University Press, 1971.

107. Von Karman, T., *"Festigkeitsprobleme in Maschinenbau Encyklopaedia der Mathematischen Wissenschaften"*, 1910.

108. Walz, J.E., Fulton, R.E., and Cyrus, N.L., "Accuracy and Convergence of Finite Element Approximation", *Proceedings of the 2nd Conference on Matrix Methods in Structural Mechanics*, W.P.A.F.B., Dayton, Ohio, 1968.

109. Way, S., "Uniformly Loaded Clamped Rectangular Plates with Large Deflections", *5th International Congress of Applied Mechanics*, Cambridge, 1938, pp. 123-128.

110. Williams, D.J., "Initially Deformed Bridge Panels", *Civil Engineering and Public Works Review*, Oct., 1971, pp. 1107-1112.

111. Wilson, E.L., "SOLID SAP", *Structural Engineering and Structural Mechanics Research Report*, Department of Civil Engineering, University of California, Berkeley, Report No. 71-19, Sept., 1971.

112. Wolf, J.P., "Stress Finite Element Models with Independent Strains", *Int. J. Solids and Structures*, Vol. 11, 1975, pp. 555-568.

113. Yang, H.T.Y., "Finite Displacement Plate Flexure by the use of Matrix Incremental Approach", *Int. J. Numerical Methods in Engineering*, Vol. 4, No. 3, 1972, pp. 415-432.

114. Yang, T.Y., and Wagner, R.J., "Snap-Buckling of Nonlinearly-Elastic Finite Element Bars", *Computers and Structures*, Vol. 3, pp. 1473-1481, 1973.

115. Zienkiewicz, O.C., and Cheung, Y.K., "The Finite Element Method in Structural and Continuum Mechanics", *McGraw-Hill*, 1967.

116. Zienkiewicz, O.C., Irons, B.M., Ergatoudis, J., Abmad, S., and Scott, F.C., "Isoparametric and Associated Element Families for Two and Three Dimensional Analysis", Proceedings of a *Course on Finite Element Methods in Stress Analysis*, ed. Holand, I., and Bell, K., Trondheim Tech. University, 1969.

117. Zienkiewicz, O.C., *"The Finite Element Method in Engineering Science"*, McGraw-Hill, 1971.

118. Zienkiewicz, O.C., Too, J., and Taylor, R.L., "Reduced Integration Technique in General Analysis of Plates and Shells", *Int. J. Numerical Methods in Engineering*, Vol. 3, 1971, pp. 273-290.

APPENDIX A

CONSISTENT NODAL LOADING FOR APPLIED POINT LOADS

In order to translate externally applied loads into generalised loads, in a manner consistent with the element formulation, it is necessary to express the transverse displacement w of the plate in terms of the generalised displacements. Suppose that in each subelement i ; $i = 1, 2, 3, 4$, w is expressed as a function of the subelement nodal parameters $\{q_i\}$. For example, over subelement 1

$$w = w_o W_{o,1}(x,y) + \phi_o \Phi_{1,1}(x,y) + \psi_o \bar{\Psi}_{o,1}(x,y) + w_1 W_{1,1}(x,y)$$

$$+ \phi_1 \Phi_{1,1}(x,y) + \psi_1 \bar{\Psi}_{1,1}(x,y) + w_2 W_{2,1}(x,y) + \phi_2 \Phi_{2,1}(x,y)$$

$$+ \psi_2 \bar{\Psi}_{2,1}(x,y) + \phi_{12} \Phi_{12}(x,y)$$

where $W_{o,1}(x,y)$, $\Phi_{o,1}(x,y)$ and $\bar{\Psi}_{o,1}(x,y)$ etc. are weighting functions.

The elements of the consistent load vector are obtained by multiplication of the point load F, applied at a point (x_n, y_n) within a subelement i, or on it's interface, by the local values of the weighting functions $W_{o,1}(x,y)$ etc, evaluated at the point (x_n, y_n). The total virtual work is obtained by adding the four subelement contributions

$$w(x_n,y_n)\ F = \sum_{i=1}^{4} \{q_i\}^T \{f_i\} = \{P\}^T \sum_{i=1}^{4} [M_i]^T \{f_i\}$$

$$= \{P\}^T \{f\},$$

where $\{P\}^T = \langle w_1, \phi_1, \psi_1, w_2, \phi_2, \psi_2, w_3, \phi_3, \psi_3, w_4, \phi_4, \psi_4, w_o, \phi_o, \psi_o, \phi_{12}, \phi_{23}, \phi_{34}, \phi_{41} \rangle$;

$\{f\}$ is the generalised (consistent) load vector conjugate to the nineteen nodal parameters $\{P\}$

and $\{q_i\} = [M_i]\ \{P\}$, where $[M_i]$; $i = 1,4$ represent the localising matrices which address the subelement parameters to the element parameters $\{P\}$. Hence

$$\{f\} = \sum_{i=1}^{4} [M_i]^T \{f_i\}$$

To obtain the generalised loads conjugate to the final conforming generalised displacements $\{\delta\}$ it is necessary to incorporate a transformation matrix $[N]$ relating $\{P\}$ to the 12 global degrees of freedom $\{\delta^e\}$, $\{P\} = [N]\{\delta^e\}$ which may be derived according to the procedures described in Section II-6. Thus, the consistent load vector to represent a point load F applied transversely to the CQ12 element,

$$\{R\} = [N]^T \left(\sum_{i=1}^{4} [M_i]^T \{f_i\} \right)$$

If the point load is applied on a subelement interface, then the average of the contributions of the virtual work associated with the displacement function of the adjacent subelements was considered to represent the total virtual work.

The weighting functions for subelement 1 are as follows

$$W_{o,1} = \left(1 - \frac{x}{a} - \frac{y}{b} \right)^2 \left(1 + 2\frac{x}{a} + 2\frac{y}{b} \right)$$

$$\Phi_{o,1} = x \left(1 - \frac{x}{a} - \frac{y}{b} \right)^2$$

$$\underline{\psi}_{o,1} = y \left(1 - \frac{x}{a} - \frac{y}{b} \right)^2$$

$$W_{1,1} = \frac{x}{a} \left(3\frac{x}{a} + 6\frac{y}{b} - 2\frac{x^2}{a^2} - 6\frac{x}{a}\frac{y}{b} - 6\frac{y^2}{b^2} \right)$$

$$\Phi_{1,1} = x \left(-\frac{x}{a} - \frac{y}{b} + \frac{x^2}{a^2} + \frac{x}{a}\frac{y}{b} + \frac{y^2}{b^2} \right)$$

$$\underline{\psi}_{1,1} = y\frac{x}{a} \left(2 - \frac{x}{a} - 2\frac{y}{b} \right)$$

$$W_{2,1} = \frac{y^2}{b^2} \left(3 - 2\frac{y}{b} \right)$$

$$\Phi_{2,1} = x\frac{y}{b} \left(1 - \frac{x}{a} \right)$$

$$\underline{\psi}_{2,1} = y\frac{y}{b} \left(-1 + \frac{y}{b} \right)$$

$$\Phi_{12} = 4x\frac{y}{b} \left(-1 + \frac{x}{a} + \frac{y}{b} \right)$$

To obtain the weighting functions for subelement 2 it is necessary to change a into -c and the functions of node 1 correspond to the functions of node 2, and for subelement 3 it is necessary to change b into -d and the functions of node 2 correspond to the functions of node 4. To obtain the weighting function for subelement 4 it is necessary to incorporate both changes [35].

APPENDIX B - DERIVATION OF GEOMETRICALLY NONLINEAR STIFFENED MATRICES

B-1 SECANT AND TANGENT STIFFNESS OF PLANAR SHELL ELEMENT

This section describes an arrangement of terms which enables the geometrically nonlinear secant and tangent stiffness matrices (or the corresponding pseudo force vectors due to nonlinearities) of a thin planar shell element to be evaluated with the minimum computational effort. One matrix may be derived as the linear combination of the terms of another.

The total potential energy of a continuum, V , may be divided into two components

$$V = \sum_e U^e - \{\delta\}^T\{R\}$$

where the strain energy of an element e

$$U^e = \frac{1}{2}\int_{vol} \{\varepsilon\}^T [D]\{\varepsilon\} d\,vol$$

and $\{\sigma\} = [D]\{\varepsilon\}$ as discussed in chapter I.

Employing the Von Karman theory of large displacements, the generalised strain vector of a thin planar shell element (see equation (X-2)) may be divided into linear and nonlinear componenets, denoted by subscripts o and N respectively.

$$\{\varepsilon\} = \begin{Bmatrix} e_o \\ \chi_o \end{Bmatrix} + \begin{Bmatrix} e_N \\ 0 \end{Bmatrix} \text{ where } \{e_N\} = \begin{Bmatrix} \frac{1}{2} w,x^2 \\ \frac{1}{2} w,y^2 \\ w,x\,w,y \end{Bmatrix}$$

The generalised strain vector is related to the nodal parameters $\{\delta\}$ by differentiating the displacement functions. Thus

$$\{\varepsilon\} = [B]\begin{Bmatrix} \delta^{p\ell} \\ \delta^b \end{Bmatrix} \text{ where } [B] = \begin{bmatrix} [B_o^{p\ell}] & . \\ . & [B_o^b] \end{bmatrix} + \begin{bmatrix} . & [B_N^b(\delta^b)] \\ . & . \end{bmatrix}$$

where the superscripts $p\ell$ and b are used to differentiate between terms associated with the plane stress and plate bending nodal parameters respectively.

It is convenient to write the nonlinear strain component in the form

$$\{e_N\} = \frac{1}{2}[A][G]\{\delta^b\}$$

where $[A] = \begin{bmatrix} w,x & . \\ . & w,y \\ w,y & w,x \end{bmatrix}$ and $\begin{Bmatrix} w,x \\ w,y \end{Bmatrix} = [G]\{\delta^b\}$

The expression for the strain energy of the element may then be expanded to

$$U^e = \frac{1}{2}\begin{Bmatrix}\delta^{pl}\\ \delta^b\end{Bmatrix}^T \int_{vol} \left[\begin{array}{c|c} [B_o^{pl}]^T[D^{pl}][B_o^{pl}] & [B_o^{pl}]^T[D^{pl}]\tfrac{1}{2}[A][G] \\ \hline \tfrac{1}{2}[G]^T[A]^T[D^{pl}][B_o^{pl}] & [B_o^b]^T[D^b][B_o^b] \\ & +\tfrac{1}{2}[G]^T[A]^T[D^{pl}][A][G] \end{array}\right] d\,vol \begin{Bmatrix}\delta^{pl}\\ \delta^b\end{Bmatrix} \quad \ldots \quad (B\text{-}1.1)$$

where $\{\sigma\} = \begin{Bmatrix} S \\ M \end{Bmatrix} = \begin{bmatrix} [D^{pl}] & . \\ . & [D^b] \end{bmatrix} \begin{Bmatrix} e_o + e_N \\ \chi_o \end{Bmatrix}$

The generalised approach to the derivation of the geometrically nonlinear stiffness matrices presented by Rajasekaran and Murray [82] is shown in Appendix B-2 to result in an expression for the strain energy of the form

$$U^e = \begin{Bmatrix}\delta^{pl}\\ \delta^b\end{Bmatrix}^T \int_{vol} \left[\begin{array}{c|c} \tfrac{1}{2}[B_o^{pl}]^T[D^{pl}][B_o^{pl}] & \tfrac{1}{6}[B_o^{pl}]^T[D^{pl}][A][G] \\ \hline \tfrac{1}{6}[G]^T[A]^T[D^{pl}][B_o^{pl}] & \tfrac{1}{2}[B_o^b][D^b][B_o^b] \\ & +\tfrac{1}{12}[G]^T[A]^T[D^{pl}][A][G] \\ & +\tfrac{1}{6}[G]^T[N_o][G] \\ & +\tfrac{1}{12}[G]^T[N_N][G] \end{array}\right] d\,vol \begin{Bmatrix}\delta^{pl}\\ \delta^b\end{Bmatrix} \quad \ldots \quad (B\text{-}1.2)$$

where $[N_o]$ and $[N_N]$ are the components of the membrane stress related to the linear and nonlinear strain components respectively.

$$[N] = [N_o] + [N_N] = \begin{bmatrix} S_x & S_{xy} \\ S_{xy} & S_y \end{bmatrix}$$

This form is "repeated" in the secant and tangent stiffness matrices where the integrand terms with coefficients of ($\frac{1}{2}$, $\frac{1}{6}$ $\frac{1}{12}$) in the strain energy expression take the coefficients of (1, $\frac{1}{2}$, $\frac{1}{3}$) and (1, 1, 1) in the secant and tangent stiffness matrices respectively. It is shown in Appendix B-2 that these alternative forms of the strain energy are equivalent. However, the latter form has a disadvantage in that it is not possible to retain the geometric stiffness component $[K_g]$, and the initial displacement stiffness component $[K_i]$, as separate identities [31], and for many problems the geometric stiffness is required to measure the stability of the structure [117]

$$[K_t] = [K_o] + [K_i] + [K_g]$$

where $$[K_g] = \int_{vol} [G]^T [N] [G] d\,vol$$

accounts for the energy released when membrane stresses act through strains produced by transverse displacements. The former approach is therefore preferred here.

The equilibrium equations may be derived by applying the principle of stationary total potential energy;

$$\{R\} = \frac{\partial U}{\partial \{\delta\}} = [K_s]\{\delta\}$$

The secant stiffness of the continuum is most conveniently determined by considering each element separately and evaluating each component of the strain-energy gradient in turn:

i) $$\partial/\partial\{\delta\} \left(\tfrac{1}{2}\{\delta^{p\ell}\}^T \int_{vol} [B_o^{p\ell}]^T [D^{p\ell}] [B_o^{p\ell}] d\,vol\ \{\delta^{p\ell}\}\right)$$

$$= \int_{vol} [B_o^{p\ell}]^T [D^{p\ell}] [B_o^{p\ell}] d\,vol\ \{\delta^{p\ell}\}$$

considering one nodal parameter at a time

ii) $$\partial/\partial\{\delta\} \left(\tfrac{1}{2}\{\delta^{b}\}^T \int_{vol} [B_o^{b}]^T [D^{b}] [B_o^{b}] d\,vol\ \{\delta^{b}\}\right)$$

$$= \int_{vol} [B_o^{b}]^T [D^{b}] [B_o^{b}] d\,vol\ \{\delta^{b}\}$$

iii) $$\partial/\partial\{\delta\} \left(\tfrac{1}{2}\{\delta^{p\ell}\}^T \int_{vol} [B_o^{p\ell}]^T [D^{p\ell}] \tfrac{1}{2}[A] [G] d\,vol\ \{\delta^{b}\}\right)$$

$$= \tfrac{1}{2} < \{\delta^{p\ell}\}^T \int_{vol} [B_o^{p\ell}]^T [D^{p\ell}] [A] [G] d\,vol >^T$$

$$+ \tfrac{1}{2} \int_{vol} [B_o^{p\ell}]^T [D^{p\ell}] \tfrac{1}{2} [A] [G] d\,vol\ \{\delta^{b}\}$$

The first term is derived from the chain rule of partial derivatives [117];

$$d\left(\tfrac{1}{2}[A] [G] \{\delta^b\}\right) = \tfrac{1}{2}(d[A]) [G] \{\delta^b\} + \tfrac{1}{2}[A] (d[G] \{\delta^b\})$$

$$= [A] [G]\, d\{\delta^b\}$$

iv) Similarly

$$\partial/\partial\{\delta\} \left(\tfrac{1}{2}\{\delta^{b}\}^T \int_{vol} \tfrac{1}{2}[G]^T [A]^T [D^{p\ell}] [B_o^{p\ell}] d\,vol \{\delta^{p\ell}\}\right)$$

$$= \tfrac{1}{2} \int_{vol} [G]^T [A]^T [D^{p\ell}] [B_o^{p\ell}] d\,vol \{\delta^{p\ell}\}$$

$$+ \tfrac{1}{2} \int_{vol} [B_o^{p\ell}]^T [D^{p\ell}] \tfrac{1}{2} [A] [G] d\,vol\ \{\delta^{b}\}$$

v) $$\partial/\partial\{\delta\}\left(\tfrac{1}{2}\{\delta^b\}^T \int_{vol} \tfrac{1}{4}[G]^T[A]^T[D^{p\ell}][A][G]\,d\,vol\,\{\delta^b\}\right)$$

$$= \tfrac{1}{2}\int_{vol} [G]^T[A]^T[D^{p\ell}][A][G]\,d\,vol\,\{\delta^b\}$$

Thus

$$[K_s]\begin{Bmatrix}\delta^{p\ell}\\ \delta^b\end{Bmatrix} = \int_{vol}\left[\begin{array}{c|c} [B_o^{p\ell}]^T[D^{p\ell}][B_o^{p\ell}] & \tfrac{1}{2}[B_o^{p\ell}]^T[D^{p\ell}][A][G] \\ \hline [G]^T[A]^T[D^{p\ell}][B_o^{p\ell}] & [B_o^b]^T[D^b][B_o^b] \\ & +\tfrac{1}{2}[G]^T[A]^T[D^{p\ell}][A][G] \end{array}\right] d\,vol \begin{Bmatrix}\delta^{p\ell}\\ \delta^b\end{Bmatrix} \quad \ldots \text{(B-1.3)}$$

It is convenient to rearrange the secant stiffness to a symmetric form. This may be achieved by combining half the first order coupling terms with half the second order terms. i.e.,

$$\int_{vol} \tfrac{1}{2}[G]^T[A]^T[D^{p\ell}][B_o^{p\ell}]\{\delta^{p\ell}\} + \tfrac{1}{4}[G]^T[A]^T[D^{p\ell}][A][G]\{\delta^b\}\,d\,vol \quad \ldots \text{(B-1.4)}$$

$$= \int_{vol} \tfrac{1}{2}[G]^T[A]^T[D^{p\ell}]([B_o^{p\ell}]\{\delta^{p\ell}\} + \tfrac{1}{2}[A][G]\{\delta^b\})\,d\,vol$$

$$= \int_{vol} \tfrac{1}{2}[G]^T[A]^T\{S\}\,d\,vol$$

But $$[A]^T\{S\} = [N][G]\{\delta^b\}$$

Thus the secant stiffness may be written

$$[K_s] = \left[\begin{array}{c|c} [B_o^{p\ell}]^T[D^{p\ell}][B_o^{p\ell}] & \tfrac{1}{2}[B_o^{p\ell}][D^{p\ell}][A][G] \\ \hline & [B_o^b]^T[D^b][B_o^b] \\ \tfrac{1}{2}[G]^T[A]^T[D^{p\ell}][B_o^{p\ell}] & +\tfrac{1}{4}[G]^T[A]^T[D^{p\ell}][A][G] \\ & +\tfrac{1}{2}[G]^T[N][G] \end{array}\right] \quad \ldots \text{(B-1.5)}$$

$$= \left[\begin{array}{c|c} [K_o^{p\ell}] & \tfrac{1}{2}[SR] \\ \hline \tfrac{1}{2}[SR]^T & [K_o^b] + \tfrac{1}{4}[R^*R] + \tfrac{1}{2}[Kg] \end{array}\right] \quad \ldots \text{(B-1.6)}$$

The secant stiffness matrix is not unique. However, the strain energy U^e of an element is a unique scalar quantity, although any expression defining this quantity can be rearranged with a different grouping of terms while retaining the same definition (see equations B-1.1 and B-1.2). This is demonstrated in Appendix B-2. Therefore, the force vector $[K_s]\{\delta\} = \frac{\partial U^e}{\partial\{\delta\}}$ (see equation (B-1.3)) will always be unique, although the components of the individual terms may be rearranged at will, and consequently no difficultues are experienced during the equation solving procedure.

The tangent stiffness may be derived by computing the second derivative of the strain energy with respect to the generalised displacements $\{\delta\}$, and is of the same form as the secant stiffness defined in equation (B-1.6) but all coefficients of the component terms take the value of one [117].

$$[K_t] = \left[\begin{array}{c|c} [K_o^{p\ell}] & [SR] \\ \hline [SR]^T & [K_o^b] + [RR] + [Kg] \end{array}\right]$$

B-2 GENERALISED DERIVATION OF SECANT AND TANGENT STIFFNESS

In this section a generalised approach to the derivation of the geometrically nonlinear stiffness matrices, applicable to any type of finite element, is described. The strain energy expression resulting from this approach is shown to be equivalent to the expression described in equation (B-1.1).

Rajasekaran and Murray [82] have shown that, if the strain energy associated with an elastic geometrically nonlinear deformation of a finite element are written in suitable form, the total potential energy may be expressed in terms of Lagrangian coordinates as,

$$V = S^T[\ \tfrac{1}{2}K + \tfrac{1}{6}N_1 + \tfrac{1}{12}N_2]\ \delta - \delta^T R \qquad \ldots \quad (B\text{-}2.1)$$

The equilibrium equations are obtained by differentiating the total potential energy with respect to the generalised displacements,

$$[K + \tfrac{1}{2}N_1 + \tfrac{1}{3}N_2]\delta = R \qquad \ldots \quad (B\text{-}2.2)$$

which may be differentiated in turn to obtain the linearised incremental equations

$$[K + N_1 + N_2]\Delta\delta = \Delta R \qquad \ldots \quad (B\text{-}2.3)$$

This simple progression is justified as follows:

If the generalised strain components are designated as ε_i and the corresponding stresses as σ_i then for a linear elastic constitutive matrix C_{ij}

$$\sigma_i = C_{ij}\,\varepsilon_j \qquad \ldots \quad (B\text{-}2.4)$$

in which summation convention is implied. The strain energy may then be evaluated from the expression

$$U = \tfrac{1}{2}\int_{vol} \varepsilon_i\, C_{ij}\, \varepsilon_j\, d\,vol \qquad \ldots \quad (B\text{-}2.5)$$

Each generalised strain component may be decomposed into linear and nonlinear components, denoted by superscripts o and N respectively

$$\varepsilon_i = \varepsilon_i^o + \varepsilon_i^N \qquad \ldots \quad (B\text{-}2.6)$$

and the total potential energy of an element expressed as

$$V = \tfrac{1}{2} \int_{vol} C_{ij} \, (\varepsilon_i^o \, \varepsilon_j^o + 2\,\varepsilon_i^o \, \varepsilon_j^N + \varepsilon_i^N \, \varepsilon_j^N) \, d\,vol - \delta^T R \quad \ldots \quad (B\text{-}2.7)$$

It is now convenient to express the strains in matrix notation

$$\varepsilon_i = L_i^T d + \tfrac{1}{2} d^T H_i d \qquad \ldots \quad (B\text{-}2.8)$$

where L_i is a vector, H_i a symmetric matrix, and d is the vector of displacement gradients contributing to the strains ε_i .

Consider, for example, the membrane strains of a thin planar shell element

$$\begin{aligned} \varepsilon_1 &= u,x + \tfrac{1}{2}(w,x)^2 \\ \varepsilon_2 &= v,y + \tfrac{1}{2}(w,y)^2 \\ \varepsilon_3 &= u,y + v,x + w,x.w,y \end{aligned} \qquad \ldots \quad (B\text{-}2.9)$$

Thus, $d^T = \langle u,x, \; u,y, \; v,x, \; v,y, \; w,x, \; w,y \rangle$

$$L_1^T = \langle 1 \quad 0 \quad 0 \quad 0 \quad 0 \quad 0 \rangle$$

$$L_2^T = \langle 0 \quad 0 \quad 0 \quad 1 \quad 0 \quad 0 \rangle$$

$$L_3^T = \langle 0 \quad 1 \quad 1 \quad 0 \quad 0 \quad 0 \rangle$$

$$H_1 = \text{diag} \; \langle 0 \quad 0 \quad 0 \quad 0 \quad 1 \quad 0 \rangle \qquad \ldots \quad (B\text{-}2.10)$$

$$H_2 = \text{diag} \; \langle 0 \quad 0 \quad 0 \quad 0 \quad 0 \quad 1 \rangle$$

$$H_3 = \begin{bmatrix} . & . & . & . & . & . \\ . & . & . & . & . & . \\ . & . & . & . & . & . \\ . & . & . & . & . & . \\ . & . & . & . & . & 1 \\ . & . & . & . & 1 & . \end{bmatrix}$$

Substituting this expression for the strains, the total potential energy of an element

$$V = \tfrac{1}{2} \int_{vol} C_{ij} d^T \, [L_i L_j^T + L_i d^T H_j + \tfrac{1}{4} H_i d d^T H_j] \, d\,vol - \delta^T R \quad \ldots \quad (B\text{-}2.11)$$

$$= \int_{vol} I_1 \, d\,vol + \int_{vol} I_2 \, d\,vol + \int_{vol} I_3 \, d\,vol - \delta^T R \qquad \ldots \quad (B\text{-}2.12)$$

in which I_1, I_2, and I_3 are the integrands defined by identification

with the corresponding terms of equation (B-2.11).

Equation (B-2.11) must be written in the form

$$V = \int_{vol} d^T [\tfrac{1}{2}\hat{K} + \tfrac{1}{6}\hat{N}_1 + \tfrac{1}{12}\hat{N}_2]d \; d\,vol - \delta^T R \qquad \ldots \quad (B\text{-}2.13)$$

in order to obtain the progression expressed in equations (1), (2) and (3) Rajasekaran and Murray [82] have selected the following grouping of terms to achieve this purpose:

$$I_1 = \tfrac{1}{2}d^T \hat{K} d = d^T C_{ij} L_i L_j^T d \qquad \ldots \quad (B\text{-}2.14)$$

$$I_2 = \tfrac{1}{6}d^T \hat{N}_1 d = \tfrac{1}{6}C_{ij}\, d^T (L_i d^T H_j + d^T L_i H_j + H_i\, d\, L_j^T)d \quad \ldots (B\text{-}2.15)$$

$$I_3 = \tfrac{1}{12}\, d^T \hat{N}_2 d = \tfrac{1}{12}C_{ij} d^T (H_i d d^T H_j + \tfrac{1}{2} d^T H_j\, d\, H_i)d \quad \ldots \quad (B\text{-}2.16)$$

which are valid because $L^T d$, $d^T L$, and $d^T H d$ are scalars and thus may be commuted, transposed, and inserted in arbitrary locations within other matrix products. Also, since C_{ij} is symmetric the summation indices may be changed at will.

The integrand terms of the membrane component of a thin plate element, derived by Rajasekaran and Murray [82] for an isotropic material, are as follows:

how to get this matrix

$$\hat{K} = \begin{bmatrix} C_{11} & \cdot & \cdot & C_{12} & \cdot & \cdot \\ & C_{33} & C_{33} & \cdot & \cdot & \cdot \\ & & C_{33} & \cdot & \cdot & \cdot \\ \text{(Symmetric)} & & & C_{22} & \cdot & \cdot \\ & & & & 0 & \cdot \\ & & & & & 0 \end{bmatrix} \qquad \ldots \quad (B\text{-}2.17)$$

$$\hat{N}_1 = \begin{bmatrix} 0 & \cdot & \cdot & \cdot & \begin{bmatrix} C_{11} w_{,x} & C_{12} w_{,y} \end{bmatrix} \\ & 0 & \cdot & \cdot & \begin{bmatrix} C_{33} w_{,y} & C_{33} w_{,x} \end{bmatrix} \\ & & 0 & \cdot & \begin{bmatrix} C_{33} w_{,y} & C_{33} w_{,x} \end{bmatrix} \\ & & & 0 & \begin{bmatrix} C_{12} w_{,x} & C_{22} w_{,y} \end{bmatrix} \\ & & & & (C_{11} u_{,x} + C_{12} v_{,y}) \; C_{33}(u_{,y} + v_{,x}) \\ \text{(Symmetric)} & & & & (C_{22} v_{,y} + C_{12} u_{,x}) \end{bmatrix} \qquad \cdots (B\text{-}2.18)$$

$$\hat{N}_2 = \begin{bmatrix} 0 & . & . & . & . & . \\ & 0 & . & . & . & . \\ & & 0 & . & . & . \\ & & & 0 & . & . \\ & \text{(Symmetric)} & & & A & B \\ & & & & & C \end{bmatrix} \qquad \ldots \quad \text{(B-2.19)}$$

where $A = \frac{3}{2} C_{11} w,x^2 + \frac{1}{2} C_{12} w,y^2 + C_{33} w,y^2$

$B = 2 C_{33} w,x.w,y + C_{12} w,x\, w,y$

$C = \frac{3}{2} C_{22} w,y^2 + C_{33} w,x^2 + \frac{1}{2} C_{12} w,x^2$

It will now be demonstrated that this approach leads to the strain energy expression described in equation (B-1.2).

Considering each nonlinear term in turn:

i) $$\{\delta^{p\ell}\} \int_{vol} \tfrac{1}{6} [B_o^{p\ell}]^T [D^{p\ell}] [A] [G] d\,vol \{\delta^b\}$$

$$= \tfrac{1}{6} \int_{vol} \begin{Bmatrix} u,x \\ u,y \\ v,x \\ v,y \end{Bmatrix} \begin{bmatrix} 1 & 0 & 0 \\ 0 & 0 & 1 \\ 0 & 0 & 1 \\ 0 & 1 & 0 \end{bmatrix} \begin{bmatrix} C_{11} & C_{12} & 0 \\ C_{12} & C_{22} & 0 \\ 0 & 0 & C_{33} \end{bmatrix} \begin{bmatrix} w,x & 0 \\ 0 & w,y \\ w,y & w,x \end{bmatrix} \begin{Bmatrix} w,x \\ w,y \end{Bmatrix} d\,vol \qquad \ldots \quad \text{(B-2.20)}$$

$$= \tfrac{1}{6} \int_{vol} \begin{Bmatrix} u,x \\ u,y \\ v,x \\ v,y \end{Bmatrix} \begin{bmatrix} C_{11} w,x & C_{12} w,y \\ C_{33} w,y & C_{33} w,x \\ C_{33} w,y & C_{33} w,x \\ C_{12} w,x & C_{22} w,y \end{bmatrix} \begin{Bmatrix} w,x \\ w,y \end{Bmatrix} d\,vol \qquad \ldots \quad \text{(B-2.21)}$$

which corresponds with the component of the strain energy expression associated with the submatrix of $\hat{N}_1$ in equation (B-2.13)

ii) The transpose of term i) follows automatically because the matrix $\hat{N}_1$ is symmetric.

iii) $$\{\delta^b\}^T \int_{vol} \tfrac{1}{6} [G]^T [N_o] [G] d\,vol \{\delta^b\}$$

$$= \tfrac{1}{6} \int_{vol} \begin{Bmatrix} w,x \\ w,y \end{Bmatrix}^T \begin{bmatrix} S_{x_o} & S_{xy_o} \\ S_{xy_o} & S_{y_o} \end{bmatrix} \begin{Bmatrix} w,x \\ w,y \end{Bmatrix} d\,vol \qquad \ldots \quad \text{(B-2.22)}$$

$$= \tfrac{1}{6} \int_{vol} \begin{Bmatrix} w,x \\ w,y \end{Bmatrix}^T \begin{bmatrix} C_{11}\, u,x + C_{12}\, v,y & C_{33}(u,y + v,x) \\ \text{(Symmetric)} & C_{22}\, v,y + C_{12}\, u,x \end{bmatrix} \begin{Bmatrix} w,x \\ w,y \end{Bmatrix} d\,vol$$

... (B-2.23)

which corresponds with the component of the strain energy expression associated with the remaining terms of matrix $\hat{N}_1$

iv) $$\{\delta^b\}^T \int_{vol} \tfrac{1}{12} [G]^T [A]^T [D^{p\ell}] [A] [G] d\,vol \{\delta^b\}$$

$$= \tfrac{1}{12} \int_{vol} \begin{Bmatrix} w,x \\ w,y \end{Bmatrix}^T \begin{bmatrix} w,x & 0 & w,y \\ 0 & w,y & w,x \end{bmatrix} \begin{bmatrix} C_{11} & C_{12} & 0 \\ C_{12} & C_{22} & 0 \\ 0 & 0 & C_{33} \end{bmatrix} \begin{bmatrix} w,x & 0 \\ 0 & w,y \\ w,y & w,x \end{bmatrix} \begin{Bmatrix} w,x \\ w,y \end{Bmatrix} d\,vol$$

... (B-2.24)

$$= \tfrac{1}{12} \int_{vol} \begin{Bmatrix} w,x \\ w,y \end{Bmatrix}^T \begin{bmatrix} C_{11} w,x^2 + C_{33} w,y^2 & C_{11} w,x\, w,y + C_{33} w,x\, w,y \\ \text{(Symmetric)} & C_{22} w,y^2 + C_{33} w,x^2 \end{bmatrix} \begin{Bmatrix} w,x \\ w,y \end{Bmatrix} d\,vol$$

... (B-2.25)

which corresponds with the component of the strain energy expression associated with a fraction of the terms of the matrix $\hat{N}_2$ in equation (B-2.13).

v) $$\{\delta^b\}^T \int_{vol} \tfrac{1}{12} [G]^T [N_N] [G] d\,vol \{\delta^b\}$$

$$= \tfrac{1}{12} \int_{vol} \begin{Bmatrix} w,x \\ w,y \end{Bmatrix}^T \begin{bmatrix} S_{x_N} & S_{xy_N} \\ S_{xy_N} & S_{y_N} \end{bmatrix} \begin{Bmatrix} w,x \\ w,y \end{Bmatrix} d\,vol \qquad \ldots \text{(B-2.26)}$$

$$= \tfrac{1}{12} \int_{vol} \begin{Bmatrix} w,x \\ w,y \end{Bmatrix}^T \begin{bmatrix} \tfrac{1}{2} C_{11} w,x^2 + \tfrac{1}{2} C_{12} w,y^2 & C_{33} w,x\, w,y \\ \text{(Symmetric)} & \tfrac{1}{2} C_{22} w,y^2 + \tfrac{1}{2} C_{12} w,x^2 \end{bmatrix} \begin{Bmatrix} w,x \\ w,y \end{Bmatrix} d\,vol$$

... (B-2.27)

which corresponds with the component of the strain energy expression of equation (B-2.13) associated with the remaining terms of $\hat{N}_2$

The correspondence of the terms associated with the matrix $[\hat{K}]$ is immediately evident.

It remains to show that the two forms of the strain energy described in equations B-1.1 and B-1.2 are equivalent. Thus it must be shown that:

i) the terms $$\{\delta^b\}^T \int_{vol} \tfrac{1}{6} [G]^T [A]^T [D^{p\ell}] [B_o^{p\ell}] d\,vol \{\delta^{p\ell}\}$$

and $\{\delta^b\}^T \int_{vol} \frac{1}{6} [G]^T [N_o] [G] d\,vol \{\delta^b\}$ are equivalent.

Expanding the expression for the first term, given by equation (B-2.21) yields

$$\frac{1}{6}\int_{vol} [w,x^2 (u,x\, C_{11} + v,y C_{22}) + w,y^2 (C_{12} u,x + C_{22} v,y) + w,x\, w,y 2C_{33} (u,y + v,x)]\, d\,vol$$

This is the same result as obtained by expanding the expression for the second term, given by equation (B-2.23).

ii) the terms $\{\delta^b\}^T \int_{vol} \frac{1}{12} [G]^T [A]^T [D^{p\ell}] [A] [G] d\,vol \{\delta^b\}$

and $\{\delta^b\} \int_{vol} \frac{1}{6} [G]^T [N_N] [G] d\,vol \{\delta^b\}$ are equivalent.

Expanding the expression for the first term, given by equation (B-2.25) yields

$$\frac{1}{12}\int_{vol} [w,x^4 C_{11} + w,y^4 C_{22} + w,x^2\, w,y^2 (2C_{12} + 4C_{33})]\, d\,vol$$

This is the same as the result obtained by expanding the expression for the second term given by equation (B-2.27).

Felippa [31] has noted that it would be more useful if the strain energy expression obtained from this generalised approach was repeatable in the "geometric" stiffnes K_g and the "initial displacement" stiffness K_i rather than $\hat{N}_1$ and $\hat{N}_2$ but this is not possible.

B-3 SECANT AND TANGENT STIFFNESS OF BEAM ELEMENT

The following interpolatory displacement functions were used to derive the geometrically nonlinear stiffness matrices of a beam element:

Axial displacement

$$v_c = (1 - \frac{y}{L}) v_1 + \frac{y}{L} v_2 \qquad \ldots \quad (B\text{-}3.1)$$

Horizontal transverse displacement

$$u_c = (1 - \frac{3y^2}{L^2} + \frac{2y^3}{L^3}) u_1 + (\frac{3y^2}{L^2} - \frac{2y^3}{L^3}) u_2 + (-y + \frac{2y^2}{L} - \frac{y^3}{L^2}) \theta z_1 + (\frac{y^2}{L} - \frac{y^3}{L^2}) \theta z_2 \qquad \ldots \quad (B\text{-}3.2)$$

Vertical transverse displacement

$$w_c = (1 - \frac{3y^2}{L^2} + \frac{2y^3}{L^3})w_1 + (\frac{3y^2}{L^2} - \frac{2y^3}{L^3})w_2$$

$$- (-y + \frac{2y^2}{L} - \frac{y^3}{L^2})\Theta x_1 - (\frac{y^2}{L} - \frac{y^3}{L^2})\Theta x_2 \quad \ldots \quad (B\text{-}3.3)$$

Twisting rotation

$$\Theta y_c = (1 - \frac{y}{L})\Theta y_1 + \frac{y}{L}\Theta y_2 \quad \ldots \quad (B\text{-}3.4)$$

which define the displacements (v_c, u_c, w_c, Θy_c) along the centroidal y-axis (see Fig. VI-1) but neglect shear deformations, as discussed in section (X-10).

The displacements at any point (x,z) across the section may be determined from the relationships;

$$v = v_c - \frac{\partial u_c}{\partial y}.x - \frac{\partial w_c}{\partial y}.z \quad \ldots \quad (B\text{-}3.5)$$

$$u = u_c + \Theta y_c.z \quad \ldots \quad (B\text{-}3.6)$$

$$w = w_c - \Theta y_c.x \quad \ldots \quad (B\text{-}3.7)$$

Green's strain tensor [9,117] were used to define the strain-displacement relationships for a three dimensional solid,

$$\varepsilon_{xx} = \frac{\partial u}{\partial x} + \tfrac{1}{2}\left[(\frac{\partial u}{\partial x})^2 + (\frac{\partial v}{\partial x})^2 + (\frac{\partial w}{\partial x})^2\right] \quad \ldots \quad (B\text{-}3.8)$$

$$\varepsilon_1 = \varepsilon_{yy} = \frac{\partial v}{\partial y} + \tfrac{1}{2}\left[(\frac{\partial u}{\partial y})^2 + (\frac{\partial v}{\partial y})^2 + (\frac{\partial w}{\partial y})^2\right]$$

$$= v_{c,y} - x.u_{c,yy} - z.w_{c,yy} + \tfrac{1}{2}\left[u_{c,y}^2 + v_{c,y}^2 + w_{c,y}^2\right.$$

$$+ 2u_{c,y}.\Theta y_{c,y}.z + \Theta y_{c,y}^2.z^2 + 2u_{c,yy}.w_{c,yy}.xz - 2v_{c,y}.u_{c,yy}.x$$

$$\left. - 2v_{c,y}.w_{c,yy}.z + u_{c,yy}^2.x^2 + w_{c,yy}^2.z^2 - 2w_{c,y}.\Theta y_{c,y}.x + \Theta y_{c,y}^2.x^2\right] \quad \ldots \quad (B\text{-}3.9)$$

$$\varepsilon_{zz} = \frac{\partial w}{\partial x} + \tfrac{1}{2}\left[(\frac{\partial u}{\partial z})^2 + (\frac{\partial v}{\partial z})^2 + (\frac{\partial w}{\partial z})^2\right] \quad \ldots \quad (B\text{-}3.10)$$

$$\varepsilon_2 = \varepsilon_{xy} = \frac{\partial u}{\partial y} + \frac{\partial v}{\partial x} + \left[\frac{\partial u}{\partial y}.\frac{\partial u}{\partial x} + \frac{\partial v}{\partial y}.\frac{\partial v}{\partial x} + \frac{\partial w}{\partial y}.\frac{\partial w}{\partial x}\right]$$

$$= u_{c,y} + \Theta y_{c,y}.z - u_{c,y} - u_{c,y}.v_{c,y} + u_{c,y}.u_{c,yy}.x$$

$$+ \left[u_{c,y}.w_{c,yy}.z - w_{c,y}.\Theta y_c + \Theta y_c.\Theta y_{c,y}.x\right] \quad \ldots \quad (B\text{-}3.11)$$

$$\varepsilon_3 = \varepsilon_{yz} = \frac{\partial v}{\partial z} + \frac{\partial w}{\partial y} + [\frac{\partial u}{\partial y} \cdot \frac{\partial u}{\partial z} + \frac{\partial v}{\partial y} \cdot \frac{\partial v}{\partial z} + \frac{\partial w}{\partial y} \cdot \frac{\partial w}{\partial z}]$$

$$= - w_{c,y} + w_{c,y} - \Theta y_{c,y} \cdot x + [\Theta y_c (u_{c,y} + \Theta y_{c,y} \cdot z)$$

$$- v_{c,y} \cdot w_{c,y} + w_{c,y} \cdot u_{c,yy} \cdot x + w_{c,y} \cdot w_{c,yy} \cdot z] \quad \ldots \quad (B\text{-}3.12)$$

$$\varepsilon_4 = \varepsilon_{zx} = \frac{\partial w}{\partial x} + \frac{\partial u}{\partial z} + [\frac{\partial u}{\partial z} \cdot \frac{\partial u}{\partial x} + \frac{\partial v}{\partial z} \cdot \frac{\partial v}{\partial x} + \frac{\partial w}{\partial z} \cdot \frac{\partial w}{\partial x}]$$

$$= - \Theta y_c + \Theta y_c + u_{c,y} \cdot w_{c,y} \quad \ldots \quad (B\text{-}3.13)$$

Note that the two stress components σ_{xx} and σ_{zz} are zero throughout a three dimensional beam element so the conjugate strain components ε_{xx} and ε_{zz} can be neglected because they do not contribute to the strain energy.

The derivation of the stiffness matrices will continue along the lines of the generalised approach suggested by Rajasekeran and Murray [82] and discussed in Appendix B-2. The generalised strains may be expressed in the form

$$\varepsilon_i = L_i^T d + \tfrac{1}{2} d^T H_i d \; ; \quad i = 1,4 \quad \ldots \quad (B\text{-}3.14)$$

for which L_i is a vector, H_i a symmetric matrix, and d is the vector of displacement gradients contributing to the generalised strains $\varepsilon_i = \varepsilon_{yy}, \varepsilon_{xy}, \varepsilon_{yz}, \varepsilon_{zx}$. Thus, for a three dimensional beam element

$$d^T = < u,y \;\; v,y \;\; w,y \;\; w,yy \;\; w,x(=-\Theta y) \;\; u,yy \;\; \Theta y,y \; >$$

and the nodal parameters are

$$\delta^T = < u_1 \; v_1 \; w_1 \; \Theta x_1 \; \Theta y_1 \; \Theta z_1 \; u_2 \; v_2 \; w_2 \; \Theta x_2 \; \Theta y_2 \; \Theta z_2 >$$

The vectors L_i and matrices H_i may be identified from equations (B-3.8) and (B-3.13)

$$\begin{aligned}
L_1^T &= < 0 \;\; 1 \;\; 0 \;\; -z \;\; 0 \;\; -x \;\; 0 > \\
L_2^T &= < 0 \;\; 0 \;\; 0 \;\; 0 \;\; 0 \;\; 0 \;\; z > \\
L_3^T &= < 0 \;\; 0 \;\; 0 \;\; 0 \;\; 0 \;\; 0 \;\; -x > \\
L_4^T &= < 0 \;\; 0 \;\; 0 \;\; 0 \;\; 0 \;\; 0 \;\; 0 >
\end{aligned} \quad \ldots \quad (B\text{-}3.15)$$

$$H_1 = \begin{bmatrix} 1 & . & . & . & . & . & z \\ & 1 & . & -z & . & -x & . \\ & & 1 & . & . & . & -x \\ & & & z^2 & . & xz & . \\ & & & & . & . & . \\ & \text{(Symmetric)} & & & & x^2 & . \\ & & & & & & (x^2+z^2) \end{bmatrix} \quad \ldots \quad \text{(B-3.16)}$$

$$H_2 = \begin{bmatrix} 0 & -1 & . & z & . & x & . \\ & 0 & . & . & . & . & . \\ & & 0 & . & . & . & . \\ & & & 0 & . & . & . \\ & & & & 0 & . & -x \\ & \text{(Symmetric)} & & & & 0 & . \\ & & & & & & 0 \end{bmatrix} \quad \ldots \quad \text{(B-3.17)}$$

$$H_3 = \begin{bmatrix} 0 & . & . & . & -1 & . & . \\ & 0 & -1 & . & . & . & . \\ & & 0 & z & . & x & . \\ & & & 0 & . & . & . \\ & & & & 0 & . & -z \\ & \text{(Symmetric)} & & & & 0 & . \\ & & & & & & 0 \end{bmatrix} \quad \ldots \quad \text{(B-3.18)}$$

$$H_4 = \begin{bmatrix} . & . & 1 & . & . & . & . \\ . & . & . & . & . & . & . \\ 1 & . & . & . & . & . & . \\ . & . & . & . & . & . & . \\ . & . & . & . & . & . & . \\ . & . & . & . & . & . & . \\ . & . & . & . & . & . & . \end{bmatrix} \quad \ldots \quad \text{(B-3.19)}$$

The constitutive relationship between stress and strain may be written

$$\begin{Bmatrix} \sigma_{yy} \\ \sigma_{xy} \\ \sigma_{yz} \\ \sigma_{zx} \end{Bmatrix} = \begin{bmatrix} E & . & . & . \\ & \tfrac{1}{2}E/(1+\nu) & . & . \\ & & \tfrac{1}{2}E(1+\nu) & . \\ & \text{(Symmetric)} & & \tfrac{1}{2}E(1+\nu) \end{bmatrix} \begin{Bmatrix} \varepsilon_{yy} \\ \varepsilon_{xy} \\ \varepsilon_{yz} \\ \varepsilon_{zx} \end{Bmatrix} \quad \ldots \quad \text{(B-3.20)}$$

or in tensor notation, $\sigma_i = C_{ij}\,\varepsilon_j$.

$$V = \tfrac{1}{2}\int_{vol} \varepsilon_i^T C_{ij}\,\varepsilon_j \, d\,vol - \delta^T R$$

which may be expressed in the form

$$V = \int_{vol} C_{ij} d^T [\tfrac{1}{2} L_i L_j^T + \tfrac{1}{6}(L_i d^T H_j + d^T L_i H_j + H_i dL_j^T) + \tfrac{1}{12}(H_i dd^T H_j + \tfrac{1}{2} d^T H_j dH_i)]d\,vol - \delta^T.R \quad \ldots \quad (B\text{-}3.22)$$

(see appendix B-2).

$$= \int_{vol} d^T [\tfrac{1}{2}\hat{K} + \tfrac{1}{6}\hat{N}_1 + \tfrac{1}{12}\hat{N}_2]d\,vol - \delta^T.R \quad \ldots \quad (B\text{-}3.23)$$

$$= \delta^T \int_{vol} D^T [\tfrac{1}{2}\hat{K} + \tfrac{1}{6}\hat{N}_1 + \tfrac{1}{12}\hat{N}_2]D\,d\,vol\,\delta - \delta^T.R \quad \ldots \quad (B\text{-}3.24)$$

$$(\text{where } d = D\delta) = \delta^T \int_{vol} [\tfrac{1}{2}K + \tfrac{1}{6}N_1 + \tfrac{1}{12}N_2]d\,vol\,\delta - \delta^T.R \quad \ldots \quad (B\text{-}3.25)$$

The secant stiffness $K_s = K + \tfrac{1}{2}N_1 + \tfrac{1}{3}N_2$
and the tangent stiffness $K_t = K + N_1 + N_2$ as discussed in appendix B-2.

The geometrically nonlinear stiffnes matrices N_1, N_2, for a three dimensional beam element were derived by first forming the matrices $\hat{N}_1$ and $\hat{N}_2$, then pre- and post-multiplying by the matrix D which relates the vector of displacement gradients d to the generalised elements displacements δ , and finally performing the routine analytic integration associated with equation (B-3.24).

The partially integrated matrices, $N_1^* = \int N_1\,dx\,dy$ and $N_2^* = \int N_2\,dx\,dz$, derived for a prismatic three dimensional beam element , are listed in tables B-3.1 and B-3.2 respectively. The elements of the nonlinear stiffness matrices were determined by integrating the terms of the matrices N_1^* and N_2^* along the beam axis.

TABLE B-3.1 THREE DIMENSIONAL BEAM ELEMENT

$$N_l^* = \int C_{ij} \left[L_i d^T H_j + d^T L_i H_j + H_i d L_j^T \right] dxdz$$

$EA\, v,y$	$EA\, u,yy$	.	$-EI_{xx}\, \Theta y,y$ $+GI_{xx}\, \Theta y,y$	.	.	$-EI_{xx}\, w,yy$ $+GI_{xx}\, w,yy$
	$3EA\, v,y$	$EA\, w,y$	$3EI_{xx}\, w,yy$	.	$3EI_{zz}\, u,yy$	$EI_{xx}\, \Theta y,y$ $+EI_{zz}\, \Theta y,y$
		$EA\, v,y$	.	.	$EI_{zz}\, \Theta y,y$ $-GI_{zz}\, \Theta y,y$	$-GI_{zz}\, u,yy$ $+EI_{zz}\, u,yy$
			$3EI_{xx}\, v,y$	.	.	$-EI_{xx}\, u,y$ $+GI_{xx}\, u,y$
	(SYMMETRIC)			.	.	.
					$3EI_{zz}\, v,y$	$EI_{zz}\, w,y$ $-GI_{zz}\, w,y$
						$EI_{xx}\, v,y$ $+GI_{xx}\, v,y$

TABLE B-3.2 THREE DIMENSIONAL BEAM ELEMENT

$$N_2^* = \int C_{ij} [H_i \, dd^T H_j + \tfrac{1}{2} d^T H_j \, d H_i] dx \, dz$$

$$N_2^*(1,1) = EA\,u,y^2 + GA\,v,y^2 + GA\,w,y^2 + GI_{xx}\,w,yy^2 + GI_{zz}\,u,yy^2 + EI_{xx}\,\Theta y,y^2 + GA\,w,x^2 + \alpha$$

where

$$\alpha = \tfrac{1}{2}[EA(u,y^2 + v,y^2 + w,y^2) + EI_{xx}\,w,yy^2 + EI_{zz}\,u,yy^2 + E(I_{xx} + I_{zz})\Theta y,y^2],$$

A = cross-sectional area of beam element

I_{xx} = moment of inertia about local x axis of beam element = $bt^3/12$

I_{zz} = moment of inertia about local z axis of beam element = $tb^3/12$

E = Young's modulus of elasticity

G = Shear modulus

$$N_2^*(1,2) = (EA + GA)u,y\,v,y - EI_{xx}\Theta y,y\,w,yy + \tfrac{1}{2}[GA(2u,y\,v,y - 2w,x\,w,y]$$

$$N_2^*(1,3) = (EA + GA)\,u,y\,w,y + \tfrac{1}{2}[2GAu,y\,w,y]$$

$$N_2^*(1,4) = (EIX + 2GI_{xx})u,y\,w,yy - EI_{xx}\Theta y,y\,v,y$$

$$N_2^*(1,5) = 2GA\,u,y\,w,x - GI_{zz}\Theta y,y\,u,yy$$

$$N_2^*(1,6) = (EI_{zz} + 2GI_{zz})u,y\,u,yy - GI_{zz}\,\Theta y,y\,w,x$$

$$N_2^*(1,7) = (3EI_{xx} + EI_{zz})u,y\,\Theta y,y - GI_{zz}\,w,x\,u,yy - EI_{xx}\,v,y\,w,yy$$

$$N_2^*(2,2) = GA\,u,y^2 + EA\,v,y^2 + GA\,w,y^2 + EI_{xx}\,w,yy^2 + EI_{zz}\,u,yy^2 + \alpha$$

$$N_2^*(2,3) = (EA + 2GA)\,v,y\,w,y + EI_{zz}\,\Theta y,y\,u,yy$$

$$N_2^*(2,4) = 3EI_{xx}\,v,y\,w,yy - EI_{xx}\,u,y\,\Theta y,y$$

$$N_2^*(2,5) = (GA - EA)\,u,y\,w,y$$

$$N_2^*(2,6) = 3EI_{zz}\,v,y\,u,yy + EI_{zz}\Theta y,y\,w,y$$

$$N_2^*(2,7) = (EI_{xx} + EI_{zz})\,v,y\,\Theta y,y - EI_{xx}\,u,y\,u,yy + EI_{zz}\,w,y\,w,yy$$

$$N_2^*(3,3) = GA\,u,y^2 + GA\,v,y^2 + EA\,w,y^2 + GI_{xx}\,w,yy^2 + GI_{zz}\,u,yy^2 + EI_{zz}\,\Theta y,y^2 + GA\,w,x^2 + \alpha$$

$$N_2^*(3,4) = (EI_{xx} + 2GI_{xx})\,w,y\,w,yy - GI_{xx}\,\Theta y,y\,w,x$$

$$N_2^*(3,5) = 2GA\,w,y\,w,x - GI_{xx}\,\Theta y,y\,w,yy$$

$$N_2^*(3,6) = (EI_{zz} + 2GI_{zz})\, w,y\, u,yy^2 + EI_{zz}\, \Theta y,y\, v,y$$

$$N_2^*(3,7) = (3EI_{zz} + EI_{xx})\, \Theta y,y\, w,y - GI_{xx}\, w,x\, w,yy + EI_{zz}\, v,y\, u,yy$$

$$N_2^*(4,4) = (GI_{xx} + \tfrac{1}{2}EI_{xx})\, u,y^2 + \tfrac{3}{2}\, EI_{xx}\, v,y^2 + (GI_{xx} + \tfrac{1}{2}EI_{xx})\, v,y^2 + \tfrac{9}{20}EI_{xx}\, t^2 w,yy^2$$
$$+ \tfrac{3}{24}EI_{xx}\, b^2\, u,yy^2 + (\tfrac{3}{40}EI_{xx}\, t^2 + \tfrac{1}{24}EI_{xx}\, b^2)\, \Theta y,y^2$$

$$N_2^*(4,5) = -\, GI_{xx}\, \Theta y,y\, w,y$$

$$N_2^*(4,6) = \tfrac{1}{4}\, EI_{xx}\, b^2\, w,yy\, u,yy$$

$$N_2^*(4,7) = -\, EI_{xx}\, u,y\, v,y - GI_{xx}\, w,y\, w,x$$
$$+ (\tfrac{1}{12}\, b^2 + \tfrac{3}{20}\, t^2)\, EI_{xx}\, \Theta y,y\, w,yy$$

$$N_2^*(5,5) = GA\, u,y^2 + GA\, w,y^2 + (GI_{xx} + GI_{zz})\, \Theta y,y^2$$

$$N_2^*(5,6) = -\, GI_{zz}\, u,y\, \Theta y,y$$

$$N_2^*(5,7) = (EI_{xx} + EI_{zz} + GI_{xx} + GI_{zz})\, \Theta y,y\, w,x - GI_{zz}\, u,y\, u,yy - GI_{xx}\, w,y\, w,yy$$

$$N_2^*(6,6) = (GI_{zz} + \tfrac{1}{2}\, EI_{zz})\, u,y^2 + \tfrac{3}{2}\, EI_{zz}\, v,y^2 + (GI_{zz} + \tfrac{1}{2}\, EI_{zz})\, w,y^2$$
$$+ \tfrac{1}{8}\, EI_{xx}\, b^2\, w,yy^2 + \tfrac{9}{40}\, EI_{zz}\, b^2\, u,yy^2$$
$$+ (\tfrac{3}{20}\, EI_{zz}\, b^2 + \tfrac{1}{12}\, EI_{xx} b^2)\, \Theta y,y^2$$

$$N_2^*(6,7) = EI_{zz}\, v,y\, w,y - GI_{zz}\, u,y\, w,x + (\tfrac{3}{20}\, EI_{zz}\, b^2 + \tfrac{1}{12}\, EI_{xx}\, b^2)\, \Theta y,y\, u,yy$$

$$N_2^*(7,7) = EI_{xx}\, u,y^2 + GI_{zz}\, w,y^2 + (GI_{xx} + GI_{zz})\, w,x^2$$
$$+ (\tfrac{3}{20}\, EI_{xx}\, t^2 + \tfrac{3}{20}\, EI_{zz}\, b^2 + \tfrac{1}{6}\, EI_{xx}\, b^2)\, \Theta y,y^2$$
$$+ \tfrac{1}{2}[EI_{xx} + EI_{zz}]\, (u,y^2 + v,y^2 + w,y^2) + \tfrac{1}{12}\, EI_{xx}\, b^2\, (u,yy^2 + w,yy^2 + 2\Theta y,y^2)$$
$$+ \tfrac{3}{20}\, EI_{xx}\, t^2 (w,yy^2 + \Theta y,y^2) + \tfrac{3}{20}\, EI_{zz}\, b^2 (u,yy^2 + \Theta y.y^2)$$

$$N_2^*(j,i) = N_2^*(i,j)\ ;\quad i = 1,7\ ,\quad j = 1,7$$